Myoendothelial junction heterogeneity and pathways of vasodilation

Claire A. Ruddiman
Cary, North Carolina

B.S., Biochemistry, North Carolina State University, 2017
B.S., Chemical Engineering, North Carolina State University, 2017
M.S., Biological Sciences, University of Virginia, 2019

A Dissertation presented to the Graduate Faculty of the University of Virginia in Candidacy for the Degree of Doctor of Philosophy

Department of Pharmacology

University of Virginia
August 2022

Brant E. Isakson, PhD

Shayn Peirce-Cottler, PhD

Thurl Harris, PhD

Swapnil Sonkusare, PhD

Abstract

Myoendothelial junctions (MEJ) are key signaling microdomains in resistance arteries, the key component of the vasculature in regulating blood pressure. Anatomically, they are endothelial cell (EC) projections that connect with smooth muscle cells (SMC) in the arterial wall through projecting through holes in the internal elastic lamina (HIEL), the extracellular matrix that separates the two cell types. Specific protein localization to the MEJ coordinates vasodilation in resistance arteries through endothelial derived hyperpolarization (EDH).

In **Chapter 2**, I describe the structural and functional consequences of inducing MEJ formation in a conduit artery, which results in a shift from nitric oxide (NO) to EDH based signaling. In **Chapter 3**, I (1) provide evidence that every HIEL contains an MEJ, (2) demonstrate that MEJs are randomly distributed in endothelium, (3) implicate lipid localization as a determinant for MEJ heterogeneity, (4) propose a function for PS localization at a subpopulation of MEJs, and (5) introduce a mouse model for disrupting MEJ signaling. In **Chapter 4**, I (1) show that a mouse model with elastin deleted from ECs disrupts IEL morphology in resistance arteries, (2) vasodilation shifts from EDH to NO based signaling, and (3) SMC function is affected by EC elastin deposition. In **Chapter 5**, I investigate the molecular composition of the IEL in resistance arteries and speculate how this may contribute to HIEL stability. In **Chapter 6**, I report on an effort to create a custom antibody to identify vascular connexins.

Altogether, my data converges on the following key ideas: (1) MEJs are stable structures with heterogenous protein composition that is determined by local

lipid composition, (2) the anatomical MEJ coordinates protein expression and localization to form functional microdomains, and (3) EC-derived elastin deposition coordinates MEJ formation and signaling within the resistance arterial wall.

Table of Contents

List of Abbreviations

AA	abdominal aorta
ACE	angiotensin converting enzyme
Ach	acetylcholine
Akap	A-kinase anchoring protein
BUN	blood urea nitrogen
bpm	beats per minute
CA	carotid artery
Cav1	caveolin-1
CBC	complete blood count
cGMP	cyclic guanosine monophosphate
CHRM3	acetylcholine muscarinic M3 receptor
CO	cardiac output
Col	collagen
CO_2	carbon dioxide
Cspg	chondroitin sulfate proteoglycan
CTD	cytoplasmic domain
Cx37	connexin 37
Cx40	connexin 40
Cx43	connexin 43
DAG	diacylglycerol
EC	endothelial cell
eNOS	endothelial nitric oxide synthase

ECM	extracellular matrix
EDH	endothelial derived hyperpolarization
EEL	external elastic laminae
EETs	epoxyeicosatrienoic acids
EMILIN	elastin microfibril interface located protein
ER	endoplasmic reticulum
Hba	hemoglobin alpha or alpha globin
HEK293T	human embryonic kidney 293T cells
Hspg	heparan sulfate proteoglycan
IEL	internal elastic lamina
IK_{Ca}	intermediate Ca^{2+} activated-potassium channel
IP_3R	inositol-1,4,5-triphosphate receptor
K^+	potassium
KCl	potassium chloride
Kir2.1	inwardly rectifying potassium channel 2.1
HIEL	hole in the internal elastic lamina
L-NAME	L-N^G-Nitro arginine methyl ester
LTP	lipid transfer protein
MAGP	microfibril associated glycoproteins
MCH	mean corpuscular hemoglobin
MCHC	mean corpuscular hemoglobin concentration
MCS	membrane contact sites
MCV	mean corpuscular volume

MEJ	myoendothelial junction
MLC	myosin light chain
MLCK	myosin light chain kinase
MLCP	myosin light chain phosphatase
MMP	matrix metalloproteinase
MPV	mean platelet volume
Myh	myosin
NC	negative control
NO	nitric oxide
ORP	oxysterol-binding protein-related proteins
O_2	oxygen
PAI-1	plasminogen activator inhibitor-1
PC	positive control
PC	phosphatidylcholine
PE	phenylephrine
PE	phosphatidylethanolamine
PH	pleckstrin homology
PIP_2	phosphatidylinositol 4,5-bisphosphate
PI4P	phosphatidylinositol 4-phosphate
PKC	protein kinase C
PKG	protein kinase G
PLA	proximity ligation assay
PLC	phospholipase C

PM	plasma membrane
PS	phosphatidylserine
PSD	phosphatidylserine decarboxylase
PSS	phosphatidylserine synthase
RAND	random
RDW	red cell distribution width
RBC	red blood cell
SEM	scanning electron microscope
SERCA	sarco-/endoplasmic reticulum Ca-ATPase
sGC	soluble guanylyl cyclase
SK_{Ca}	small conductance potassium channel
SMC	smooth muscle cell
SR	sarcoplasmic reticulum
TDA	thoracodorsal artery
TEM	transmission electron microscopy
TH	tyrosine hydroxylase
TMD	transmembrane domain
TPR	total peripheral resistance
TRPV4	transient receptor potential vanilloid-type 4
VCCC	vascular cell co-culture
WBC	white blood cells
α-GA	α-glycyrrhetinic acid
$[Ca^{2+}]$	calcium concentration

Dedication

There are so many people to thank who have supported me throughout my time here in the BIMS program at UVA. First, I want to take the time to thank my mentor, Brant Isakson. Thank you for giving me so many opportunities to grow in your lab, including working on the PAI-1 project, writing and scoring 5% on the F31, and doing science in Dusseldorf, Germany. I am forever grateful for the generosity you have shown towards me in providing all of these opportunities. Thank you also for letting me create a project from questions that intrigued both of us. At the beginning of my time in the lab, I was fixated on how HIEL were patterned, and at times I was unsure how it would tie into the rest of my work, but you believed in me and had faith that it would come together in the end. And you were right! It tickles me to see how some of my very first data got incorporated into the final publication. Your positivity and trust in my ideas has kept me motivated to complete this project.

To past members of the lab, Miranda Good, Steven Keller, Leon DeLalio, Scott Johnstone, Yang Yang: thank you for welcoming me into the Isakson Lab! To Miranda, thank you for teaching me vasoreactivity. That technique has been such an integral part of my work and I am so proud to say that I learned from the best. I hope I have made you proud! To Steven, I will never forget you sending me home with a 50ml conical to practice opening it with one hand so that sterile technique was much easier in cell culture experiments. Thanks for always being there to chat and give me encouragement. Leon, thank you for letting me collaborate on your Panx1 project and for giving me constructive criticism on

project design early on. Your productivity has always been inspiring to me! Scott, I am glad my time in Brant's lab overlapped with your second tour. I have learned so much molecular biology from you. And, of course, it's not a party without you, thanks for all the laughs! Yang, I am so happy I joined the lab at the beginning of your two years in Charlottesville. Thanks for always being a positive voice. I miss you all the time and I hope our paths will cross again in the future. Thank you also to other past members, Isola Brown, Alex Keller, Edgar Macal, and Sarah Murphy.

To current members, we endured the COVID-19 pandemic together and I am so thankful to have been with a fun and supportive group of people. To Abby, thank you for all the times you have talked me through data, ideas, and panic attacks. To Melissa, I am so glad that you joined the Isakson Lab and I know the vaso room is in great hands with you. You two are extremely talented and I know you are going far in life. I am happy to have overlapped with you. To Angie, thank you for keeping the lab running and handling all protocols and orders. I am so thankful to have been able to focus on science knowing you were taking care of all of that. To Luke, good luck fellow southerner!

I am also thankful for my time spent with the graduate student society Women in Medical Sciences. I enjoyed serving on the board and working with a great group of women to promote community and science outreach. I'm also extremely thankful for the GBS events that helped me settle into Charlottesville when I first moved here, like tubing on the James River and the Sunset Series at Carter Mountain

David, thank you for being such a strong positive force in my life. In grad school, we have evolved from boyfriend and girlfriend, to fiancés, to husband and wife. Your constant encouragement and support have carried me through grad school and I am so grateful for that. Thank you for always researching fun things to do in Charlottesville and having something planned on the weekend for us. I'm so thankful that we lived in Charlottesville together, where we found our beautiful, sweet puppy, Tessie. I love you so much and I am excited for our next chapter!

Diane, thank you for being the best sister and always answering the phone and talking to me at almost any time of the day. As my older sister, I always have looked up to you and your interest in science made me think it was so cool! And, you were right. You're my best friend and I am so thankful for your pep talks and our random conversations. Also, thank you for marrying, Orlando (Love you, O!), and having the cutest possible kids, Mason, and Miles, who always know how to make me smile.

To the rest of my family, I cannot thank you enough for your support. To my parents, thank you for always believing in me and encouraging me to pursue math and science. I would not be where I am today without your support of my education. To my brothers, Don, Chris, Phil, and my twin, Jon, you have always showed up for me. To my in-laws, Kevin and Sharon O'Donnell, and my brother-in-laws, Bill and Jason O'Donnell, thank you for always checking on me and for your support over the past 12 years.

Thank you to my friends who I've had the pleasure of making memories with throughout the time in grad school and who have always had encouraging words

-- Chelsea, Andrea, Erin, Carly, and Katie – thank you for being part of my life! And a special shout out to Carly, who refused to let me fly alone to Dusseldorf, Germany, for the lab rotation.

Last, but not least, for any graduate student who is interested in MEJs and may have picked up this thesis…. Grad school is challenging. We all expect the intellectual challenge, but there will be times where it can be physically and emotionally challenging, too. If you enter the “valley of despair” (where you are unsure of where your project is heading or if you should be working on that project at all), don’t worry, there is a light at the end of the tunnel, especially in the Isakson Lab. Good luck!

Chapter 1. The role of the circulation in blood pressure homeostasis

Some sections adapted from: Francesca Leo, Beate Hutzler, Claire A. Ruddiman, Brant E. Isakson, Miriam Cortese-Krott. Cellular microdomains for nitric oxide signaling in endothelium and red blood cells. Nitric Oxide. 1 March 2020.

Some sections adapted from (* indicates co-first authorship):

Wolpe AG*, Ruddiman CA*, Hall PJ, Isakson BE. Polarized Proteins in Endothelium and Their Contribution to Function. J Vasc Res. 2021;58(2):65-91. doi: 10.1159/000512618. Epub 2021 Jan 27. PMID: 33503620; PMCID: PMC7954879.

Introduction to the circulation

The circulatory system is comprised of the heart and vasculature and provides the body with oxygen and nutrients to sustain life. The heart is divided into four chambers to keep oxygenated blood and deoxygenated blood separated and to ensure directional flow. The right atrium collects deoxygenated blood from the systemic circulation and when full opens the tricuspid valve to dispense blood into the right ventricle, which pumps this deoxygenated blood through the pulmonary valve where the blood then circulates through the pulmonary circulation to re-oxygenate. This freshly oxygenated blood travels back to the left atrium and

through the mitral valve into the left ventricle. The left ventricle contracts to push the blood through the aortic valve and into the aortic arch. The blood circulates through the arterial side of the circulation where arteries branch off from the aorta and get consecutively smaller as the distance from the heart increases until they reach the capillary beds. After gas exchange at the capillary level, the blood returns to the heart to be re-oxygenated by flowing into the veins, which increase in size as they approach the heart.

The arterial wall is composed of three main layers, endothelial cells (ECs) that line the lumen, the vascular smooth muscle cells (VSMCs) on the exterior of the vessel that are aligned perpendicularly to EC, and an extracellular matrix layer that separates the two cell types termed the internal elastic lamina (IEL). As the arteries branch and become smaller in diameter, the number of VSMC layers decrease and the IEL morphology also changes (discussed at length later in this chapter). The continual branching and reduction of VSMC eventually leads into capillary beds, where an individual capillary consists only of an endothelial cell layer and is equivalent in diameter to an erythrocyte or red blood cell (RBC). This allows single-file flow of RBC through capillaries to facilitates the nutrient and gas exchange to allow for continued tissue metabolism and function. As the blood flows through venules and veins on its way back to the heart to be re-oxygenated, it encounters numerous valves that ensure correct directional flow in the opposite direction of gravity.

RBC comprise approximately 40% of blood with the role of delivering oxygen (O_2) to tissues and to eliminate the waste product carbon dioxide (CO_2)

through gas exchange. RBCs are unusual because they do not contain organelles or nuclei like other cell types, rather they contain large amounts of the protein hemoglobin. Hemoglobin assembles as a tetramer, canonically with two alpha chains and two beta chains, where each subunit contains a polypeptide chain and a heme group containing an iron molecule that can bind oxygen; thus, each functional tetramer can cooperatively bind four molecules of O_2. CO_2 does not bind to the heme sites, but rather binds to another part of the protein that induces conformational changes that do not support O_2 binding. In the lungs, when the partial pressure of O2 is high, hemoglobin favors O_2 binding; in contrast, in the tissues, CO_2 partial pressures are high such that CO_2 competes for binding on the protein. These concentration gradients allow for unloading and loading of gases onto hemoglobin to facilitate gas exchange for O_2 delivery to tissue and CO_2 exhalation. Following O_2 delivery, blood flows to the venous circulation that will eventually brought back to the right atrium via the vena cava in order to get re-oxygenated in the pulmonary circulation before returning to the systemic circulation.

Blood pressure (BP) is a crucial component to the proper functioning of the circulatory system and without pressure driving blood flow, gas and nutrient exchange would not occur. Blood pressure must be maintained in a specific range because hypotension (low BP) is not adequate for normal tissue function and hypertension (high BP) leads to blood vessels and organ damage. In 2017, the American Heart Association defined normal BP as 120mmHg systolic and less than 80mmHg diastolic, with 121-129 mmHg systolic readings classified as

elevated (**Table 1**), and 80-89 mmHg diastolic readings characteristic of stage 1 hypertension. Thus, even small changes in blood pressure that deviate from homeostasis can be pathological and the human body has evolved to tightly regulate these pressures.

Cardiac output is one of the determinants of BP and is the product of heart rate and stroke volume, which is the volume of blood that is ejected from the ventricle following its contraction. This corresponds with the systolic blood pressure measurement. The peripheral vasculature contributes to blood pressure by providing resistance to flow, and this is referred to as total peripheral resistance and corresponds with the diastolic measurement.

The major contributors to TPR are resistance arteries that are between 100 and 200μm in diameter, whereas large arteries function mainly as a conduit for flow. As arteries branch off of the aorta, they decrease in vessel size and increase in number such that they have a surface area several magnitudes higher than large conduit arteries. The mathematical definition of pressure is $P = \frac{F}{A}$, where F is force and A is area; thus, in the resistance arteries, the denominator of this equation increases and drives a large decrease in pressure in the resistance sized arteries. This is why there is such a large pressure drop over the arterioles and not the conduit arteries. This pressure drop is functionally important in order to regulate the amount of flow into local capillary beds, which can be damaged easily by unregulated flow or may need more flow based on metabolic need such as in exercise.

Since the largest pressure drop occurs in resistance arteries, any vasodilation or vasoconstriction in these vessels will have the largest influence on diastolic blood pressure measurements. This change in pressure can be understood by Poiseuille's Law, $\Delta P = \frac{8\eta LQ}{\pi R^4}$, which assumes laminar flow and that flow is occurring in an enclosed tube, and where η is blood viscosity, L is length of the artery, Q is flow rate, and R is radius of the artery. This equation reveals that the most important factor in determining the pressure within an enclosed tube is its radius. The inverse relationship of pressure and radius of the blood vessel to the fourth power (r^4) demonstrates that any small change in the resistance arterial diameter via vasodilation or vasoconstriction will have large effects on intraluminal pressure and thus the TPR component of BP. It therefore follows that the molecular pathways that dictate changes in arterial diameter are tightly regulated in these resistance arteries in order to prevent or facilitate significant changes in overall blood pressure.

BLOOD PRESSURE CATEGORY	SYSTOLIC mm Hg (upper number)	and/or	DIASTOLIC mm Hg (lower number)
NORMAL	LESS THAN 120	and	LESS THAN 80
ELEVATED	120 – 129	and	LESS THAN 80
HIGH BLOOD PRESSURE (HYPERTENSION) STAGE 1	130 – 139	or	80 – 89
HIGH BLOOD PRESSURE (HYPERTENSION) STAGE 2	140 OR HIGHER	or	90 OR HIGHER
HYPERTENSIVE CRISIS (consult your doctor immediately)	HIGHER THAN 180	and/or	HIGHER THAN 120

Table 1. American Heart Association blood pressure guidelines. Table taken from www.heart.org.

Pathways of vasodilation

As described in the previous section, resistance arteries are crucial determinants of blood pressure. In resistance arteries, the IEL is unique in that it has a high incidence of holes in the IEL (HIEL), where there is an absence of ECM proteins such as collagen, elastin, laminin, and fibrinogen. The ECs of these arteries send projections through these HIEL and make direct contact with the smooth muscle, forming a signaling microdomain that is imperative to regulating diameter in the resistance arteries termed the myoendothelial junction (MEJ). Although rare, SMC projections through HIEL have also been reported. (1) In a study of the dog pulmonary vasculature, MEJs that were EC projections into HIEL were most common compared to SMC extension or both EC and SMC extension into HIEL, (1) and in humans arterioles, 40% of MEJs originate from SMC.(2)

The MEJ was first discovered in electron micrographs of coronary and kidney arterioles as an anatomical structure that positioned the membranes of EC and SMC in close apposition with each other. (3, 4) The incidence of MEJ depends on vascular bed and species varies, but it is been well demonstrated that incidence increases as vessel diameter decreases. (5) The unique protein localization that occurs at MEJs facilitate endothelial derived hyperpolarization (EDH), the dominant vasodilatory signaling mechanism in resistance arterioles (**Table 2**). (6-10) (5, 11)

Key players of EDH which localize to the MEJ include transient receptor potential vanilloid 4 (TRPV4), calcium-activated intermediate conductance potassium (IK_{Ca}) channels, and hemoglobin alpha (Hba or alpha globin). TRPV4

channels facilitate calcium influx at the MEJ, (12, 13) (14) downstream of acetylcholine activation of the muscarinic 3 receptor (CHRM3) on EC. The increased cytoplasmic concentration of calcium leads to potassium efflux from the IK_{Ca} channel. (15) Given the close proximity of the EC and SMC membranes at the MEJ, this efflux of potassium ions makes the SMC relatively more negative compared to the extracellular environment, results in a hyperpolarization of SMC membranes, (6, 8, 16, 17) deactivates voltage dependent calcium channels, and leads to vasodilation. (18) The calcium-activated small conductance potassium channel (SK_{Ca}) also participate in EDH-based vasodilation (19) (20) despite their primary localization to interendothelial junctions opposed to the MEJ. (15) The inwardly rectifying potassium channel Kir2.1 has also been implicated in the EDH pathway (21) although its localization to the MEJ has not yet been demonstrated.

Full Name	Tissue	Cell Culture	Luminal	MEJ-Localized	Inter-endothelial
A kinase anchoring protein 150 (AKAP150)	Mouse mesenteric artery(13)			(13)	
Calnexin (Calnx)	Third order mesenteric artery(22)			(22)	
Calreticulin (Calr)	Third order mesenteric artery(23)	HCAEC (24)		(23, 24)	
Caveolin 1 (Cav1)	Mouse carotid(25) Mouse mesenteric artery(26)	HCAEC (24) HMVEC (27) BCAEC (28)	(25, 27, 28)	(26)	
Connexin 37 (Cx37)	Rat mesenteric artery(15) Mouse mesenteric artery(26) Mouse cremaster arterioles(29) Hamster cheek pouch arteriole(30, 31)			(15, 29)	(15, 26, 31)
Connexin 40 (Cx40)	Rat mesenteric artery(15, 32) Mouse mesenteric artery(26) Mouse cremaster arteriole (29) Hamster cheek pouch arteriole(30, 31)			(29, 32)	(15, 26, 30, 31)
Connexin 43 (Cx43)	Rat mesenteric artery(15) Mouse mesenteric artery(26)			(29)	(15, 26, 30, 31)

Full Name	Tissue	Cell Culture	Luminal	MEJ-Localized	Inter-endothelial
	Mouse cremaster arteriole (29) Hamster cheek pouch arteriole(30, 31)				
Endothelial nitric oxide synthase (eNOS)	Mouse carotid(33) Mouse thoracodorsal artery(34)	Primary HCAEC (24)	(24, 33)	(24),(34)	
Filamentous actin (F-actin)	Mouse cremaster arterioles (29)	HUVEC (35) VCCC (36, 37)		(29, 36, 37)	(35)
Hemoglobin alpha (alpha globin or Hba)	Mouse thoracodorsal artery(38)	HCAEC (39)	(38)	(38, 39)	
Inositol trisphosphate receptor 1 (IP3R1)	Mouse mesenteric artery(22)	VCCC (40, 41)		(22, 40, 41)	
Intermediate conductance calcium-activated potassium channel (IK_{Ca})	Rat cremaster arteriole (42) Rat mesenteric artery(15)			(15, 42)	
N-Cadherin (NCAD)	Mouse cremaster arterioles (29)			(29)	
Plasminogen activator inhibitor 1 (PAI-1)		VCCC (36, 37, 43)		(36, 37, 43)	
Sarco/endoplasmic reticulum Ca^{2+}-ATPase (SERCA)	Mouse thoracodorsal artery(44)			(44)	
Small conductance calcium-activated potassium channel 3 (SK3)	Rat cremaster arteriole (45) Rat mesenteric artery(15)		(45)	(45)	(15)

Full Name	Tissue	Cell Culture	Luminal	MEJ-Localized	Inter-endothelial
Sphingosine-1- phosphate receptor (S1P)	Rat brain capillary endothelium (46)		(46)	(46)	
Transient receptor potential channel subfamily V member 4 (TRPV4)	Mouse 3rd order mesenteric artery (12) Mouse carotid artery(47) Rat cremaster arteriole (42)		(47)	(12, 42)	

Table 2. Protein localization to the MEJ.

Another major contributor to the EDH pathway is metabolites of aracadonic acid. An influx of Ca^{2+} into the cell can activate phospholipase A2 which cleaves glycerophospholipids to mobilize arachidonic acid in the cell, which undergoes enzymatic cleavage to produce vasoactive molecules: (48) where cyclooxygenase-1 produces prostaglandins in vascular endothelium (49), lipoxygenase (LOX) produces leukotrienes, lipoxines and hydroxyeicosatrienoic acids, and cytochrome P450 epoxygenase to produces epoxyeicosatrienoic acids (EETs). Prostacyclin can promote the opening of various potassium channels that lead to hyperpolarization of SMC membrane, (50) and EETs activate TRPV4 Ca^{2+} sparklets and BK_{Ca} channels on SMC (51). It remains unclear how LOX produced metabolites specifically contribute to the EDH pathway. (52)

The hyperpolarization that leads to vasodilation can be communicated from EC to SMC via gap junctional communication. In small arterioles, connexin 37, 40, and 43 are most prevalent (Cx37, Cx40, Cx43, respectively), (15, 29) with Cx40 exhibiting arterial specificity in mice. (53) When assembled as hexamers, connexins form gap junctions that physically link the cytoplasm of two cells. This is the case at the MEJ, where gap junctions can link the cytoplasm of EC and SMC to coordinate vasodilation. (5, 40, 41, 54-56) Heterocellular communication occurs through gap junctions to facilitate EDH (32, 57) and myoendothelial feedback (41, 58, 59).

Myoendothelial feedback is critical in regulating the degree of constriction elicited through -adrenergic activation on SMCs, which occurs when inositol 1,4,5-trisphosphate (IP_3) generated in SMC diffuses through MEJ-localized gap

junctions to activate vasodilatory pathways in ECs as negative feedback regulation. (41, 60-63) When Cx40 gap junctions are blocked by loading inhibitory antibodies, this negative regulation is lost, illustrating the functional importance of gap junctions within this microdomain. (32) The localization of gap junctions to the abluminal surface of the endothelium, and within the MEJ signaling microdomains, is essential for facilitating heterocellular communication via IP_3, Ca^{2+}, and propagating hyperpolarization from EC to SMC. (10)

The endothelium is a major regulator of smooth muscle relaxation and in general communicates vasodilatory signaling via nitric oxide (NO) and/or via endothelial derived hyperpolarization (EDH). The relative contribution of each pathway to vasodilation is correlated with vessel size, where large arteries primarily dilate via NO and small arteries, with a high incidence of MEJs, via EDH. (11, 39, 64-66) NO is produced by nitric oxide synthase (NOS) enzymes, of which there are three isoforms: neuronal NOS, inducible NOS, and endothelial NOS (eNOS), which produce L-citrulline and NO by degrading L-arginine. In endothelium, the NO will diffuse to nearby SMC where binds to soluble guanylyl cyclase (sGC), produces cyclic guanosine monophosphate (cGMP), (67) and activates of myosin light chain phosphatase (MLCP) and protein kinase G (PKG), (68) which leads to SMC relaxation and subsequent vasodilation. (69) Myosin light chain (MLC) is a critical component in SMC contractility and requires phosphorylation by MLC kinases (MLCK) to participate in SMC contractility. (70) Thus, MLCP removes the crucial phosphate groups thereby preventing MLC from contributing to SMC contraction. This method of relaxation acts by preventing

proper contraction in SMC. PKG acts in a similar manner. PKG will activate SERCA and inhibit IP3-R, two channels localized on the sarcoplasmic reticulum that regulate [Ca^{2+}] in the cytosol and SR lumen. Collectively, NO drives Ca^{2+} sequestration to the SR lumen, reducing cytosolic [Ca^{2+}] and calmodulin activation, and ultimately leading to MLCK inhibition. (71) The storage of Ca^{2+} in the SR is therefore another way to prevent SMC contractility and promote vasorelaxation.

One explanation for the higher EDH component in smaller arteries is the expression of hemoglobin alpha (Hba or alpha globin) specifically in resistance artery endothelium. (10, 39) As described previously in this section, the function of hemoglobin in RBC is to transport O_2 to the tissues and deliver CO_2 to the lungs to be exhaled. However, the specific expression of alpha globin in resistance arteries is to regulate signaling of another gaseous molecule: NO.(39) Alpha globin can bind to eNOS such that when eNOS produces NO it is chelated by alpha globin's heme group thereby preventing the diffusion of NO to the SMC layers to promote vasodilation. Alpha globin is specifically enriched within the MEJ of resistance arteries (38, 39). In **Chapter 2**, the data demonstrates that upon induction of MEJs in a conduit artery, alpha globin expression is increased and localized specifically to the newly synthesized MEJs. This protein expression coincides with a switch in vasodilatory pathway from predominately NO to EDH. Together, all these data suggest that the specific expression of alpha globin in resistance arteries, and its targeted localization to the MEJ may influence the dominance of EDH-based vasodilation. (10)

Chapter 2. Heterocellular contact dictates vasodilatory mechanisms, protein expression, and arterial function

Sections adapted from (* indicates co-first authorship):

Shu X*, Ruddiman CA*, Keller TCSt, Keller AS, Yang Y, Good ME, Best AK, Columbus L, Isakson BE. Heterocellular contact can dictate arterial function. *Circ Res*. 2019;124:1473-1481

Abstract

Conduit arteries primarily use nitric oxide (NO) to achieve vasodilation, which can diffuse across the several layers of SMC in those arteries. As arterial diameter decreases, the contribution of NO-based vasodilation also decreases. This is correlated with the presence of MEJs, which are EC extensions that make contact with SMC through holes in the internal elastic lamina, an extracellular matrix layer that separates the two cell types. The MEJs are anatomical hallmarks of resistance arteries and are signaling microdomains that facilitate endothelial-derived hyperpolarization (EDH) through close apposition to and direct contact with the SMC membrane. We sought to determine if the induction of MEJs in conduit arteries could induce heterocellular signaling and alter vasodilation mechanism.

We have previously shown that plasminogen activator inhibitor-1 (PAI-1) can regulate formation of MEJs.(36) Thus our experimental approach was to apply pluronic gel containing PAI-1 directly to the left carotid artery (CA) and to determine if MEJs were induced. Indeed, we found a significant increase in EC projections resembling MEJs in TEM transverse views. This correlated with an increase in biocytin dye transfer from ECs to SMCs in an *ex vivo* assay. We then used pressure myography on PAI-1-treated CA to investigate if the presence of EC projections was accompanied by a functional change in vasodilatory signaling. We found that the PAI-1-treated CAs exhibited diminished NO signaling and increased EDH signaling in response to the EC-dependent dilators Ach and NS309, indicating that these arteries switched their vasodilatory profile to resemble a resistance artery. We also found a significant increase in CA expression of endothelial alpha globin, a protein that is specifically expressed in the resistance arterial endothelium where it can negatively regulate eNOS function. This switch did not occur in PAI-1-treated CA from mice lacking alpha globin ($Hba1^{-/-}$), indicating that alpha globin is critical in facilitating the mechanism of vasodilation. This data indicates that MEJs are a critical component in determining pathways of vasodilation. In particular, alpha globin expression, induced within newly formed EC projections, may influence the balance between EDH vs NO-mediated signaling.

Introduction

Vasodilation is a critical homeostatic process that contributes to blood pressure regulation and generally occurs through two major mechanisms, either via nitric oxide (NO) and/or via endothelial derived hyperpolarization (EDH). NO is produced by nitric oxide synthase (NOS) enzymes, endothelial NOS (eNOS) in the endothelium, ultimately driving Ca^{2+} sequestration to the SR lumen, reducing cytosolic [Ca^{2+}] and calmodulin activation, and thus leading to vasodilation via MLCK inhibition. (71) The EDH based pathway occurs when calcium activates SK_{Ca} and IK_{Ca} to generate a potassium efflux from the cell that hyperpolarizes the SMC membrane and inactivates the voltage dependent calcium channels needed for constriction.(6, 8, 16, 17)

EDH is the major pathway in resistance arteries compared to conduit arteries where NO-based signaling predominates. An anatomical difference exists in the structure of the conduit and resistance arteries that may account for the difference in functional dilation. ECs in resistance arteries have unique signaling microdomains termed MEJs that extend through gaps or holes in the fibrous internal elastic lamina (IEL, and HIEL) to make heterocellular contact with SMCs via gap junctions. (3-5, 72, 73) This direct heterocellular contact allows for rapid communication of the electrochemical changes generated via EDH signaling.(8, 11, 61, 74, 75) Since the MEJ is a crucial facilitator of EDH, it follows that resistance arteries rely primarily on EDH-based vasodilation. In contrast, conduit arteries have a significantly reduced number of MEJs compared to resistance arteries, as well as a significantly thicker IEL (~0.5μm in resistance arteries

compared to up to 10μm in aorta) that allows them to handle high transmural pressures in proximity to the heart. (76-79) Conduit arteries preferentially dilate via the NO pathway, presumably because NO is a highly diffusible signaling molecule that can cross the multiple thick IEL layers.(11, 39, 64-66)

In addition to the high incidence of MEJs, the expression of hemoglobin alpha, or alpha globin, in ECs of resistance arteries likely also contributes to the predominance of EDH based signaling through its negative regulation of nitric oxide.(38, 39, 80) Alpha globin is the one of the subunits of hemoglobin in RBCs and has a high affinity for NO. Its expression and function in resistance arteries has been a focus of the Isakson lab for more than a decade, where we have shown that it forms a complex with eNOS and chelates NO produced by the enzyme, preventing it from diffusing across the IEL to promote SMC relaxation.(39, 80, 81) Thus, alpha globin likely contributes to the EDH predominance in resistance arteries by preventing NO-based signaling from having vasodilatory action.

The Isakson Lab has previously demonstrated that plasminogen activator inhibitor-1 (PAI-1) is enriched at the MEJ and that its depletion results in decreased MEJ formation,(36, 37) indicating that it can mediate MEJ formation. However, it remains to be demonstrated if PAI-1 is sufficient to induce MEJ formation in a large artery. In this study, we investigate the formation of HIEL in the carotid artery (a conduit artery) after direct application of PAI-1 to the vessel in live mice. We observed transient formation of EC projections/MEJs after 7 days that retreat by day 21. This anatomical phenotype was accompanied by an increased proportion of non-NO, likely EDH-based arterial relaxation. Treatment with PAI-1 also induced

the expression of the resistance artery-specific protein, alpha globin. These data indicate that treating a conduit artery with PAI-1 is a model system to sufficiently induce a resistance artery phenotype through inducing EC projections that correlate with an increased reliance on EDH-based vasodilation. Altogether, this data underscores the importance of the MEJ as a functional signaling microdomain that directs the pathways of vasodilation in arteries, and highlights how coordinated heterocellular communication can impact arterial function.

Materials and Methods

Mice

All mice and procedures were approved by the University of Virginia Animal Care and Use Committee. Male C57Bl/6 (Taconic Biosciences) and Hba1$^{-/-}$ (Jackson Labs) mice were used between 10-12 weeks of age. Male mice were used in this study for consistency in comparison of results to our previous work, as well as to minimize possible variability given N-values.

Plasminogen activator inhibitor-1 (PAI-1)

Lyophilized PAI-1 (500 IU, Technoclone, Vienna) powder was reconstituted by addition of 200µl distilled water followed by gentle agitation for 5 minutes at room temperature (2.5 x 10^6 IU/L stock solution). 40µl/tube aliquots were stored at -70°C. At 4°C immediately prior to use, 40µl stock solution of PAI-1 was mixed with 460µl of sterile saline solution containing 35% F127 Pluronic Gel (Molecular Probes).

Mouse surgery

Mice were anesthetized with an intraperitoneal (i.p.) injection of a freshly made ketamine/xylazine mixture (Fort Dodge; 80 mg/kg and Vedco; 6 mg/kg, respectively), followed by a subcutaneous injection of 10 mg/kg buprenorphine. The mouse was placed in the supine position, the hair of the neck area was removed with Nair lotion, and the neck skin was washed with 70% ethanol followed by iodine solution. A 10 mm incision was made on the anterior neck from the

clavicle towards the chin and the skin was carefully cut open with scissors. The two lobes of thymus were carefully separated with forceps to expose the left common carotid artery (CA) lateral to the trachea. The CA was carefully separated from the vagus nerve and the tissue around the trachea. The tip of the forceps was carefully placed under the carotid, and the carotid was lifted slightly away from surrounding tissue (see **Figure 1** for visual representation).

The pluronic gel/PAI-1 mixture (preparation described above) and pipettes were kept at 4°C and placed on ice just before use. While holding the CA away from surrounding tissues, the pluronic gel/PAI-1 mixture (100 IU PAI-1 in 500µl for a 2.68 x 10^5 IU/L solution) or pluronic gel (500µl of 35% pluronic gel) was applied to the outside of the left CA and solidified within one minute of application. The lobes of the thymus were placed back to the original position, and the skin was pulled together and closed using interrupted sutures. Finally, the mouse was given a dorsal subcutaneous injection of 1 ml sterile saline and allowed to recover. Pluronic gel/PAI-1 mixture or pluronic gel only was kept on CAs for 1, 2, 3, 4, 5, 7, 14 or 21 days.

Dissection of the Carotid Artery

At the end of the PAI-1 or pluronic gel incubation, mice were sacrificed using CO_2 asphyxia, placed in the supine position, and the neck area was sprayed with 70% ethanol. A 10-15 mm incision was performed and the CA was carefully dissected using a stereomicroscope. Tissues were constantly kept moist with ice cold Krebs-HEPES containing (in mmol/L) NaCl 118.4, KCl 4.7, $MgSO_4$ 1.2,

$NaHCO_3$ 4, KH_2PO_4 1.2, $CaCl_2$ 2, HEPES 10, glucose 6, and supplemented with 1% BSA. Once free of surrounding tissues and cleaned, the CA was used for experiments (see **Figure 1** for visual representation).

Fluorescent microscopy measurement of HIEL

To evaluate whether PAI-1 could induce the formation of holes in the IEL where potential myoendothelial junctions could project, CAs treated as described above (N=minimum 4 for each treatment) were cut longitudinally and pinned open to expose the endothelium in plane (***en face***). Next, CAs were fixed with 4% paraformaldehyde (PFA) in PBS for 60 minutes at room temperature followed by four 10-minute PBS washes. CAs were stained with 0.25µmol/L Alexa Fluor 633 hydrazide (Molecular Probes) at RT for 1 hour, followed by a PBS wash for 10 minutes. CAs were mounted in DAPI ProLong Gold Antifade reagent (Invitrogen, Grand Island) and imaged in three sections along the length of each carotid using an Olympus Fluoview 1000 confocal microscope. At least three images were used per mouse per treatment. Each image was analyzed with MetaMorph software (Universal Imaging Corps, version 7.5.6.0), counting the mean number of IEL holes (visualized as dark spots) in 100µm x 100µm regions (1000 μm^2) of each CA. The mean numbers for each group were calculated, and data were analyzed using a one-way ANOVA test (Bonferroni post-hoc) where $p<0.05$ was considered significantly different. The thoracodorsal artery (TDA) and third-order mesenteric artery (MA) were also obtained, prepared, and analyzed as described above (see **Figure 6**).

Scanning Electron Microscopy (SEM) measurement of HIEL

Mice were subjected to PAI-1 treatment as described above. At the end of the treatment, the mice (N=minimum 4 per group) were perfused transcardially with 5 ml Ca^{2+}-free Krebs-HEPES solution containing 10 unit/ml heparin, then with a 4% paraformaldehyde (PFA) and 2.5% glutaraldehyde solution. Following perfusion, CAs were isolated as described above, opened longitudinally, and endothelium was removed with a cotton swab before being washing again with PBS. CAs were then post-fixed in 4% PFA and 2.5% glutaraldehyde in PBS overnight at 4°C. CAs were prepared and viewed on the Scanning Electron Microscope (SEM) as previously described by us.**(82)** At least three images were used per mouse per treatment. Each image was analyzed with ImageJ and the mean number of IEL holes (visualized as holes) from 100µm x 100µm regions (1000 μm^2) of each CA was collated. The averages for each group were calculated and analyzed using one-way ANOVA test (Bonferroni post-hoc) where $p<0.05$ was considered significantly different.

Transmission Electron Microscopy (TEM) measurement of HIEL

Mice were subjected to PAI-1 treatment as described above. At the end of the treatment, the mice (N= 4 minimum per group) were perfused transcardially with 5 ml Ca^{2+}-free Krebs-HEPES solution containing 10 unit/ml heparin, then with a 4% paraformaldehyde (PFA) and 2.5% glutaraldehyde solution. Following perfusion, CAs were isolated as described above, then were fixed in 4% PFA and

2.5% glutaraldehyde overnight at 4°C. The vessels were post-fixed with 1% osmium tetroxide, dehydrated in a gradient of alcohols, and embedded in Epon. Ultrathin sections of approximately 75 nm were cut, carbon coated, and imaged on a JEOL 1230 Transmission Electron Microscope (TEM) as previously described.**(83)** At least three images were used per mouse per treatment. Each image was analyzed with ImageJ and the mean number of endothelial cell extensions (>2 μm from endothelial cell basement membrane into IEL) from 100μm long regions of each CA was calculated. Data were analyzed using a one-way ANOVA test (Bonferroni post-hoc) where $p<0.05$ was considered significantly different.

Measurements of carotid artery vasoreactivity

CAs were isolated after treatment as described above, cannulated in a pressure myograph chamber (Danish MyoTechnology), and secured with 10.0 nylon sutures.**(82)** Carotid arteries were placed in a circulating bath of Krebs-HEPES buffer, perfused with the same, and equilibrated for 30-60 minutes at 100 mmHg and 37°C. After equilibration, 50μmol/L phenylephrine (PE, Sigma) was added to the bath solution to constrict the CAs to 60–80% of their baseline diameter. After stabilization of vasoconstriction, dose-dependent relaxation was measured in response to the application of cumulative concentrations of the vasodilator acetylcholine (Ach, 10^{-9} to 10^{-4} mol/L; Sigma). At the end of the experiments, the solution was replaced with a Ca^{2+}-free Krebs-HEPES supplemented with 2 mmol/L Ethyleneglycol-O,O'-bis(2-aminoethyl)-N,N,N',N'-

tetraacetic acid (EGTA; Sigma) and 10μmol/L sodium nitroprusside (SNP, Sigma) in order to measure the maximal diameter. Vasoconstriction to PE was calculated as percent of initial diameter: %constriction = D_{PE} / $D_{initial}$ * 100 and relaxation to Ach or NS309 was calculated as a % relaxation: % relaxation = [(D_{Ach} – D_{PE}) * 100]/(D_{max}-D_{PE}), where D_{PE} was the diameter of the CA 10 minutes after application of 50μmol/L PE; $D_{initial}$ was the diameter prior to the addition of PE; D_{Ach} was the diameter of the CA after application of a given dose of Ach; and D_{max} was the maximal diameter of the CA measured at the end of experiment as described above. Data were analyzed with a two-way ANOVA test one-way ANOVA test (Bonferroni post-hoc) where $p < 0.05$ was considered significant.

In order to evaluate the effect of PAI-1 on the vasoreactivity of CA, where indicated, experiments were conducted in the presence or absence of selective blockers of endothelium-mediated vasodilator pathways. In order to block NO generation alone, we used the nitric oxide synthase (NOS) inhibitor L-nitro-arginine methyl ester (L-NAME, 300μmol/L; Sigma). In order to block the EDH pathway, we used both 300μmol/L L-NAME and also (1) the cyclooxygenase inhibitor indomethacin (10μmol/L; Sigma), (2) the intermediate-conductance calcium-activated potassium channel (IK_{Ca}) blocker 1-[(2-chlorophenyl) diphenylmethyl]-1H-pyrazole (TRAM 34, 10μmol/L; Sigma), and (3) the small-conductance calcium-activated potassium (SK_{Ca}) channel blocker apamin (300 nmol/L). Both groups of inhibitors were preincubated with CAs intraluminally and extraluminally. After a 30-minute stabilization period in the circulating bath, the arteries were pre-constricted with 50μmol/L PE, followed by cumulative concentrations of Ach (10^{-9}

to 10^{-4} mol/L). Maximal diameter was measured after washing with a Ca^{2+}-free Krebs-HEPES solution supplemented with 2 mmol/L EGTA and 10 µmol/L sodium nitroprusside at the end of the experiment. Internal diameters were used in calculations and results were expressed as a percentage of relaxation as described above. Lastly, the small and intermediate potassium channel activator NS309 (3µmol/L) was added to pre-constricted CAs (described above) and dilation assessed as described above. Data were analyzed with a one-way ANOVA test (Bonferroni post-hoc) where $p < 0.05$ was considered significant.

Biocytin dye transfer

CAs were removed as described above, cannulated, and flushed with Ca^{2+}-free Krebs-HEPES buffer. CAs were perfused with new buffer supplemented with 0.01% Tween20 + 1 mg/ml biocytin for 15 minutes at room temperature, washed with Ca^{2+}-free Krebs-HEPES buffer. To test the effect of dye transfer following gap junction inhibition, day 7 PAI-1-treated CAs were treated with 100µM α-glycyrrhetinic acid (α-GA) for 20 minutes prior to perfusion with buffer containing biocytin. CAs were removed from the cannula and fixed in 4% PFA for an hour at room temperature, washed with PBS, and cut open longitudinally with the endothelium facing upwards (*en face)*. CAs were then permeabilized for 30 minutes in PBS containing 0.01% TritonX-100, incubated for 60 minutes in 1:500 streptavidin conjugated with Alexa 568 in PBS with 0.01% TritonX-100, washed with PBS, mounted with DAPI, and imaged on an Olympus Fluoview 1000 confocal microscope. Endothelial cells were viewed initially, then smooth muscle cell

layers. Data were analyzed with a one-way ANOVA test (Bonferroni post-hoc) where $p < 0.05$ was considered significant.

Western blotting

CAs and third-order mesenteric arteries were isolated, homogenized in ice cold protein lysis buffer, and sonicated. Samples were mixed with Laemmli buffer and subjected to protein electrophoresis using 4-15% Bis-Tris gels, then transferred to a polyvinylidene fluoride (PVDF) membrane. Blots were incubated with anti-alpha hemoglobin or anti-VE-cadherin primary antibodies (Abcam) overnight at 4ºC, respectively, followed by fluorescently tagged secondary antibodies (LICOR) for 1 hour at RT. They were visualized and quantitated using Licor Odyssey as previously described (N=minimum of 4 mice).**(83)** Data were analyzed with a one-way ANOVA test (Bonferroni post-hoc) where $p < 0.05$ was considered significant.

Statistics

All statistical tests are listed with experimental conditions above. Data are expressed as mean +/- SEM.

Results

Functional MEJs form in the IEL of carotids after application of PAI-1

CAs have a thick IEL separating the endothelium and smooth muscle and contain very few MEJs. (84, 85) We have previously demonstrated that PAI-1 can regulate the formation of MEJs (36) and sought to test if it could induce MEJ formation in CAs. We applied PAI-1 directly to CAs of C57Bl/6 mice using a pluronic gel to determine if functional MEJs could form in these conduit arteries (**Figure 1**). We verified our treatment method by performing an immunostaining experiment on arterial cross-sections and found that PAI-1 was throughout the arterial wall after *in vivo* application using a pluronic gel (**Figure 2**). Initially we screened for extent of HIEL formation via autofluorescence of carotids prepared *en face* (**Figure 3**), and found that the maximum number of HIEL occurred 7 days after PAI-1 application. After that timepoint, HIEL density steadily regressed more than halfway to baseline by 21 days post PAI-1 application. Based on these results, we performed experiments at 0, 1, 7, and 21 days post PAI-1 application. We quantified HIEL incidence in *en face* views of carotid artery autofluorescence and found a significant increase 7 days post-application of PAI-1 (**Figure 4A-G**). We confirmed the formation of HIEL by imaging carotids stripped of endothelium with SEM (**Figure 4H-N**). There are several examples in the literature demonstrating heterogeneous protein localization to HIEL;[12] therefore, we wanted to identify the presence of EC projections through these HIEL without relying on any individual protein marker. We used a TEM based approach on transverse CA sections to identify EC projections through HIEL at each of the timepoints (**Figure4O-U**). We

observed a significant increase in EC projection incidence at day 7 with a reversion to almost to baseline by day 21 post treatment, indicating a transient nature to these induced projections. The EC projections could not be observed to physically touch SMC (**Figure 5**). In addition, the width of induced HIEL in CAs following PAI-1 treatment was similar to those found in mesenteric or skeletal muscle beds (**Figure 6**). The formation of HIEL and corresponding EC projections did not affect the thickness of the IEL (**Figure 7**) or interendothelial junctions were preserved (**Figure 8**), indicating a specific function of PAI-1 in initiating MEJ formation without altering other morphological hallmarks in the arterial wall. Overall, exogenous PAI-1 application to the CA was sufficient to induce the formation of EC projections through HIEL, structures that are normally restricted to small-diameter arterioles and resistance arteries.

We next wanted to investigate if the anatomical structures we identified in TEM corresponded to canonical MEJ function. One important test of functional MEJs is the electrochemical coupling of ECs to SMCs through gap junctions, which we examined using a dye transfer experiment to determine the presence of functional gap junctions. ECs of a cannulated CA were loaded with biocytin, a small, uncharged molecule that can transverse gap junctions, using a pinocytotic method that loads >90% of ECs (Molecular Probes). The biotin moiety facilitates detection using fluorescently-labeled streptavidin. At day 0 we were not able to observe biocytin in the SMC layer due to the absence of gap junctional communication and functional MEJs in the CA (**Figure 9A-B**). At day 7 post-PAI-1 application, when the EC projections are present, we were able to detect biocytin

transfer to the SMC layer. While there are no truly specific pharmacological means to block gap junctions (e.g.,(85, 86)), the addition of α-glycyrrhetinic acid (α-GA), a purported gap junction inhibitor, prevented the biocytin dye transfer (**Figure 9A-B**). We conclude that the induced MEJs in the PAI-1-treated CA physically couple ECs to SMCs via gap junctions. It is well understood that MEJs facilitate EDH-based vasodilation in resistance arteries; thus, we wanted to evaluate the EDH component of vasodilation in the PAI-1-treated CAs. We used a vasoreactivity approach to assess changes in relaxation to NS309 (an activator of SK_{Ca} and IK_{Ca} channels; 3μmol/L). Dilation to NS309 indicates the presence of EDH machinery and signaling within the artery. (87) The dilation to NS309 in sham- and gel-treated CAs was not significantly different from CAs taken from day 0 PAI-1-treated animals (**Figure 9C**). NS309 induced a significantly higher vasodilation at day 7 post PAI-1 treatment, which was inhibited after denuding endothelium or adding α-GA. Day 7 post-PAI-1 application was the only day and treatment condition to demonstrate increased relaxation to NS309 in these conduit arteries. Immunohistochemistry on *en face* preparations of day 7 PAI-1-treated CAs demonstrate a localization of Cx40 to HIEL after 7 days of PAI-1 (**Figure 8**). These results indicate that the formation of HIEL and EC projections are coupled with functional heterocellular communication that resembles canonical MEJ function.

MEJs are necessary, but not sufficient, to alter endothelial-induced dilation

In arteries with a high incidence of MEJs (e.g., resistance arteries), endothelial derived vasodilation using cholinergic stimulation (via acetylcholine, Ach) occurs primarily via EDH (8, 11, 61, 75); whereas in arteries with few MEJs,

NO signaling predominates.(6, 67) We reasoned that the new formation of MEJs in a conduit artery could alter the endothelial-dependent mechanism of vasodilation. Dose-responses with Ach on control CAs demonstrated that eNOS inhibition significantly inhibited vasodilation in agreement with the literature (with 300 μmol/L L-NAME, a non-specific NOS inhibitor, **Figure 10A-B**; **Figure 11**). (65, 88) At day 7 post PAI-1 treatment, when HIEL and MEJs were maximally present and both heterocellular dye transfer and NS309 both were significantly increased, L-NAME alone did not inhibit vasorelaxation to similar levels as seen in the control CAs. It was only with the addition of apamin, TRAM-34, and indomethacin (SK_{CA}, IK_{CA}, cyclooxygenase inhibitors, respectively) that vasodilation to Ach was significantly inhibited (**Figure 10A-B**; **Figure 11**). In experiments on CAs treated with PAI-1 for 7 days, an inhibitory response was observed with the combination of indomethacin, TRAM-34, and apamin, as well as with only TRAM-34, apamin, and L-NAME (**Figure 12**). These data indicate that the PAI-1-treated carotids have an increased reliance on EDH-based signaling, a predominance usually only observed in resistance arteries where MEJs are prevalent.

Lastly, we tested if the formation of MEJs alone was sufficient to alter the mechanism for endothelial-derived vasodilation. We have previously demonstrated that alpha globin is a potent chelator of NO and is specifically expressed in the endothelium of resistance arteries, with little to no expression in conduit arteries.(39, 80) At day 7 post PAI-1 application, when MEJs and Ach-induced non-NO vasodilation are maximal, we found a significant increase in expression of alpha globin (**Figure 13A-B**). We also observed alpha globin in the

HIEL at day 7 in *en face* preparations of CAs (**Figure 8**). In mice with a disrupted Hba1 gene ($Hba1^{-/-}$), we found no alpha globin expression at day 7 post-PAI-1 application, whereas in littermate controls ($Hba1^{+/+}$) the protein was produced at normal levels similar to that seen in C57Bl/6 (**Figure 13A-B**; **Figure 14**). The absence alpha globin expression at day 7 post-PAI-1 application in $Hba1^{-/-}$ mice had no effect on (1) the number of HIEL (**Figure 13C-D**), (2) EC projections through HIEL (**Figure 13E**), (3) dye transfer to SMC (**Figure 13F**), or (4) relaxation to NS309 (**Figure 13G**). However, CAs of mice lacking alpha globin expression were unable to switch their dominant vasodilatory mechanism from NO to non-NO. As expected, CAs from $Hba^{+/+}$ littermate controls 7 days after PAI-1 application appeared similar to those seen in C57Bl/6 (**Figure 13H**), with non-NO dominating the vasodilatory response. In $Hba1^{-/-}$ mice at the same treatment time point, L-NAME alone was able to significantly blunt relaxation, indicating that NO was still the dominant dilatory pathway (**Figure 13I**). MEJs, and MEJ-localized alpha globin, are crucial components in enabling EC-driven SMC vasodilation. Through limiting the role of NO signaling, the expression of alpha globin at MEJs may encourage non-NO based signaling (e.g., EDH) to predominate in resistance arteries.

Figure 1. Representation of experimental set-up used in Chapter 3 for carotid exposure.

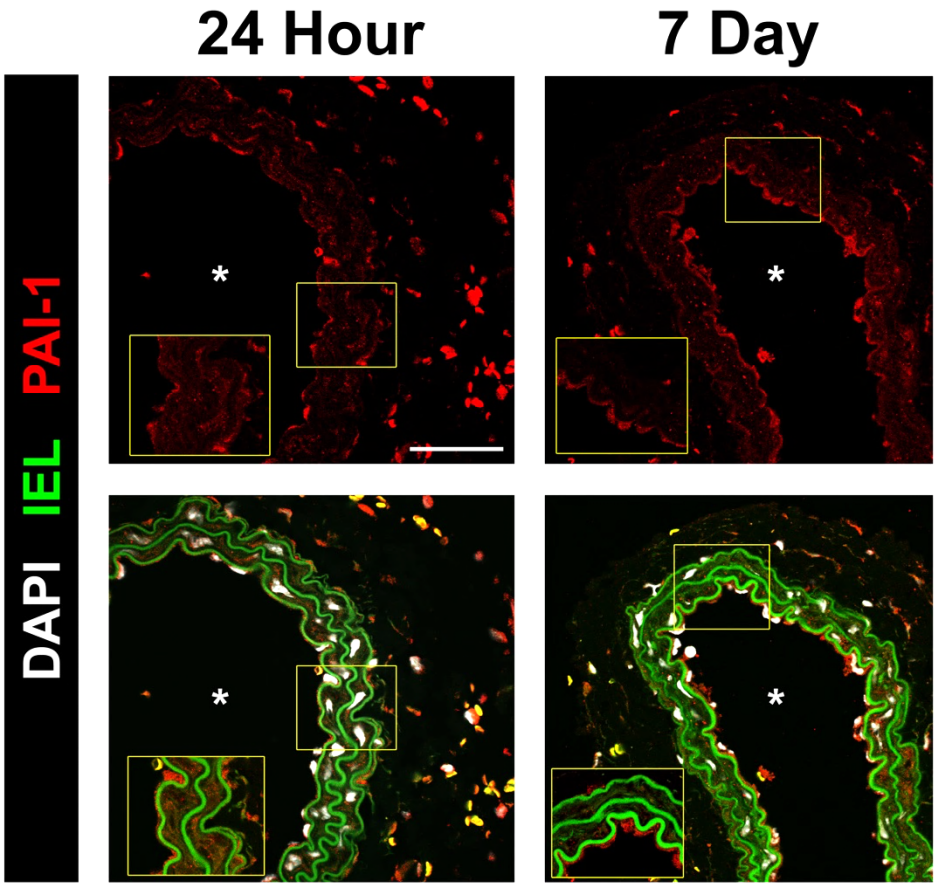

Figure 2. **PAI-1 is present in the endothelium of the carotid after treatment with pluronic gel/PAI-1 mixture at 24 hours, and increased at 7 days.** Immunofluorescence images of carotid arteries treated for 24 hours or 7 days with pluronic gel/PAI-1 mixture. PAI-1 is shown in red, the autofluorescence of the layers of internal elastic lamina (IEL) in green, and DAPI denoting cell nuclei in white. A portion of the vessel (yellow box) is magnified in the lower left of each image. PAI-1 is enriched in the endothelial layer of both time points, but is more prominent with treatment for 7 days. Asterisks denote lumen of the vessel, and scale bar in upper left image is 50 μm.

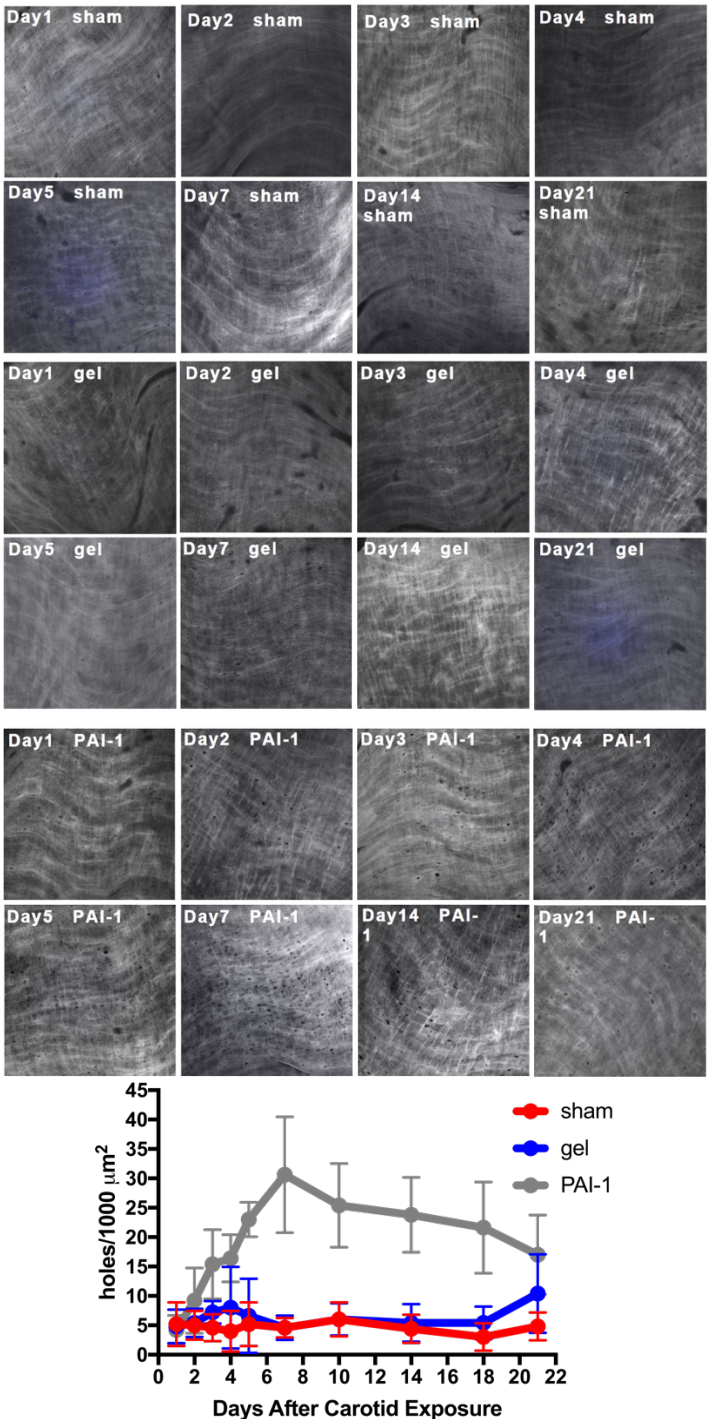

Figure 3. Time course after surgical carotid exposure and formation of holes in the carotid internal elastic lamina (IEL). Carotid images (top) were obtained via Alexa Fluor 633 hydrazide staining; each image is 200 μm x 200 μm. Blue is remnant of DAPI stain. In these experiments, N=3 mice per treatment group for

each of the 10 days analyzed (90 mice total). In the graph below, the number of holes is averaged for sham surgery (red), pluronic gel only (blue), and following PAI-1 treatment (gray). Data is presented +/- SEM.

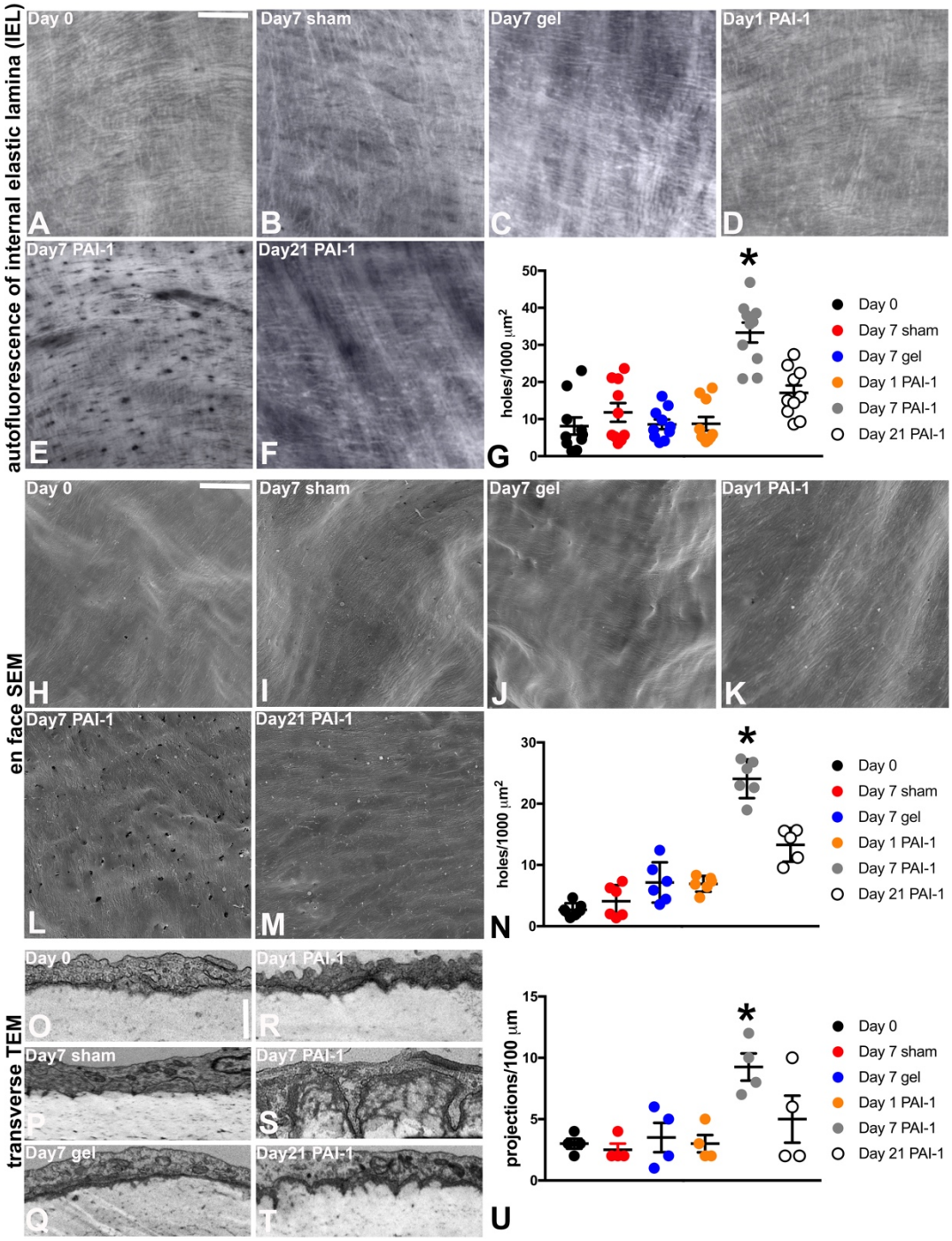

Figure 4. Formation of holes and cellular extensions into the internal elastic lamina of carotids after PAI-1 application. (A-F) Representative confocal images of the IEL from CA *en face* preparations at 0, 7, and 21 days following PAI-1 treatment and from sham control. The number of holes per 1000μm^2 is quantified

in G. Scale bar in A is 20μm and representative for A-F. (**H-M**) SEM images of the IEL from CA *en face* preparations at 0, 7, and 21 days following PAI-1 treatment and from sham control, with quantification of holes per 1000μm^2 in N. Scale bar in H is 2μm and representative for H-M. (**O-T**) TEM images on transverse sections at 0, 7, and 21 days following PAI-1 treatment and the sham controls, with number of projections per 100 linear μm quantified in **U**. In all cases, each dot on graphs in G, N, and U indicates the average of 3 random fields of view from 1 mouse. Scale bar in O is 1 μm and representative for O-T. In each graph, N=4 mice per experimental time point; *=$p<0.05$.

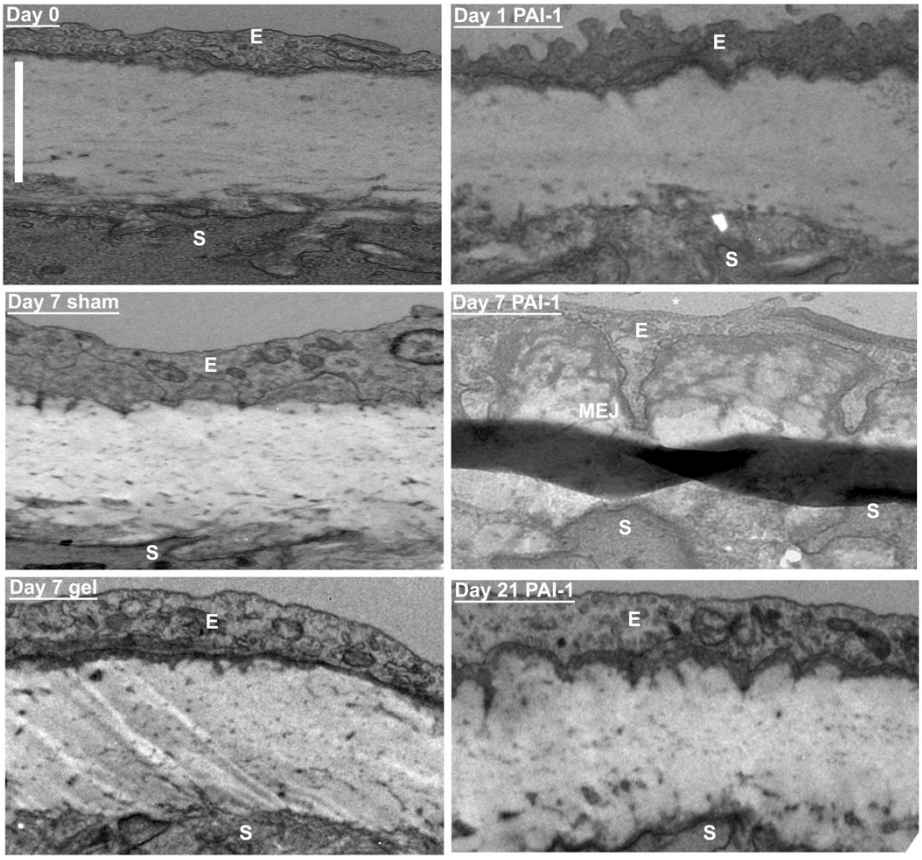

Figure 5. Time course after surgical carotid exposure and formation of endothelial extensions in the carotid internal elastic lamina (IEL). In each transmission electron micrograph (TEM), E is endothelial cells, S is smooth muscle cells, and MEJ is myoendothelial junction. Scale bar is 2 μm and representative for all images. Note the uranyl acetate precipitate in day 7 PAI-1 carotids.

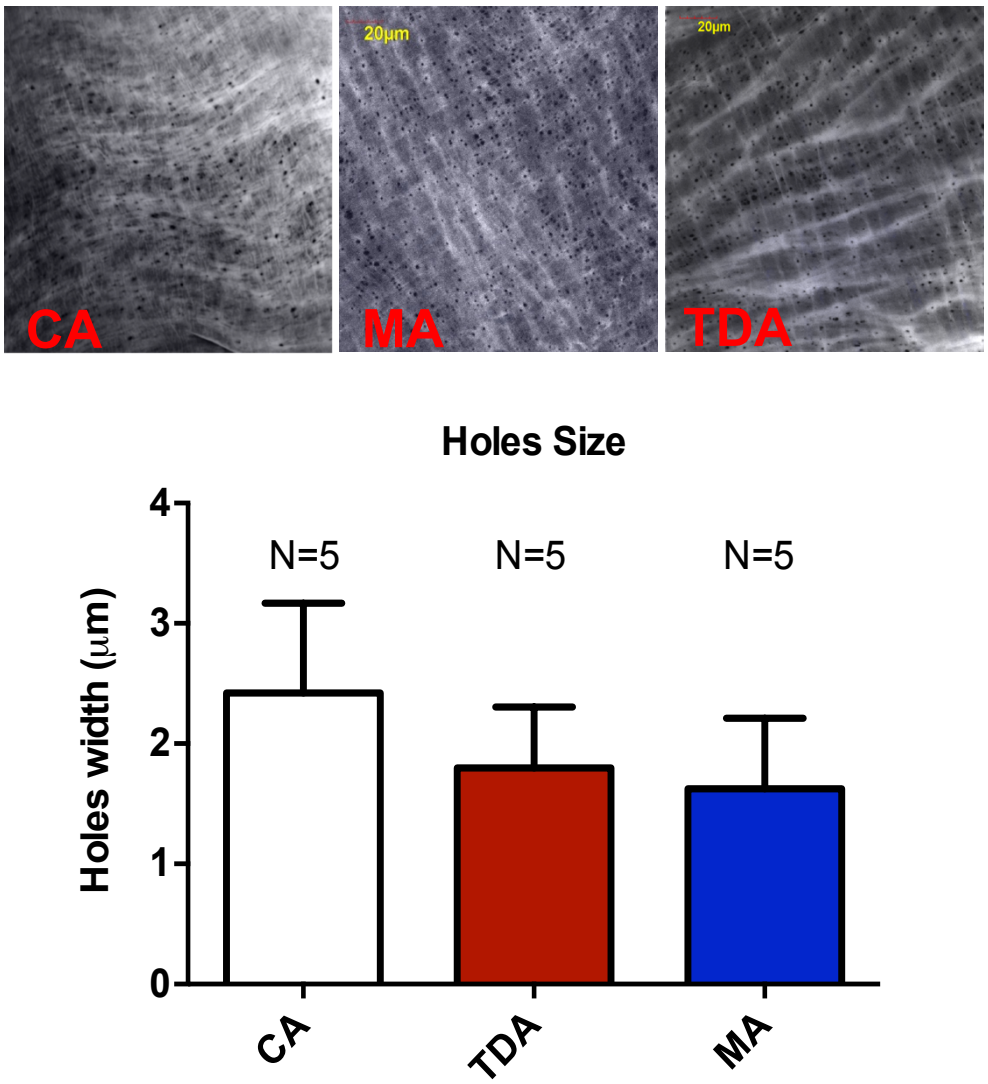

Figure 6. Comparative hole size in the IEL between carotid with PAI-1 post-7 days (CA), skeletal muscle thoracodorsal artery (TDA), and third-order mesenteric artery (MA).

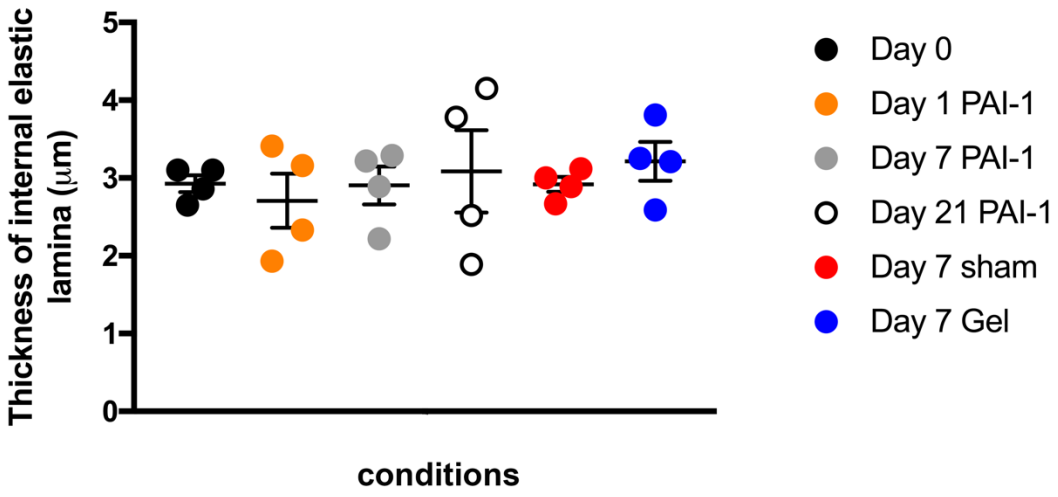

Figure 7. Thickness of the internal elastic lamina does not change with application of PAI-1. At least three images were used per mouse per treatment and N=4.

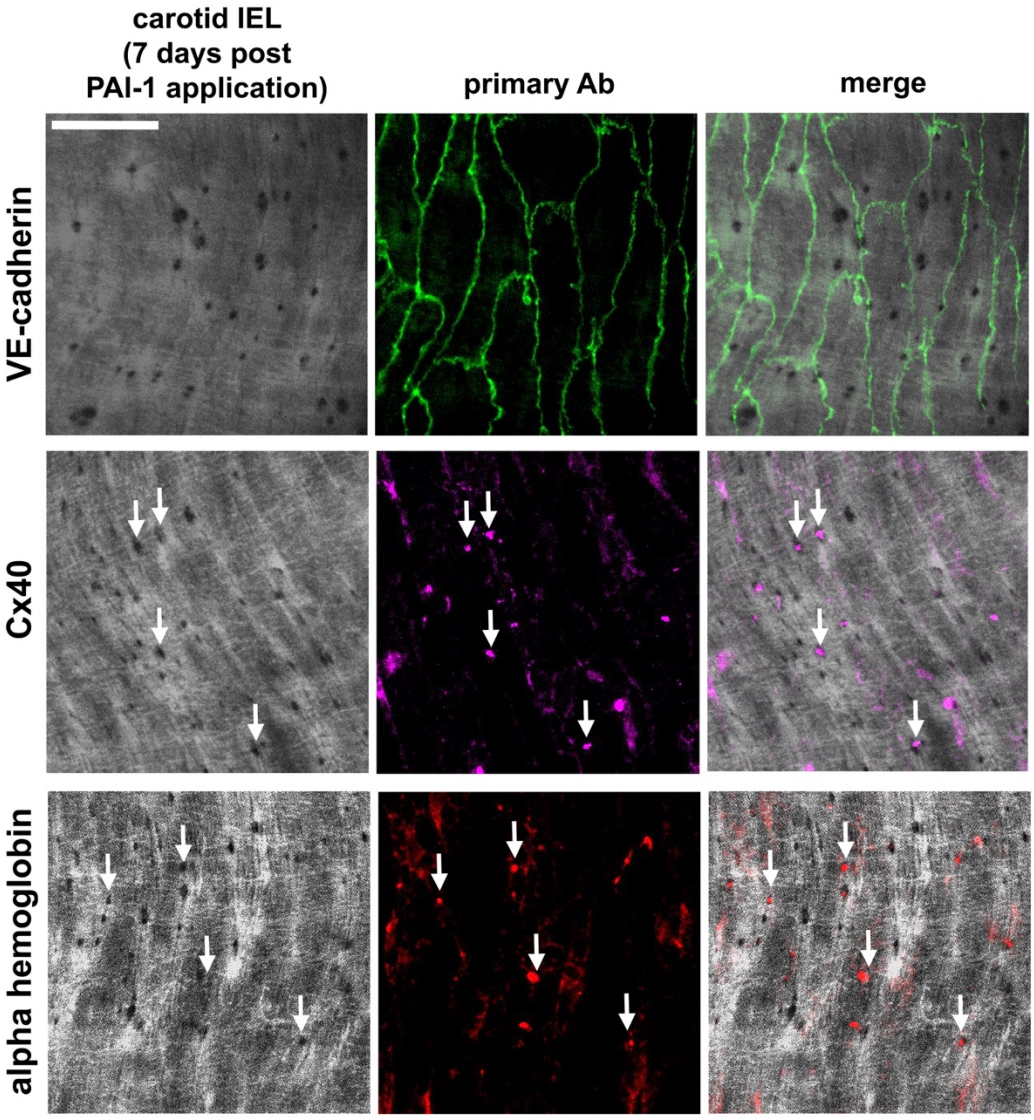

Figure 8. Expression of proteins in carotids treated with PAI-1 for 7 days. Upper panel is VE-cadherin (green) denoting intact endothelium. In the bottom two rows, the Z-focus is slightly lower to better show protein within the internal elastic lamina (IEL) holes. Middle row shows Cx40 (magenta) and bottom row shows alpha hemoglobin (red). In all cases, IEL is counterstained with Alexa Fluor 633 hydrazide. Arrows point to representative Cx40- or alpha globin-occupied holes in the IEL. Scale bar in upper left is 20 μm and is representative for all images.

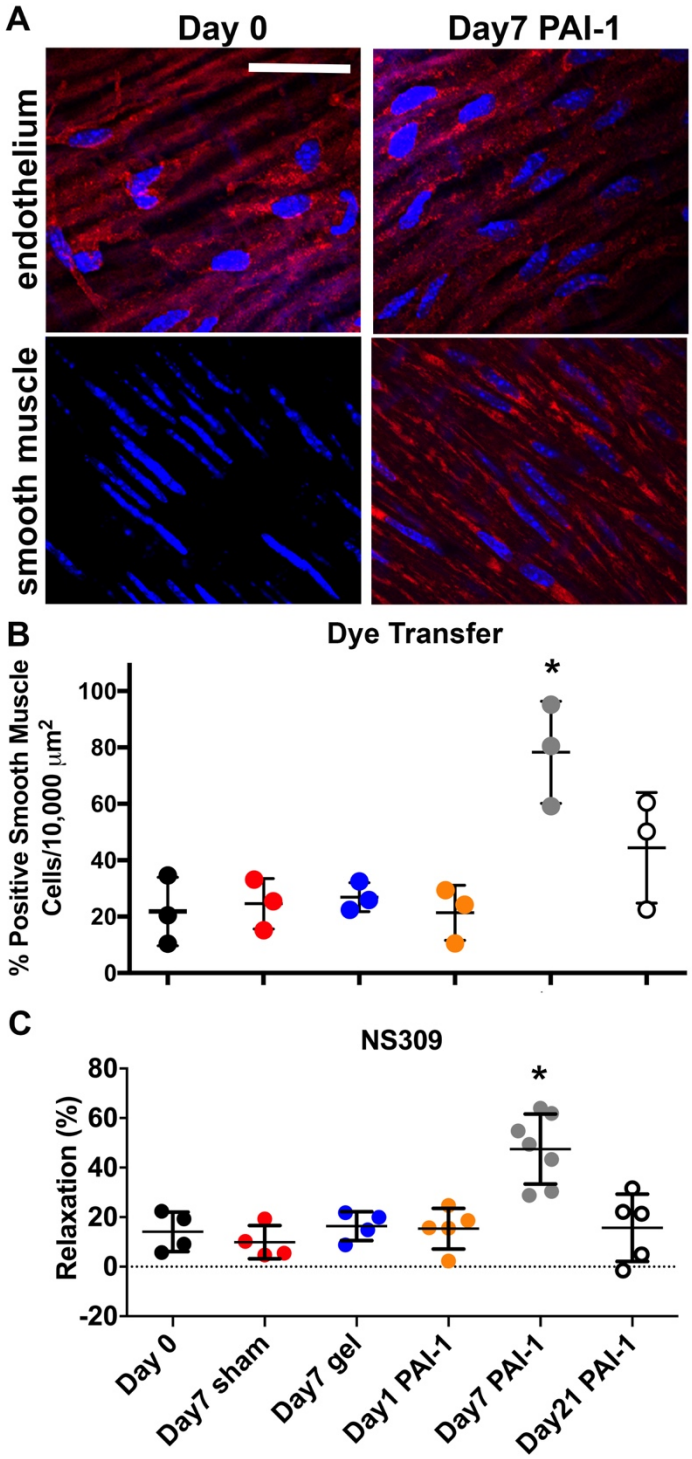

Figure 9. Endothelium and smooth muscle cells of the carotid are functionally coupled after PAI-1 application. (**A**) Representative images of biocytin highlighted with streptavidin conjugated Alexa 568 fluorophore (red); nuclei in blue (DAPI). The XY-plane of endothelium is shown in the top row and

smooth muscle in the one below. Note the addition of α-GA blocked biocytin transfer to smooth muscle in carotids treated with PAI-1 for 7 days. Scale bar is 20 μm. (**B**) Percent streptavidin-positive smooth muscle cells per 10,000 μm^2 after loading of endothelium with biocytin. (**C**) Carotids were stimulated with 3 μmol/L NS309 and relaxation was measured. Each dot on graphs in B and C indicates the average of 3 random fields of view from 1 mouse, minimum N=3 mice per experimental condition. Note the addition of α-GA, and denuding endothelium, prevented relaxation of carotids treated with PAI-1 for 7 days. In each graph, *=$p<0.05$.

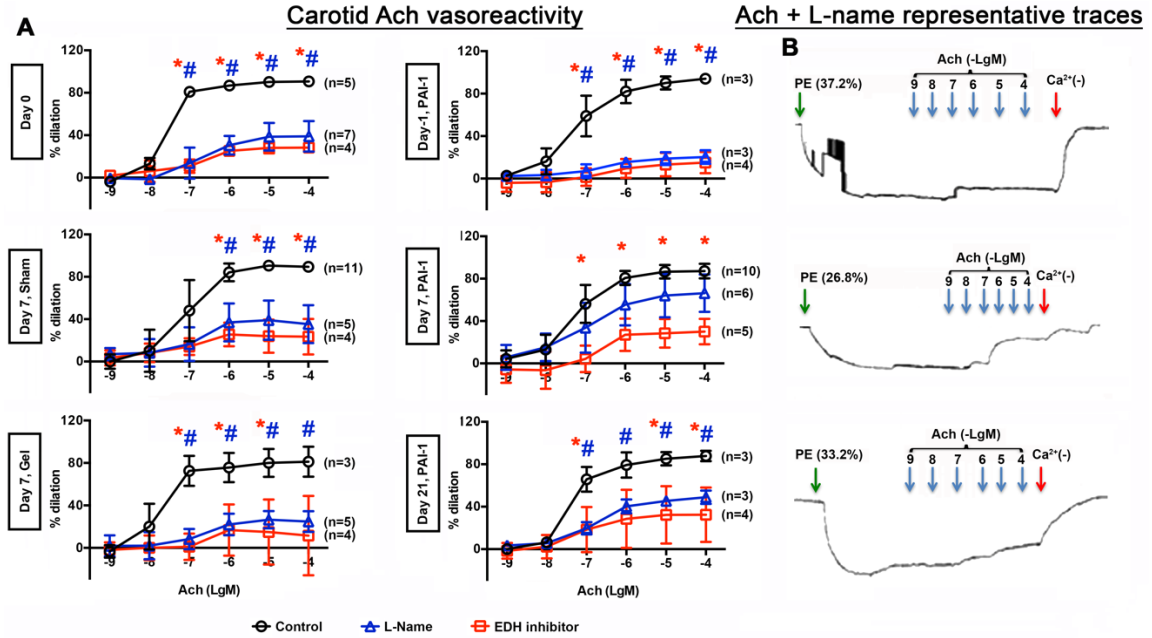

Figure 10. When myoendothelial junctions are present in carotids, acetylcholine-induced relaxation is no longer reliant on nitric oxide. (**A**) Dose response curves to Ach; black circles are untreated control carotids, blue triangles are carotids treated with L-NAME, and red squares are carotids treated with L-NAME plus the inhibitors TRAM-34, indomethacin, and apamin. N values indicate the number of carotids. In all experiments, a minimum of N=3 mice were used per time point per experimental condition. (**B**) Representative traces of Ach dose-response curves in the presence of L-NAME; green arrow is initial phenylephrine (PE) constriction (in %), with each Ach dose indicated by a blue arrow. Red arrows indicate perfusion with Ca^{2+}-free buffer. *=$p<0.05$ indicates control compared to L-NAME, TRAM-34, indomethacin, and apamin; #=$p<0.05$ indicates control compared to L-NAME.

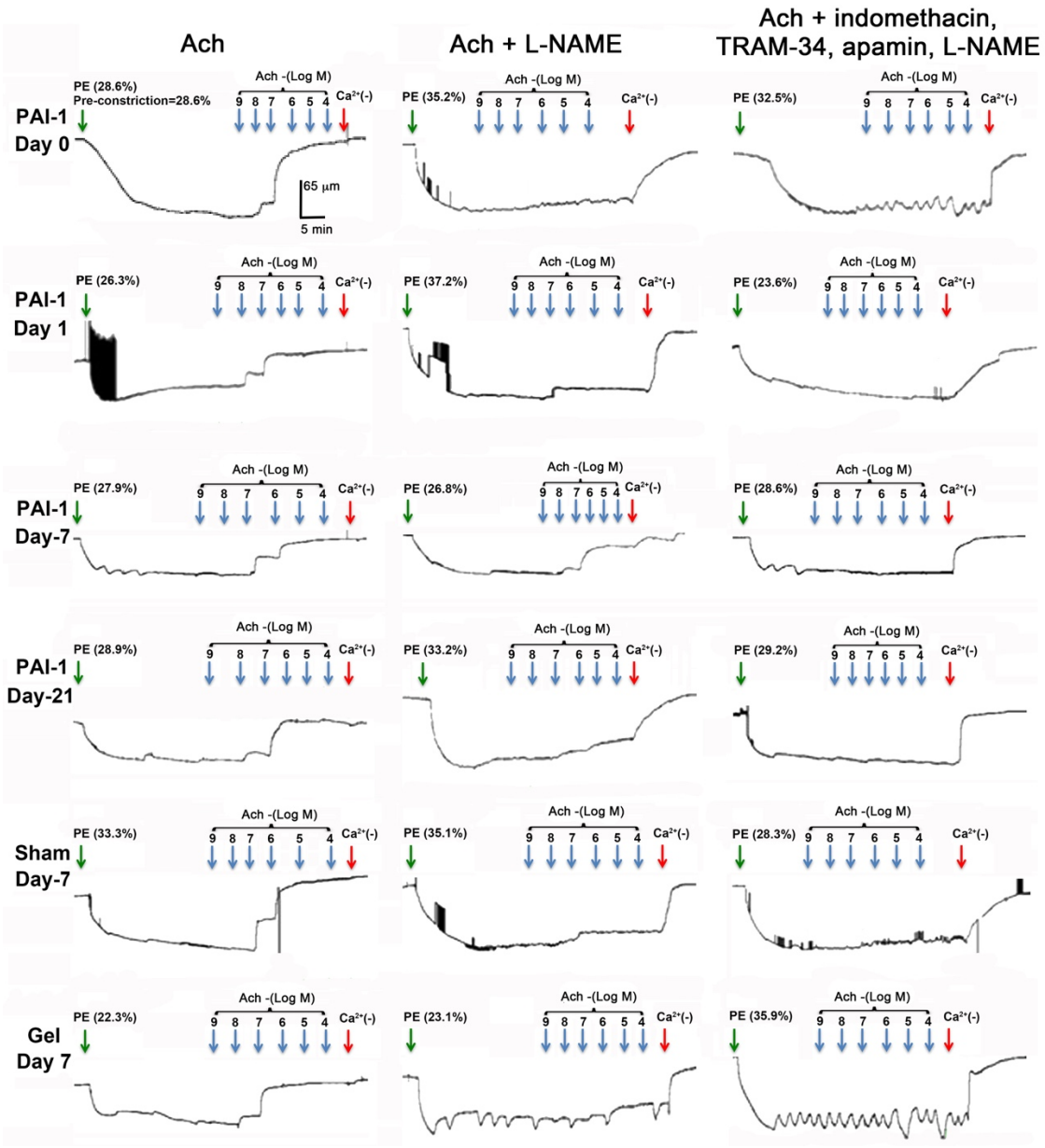

Figure 11. Representative acetylcholine traces for all of the experimental conditions with carotids. For all traces, green arrows indicate application of phenylephrine (PE) and the percentage in parentheses above is the amount of pre-constriction achieved; blue arrows indicate the cumulative concentrations of subsequent applications of acetylcholine (Ach); and red arrows indicate the start of perfusion with Ca^{2+}-free buffer.

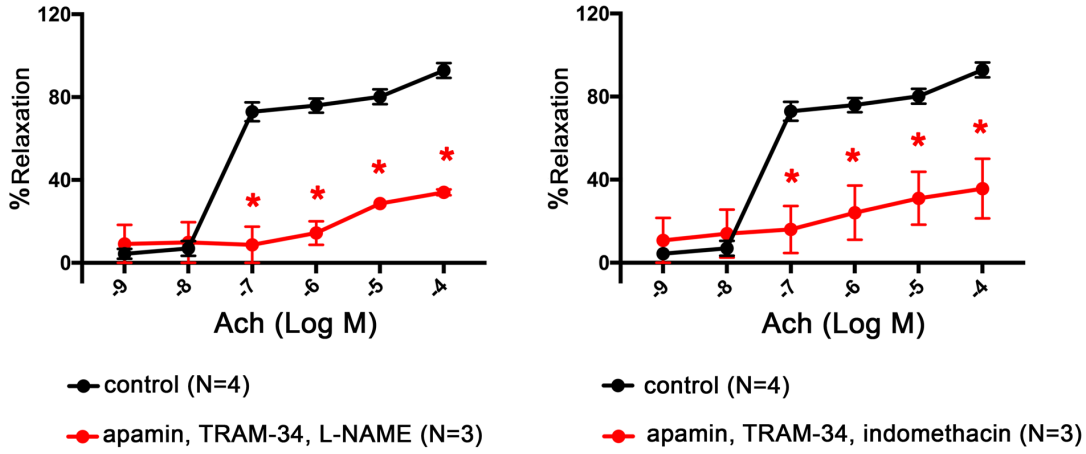

Figure 12. Carotids treated with PAI-1 for 7 days were subject to pressure myography in the presence of inhibitors. In each case, a minimum of 3 mice were used per experimental condition, and *=p<0.05. See online methods for details of % relaxation.

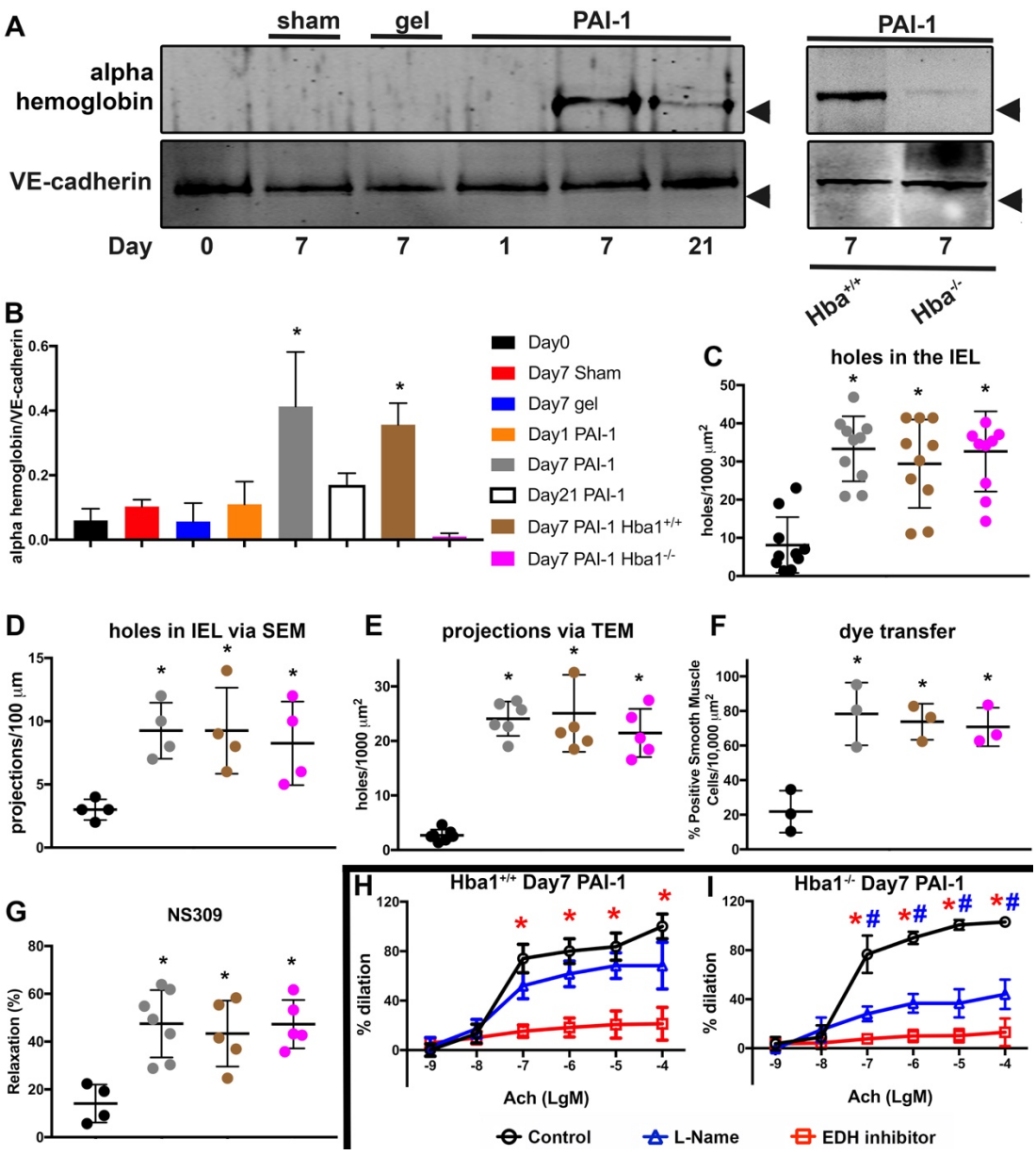

Figure 13. Induction of alpha globin expression within heterocellular contacts regulates nitric oxide diffusion, but not myoendothelial junction formation. (**A**) Western blot for alpha globin from carotids, with VE-cadherin used as loading control for endothelium. In the right panel, expression of alpha globin at 7 days post-PAI-1 application is shown in samples from $Hba1^{+/+}$ and $Hba1^{-/-}$ mice. Arrows indicate 10 kDa for alpha globin, and 100 kDa for VE-cadherin. (**B**) Note the significant increase in alpha globin 7 days after PAI-1 treatment that decreases

by day 21, matching hole and endothelial projection prevalence. (**C-D**) the number of holes in the IEL were assessed via fluorescent microscopy (**C**) and SEM (**D**). **(E**) Endothelial projections down into the IEL were assessed the same way as in Figure 1. Coupling of endothelium and smooth muscle was experimentally determined using biocytin dye transfer (**F**) and relaxation to NS309 (**G**). (**B-G**) Colors indicate identical time points; black is day 0 after PAI-1 on a C57Bl/6 mouse, grey is day 7 after PAI-1 on a C57Bl/6 mouse, brown is day 7 after PAI-1 on a $Hba^{+/+}$ mouse, and pink is day 7 after PAI-1 on a $Hba^{-/-}$ mouse. (**H-I**) CAs were collected from $Hba^{+/+}$ (**H**) or $HBA1^{-/-}$ (**I**) mice 7 days after PAI-1 application, cannulated, pressurized, and tested in the presence of L-NAME or L-NAME with the inhibitors, indomethacin, TRAM-34, and apamin. Loss of alpha globin had no effect on the number of holes in the IEL, cellular extensions, dye transfer, or NS309 induced relaxation (IK_{Ca}/SK_{Ca}), indicating MEJs were still capable of forming (**C-G**). However, data in H-I demonstrate the mechanism of endothelial vasodilation was altered without alpha globin present. In all cases, each dot on graphs in C-G indicates the average of 3 random fields of view from 1 mouse. N=4 mice per experimental time point for all experimental conditions in A-I. In each graph, * and # = $p<0.05$. In B-G, * indicates control compared to respective carotid treatment. In H and I, * indicates control compared to inhibitors L-NAME, TRAM-34, indomethacin, and apamin; # indicates control compared to L-NAME.

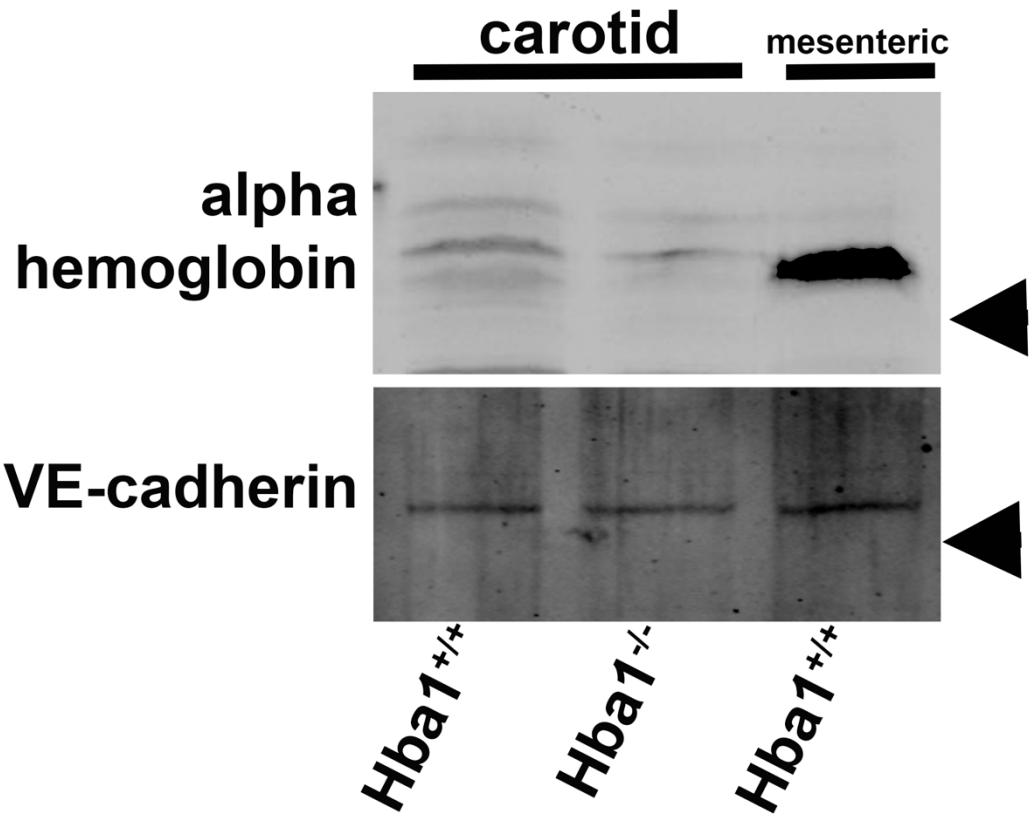

Figure 14. Baseline expression of alpha hemoglobin in resistance versus carotid arteries. Alpha hemoglobin arrow indicates 10 kDa and VE-cadherin arrow indicates 100 kDa. All samples are from untreated arteries.

Discussion

We have previously demonstrated that PAI-1 regulates MEJ formation.(36) In this study, we further investigated the involvement of PAI-1 in MEJ formation by delivering a high concentration of PAI-1 directly to CAs of live mice via a pluronic F-127 gel while avoiding adverse systemic effects. The local increase in PAI- resulted in structural and functional changes in the CA that phenotypically shifted it to resemble a resistance artery. CAs normally have few HIEL and EC projections through those breaks in the lamina; however, after 7 days of PAI-1 directly on the CA, both of these anatomical phenomena developed. Evidence of direct heterocellular coupling between endothelium and smooth muscle were also observed following PAI-1 treatment, including Cx40 expression in the newly formed HIEL and biocytin transfer that was blocked when α-GA, a purported gap junction inhibitor, was included in the experimental setup. However, direct evidence of heterocellular coupling via electrical coupling (e.g.,(17, 89)) could not be demonstrated. Regardless, the significant upregulation of HIEL, EC projections, and heterocellular movement of molecules represents an important anatomical shift in this conduit artery.

Our results show that the formation of HIEL is transient, achieving a maximum by day 7 of PAI-1 treatment and dissipating by day 21. The underlying mechanism of this transient formation is unclear, but it could represent either an unresolved inflammatory response or, more simply, degradation of the exogenously applied PAI-1. This temporal loss of the HIEL formed following PAI-1 treatment also suggests a dynamic nature of HIEL/MEJ, with the potential

necessity of a constant stimulus to maintain the ability to form MEJs. Since exogenous application of PAI-1 alone induces formation of HIEL and MEJ-like projections within the carotid, this represents an important advancement in our understanding of the development of these critical vascular signaling domains. The spatial distribution of PAI-1 across the vascular wall may be one such avenue to explore—with its local translation and thus protein enrichment at MEJs (90), it is possible the MEJ signaling domain may be capable of regulating formation of holes in the matrix. Lastly, the role of inflammation on formation of HIEL and/or EC projections will be an important expansion on this work that will be elaborated on in future studies.

Functionally, the induction of these MEJs in the carotid was able to switch the vasodilatory profile of these conduit arteries to be more reliant on EDH based vasodilation compared to NO. Pressure myography experiments revealed increased relaxation via the IK_{Ca}/SK_{Ca}-channel activator NS309, and that L-NAME, an inhibitor of NO production, was unable to prevent vasodilation via the Ach pathway in PAI-1-treated CAs at 7 days post-treatment. These results indicate a switch from primarily NO-based signaling, normally characteristic of conduit arteries, to a predominantly EDH-based mechanism, characteristic of resistance arteries. The correlation of this switch in dilatory mechanism alongside increased MEJ formation mimics the anatomical and functional observations of resistance vessels; thereby demonstrating that the MEJ is a crucial regulator in determining the vasodilation pathways in arteries.

Alpha globin expression is normally limited to resistance arteries where it localizes to the MEJ.(38) Alpha globin has been shown to complex with eNOS to regulate NO-signaling in the resistance vasculature, (80, 81) where it can scavenge NO produced by eNOS and limit the amount available for diffusion across the vessel wall to result in vasodilation. (38, 39) Its expression at the MEJ finely controls vasodilation by limiting the diffusion of eNOS-derived NO from the MEJ to the SMC.(38) As follows with our other data, the expression of this resistance artery specific protein was increased in CAs following PAI-1 treatment in the newly formed MEJs. This aligns with previous data that indicated protein expression of alpha globin is dependent on the heterocellular contact between ECs and SMCs (39). The PAI-1-induced expression of alpha globin in CA MEJs limited the dilatory effect of NO in these vessels (Figure 4H). In mice with a disrupted alpha globin gene product, vasodilation still occurs via NO, with Ach-mediated vasodilation nearly completely inhibited with L-NAME alone, with little additive effect from EDH inhibitors (Figure 4I).

Within the vasculature, cell-cell interactions induce protein expression to influence cellular function (39, 91-94) and our results embody this motif: alpha globin expression is induced upon heterocellular contact (EC-SMC coupling) and alters cellular function (altered mechanism of arterial relaxation). This data also fits well with previous work demonstrating alpha globin's regulation of eNOS (80, 81) and suggests that alpha globin expression is imperative for EDH-based signaling to predominate. Our lab has demonstrated that the disruption of the alpha globin/eNOS interaction via a mimetic peptide leads to increased NO signaling.

(38, 80) Based on this and the data we show in this paper, alpha globin at newly formed MEJs in PAI-1-treated carotids likely participates in the switch to EDH-based relaxation through limiting the effects of NO-based vasodilation. It is also possible that the PAI-1 enzyme may be simultaneously acting on eNOS to reduce NO-availability, enhancing the inhibitory effect to ensure EDH predominates. The interaction between PAI-1 and eNOS may be an interesting avenue to explore in future studies.

Since the major anatomical differences between a conduit and resistance artery are the IEL and points of heterocellular contact via MEJs, our finding that the induction of MEJs can switch a conduit artery's dilatory mechanism from NO-dominated to likely EDH-dominated demonstrates a match between form and function. Our data suggests that MEJs are an anatomical platform for EDH signaling with alpha globin expression, and could be the reason why EDH predominates in resistance arteries.

Appendix

Contributions from authors:

X Shu and CA Ruddiman performed experiments, especially *en face* imaging and vasoreactivity. ME Good, Y Yang, and AS Keller performed vasoreactivity and other experiments as needed. X Shu and TCS Keller were responsible for carotid/PAI-1 surgeries. AK Best supervised mouse colon management, L Columbus and BE Isakson supervised project.

CA Ruddiman amended figures and manuscript for this version to be incorporated into her thesis.

Chapter 3. Myoendothelial heterogeneity enables phosphatidylserine regulation of Kir2.1

Abstract

Total peripheral resistance is a major component of blood pressure that is dictated by resistance arteries. Poiseuille's Law describes that flow is proportional to the radius of the blood vessel to the fourth power (r^4), indicating that minute changes in the resistance arterial diameter have large effects on blood pressure; thus, the vasodilatory pathways that dictate their diameter is tightly regulated. The myoendothelial junction (MEJ) is an anatomical hallmark of resistance arteries and is a crucial signaling microdomain that coordinates vasodilation through heterocellular communication. The MEJ forms when endothelial cells (EC) extend through holes in internal elastic lamina (HIEL) and make contact with smooth muscle. It is well-known that gap junction proteins, potassium channels, and calcium channels localize to the MEJ. However, *en face* immunohistochemistry throughout the literature demonstrates heterogeneous protein localization to HIEL, posing the question if each HIEL contains an MEJ or if functionally distinct subpopulations of MEJs exist.

In order to answer this question, I first sought to determine if every HIEL contained an MEJ via a transmission electron microscopy approach. I predicted how many MEJs I would expect to see in TEM cross-sections based on quantitative measurements of HIEL in *en face* images. This approach allowed me

to identify a cellular projection independent of protein localization. The number of MEJs detected was within the predicted range, thus I conclude that every HIEL contains an MEJ. Since this was the case, it was unclear to us why protein localization to these domains was heterogenous.

We hypothesized that the local lipid composition of MEJs could in part regulate the protein composition, given the growing evidence that lipids regulate protein function and localization. Previously, we demonstrated that phosphatidylserine (PS), an anionic lipid species, localizes to the MEJ in an *in vitro* vascular cell co culture model. We show that this lipid is also present in intact, third order mesenteric arteries and is enriched in only 13.8% of MEJs, with 1.18 PS-MEJs per EC. We wanted to better understand the function of this unique subpopulation of MEJs. Recent in silico data indicate that PS has a binding site on the Kir2 channel and can compete for the PIP_2 binding site, which is a known activator of channel function. Due to the evidence that Kir2.1 is crucial for facilitating vasodilation and is active in endothelial cells, **we hypothesized that PS could regulate Kir2.1 function at the MEJ.**

Indeed, we found that 83.33% of Kir2.1-MEJs also contained PS. In contrast, only 14.64% of Cx40-MEJs also contained PS. This demonstrated to us that the PS-Kir2.1 interaction at the MEJ was an intentional, specific interaction. We next tested this interaction functionally, and found that in an *ex vivo* pressure myography setup, addition of exogenous PS blunted Kir2.1-mediated vasodilation to similar levels of the known $K_{ir}2.1$ inhibitors, Ba^{2+} (100μM) and ML-133 (3.6 μM). Based on this inhibition and *in silico* data suggesting PS can bind to the PIP_2

binding site, **we hypothesized that PS may compete for the PIP_2 binding site on Kir2.1**. We tested this using whole-cell patch clamp electrophysiology and found that the addition of PS to the system inhibited PIP_2-mediated Kir2.1 activation. We next tested the impact of PS on PIP_2-mediated dilation on intact arteries. We demonstrated that exogenous addition of PIP_2 to arteries resulted in a consistent vasodilatory response that was inhibited by Ba^{2+}, ML-133, and PS. Since exogenous PS was able to block PIP_2-mediated vasodilation in intact arteries to a similar level of known Kir2.1 inhibitors, we conclude that PS at the MEJ can compete for and block PIP_2 access to its binding site on Kir2.1. *In vivo*, this interaction may have a dampening effect to prevent excessive vasodilation.

The MEJ is the anatomical location that facilitates the interaction between PS-Kir2.1. We hypothesized that the absence of MEJs *in vivo* would prevent this lipid-protein interaction. We sought to use a genetic mouse model to disrupt canonical MEJ formation, and were inspired by a recent study that demonstrated IEL disruption via TEM cross-sections from an endothelial cell-specific elastin knockout ($Eln^{fl/fl}$/$Cdh5Cre^{+}$) mouse model. We followed up on this study and found that canonical HIEL were no longer detectable in the *en face* view. In addition, PS was disrupted with fewer high intensity puncta and reduced surface area coverage. The protein expression of Kir2.1 was unchanged between genotypes; however, the dilation to exogenous PIP_2 was significantly increased in EC-Eln KO mice. This suggests that Kir2.1 is more susceptible to PIP_2 activation in EC-Eln KO arteries. Since PS is disrupted in the endothelium, and Kir2.1 protein expression is unchanged in KO, we conclude that PS is no longer competing for the PIP_2 binding

site on the channel which results in an increased dilation. We tested this experimentally by adding back PS *ex vivo* prior to PIP_2 dilation. Indeed, addition of exogenous PS reduced PIP_2 dilation back to control levels. Taken together, this evidence indicates that the directed localization of PS to MEJs functions to modulate Kir2.1 function in resistance arteries.

Introduction

Kir2.1 important in regulating cardiovascular homeostasis and is expressed in both the heart and peripheral vasculature. (21, 95) This channel is important in maintaining homeostatic potassium levels inside the cell by generating a potassium efflux. In resistance arteries, active currents have been observed in endothelium but not smooth muscle (21), and global heterozygous knockout of Kir2.1 leads to hypertension in mice. (95) In addition to its role in nitric oxide-based flow-mediated vasodilation (96), Kir2.1 is also a contributor to endothelial derived hyperpolarization (EDH), the predominate dilation pathway in resistance arteries. (10, 21) Resistance arteries contain a signaling microdomain called the myoendothelial junction (MEJ), which is an endothelial cell (EC) projection through holes in the internal elastic lamina (HIEL) that makes contact with smooth muscle cells (SMC). The MEJ is a critical site of heterocellular communication that facilitates EDH-based vasodilation through gap junction formation and localization of ion channels, (5, 9, 56) such as the Ca^{2+}-activated intermediate conductance potassium channel (IK_{Ca}), and Transient Receptor Potential Cation Channel Subfamily V Member 4 (TRPV4) (13, 97). While functional data implicates that Kir2.1 may be at the MEJ, it has not been demonstrated to localize there via microscopy. Further, Kir2.1 channel function is regulated by lipids, where cholesterol prevents normal activation (96, 98, 99) and PIP_2-Kir2.1 interaction lead to channel opening and activation (100). Thus, we sought to determine if Kir2.1 was localized to the MEJ and how channel function was regulated by the local lipid environment.

Our lab demonstrated that phosphatidylserine (PS) was enriched in *in vitro* MEJs that were isolated from a vascular cell co-culture model (VCCC) (24). PS is an anionic phospholipid that is enriched on the inner leaflet of lipid bilayers and comprises between 3-10% of the lipid composition of a cell. (101) Given that PS has been implicated in regulating protein localization and inward rectifying potassium channel function, (102, 103) we sought to determine the contribution of PS to localization and function of Kir2.1 in resistance arteries. While some data indicate PS as a co-activator of Kir2.1 function, (104, 105) a recent *in silico* model demonstrated that PS can also bind to the PIP_2 activation site, (102) implicating that PS may be capable preventing the necessary binding of PIP_2 for Kir2.1 channel activity. We therefore hypothesized that PS and Kir2.1 localized together at a unique subpopulation of MEJs, where PS could negatively regulate PIP_2 activation of Kir2.1 and thus modulate the magnitude of vasodilation and thus total peripheral resistance.

Introduction to Kir

Maintenance of intracellular ion concentrations is imperative for healthy cellular function and processes, where normal homeostatic K^+, Na^+, and Ca^{2+} are approximately 150mM, 15mM, and 0.1μM, respectively. Small deviations from homeostatic concentrations are immediately sensed within the cell and often trigger downstream events. The cell has evolved to produce machinery to tightly control these concentrations including ion channels and transporters that localize to PM. Cytoplasmic concentrations can also be regulated by ion channels localized to organelles such as the endoplasmic reticulum. The mechanism of how a heart beats or how a neuron fires are iconic examples of ions coordinating cellular events that sustain the human body. Vasodilation and constriction are also tightly controlled by the movement of ions into and out of the cell. The level of dilation and constriction in resistance arteries is most impactful in determining TPR and ultimately blood pressure. This section will focus on the role of potassium (K^+) its contribution to vasodilation and its regulation by the inward rectifying potassium channel 2.1 (Kir2.1).

Kir channels are found in a plethora of cell types throughout the body, including excitable cells such as cardiac myocytes (106, 107) and neurons, (108, 109) non-excitable cells such as osteoclasts, (110) glial cells, (111) epithelial cells, (112) oocytes, (113) and non-excitable vascular cells such as blood cells,(114) endothelial cells, (21, 100, 115, 116) and smooth muscle cells. (117) In the vasculature, Kir2.1, Kir2.2 are the most highly expressed isoforms, with Kir2.1 being the most predominate in the endothelium. (118) SMC Kir2.1 does not have

active currents in mouse mesenteric arteries.(21) Channel mutations in humans are associated with Andersen's syndrome which is characterized by cardiac arrhythmias. (119, 120) Downregulation or disruption of Kir channels are associated with heart failure and reduced dilation in cerebral arteries. (121) (122) Global constitutive knockout Kir2.1$^{-/-}$ mice die within 12 hours of birth (122) and Kir2.1$^{+/-}$ mice are hypertensive. (95) Together, this demonstrates the importance of this channel in cardiovascular homeostasis and function.

The Kir channel family consists of 16 KCNJ genes divided into seven families (Kir1.x to Kir7.x), where Kir2.x and Kir3.x are strong rectifiers, Kir4.x are intermediate rectifiers, and Kir1.x and Kir6.x are weak rectifiers.(123) The channels can also be classified into different functional groups, where Kir2.x are classical Kir channels, Kir3.x are G protein gated Kir channels, and Kir6.x are ATP sensitive.(124) Kir were first discovered in skeletal muscle,(125, 126) and they were particularly interesting because their ion flow did not follow the outward rectification as predicted by the Nernst equation or Hodgkin-Huxley kinetics,(127) with a inactivation when depolarization occurs. This is attributed to intracellular pore blockage by both polyamines and Mg^{2+} ions, otherwise referred to as "polyamine block". The Kir2 subfamily are particularly sensitive to polyamine block, in particular spermine and spermidine,(128) then somewhat regulated by cadaverine and putrescine.(129)

Overview of Kir channel structure

The Kir2.x channel subfamily are comprised of a transmembrane domain and a large cytoplasmic domain (TMD, CTD), with structural features that contribute to channel regulation in both domains. The transmembrane domain contains four alpha helices, two that traverse the membrane, one that lines the pore, and one that is on the outside of the channel. (130) At the most extracellular region of the TMD, there is a protein sequence that connects the two alpha helices on that side of the channel, with a major structural function of restricting the size of the extracellular opening.(131) This region is referred to as the turret. Right below the turret is the selectivity filter, which has sequence to similarity across the family.(132) The selectivity filter is localized in the middle of the pore and is comprised of two major features: (1) conserved disulfide bond between extracellular loops of the transmembrane domain and (2) an ion pair between intra- and extracellular sides of the loop.(133, 134) These features are required for ion movement through the pore. At the interface of the TMD and CTD is a bundle crossing region that acts as a gate for ions into the transmembrane region. The amino acid at this region varies between the different isoforms of Kir, and is a methionine in the strongly rectifying Kir2.x family. (135) The CTD is comprised of the functional units G-loop, upper ring, and lower ring. The G-loop contains residues (G285 and G300 in Kir2.1) that are involved in channel regulation through providing flexibility where a binding partner can induce conformational changes, including by PIP_2 binding.(131, 136, 137)

A single residue in the TMD of Kir channels can dictate the level of rectification, which is the acidic aspartate at 172 (D172) , and therefore is termed the “rectification controller”. (138) It is located between the selectivity filter and bundle crossing region, where an aspartate from each of the subunits of the tetramer interact and form a highly negatively charged ring, allowing polyamines to bind and block ion flux. (139) While this is a major contributor to polyamine block there are other residues within the TMD and CTD that are also crucial in regulating the strong rectification properties of Kir channels. (139)

Regulation of Kir2.1 by lipids

Phosphoinositol-4,5-bisphosphate (PIP_2), is a phosphoinositide that comprises approximately 3% of eukaryotic membranes and represents over 99% of all phosphoinositide in the cell. (140) (141) This lipid localizes primarily to the intracellular side of the plasma membrane and can be cleaved by phospholipase C downstream of Gq coupled signaling where its cleavage products, IP_3 and diacylglycerol (DAG), act as second messengers in a variety of cellular signaling events, including specifically at the MEJ. (24, 41) This small, anionic phospholipid is also a direct activator of Kir channels, (142) including Kir2.1, Kir2.1, Kir3.1, Kir3.2, Kir3.4, Kir6.1, and Kir6.2. (119)

An x-ray crystallography structure of Kir2.2 with PIP_2 revealed the structural mechanism of PIP_2 facilitating Kir channel opening and thus potassium flux. PIP_2 associates with a specific phosphoinositide binding site within the CTD and a nonspecific lipid association site in the TMD domain. Thus, the ability of PIP_2 to

interact with the two major domains of the channel induces a conformational change, specifically with the CTD shifting 6 angstroms, that promotes pore opening. (130, 135) On Kir2.2, the identified residues are: R65, R78, W79, R80, K183, R186, K188, K189, R190, and R219. (135) This was the first study to structurally define how PIP_2 was interacting with the Kir2.2 channel. Similar residues in Kir2.1 were shown to confer PIP_2 sensitivity, as when they were mutated, the ability for PIP_2 to increase Kir2.1 currents was reduced: H53, R67, K182, K185, K187, K188, R189, R218, K219, R228, H271, and R312. (119) Further, the PIP_2-mediated activation of these channels has been demonstrated to likely be independent of subsequent cleavage into diacylglycerol (DAG) and inositol-1,4,5-trisphosphate (IP3). (105)

There is also evidence of a secondary binding site, involving the residue K64 and K219 define the secondary lipid binding site on Kir2.1, (143) (102) where another anionic lipid can bind and in many cases has been shown to increase channel activation through conformational changes that favor opening. (104) Indeed, the oxidation of these residues can also have a “tethering” effect that mimics channel opening in the same way association with an anionic phospholipid would. (143) The presence of two anionic binding sites introduces lipid interplay as another variable that must be considered in channel regulation and may only be more complicated by specialized, cellular lipid environments that cannot be captured through computer simulations or liposome experimentation.

In a simulation of a cellular membrane containing Kir2.1 and modeled without PIP_2, phosphatidylserine (PS) associates equally with both the primary and

secondary lipid binding sites, (143) and clusters around the channel. (102) In contrast, other lipids such as PPA, phosphotidylethanolamine (PE), and phosphatidylcholine (PC) will primarily occupy the primary lipid binding site when PIP_2 is absent. (143) PS also interacts strongly with residues at the primary binding site, R78, R80, K183, R186, K189, and with the two defining residues of the secondary binding site, K64 and K219. (102) Altogether this suggests that PS is spatially oriented and inclined to interact with both binding sites in a low PIP_2 environment. When PIP_2 is bound to the primary site at the beginning of the simulation, PS is more likely to associate with just the secondary site. (143) This secondary site occupancy when PIP_2 is also bound has been attributed to increased channel activity. (104) (105) Interestingly, when PIP_2 is bound to its primary site at the beginning of the simulation, the only lipid other than PS that accesses the primary site is PE, a lipid product that can be synthesized by PS. (144) These data indicate that lipid environment is a strong mediator of how lipids interact with channels to regulate their function.

Of note, the previously described experiments do not control for cholesterol content, a known inhibitor of Kir2.1 activity. Cholesterol constitutes 10-45% of lipids in the cell. (145) An enrichment of cholesterol in aortic endothelial cells significantly suppresses current through Kir, (146), cholesterol suppresses flow-mediated vasodilation of Kir2.1(96), and Kir2.1 fractionates in low-density sucrose fractions indicating that it localizes to cholesterol-rich lipid rafts. (147) (148) These data suggest that cholesterol is involved in regulating Kir channel activity. Indeed, Kir channels are sensitive to cholesterol through a specific region on the CTD called

the CD loop, which houses the L222, N216, K219 residues. Specifically mutating the L222 residue has a dominant negative effect on cholesterol sensitivity. (149) While initial mutagenesis studies suggested cholesterol sensitivity was independent of PIP_2 binding, (149) follow-up studies indicate that cholesterol sensitivity is conferred through prevents the conformational changes induced by PIP_2 binding. (150) Further simulation work has suggested that cholesterol interactions with Kir2.1 actually prevent tetramer formation to prevent channel activity. (99)

Other lipid inhibitors of Kir2.1 include pyrophosphatidic acid (PPA), an anionic phospholipid that was demonstrated to be able to occupy essentially the same region as PIP_2 without contributing to an activating conformational change. (135) In further functional testing, it was confirmed that PPA alone cannot act as a substitute for PIP_2, but rather prevents PIP_2-mediated activation of Kir2.1. (143) This competitive inhibitor function of PPA is similar to that of other phosphoinositides. (104) Other antagonists of PIP_2-mediated activation are oleoyl coA and ethyl-phosphatidylcholine (EPC).

Lipid composition, organization, and function in the plasma membrane

All eukaryotic cells have plasma membrane consisting that consists of a lipid bilayer. An individual phospholipid consists of a hydrophilic phosphate head group connected to two hydrophobic fatty acid chains by an alcohol or glycerol group. When assembled in a bilayer, the hydrophilic head groups will face the cytoplasmic and extracellular space, while the fatty acid chains from adjacent phospholipids will interact with each other in the middle. The plasma membrane was initially viewed only as a protective barrier with no active role in cellular function. In 1972, Singer and Nicholson described the fluid mosaic model of plasma membranes. (151) With thermodynamic considerations, they described that the membrane was a non-uniform mixture of lipids and proteins that were continually moving. This new way of viewing the plasma membrane implicated an active role in modulating cellular function.

Lipid composition of the plasma membrane varies depending on cell types, but the four major phospholipids of mammalian cells are phosphatidylcholine (PC), phosphatidylethanolamine (PE), phosphatidylserine (PS), sphingomyelin, and cholesterol. (152) Both PS and PE are asymmetrically distributed across the bilayer with a majority localized to the inner leaflet. (152) Flippases, floppases, and scramblases regulate the localization of lipids to the cytoplasmic or extracellular side of the membrane. (153) Flippases regulate translocation of PE and PS from outer to inner leaflet, while floppases transport PC from inner to outer leaflet. Since these transport lipids against their concentration gradient both of these enzymes

require ATP. Scramblases, however, do not transport lipids in any particular direction and do not require ATP to translocate lipids to different sides of the PM. (153) PS can be flipped to the extracellular side of the plasma membrane in a Ca^{2+}-dependent manner, where calcium influxes can result in translocation to the outer leaflet via TMEM16F, and upon return to baseline calcium concentration, flippases can reactivate to reestablish asymmetrical PS distribution. (154, 155)

Phosphatidylserine

PS is negatively charged at physiological pH, unlike PC, PE, and sphingomyelin which are neutral, and comprises approximately 5-10% of mammalian cell membranes. (101) PC and PE undergo de novo synthesis via the Kennedy pathway (156), and PS can be synthesized from them via two enzymes, phosphatidylserine synthase 1 or 2 (PSS1 or PSS2). (157) Although structurally similar, the two enzymes only share 32% amino acid sequence identity and use different substrates, PC or PE, respectively. (158) There is differential localization of mRNA in mouse tissue, with PSS1 being more ubiquitously expressed and PSS2 being more concentrated in Sertoli cells (testes) and Purkinje cells (brain). Both PSS1 and PSS2-deficient mouse models are viable mice with normal development. (144, 158) In PSS2-deficient mice, phospholipid composition remains unchanged, and in PSS1-deficient mice PS content is only reduced in the liver, and is unchanged in the heart and brain. Interestingly, PSS2 mRNA expression is not significantly increased in PSS1 knockout tissues (although there is a trending upregulation in brain tissue isolated from homozygous global

knockout mice). (144) When attempting to make a double knockout mouse of both these enzymes, only mice with 3 alleles knocked out are generated, and no double knockouts were produced, indicating that PS synthesis via these enzymes is necessary for development. In mice with just one allele ($Pss1^{-/-}$ / $Pss2^{+/-}$ or $Pss1^{+/-}$ / $Pss2^{-/-}$) there is a 40% reduction in PS content (and 29% reduction in PE) but still the mice are outwardly normal. (144) Since there are no PSS1 and PSS2 double knockouts produced, it is clear that a pathway necessary for development is disrupted in their absence. However, it is difficult to interpret if PS itself or if PE derived from PS via PS decarboxylase (PSD) is the crucial developmental component, (144) since PE is functionally relevant in facilitating protein biogenesis, protein activity, membrane fusion, and oxidative phosphorylation and autophagy.(159)

Biological functions of phosphatidylserine

One of the canonical functions of PS is facilitating the hemostasis through participating in the clotting cascade. When there is damage to a blood vessel that needs to be repaired, the matrix beneath the endothelial cells is exposed. Collagen receptors on platelets that can bind to these injured areas to jumpstart the signaling pathways for clotting. This binding initiates a signaling cascade that results in a significant calcium increase within the platelet. (160) The lipid scramblase TMEM16F is activated by this calcium increase and flips the PS to the exofacial surface of the platelet. Due to the anionic nature of PS, it functions as a scaffold where the clotting factors can aggregate to facilitate downstream signaling. (161)

Patients with Scott syndrome lack a functional TMEM16F and therefore have bleeding disorders. (161, 162)

Another well-known and -studied function of PS is its role in apoptotic cell death. (163) Exofacial presentation of PS on apoptotic cells occurs over the course of hours and is well-recognized as the “eat me” signal in apoptosis. (164, 165) It is currently a debate whether PS movement to the extracellular side of the lipid bilayer is a Ca^{2+}-independent or -dependent process. (165) Interestingly, patients with Scott syndrome have normal PS exposure during apoptosis, which strongly suggests that TMEM16F is not involved in the apoptotic movement of PS.(166) The C2 domain of lactadherin binds specifically to PS and is present on macrophages, which can also interact with integrins on phagocytic cells, targeting the apoptotic cell for engulfment. (167)

PS is also an important regulator of protein function by acting as a co-activator, along with diacylglycerol (DAG), of protein kinase C (PKC). (24, 168, 169) PKC is an enzyme that can regulate the phosphorylation and thus activation of numerous proteins in a cell. In ECs, PKC can activate Akt, which in turn activates eNOS signaling. (170) PS is also implicated in the polar localization and trafficking of proteins within cells, where it can interact with numerous proteins containing a polycationic stretch of amino acids. (165) PS regulates the polarity of Cdc42 in yeast such that proper budding occurs, (171) phagosome function through localization and recruitment of Src, (172) and interacts with Ras and Rho family GTPases to regulate their function. (173) PS is also important in intracellular membranes through its enrichment to recycling endosomes through interactions

with evectin-2. (174) It is also involved in trafficking events, through being a substrate for oxysterol-binding proteins (ORPs) (175, 176) and through promoting the trafficking of other lipids to the PM (177). The localization of PS to inner or outer membranes on organelles also influences protein and lipid trafficking, with a proposed role for the PS flippases ATP8A1 and ATP8A2. (178)

PS and Cholesterol interactions in the membrane

The localization of PS within the plasma membrane tends to be enriched within lipid rafts which are high in cholesterol content. (179) PS also has been demonstrated to localize to and facilitate the formation of caveolae. (180, 181) When PS depleted from cell membranes, caveolin-1 (Cav1) proteins disassociate from their clusters and reduce the number of anatomical caveolae in the membrane.(181) PS can also influence the curvature of the membrane where it is enriched. For example, when cholesterol is depleted from a PS enriched membrane, there is a spontaneous membrane curvature inward due to the charge repulsion force of clustered anionic lipids. (182-184)

PS is also important in the trafficking and retention of cholesterol in the plasma membrane. (177) (185) When LDL cholesterol is taken up into the cell via endocytosis to enter a lysosome. This pool of cholesterol must go to the plasma membrane before being trafficked to ER. However, when PSS1 is depleted from cells, this cholesterol is trapped at the plasma membrane, implicating PS as an important determinant in cholesterol movement. Interestingly sphingomyelin has

the opposite effect on cholesterol movement and contributes to its stability and retention in the plasma membrane.(177)

Diseases associated with PS

Scott syndrome is an extremely rare disease that is characteristic of severe hemorrhagic episodes. This disease is not diagnosed by normal coagulation tests because clotting factors are present at normal levels. Diagnosis involves examining platelet aggregation under arteriolar flow (high shear stress), which is significantly reduced in patients, and also through thrombin stimulation of platelets and flow cytometry to detect the amount of PS present on platelet membranes. (186) The lack of PS flipping to the extracellular side of the bilayer is attributed to a dysfunctional scramblase, TMEM16F in these patients. (161, 162)

PS overproduction is the cause of a long-known developmental disease called Lenz-Majewski syndrome. (187, 188) This is an extremely rare disease with only eight total cases reported as of 2013 and patients present with severe developmental, intellectual, and physical abnormalities. It was identified in a study of five patients' DNA that mutations in PTDSS1 resulted in a gain of function effect for the enzyme, where it affects the negative feedback regulation of PS on PSS1 activity.(188)

Lipids at the MEJ

In our lab's in vitro VCCC model, we were able to determine the relative amounts of lipids in EC, SMC, and MEJ fractions compared to cells that were

cultured separately.(24) This data indicates that heterocellular contact can dictate the relative abundance of lipids in the cell. For example, sphinogmyelein is heavily enriched in EC monolayer culture compared to other sphingolipids, but is significantly reduced in the EC fraction of VCCC experiments. On the other hand, there is a significant increase of glycerolipids in the EC fraction of VCCC experiments, including phosphatidylethanolamine and phosphatidic acid.

In the MEJ, although not significant, cholesterol content is reduced compared to the EC fraction of the VCCC experiment. Phosphatidylserine, sphingamine, and phosphatidic acid are increased in the MEJ fraction compared to the EC or SMC layers while sphingosine 1 phosphate is decreased in MEJ fraction compared to SMC fraction. DAG is also significantly increased in the MEJ fraction, indicating the relatively high hydrolysis of PIP^2 that may occur at this signaling microdomain. These results indicate that heterocellular contact can alter the lipid composition in EC and SMC. However, it remains unclear how this lipid composition can affect MEJ heterogeneity, which will be explored in this chapter.

Caveolae are present in the endothelium and MEJ

The general definition for lipid/protein complexes at the cellular membrane is *lipid rafts*. Although individual lipid rafts are small in size and generally not detectable by electron microscopy, they have been shown to make up to 50% of the plasma membrane. They are enriched in cholesterol and glycosphingolipids, which reduces membrane fluidity compared to the surrounding plasma membrane; this high saturation allows for tight packing to facilitate microdomain formation

(189). Clustering of proteins within microdomains can facilitate signal transduction, but can also negatively regulate protein activity by sequestering proteins to prevent activating protein-protein interactions that may occur outside of the microdomain (189). On the other hand, recruitment of a protein to a microdomain could also promote a protein-protein interaction that ultimately negatively regulates it through an inhibitory interaction (189). An example of this is the eNOS/Caveolin-1 (Cav-1) interaction within caveolae (189). Moreover, proteins belonging to specific signaling cascades like tyrosine kinase or G-protein coupled receptors, glycosylphosphatidylinositol-linked proteins (GPI-linked proteins), G proteins, and protein kinases may be clustered in membrane microdomains.

Caveolae are a subset of lipid rafts and are small plasma membrane invaginations of about 50-100 nm in diameter (190), which (contrary to other lipid rafts) are visible by electron microscopy. They were initially described by G.E. Palade in 1953 from electron micrograph images of capillaries and were termed plasmalemma vesicles (191). In 1955, E. Yamada discovered them in the gall bladder epithelium (192). He viewed them as “little cave” structures and thus termed them *caveolae intracellulares*. These flask shaped microdomains were only defined in terms of morphology until 1992, when caveolin, the major coat protein of caveolae, was discovered (193). Caveolin proteins distinguish caveolae from other lipid rafts, whose binding to cholesterol is thought to stabilize their invaginated structure (189). PS is also present within caveolae (180) and facilitates their formation (181, 184), where cells depleted of PS had more freely moving Cav-1. Thus, both PS and cholesterol are needed for proper caveolae formation in ECs.

PIP_2 is also present in caveolae, but is not required for proper formation of these lipid rafts.(194)

Caveolae are highly enriched in epithelial cells, adipocytes, fibroblasts, VSMC, and EC (195). In ECs, they occur at a striking density of approximately 80 per μm^2. They facilitate macromolecular endocytosis in EC, whereas in other cell types this process is largely mediated through clathrin-coated vesicles. Moreover, they participate in mechanosensing and mechanotrasduction (25), where they flatten in response to shear stress. (196) In ECs, shear stress decreases cholesterol content and increases fluidity.(197, 198) Another crucial function of caveolae is their participation in microdomain formation within the resistance arterial endothelium where they are specifically enriched within the MEJ. (26)

Materials and Methods

Mice

The elastin gene, *Eln,* was selectively knocked out of ECs via a VE-cadherin cre ($Cdh5Cre^{+}/Eln^{fl/fl}$). These mice were on a C57Bl/6 background, and both sexes within the age range of 10-20 weeks were used for experiments. For experiments on this knockout mouse, $Cdh5Cre^{-}/Eln^{fl/fl}$ littermates were used. For all other experiments, C57Bl6/J male mice between 10-20 weeks were used. Mice were fed a normal chow and housed under a 12-hour light/dark cycle. Mice were sacrificed via CO_2 inhalation with a secondary method of cervical dislocation. All experiments were approved by the University of Virginia Animal Care and Use Committee.

Antibodies and plasmids

The following connexin plasmids were a kind gift of Janis Burt: pcDNA3.1 hygro mouse Cx37, pcDNA3.1 puro mouse Cx40, and pcDNA3 neo mouse Cx43. We purchased pEGFP-C1 neo Lactadherin-C2 (Addgene, 22852) and pCAG-Kir2.1-T2A-tdTomato (Addgene, 60598). pcDNA3.1 Panx1 was cloned in house.

Antibodies used were rabbit anti phosphatidylserine (Biomatik, CA30389), mouse anti KCNJ2 (Sigma, SAB5200027), rb anti connexin 37 (Thermofisher 40-4300, preferred), mouse anti connexin 40 (Thermofisher, 37-890, preferred), rb anti connexin 40 (Thermofisher, 36-400), mouse connexin 43 (Sigma, C8093), rb anti connexin 43 (Sigma, C6219), goat anti calnexin (Abcam, ab219644), mouse anti caveolin-1 (Novus Biologicals, NB100-615), mouse anti IKCa(Alomone, ALM-

051) Alexa-Fluor linked hydrazide 488 (Thermofisher, A10436) or 647 (Thermofisher, A20502).

En face immunohistochemistry

Mesenteric arteries were fixed with 4% paraformaldehyde at 4°C for 15 minutes. Following PBS washes, arteries were cut *en face* using microscissors and pinned out with tungsten wire (0.013mm diameter) on small sylgard squares. Next, *en face* preps were permeabilized in 0.2% NP40/PBS at RT for 30 minutes, blocked with BSA or animal serum for 1 hour, and incubated with primary antibody 1:100 at 4°C overnight in blocking solution. Blocking solutions were either 5% serum or 10% BSA (for PS detection) in 0.2% NP40/PBS, depending on the experiment.

The next day *en face* preps were washed in PBS and incubated with secondary antibodies (1:400) and hydrazide at RT for 1 hour in blocking solution. Alexa Fluor 488- or 647-linked hydrazide powder was reconstituted in diH_2O for a final concentration of 1mM and diluted 1:1250-1:2500 in secondary antibody solution to visualize IEL. Next, the arteries were washed 3x 10 minutes in PBS. The third PBS wash included DAPI at 1:5000 from a 5mg/ml stock solution. Following PBS washes, the sylgard square was placed onto a microscope slide. Next, a droplet of Prolong Gold with DAPI was dispensed on top of the sylgard square. Lab tape was used to secure a square coverslip to the microscope slide prior to imaging. Images were obtained on either a Zeiss 880 LSM with Airyscan (Matlab analysis images) or Olympus Fluoview 1000, with a 40x oil objective.

Analysis of stitched confocal *en face* images

Stitched confocal images of arteries prepared *en face* were taken as three images on a Zeiss 880 LSM confocal microscope with a 40x objective and 1.8 zoom. Each individual image was analyzed using our in-house Matlab analysis program in order to identify HIEL and PS-HIEL. Next, individual ECs were traced using claudin-5 staining in Image J and assigned a number. Individual HIEL data obtained from Matlab was then manually organized by EC number in Microsoft Excel for analysis.

In-house analysis of immunofluorescence *en face* images

Briefly, each immunofluorescence channel of an *en face* image was subject to customized thresholding in order to detect HIEL and EC signaling hub (nuclei, interendothelial junctions, or endoplasmic reticulum depending on experiment). The brightness and contrast settings were adjusted around difficult- to-detect HIEL in ImageJ prior to thresholding in Matlab. For claudin-5 experiments (not calnexin or nuclei), the ImageJ line tool was used to assist in detection of low-intensity claudin-5 signal at interendothelial junctions, and nonspecific background noise in the middle of the cell was removed to facilitate correct thresholding in Matlab program.

This thresholding was then used to calculate the minimum distance of HIEL center points to the EC signaling hub considered and this distribution was plotted as a box and whiskers plot. The distribution was then compared to positive (PC), negative (NC), and random control (RAND, via Monte Carlo) simulations in order

to determine the spatial distribution. Positive control simulations generate HIEL within 1μm of signaling hub, negative controls generate HIEL between 1.5-4.5μm of signaling hub, and Monte Carlo simulations generate randomly distributed HIEL. For positive and negative simulations, each HIEL simulated was the average diameter of all HIEL within the image. Example plots show center points of HIEL. For Monte Carlo simulations, in addition to a random position being selected for the HIEL, a random HIEL diameter was chosen within the range of HIEL sizes measured for each image.

Puncta detection of PS, Kir2.1, and Cx40 was also done in this automated Matlab program, where a puncta was defined as being within an HIEL if its center point was within 0.75μm of the HIEL center point. This definition was verified as accurate via a visual output from the program. The same PC, NC, and RAND simulations were run on PS-MEJs to determine spatial patterns. Data was transferred to GraphPrism, plotted as a box and whisker plot, and a Brown-Forsythe and Welch ANOVA statistical test was performed to detect differences. Outliers were removed via ROUT (Q=1%). N values for HIEL in figure legends include entire set and do not reflect data points removed via outlier analysis. In-house Matlab code, example images, and instructions on how to use the code are available on Github: https://github.com/claireruddiman/Spatial-Distribution.

Transmission Electron Microscopy

Third order mesenteric arteries were dissected from mice and fixed in 4% paraformaldehyde / 2.5% glutaraldehyde / PBS for a minimum of 4 hours. Arteries

were then processed at the UVA Advanced Microscopy Facility. The arteries were washed in cacodylate buffer, incubated in 2% osmium tetroxide for 1 hour, washed in cacodylate buffer, then dehydrated with ethanol washes prior to incubation in 1:1 propylene oxide:epoxy resin overnight. The next day the samples were incubated in a 1:2 PO/EPON mixture for 2 hours, then a 1:4 PO/EPON mixture for 4 hours, then 100% EPON overnight. The next day, the samples were baked in an oven at 65°C prior to sectioning. Ultrathin 70nm sections were mounted on a mesh copper grid. Sections were contrast stained with 0.25% lead citrate for 5 minutes, 2% uranyl acetate for 20 minutes, and then again 0.25% lead citrate for 5 minutes. Sections were visualized and imaged using a JEOL 1230 Transmission Electron Microscope. To avoid the possibility of double counting an HIEL, only 1 section per 5μm artery length was analyzed, and a minimum of 500μm of IEL length was analyzed per artery.

Vascular cell co-culture

Vascular cell co-culture (VCCC) was created by inverting a Transwell insert (0.4μm diameter pore, 10μm thick; Fisher, 07-200-170), in a 100mm dish and seeding human coronary artery smooth muscle cells (HCoASMCs) and human umbilical vein endothelial cells (HUVECs) Confluent SMC were removed from culture dishes with 0.25% trypsin EDTA, plated on fibronectin coated (0.3% human fibronectin for 24hrs at 37°C) insert at $1.6x10^5$cells/insert, and grown at 37°C in an incubator with 5% CO_2 atmosphere. After 4 days the VSMC were confluent and the insert was turned over. The upper membrane surface was

coated with 0.3% fibronectin for 1hr at 37°C. Next, ECs were removed from culture dishes with 0.25% trypsin-EDTA and plated on the upper membrane surface at $1.6x10^5$cells/insert. The co-culture was allowed to stabilize for at least 72 hours.

After 72 hours of co-culture, the media is suctioned off the insert and washed with PBS. The inserts were fixed with 4% PFA overnight at 4°C with gentle shaking. The inserts were then transferred to 70% ethanol (EtOH) for 24 hours. Next, serial dehydration steps were performed as follows: ETOH incubations at 70%, 85%, 95%, 100% for 30 minutes each, then 100% EtOH x2 for 45 minutes each. Rehydration was performed with Xylene x2 for 30 minutes each, and a last Xylene incubation for 45 minutes. Next, parrafin incubations were done at 60°C, twice at 30 minutes, and then once for 45 minutes. The harvested filters were then embedded in liquid paraffin, keeping the filter in the cassette. The embedded inserts were then sent to the UVA Research Histology Core for sectioning at a thickness of 5μm. Sections were placed into a 42°C water bath, picked up using positively charged slides, and dried overnight in a 42°C oven.

Before beginning the rehydration steps, bake the slides at 60°C to melt the paraffin and help adhere the VCCC sections to the slide. Cool briefly, then rehydrate the slides through two changes of xylene, 100% EtOH, 95% EtOH, one change of 70% EtOH, and two changes of distilled water. Next, using a humidity chamber, block the slides for 1 hour at RT in blocking solution (0.2% TritonX-100/5% normal serum/PBS) supplemented with 0.05% fish skin gelatin. Then incubate the slides in a humidity chamber overnight at 4°C with 1:100 primary antibody in blocking solution. The following day, incubate with 1:500 secondary

antibody in blocking solution at RT for 1 hour. Mount with Prolong Gold with DAPI, coverslip, and image on the Olympus FV1000 confocal microscope using the 60x oil objective.

Transfections for immunohistochemistry

HeLa or HEK293T were plated in 6-well dishes and grown until 70–80% confluent. Each well contained a 10mm circular glass coverslip at the bottom. Transfections were performed either with Lipofectamine 3000 or with the Lonza Nucleofector kit for HeLa cells. For validation of PS antibody, HeLa cells were plated in a 12-well dish at a 60% confluency with a coverslip and were transfected for 17 hours with 1.8µg plasmid, 3.65µl P3000, and 2.7µl Lipofectamine 3000 per well. For validation of Kir2.1 antibody, HEK293T cells were plated in a 6-well dish at a 60% confluency with a coverslip and were transfected for 24 hours with 2.25µg plasmid, 4.48µl P3000, and 3.47µl Lipofectamine 3000 per well. For validation of Cx40 antibody, HeLa cells were transfected using nucleofection (Lonza, VCA-1001) where $1x10^6$ cells were transfected with 0.50µg plasmid and split across two wells of a 12-well dish. Cells were fixed with 4% PFA for 10 minutes at 4°C, washed with PBS 3x5 minutes, then blocked for one hour with 1% fish skin gelatin, 0.20% Triton-X 100, 0.50% BSA, and 5% animal serum in PBS. Primary antibody was diluted in blocking solution at a 1:100 concentration overnight at 4°C. The next day, following 3x 5-minute PBS washes, secondary antibody incubations were performed at a concentration of 1:500 for 1 hour. After secondary incubations, samples were washed once with PBS for 10 minutes, then incubated with DAPI at

a concentration of 1:5000 for 10 minutes in PBS, and washed again for 10 minutes with DAPI prior to mounting the coverslips onto microscope slides. Images were obtained using an Olympus FV1000 confocal microscope.

Whole-cell patch-clamp electrophysiology

HEK cells at 60% confluence (10cm dish) were transfected for 24 hours with 14µg of pCAG-Kir2.1-T2A-tdTomato (Addgene, 60598) using 21.7µl Lipofectamine 3000 (Thermofisher, L3000008) and 28µl P3000 (Thermofisher, L3000008). Transfection was confirmed prior to experiment by td-Tomato fluorescence using a confocal microscope epi-lamp.

Currents were recorded in a conventional whole cell patch clamp configuration with a voltage ramp from -140 mV to 50 mV over 250 ms, and were measured with 10µM dic8PIP_2, 10µM PS, or 10µM dic8PIP_2 + 10µM PS in pipette solution. For each of these conditions, Ba^{2+}-sensitive currents were measured by adding 100µM Ba^{2+} to the bath solution and recording current 5 minutes later. For basal measurements, current was recorded after equilibration. The pipette solution consisted of 10 mM HEPES, 30 mM KCl, 10 mM NaCl, 110 mM K-aspartate and 1 mM MgCl2 (adjusted to pH 7.2 with NaOH). HEPES-PSS (10 mM HEPES, 134 mM NaCl, 6 mM KCl, 1 mM $MgCl_2$ hexahydrate, 2 mM $CaCl_2$ dihydrate, and 7 mM dextrose, pH adjusted to 7.4 using 1 M NaOH) was used as the bath solution.

Patch electrodes were pulled with a Narishige PC-100 puller (Narishige International USA, Inc, Amityville, NY) and polished using a MicroForge MF-830 polisher (Narishige International USA). The pipette resistance was (3–5 ΩM). Data

were acquired using a Multiclamp 700B amplifier connected to a Digidata 1550B system and analyzed using Clampfit 11.1 software (Molecular Devices, San Jose, CA, USA).

General Pressure Myography

For all experiments, Krebs-HEPES buffer containing (in mM) NaCl 118.4, KCl 4.7, $MgSO_4$ 1.2, $NaHCO_3$ 4, KH_2PO_4 1.2, HEPES 10, and glucose 6. On the day of the experiment, $CaCl_2$ is added to the buffer at a final concentration of 2mM. Buffer is pH measured on day of experiment and adjusted to be within 7.40-7.42 by adding NaOH or HCl. Mice are sacrificed using CO_2 asphyxiation. The mesentery was dissected out and placed in ice-cold buffer, and then pinned out on a 10cm plate filled with 0.5cm of Sylgard (Electron Microscopy Sciences, 24236-10; Fine Science Tools, 26002-10). Third order mesenteric arteries, defined as the third branch point relative to the feed artery and with a maximum diameter between 100-200μm, were cleared of surrounding adipose tissue using super fine forceps (Fine Science Tools, 11252-00) and microscissors (Fine Science Tools, 15000-03). The artery was then cut out of the mesentery, placed into the arteriograph chamber (DMT) containing Krebs-HEPES, and cannulated on glass pipette tips using super fine forceps (Fine Science Tools, 11254-20) and suture (DMT, Nylon, P/N 100115). Glass pipette tips were created from glass rods (World Precision Instruments, Inc., 1B120F-4). Buffer was gently pushed through the artery to clear remaining blood before cannulating the second side. Following cannulation, the artery was equilibrated over a 25-minute period by increasing the pressure from

20 to 80 mmHg in 20 mmHg (Big Ben Sphygmomanometer) increments and slowly heating the artery to 37°C. For experiments on $Eln^{fl/fl}/Cre^{-}$ or $Eln^{fl/fl}/Cre^{+}$ mice, arteries were equilibrated to 60mmHg. The buffer was circulated between the arteriography chamber and a beaker containing an excess reservoir of buffer by using a peristaltic pump (Atalyst Masterflex, FH30) to prevent overheating and facilitate the delivery of pharmacological agents. DMT cell culture pressure arteriography setups were used and the inner diameter of the vessel was recorded with the 2015 release of the DMT software.

NS309 dose response curves

For the NS309 curves, the total system volume was 50ml to facilitate delivery of small doses of NS309. All other experiments had a total system volume of 10ml. The artery was pre-constricted using 1μM phenylephrine (PE) in water (Sigma, P6126) and the inner diameter was recorded after 10 minutes (D_{PE}). A 10mM NS309 (Sigma, N8161) in DMSO stock solution was prepared and 10μl aliquots were stored at -20°C in amber microcentrifuge tubes. The stock solution was thawed prior to the experiment and the following NS309 concentrations (in μM) were tested in the 50ml system volume: 0.1, 0.3, 0.5, 0.6, 1, and 2, where the 0.1μM dose corresponds to 0.5μl of the NS309 stock (D_{NS309}). The inner diameter was recorded as the average over the 7-minute time period for each dose of NS309. SMC function was then assessed by adding 30mM KCl (1M stock in water), and the inner diameter was recorded as the plateau after 5-10 minutes. The bath was then replaced with Ca^{2+}-free Krebs-HEPES, containing 1mM EGTA

and 100μM SNP, and inner diameter was recorded after 10 minutes (D_{MAX}). The data was exported to Microsoft Excel to calculate percent dilation using the following equation: ($D_{NS309} – D_{PE}$) / (D_{MAX}-D_{PE}) *100. The percent vasodilation was plotted in GraphPad Prism as a dose response curve. Students t-test was performed at each dose. For experiments where Kir2.1 was inhibited, ML-133 hydrocholoride (Sigma, 422689, IC_{50} = 1.8μM) was prepared as 7.2mM stocks in DMSO, and was added at a final concentration of 3.6μM. Stocks were stored for three months at -20°C. For BaCl (Sigma, 217565) experiments, the stock solution was prepared as 100mM water and added at a final concentration of 30-100μM. The inhibitor circulated after the artery was equilibrated and before pre-constriction with PE. The NS309 curve was then performed as stated previously and smooth muscle cell function was tested with 30mM KCl and Ca^{2+}-free Krebs-HEPES.

TopFluor PS experiments

Third order mesenteric arteries were dissected from male C57Bl6/J mice and secured to Sylgard squares using tungsten wire. Arteries were place in a 1.5ml Eppendorf tube containing Krebs-HEPES supplemented with 2mM Ca^{2+} Next the arteries were incubated with DAPI at 16.67 μg/ml and Alexa Fluor 647-linked hydrazide at 3.3μM in Krebs-HEPES supplemented with 2mM Ca^{2+} for 30 minutes in a 37°C water bath. The artery was then cannulated on glass canula on a pressure myograph setup. After equilibration to 80mmHg, 10μM of TopFluor-PS was added to the bath solution and circulated for 30 minutes. The artery was then immediately prepared *en face* and secured to a microscope slide with mounting

media and a glass coverslip (no fixation step). Arteries were imaged on an Olympus Fluoview 1000 microscope.

Pressure myography in lipid experiments

For evaluation of PIP_2 dilation, third order mesenteric arteries were cannulated, pressurized to 80mmHg, and equilibrated to myogenic tone. For experiments on After myogenic tone plateaued and stabilized for a period of 10 minutes (D_{EQ}), 10μM diC8PIP_2 (10mM stock in Krebs-HEPES, Cayman Chemical, 64910) was added to the bath and circulated for 15 minutes. The maximum change in diameter was recorded for the lipids within the respective incubation period (D_{PIP2}). For experiments with Kir2.1 inhibitors, drug or lipid was added after myogenic tone developed and the diameter plateaued for 10-minutes. ML-133 and PS (10.15 mg/ml stock in 1:1 EtOH:diH_2O, Avanti, 840035) were circulated for 30 minutes, while BaCl was circulated for 15 minutes prior to adding exogenous diC8PIP_2. PS stock solution was stored at -20°C. Prior to experiments, PS was warmed in a 60°C incubator for 10 minutes and vigorously vortexed until dissolved into solution. Maximum change in diameter was recorded. Next, lipids and inhibitors were washed out of the system for 5 minutes. Arterial function was then evaluated by dilation to 1μM NS309 and constriction to 30mM KCl. As with other pressure myography experiments, Ca^{2+}-free Krebs-HEPES was circulated through the system at the end of the experiment and diameter was recorded 10 minutes later (D_{MAX}). This diameter was used as maximum diameter in following calculations. Two zones are monitored for arterial dimeter and the average of the

two measurement are reported per artery. Zones were excluded if stable myogenic tone could not be achieved for the duration of the experiment. Lastly, if observable myogenic tone constriction occurred following a transient constriction or dilation, it was not recorded as the maximum change in diameter. The dilation to diC8PIP$_2$ was measured by the percent change right before application of the lipid: ($D_{PIP2} - D_{EQ}$) / (D_{MAX}-D_{EQ})*100. The data for maximum change in diameter for PS was taken from experiments where PS was circulating on the artery for 30 minutes prior to diC8PIP$_2$ application: ($D_{PS} - D_{EQ}$) / (D_{MAX}-D_{EQ})*100. For all experiments, time to maximum dilation is reported as the nearest half minute.

Myogenic tone experiments on Eln$^{fl/fl}$/Cre^{-} and Eln$^{fl/fl}$/Cre^{+} mice

Third order arteries are cannulated, pressurized to 60mmHg, and equilibrated to 37°C. After the development of myogenic tone, EC health was evaluated using 1-2μM NS309. Maximum diameter was recorded after 5 minutes and NS309 was washed out of the system until myogenic tone returned. The active curve was completed by increasing the pressure in 20mmHg increments from 20-120mmHg. Diameter was recorded after 5 minutes equilibration at each pressure (D_{ACT}). After the active curve, pressure was brought back down to 60mmHg for 5 minutes. SMC and EC function were evaluated with a 10μM PE dose, 10μM Ach dose, and 30mM KCl dose. Next, Ca^{2+}-free Krebs-HEPES was then circulated in the system for 15 minutes. The passive curve was then completed by increasing the pressure in 20mmHg increments from 20-120mmHg. Diameter was recorded after 5 minutes equilibration at each pressure (D_{PASS}). Myogenic tone was

calculated as $((D_{ACT}-D_{PASS})/D_{PASS})*100$. For active and passive curves, the percent change in diameter relative to the diameter at 20mmHg was calculated as $((D_X-D_{20})/D_{20})*100$, where D_X is diameter at any pressure and D_{20} is the diameter at 20mmHg.

Genomic DNA gel

Genomic DNA was isolated from lung tissue from $Eln^{fl/fl}/Cre^{-}$ and $Eln^{fl/fl}/Cre^{+}$ mice between 10-12 weeks old. Lung samples were incubated at 56°C overnight in lysis buffer (20mM Tris Base; 150mM NaCl; 1mM EDTA; 1mM EGTA; 20mM NaF; 0.5% Triton x-100) supplemented with 100ug/ml of Proteinase K. Isopropanol was used to precipitate DNA and ethanol was used to wash DNA. The dried DNA pellet was resuspended in autoclaved water and incubated for 1 hour at 56°C to allow the DNA to go into solution. The concentration was measured via nanodrop, then 15ng/ul DNA stocks were stored at -20°C until PCR was per formed. The following primers were used to differentiate between wildtype and knockout mice: **WT F**: CCATGTGGGTGCTGTAAGCT, **Excision R**: GTGTGTGTAGCTGAGGAATGGG, and **LoxP Site R**: CCTACCTTTCTGGGGCCACT (ordered from Integrated DNA Technologies). Each PCR reaction contained 10ul of MyTaqRed Mix (Bioline, C755G95), 350nM of each primer, and 100ng of gDNA. Total reaction volume was 20μl. Initial denaturation temperature was 95°C for 5 minutes, followed by 28 cycles of with 30 seconds denaturation, annealing, and elongation steps at 95°C, 61°C, and 72°C, respectively. The final annealing step was 72°C for 5 minutes. PCR products

were then run on a 1% agarose gel containing 0.01% ethidium bromide for 50 minutes at 120V. Gels were imaged using a UV light source. The expected bands are 243 bp (WT), 283bp (KO LoxP site) and 410 bp (excision product).

qPCR

Mesenteric vasculature was trimmed of connective tissue, snap frozen in liquid nitrogen, and stored in -80°C. RNA isolation from tissue was achieved using a Aurum Total RNA Fatty and Fibrous Tissue Kit (BioRad, 7326870). RNA yields were between 40-200 ng/μl. cDNA synthesis was next performed using SuperScript IV Reverse Transcriptase (Thermofisher, 18090050). Total well volume is 20μl with equal amounts of cDNA for each sample loaded in 8μl, and master mix as 12μl and containing: (1) Taqman gene expression master mix (Thermofisher, 4369016), (2) probe of interest (Taqman probe Mm00514670_m1 Eln FAM-MGB, Thermofisher, 4453320) and an (3) in-well control (Taqman probe Mm00437762_m1 B2M VIC PL, Thermofisher, 4448485). Each sample was loaded in triplicate. Protocol was run using a Biorad Thermal Cycler using a standard protocol for 40 cycles. $\Delta\Delta C_T$ quantification method.

VVG stain and quantification

Arteries were isolated from mice and fixed with 4% PFA at 4°C overnight, embedded in 3% agarose/PBS, then sent to the UVA Research Histology Core to be embedded in paraffin wax cut into 5μm cross-sections. The cross-sections were deparaffinized by heating to 60°C for 1 hour in a glass slide holder, followed by

dehydration with Histoclear and a decreasing ethanol gradient. The Elastic Stain Kit (Verhoeff Van Gieson / EVG Stain) kit was purchased from Abcam (ab150667). Slides were placed into elastic stain solution for 15 minutes and rinsed with cool, running diH_2O to remove excess stain. Sections were differentiated by dipping the slides in 2% ferric chloride solution 15 times. The differentiation reaction was stopped by rinsing slides in cool, running diH_2O. Excess stain was further removed by dipping the slides in the sodium thiosulfate solution for 1 minute, followed by rinsing in cool, running diH_2O. The slides were then placed in Van Gieson solution for 2 minutes for a counterstain. Excess stain was removed by rinsing in two changes of 95% EtOH, followed by a 2-minute incubation in 100% EtOH. The slides were then quickly mounted using VectaMount media and a coverslip. Images were taken using a traditional light microscope and a 20x or 40x objective.

Image analysis was done in ImageJ. The stained arterial cross-section image was opened in ImageJ. The colors of the original image were then separated by “H PAS stain” color deconvolution (Image → Color → Color Deconvolution → H PAS). Only the indigo image was analyzed because that is the channel containing the Verhoeff elastin stain. The indigo imaged was converted to a black and white mask, and the threshold of indigo was automatically determined by the ImageJ software (Process → Binary → Convert to Mask).

En face quantification for hydrazide $Eln^{fl/fl}/Cre^{-}$ and $Eln^{fl/fl}/Cre^{+}$ mice

Images were opened in Image J. The hydrazide channel was projected as a Z-0stack image and brightness and contrast were adjusted for visualization of

HIEL. Next, Analyze → Histogram was used to see the distribution of pixel intensity. The cutoff for black pixels was determined by looking at the color-coded legend for the histogram. The number of black pixels per image was then calculated as the percentage of total pixels. Subtracting this number from 100 gives the percentage of pixels containing hydrazide signal. These are the numbers that were plotted to determine hydrazide coverage in each image.

En face quantification for PS distribution in *en face* view

En face images were opened in Image J. The PS channel was then thresholded. Next, the "Analyze Particles" Function was used to determine the area containing signaling and the number of puncta in the image, where particle size identification was set to be 0-Infiinity. The results table in ImageJ contained the number of puncta and the coverage area of puncta. These values were normalized using the average value of control samples.

For HeatMap Analysis, the Royal Lookup Table in ImageJ was used to differentiate between low and high intensity signal. The index that separated low and high intensity pixels was determined by looking at the color-coded legend for the histogram for the last blue bin. Empty pixels were considered as index 0 and were not included in the low intensity values. Number of low and high intensity pixels were then normalized using the average value obtained from control images.

Results

Part I: MEJ spatial distribution and heterogeneity

HIEL spatial distribution and determination that every HIEL contains an MEJ

In endothelium, signaling microdomains can be visualized through *en face* views of an artery, where the vessel is cut longitudinally, and the endothelial monolayer is facing upwards and potential sites of MEJ formation are detected as holes in the IEL (HIEL). Immunohistochemistry studies on *en face* views have reported heterogeneous protein localization to the MEJ (15, 23, 29, 38, 43, 199-201), possibly indicating unique juxtaposition of HIEL to other signaling organelles/structures in the endothelium. To determine if this may be the case, we initially used stitched confocal images of third order mesenteric arteries stained for nuclei, the IEL, and interendothelial junctions via claudin-5 and visualized approximately 50 fully in view EC per artery per field of view (**Figure 1A**) and quantified that there were 9.83 HIEL per EC (**Figure 1A**). We then found that the number of HIEL could be predicted by the size of an EC (**Figure 1A**). Next, we developed a Matlab program (see Methods) to calculate the minimum distance of each individual HIEL to EC signaling hubs in immunofluorescence images and compared it against simulations for a positive (PC), negative (NC), and random (RAND) spatial pattern (**Figure 1B**). We found a significant difference between real-world and simulated positive and negative values, but no differences between real-world and simulated random values in all tested conditions; nuclei (**Figure 1C-D**), endoplasmic reticulum (**Figure 1E-F**), and interendothelial junctions (**Figure 1G-H**).

I next wanted to investigate if this random distribution pattern was also present in first order arteries. As expected with previous reports, the HIEL density in third order arteries is significantly higher both when analyzing the incidence per 1000μm^2 (obtained from Matlab analysis program) and per EC (Matlab identification of HIEL and manual stitch analysis, **Figure 2**). The random distribution of HIEL was also evident in first order mesenteric arteries (**Figure 3**), indicating the random localization of the HIEL is not an outcome of high density. Thus, HIELs are randomly distributed with respect to major endothelial cell signaling domains.

This random distribution of HIEL is also supported by numerous correlations obtained from measurements of stitched confocal images in both first and third order mesenteric arteries prepared *en face* (**Figures 4-7**). These correlations involve measurements of both EC area and HIEL size, which are similar between the two artery sizes (**Figure 8**). As the number of MEJs increase within an endothelial cell, the surface area at which a new MEJ can exist decreases. For this reason, it follows that as the number of MEJs increases, so does the localization along the interendothelial junction (**Figure 9**). This correlation holds in both first and third order mesenteric arteries and supports the notion that MEJs populate randomly throughout the EC, where the positive correlation is likely due to the physical constraint of EC area (**Figure 9**).

Similarly, the number of HIEL per EC is positively correlated with EC area in third order mesenteric arteries where HIEL density is high. This positive correlation once again is likely due to the physical constraint of EC area and high

HIEL density (**Figure 10**). Thus, looking at first order arteries can be informative to understand if there is a predetermined number of HIEL per EC based on its area. There is a weak positive correlation for first order arteries, indicating that EC area is not a strong predictor of the number of HIEL within that EC (**Figure 10**). This indicates that there is not a predetermined number of HIEL that an individual EC will make based on its area, and further supports the random localization of HIEL with respect to endothelium.

Additionally, the average size of HIEL does not predict the localization within an EC (**Figure 11**), and is not associated with EC area (**Figure 12**). In other words, neither larger or smaller HIEL localize to the interendothelial junctions and larger ECs do not contain larger or smaller HIEL compared to smaller ECs. Lastly, the surface area of an EC does not predict the localization of HIEL within ECs (**Figure 13**), i.e. larger or smaller ECs do not have a higher or lower tendency of HIEL localization to interendothelial junctions. These data also indicate that HIEL are randomly distributed with respect to EC signaling domains since there is not a relationship between cellular localization and size of HIEL or EC.

A final analysis of HIEL distribution in endothelium also supports a random localization in the arterial wall. Confocal stitched images of first and third order mesenteric arteries were used to create EC maps to visualize patterns or potential groupings of similar ECs (**Figures 4-7**). In maps showing HIEL per EC (**Figure 14 and 15**), there are some instances where ECs of similar HIEL density appear to group together within each artery; however, when looking across all arteries analyzed, there is not an observable grouping pattern that occurs in each case. In

maps to visualize spatial pattern of HIEL within EC, it is apparent that a large proportion of ECs do have >66.1% of HIEL localized along the border (**Figure 16 and 17**), and that groups of ECs with this localization do form throughout the endothelium. However, there is no specific pattern to this EC grouping across arteries, and this lack of patterning also supports random localization throughout the arterial wall. Lastly, I created EC maps to visualize the distribution of HIEL sizes throughout ECs (**Figure 18 and 19**), where again there are some groups of ECs that have similar HIEL size, but that pattern does not carry over to other arteries. Thus, from the data presented in **Figures 1-19**, we conclude that the HIEL exhibit a random spatial distribution with respect to endothelium.

Given the heterogeneity of proteins observed at the HIEL, if the HIEL were not specifically localized to signaling hubs as noted above, another alternative may be that not every HIEL is an anatomical MEJ. To determine if HIEL were equal to MEJs, we used TEM to examine transverse sections of third order mesenteric arteries, where MEJs can be unequivocally identified at the ultrastructural level, thus circumventing the need to rely on an individual protein marker (**Figure 20**). We then leveraged our *en face* data obtained from our Matlab program and measurements taken from third order mesenteric arteries (**Figure 20B, Tables1-2**) to predict how many MEJs we would observe in transverse TEM images (**Figure 21**; **Tables1-3**; **Chapter 4 Appendix**). Based on our calculations, we predicted between 5 and 17.8 HIEL per 1000μm IEL length in the cross-sectional TEM view if all the HIEL were MEJs. Calculation from HIEL density in *en face* images to HIEL per 1000μm IEL length in TEM images falls within this predicted range (**Figure**

20C). The measurements taken from TEM cross-sections also fall within this predicted range, where every HIEL contained a cellular projection (**Figure 20C**). Thus, we conclude each HIEL contains a *bona fide* MEJ.

Phosphatidylserine defines a subpopulation of MEJs

If every HIEL contains an MEJ, it was unclear to us what contributes to the heterogenous localization of proteins to the MEJ, especially if there is a random distribution of MEJs with respect to endothelial signaling hubs. The possibility we considered was the lipid composition of MEJs, due to the emerging evidence of lipid regulation of membrane protein (100, 102, 135, 202). *In vitro*, we have previously demonstrated enriched PS via lipid mass spectrometry at MEJs in our vascular cell co-culture system (24) (**Figure 22**), and hypothesized the same lipid accumulation at *in vivo* MEJs. Stitched confocal images of third order mesenteric arteries viewed *en face* revealed PS localization to MEJs and endoplasmic reticulum in intact arteries (**Figure 23A-C and 24**). In co-stains with calnexin and PS, both localized to MEJs, but not to the same MEJs, in agreement with previous observations of an ER presence at the MEJ.(41, 44) The specificity of the PS antibody was confirmed using Lactadherin-C2 plasmids, a protein that specifically binds to PS(203-206) (**Figure 22**). PS was found to be heterogeneously distributed and occupied 13.8% of MEJs (**Figure 23D**). Analysis of PS-MEJs per EC reveals that on average 1.18 PS-MEJs are associated with any individual EC (100% of ECs analyzed, **Figure 23E**), or 1.95 PS-MEJs if only considering ECs that contain at least one (58.04% of all ECs analyzed, **Figure 23E**). Based on comparisons to

Matlab simulations, PS-MEJs did not exhibit a localization pattern with respect to interendothelial junctions (**Figure 23F**).

Confocal stitched images of first and third order mesenteric arteries (**Figures 4 and 6**) were used to analyze for potential explanations for PS localization in ECs. The total number of PS-MEJs demonstrates a weak positive correlation with the number of total MEJs per EC in both first and third order arteries. In other words, as the number of MEJs increases within an EC, the number of PS-MEJ also increases (**Figure 25**). The PS localization to interendothelial junction was not correlated with total MEJs per EC (**Figure 26**), total MEJs localized to the border (**Figure 27**), or to EC area (**Figure 28**). This indicates that the localization of PS-MEJs to interendothelial junctions is independent of these variables. There was also no correlation between the number of PS-MEJs and average size of MEJs within each EC (**Figure 29**), indicating that PS occupancy is independent of MEJ size. These findings support the random distribution of PS-MEJs within the endothelium (**Figure 23F**). Interestingly, in third order mesenteric arteries, the percentage of PS-MEJ per EC, but not number, demonstrates a weak negative correlation with EC area, suggesting that smaller ECs may be more likely to contain a higher percentage of PS-MEJs (**Figures 30 and 31**).

Lastly, EC maps were created from confocal stitched images (**Figures 5 and 7**) to visualize patterns or potential groupings of ECs in terms of PS-MEJs. The number of PS-MEJ per EC is visualized in first and third order mesenteric arteries (**Figures 32 and 33**). Similar to EC maps done for all MEJs (**Figures 14**

and 15), it is apparent that there is some clustering of ECs with higher numbers of PS-MEJs. In almost all arteries, there is a case of one single EC in the highest category of PS-MEJs, that is surrounded radially by ECs with incrementally fewer PS-MEJs. This appears to lead to a clustering of ECs containing PS to very distinct areas of the artery. When viewing the same data as a PS occupancy of total MEJ within the EC, this radial pattern is no longer observable, but it is clear that there are patches of ECs with and without PS-MEJs (**Figures 34 and 35**). Lastly, although randomly distributed with respect to interendothelial junctions (**Figure 23F**), there are clearly patches of ECs that demonstrate PS-MEJ localization along their interendothelial junction (**Figures 36 and 37**). However, when looking across all arteries analyzed, both first and third order, there is no pattern that clearly holds in all cases. Altogether, these data may indicate that there could be a pattern of PS-MEJ that may coincide with EC heterogeneity rather that spatial distribution throughout the endothelium as a whole. **Table 4** summarizes all of the data obtained from stitched confocal images for first and third order arteries for both MEJs and PS-MEJs.

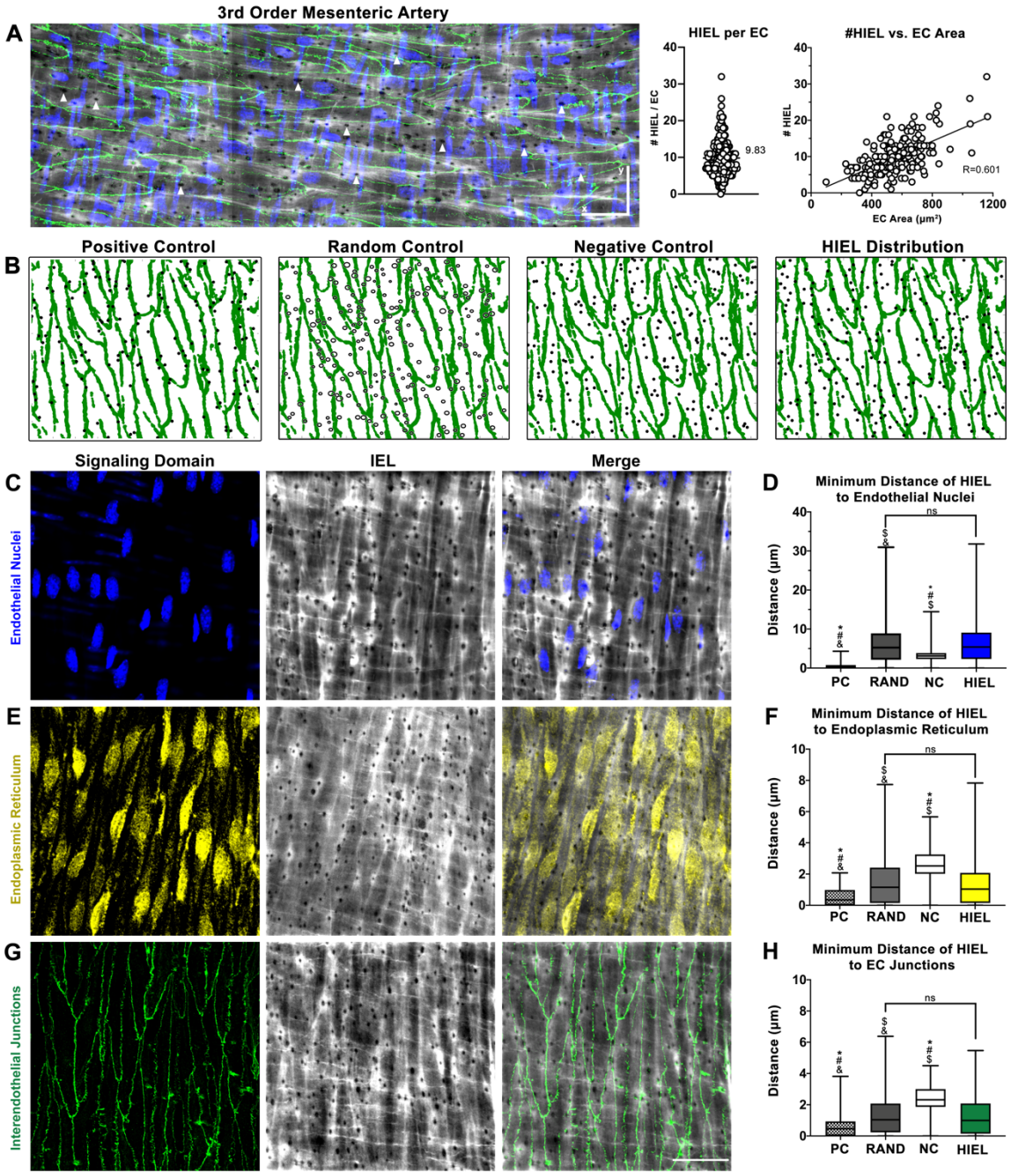

Figure 1. HIEL are randomly distributed with respect to endothelial signaling domains. (A) Representative stitched confocal image of a third order mesenteric artery prepared *en face* and stained for nuclei (blue) via DAPI, IEL (grey) via Alexa Fluor 488-linked hydrazide, and interendothelial junctions (green) via claudin-5. Scale bar is 30μm in both the x and y directions. Quantification of HIEL per EC,

and plot of HIEL per EC vs. EC area. N=4 mice, n=4 arteries, n=12 ROIs, and n=205 ECs. (**B**) Graphical outputs of Matlab thresholding and simulations. Interendothelial junction coordinates from *en face* imaged are plotted in green and real-world HIEL centers are plotted in black (HIEL Distribution). Representative outputs of Matlab simulations that generate random (RAND), positive (PC), or negative (NC) HIEL distribution patterns (in black) with respect to interendothelial junctions. Note that random simulations also took HIEL diameter size into account and that is why the output image shows circles (full HIEL) instead of dots (HIEL centers) as in positive and negative controls. (**C**) Representative *en face* confocal image of endothelial nuclei (blue) detected via DAPI and IEL (grey). (**D**) Plot of minimum distance of real-world HIEL centers to endothelial nuclei, compared to Matlab-simulated HIEL centers. N=3 mice, and n=6 arteries, n=18 ROIs, Area=$9.75x10^4 \mu m^2$, and n=1607 HIEL. (**E**) Representative *en face* confocal image of endoplasmic reticulum (yellow) detected via calnexin and IEL (grey). (**F**) Plot of minimum distance of real-world HIEL centers to endoplasmic reticulum compared to Matlab-simulated HIEL centers. N=3 mice, and n=4 arteries, n=9 ROIs, Area=$7.96x10^4 \mu m^2$, and n=1157 HIEL. (**G**) Representative *en face* confocal image of interendothelial junctions (green) detected via claudin-5 and IEL (grey). (**H**) Plot of minimum distance of real-world HIEL centers to interendothelial junctions compared to Matlab-simulated HIEL centers. N=6 mice, and n=10 arteries, n=22 ROIs, Area=$1.48x10^5 \mu m^2$, and n=2166 HIEL. Brown-Forsythe and Welch ANOVA. # indicates a $p < 0.0001$ significant difference to real-world HIEL distribution, * indicates a $p < 0.0001$ significant difference to random simulation distribution, $

indicates a $p < 0.0001$ significant difference to negative control simulation distribution, and & indicates a $p < 0.0001$ significant difference to positive control simulation distribution.

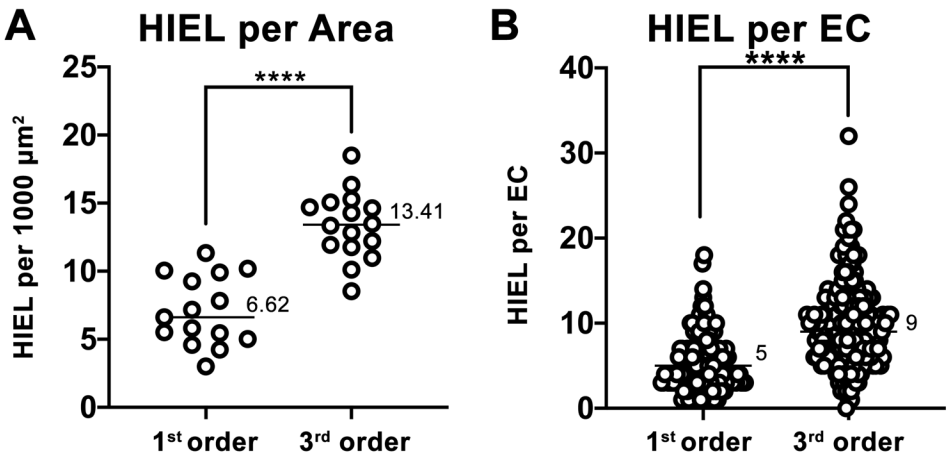

Figure 2. HIEL density in first and third order mesenteric arteries. Data obtained from stitched confocal images comparing metrics from first and third order mesenteric arteries. The IEL was visualized with Alexa Fluor 488-linked hydrazide and interendothelial junctions were defined via claudin-5. (**A**) Calculated density of HIEL per 1000μm^2 comparing first and third order mesenteric arteries. N= 6 mice, n=6 arteries, n=15 ROIs for first order mesenteric arteries, and N=8 mice, n=7 arteries, n=16 ROIs for third order mesenteric arteries. (**B**) Number of HIEL per EC comparing first and third order mesenteric arteries. N=3 mice, n=3 arteries, n=155 ECs for first order mesenteric arteries, and N=4 mice, n=4 arteries, n=205 ECs for third order mesenteric arteries. Data is presented as median. Student's t-test. **** indicates $p<0.0001$.

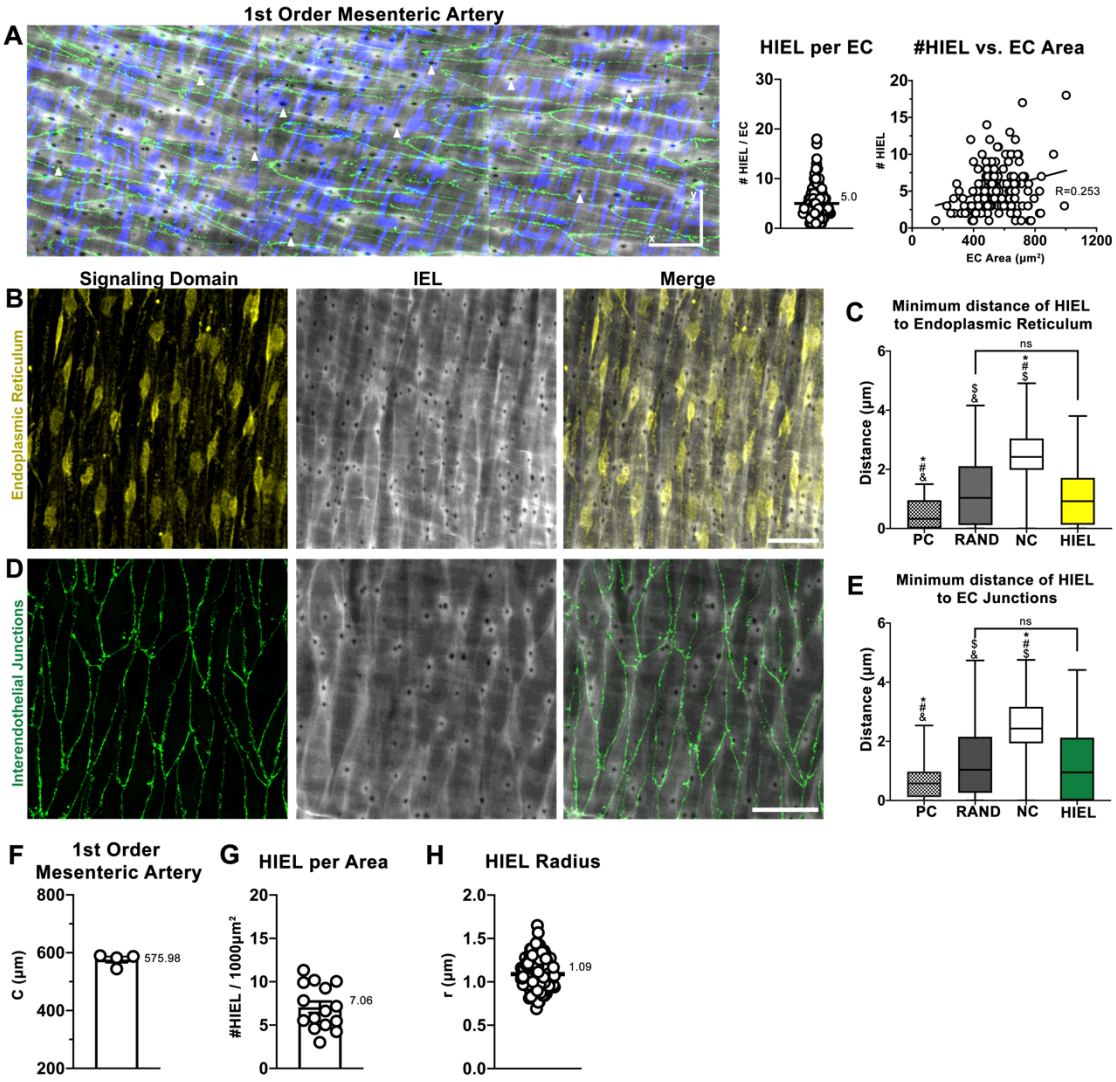

Figure 3. Quantification of HIEL in first order mesenteric arteries and evaluation of spatial distribution via Matlab simulations. (A) Representative stitched confocal image of a first order mesenteric artery prepared *en face* and stained for nuclei (blue) via DAPI, the IEL (grey) via Alexa-Fluor 488 hydrazide, and interendothelial junctions (green) via claudin-5. Scale bar is 30μm in both the x and y direction. Quantification of number of HIEL per EC and plot of HIEL per EC versus EC area. N=4 mice, n=4 arteries, n=12 ROIs, and n=155 ECs. (**B**) Representative *en face* confocal image of endoplasmic reticulum (yellow) detected via calnexin and IEL (grey), (**C**) plot of minimum distance of real-world HIEL

centers to endoplasmic reticulum compared to Matlab-simulated HIEL centers. N=1 mouse, and n=1 artery, n=2 ROIs, Area= $6.96x10^4$ μm^2, n=315 HIEL. (**D**) Representative *en face* confocal image of interendothelial junctions (green) detected via claudin-5 and IEL (grey), (**E**) plot of minimum distance of real-world HIEL centers to interendothelial junctions compared to Matlab-simulated HIEL centers. N=6 mice, and n=10 arteries, n=15 ROIs, Area=$1.66x10^5$ μm^2, n=1200 HIEL. Statistical test: Brown-Forsythe and Welch ANOVA. #### indicates a p <0.0001 significant difference to real-world HIEL distribution, **** indicates a p <0.0001 significant difference to random simulation distribution, $$$$ indicates a p <0.0001 significant difference to negative control simulation distribution, and &&&& indicates a p <0.0001 significant difference to positive control simulation distribution. (**F**) Circumference of first order mesenteric arteries measured as the width of the artery in an *en face* preparation. N=1 mouse, n=1 artery. (**G**) HIEL per area taken from *en face* images that were used for HIEL spatial pattern analysis with respect to claudin-5. Number of HIEL was determined via the in-house Matlab program. (**H**) HIEL radius measurements obtained from in-house Matlab program.

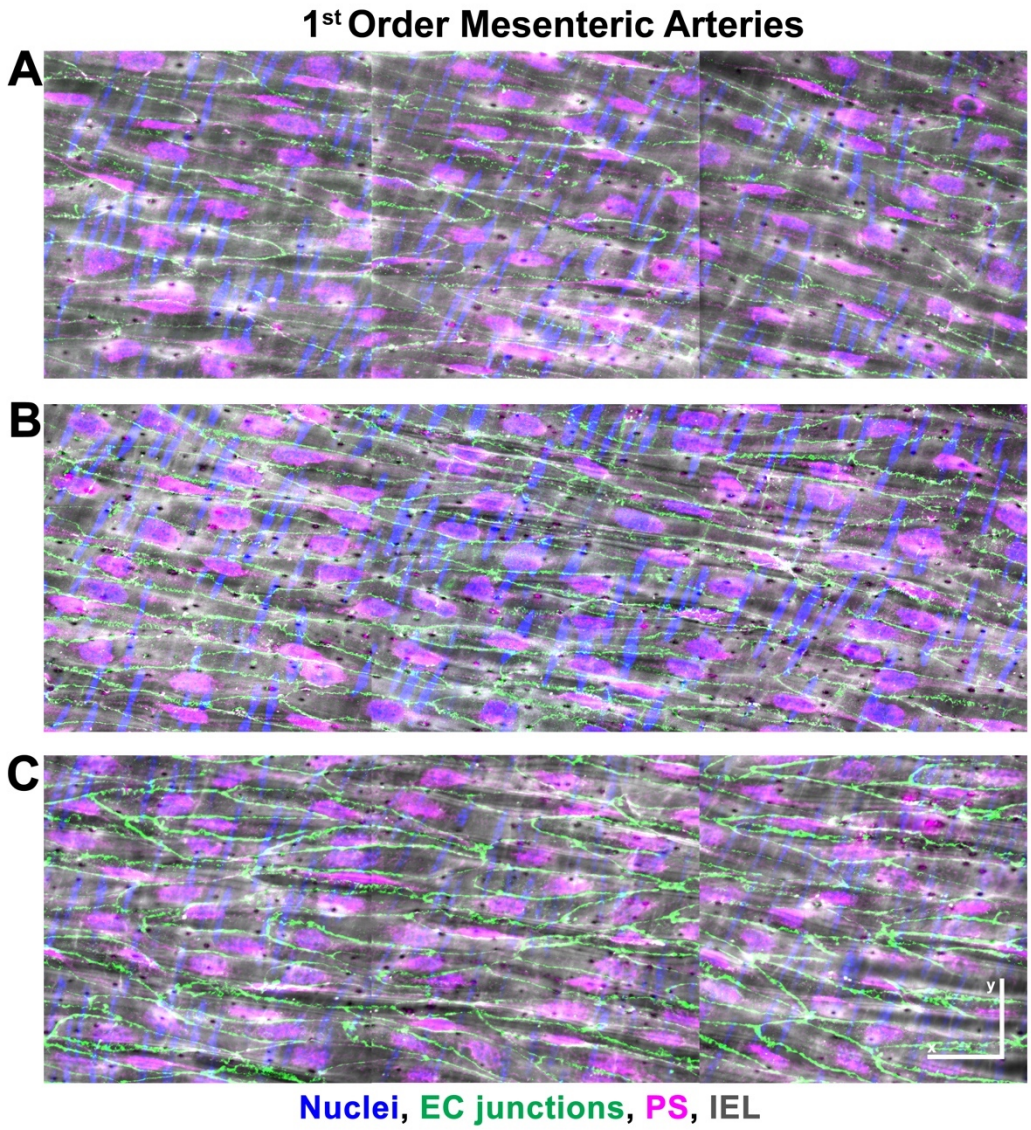

Figure 4. Stitched confocal images of first order mesenteric arteries prepared *en face*. (**A-C**) Each panel is an artery from a different mouse, where nuclei (blue) detected via DAPI, the IEL (grey) detected via Alexa-Fluor 488 hydrazide, interendothelial junctions (green) detected via claudin-5, and PS (magenta). Scale bar is 30μm in both the x and y direction. N=3 mice, n=3 arteries, n=155 ECs.

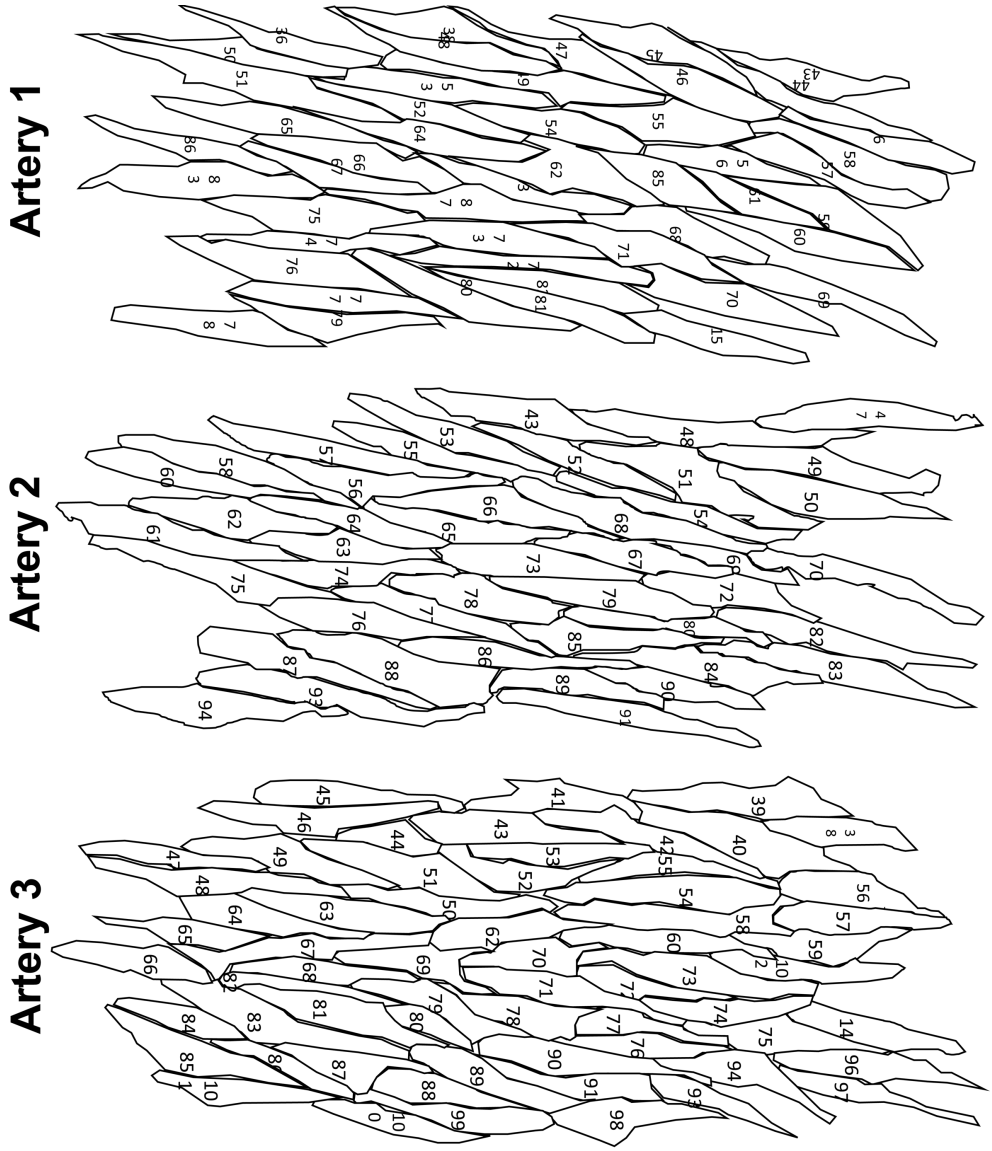

Figure 5. EC maps from stitched confocal images of first order mesenteric arteries prepared *en face*. Maps of ECs from multiple first order mesenteric arteries, where individual ECs are outlined in black. Claudin-5 staining was used to define EC borders. Borders were traced over and each EC given a number to track them for analysis. Only fully in view endothelial cells were considered. Images were taken with a 40x oil objective (1.8 zoom) on a Zeiss 880 LSM microscope. N=3 mice, n=3 arteries, n=155 ECs.

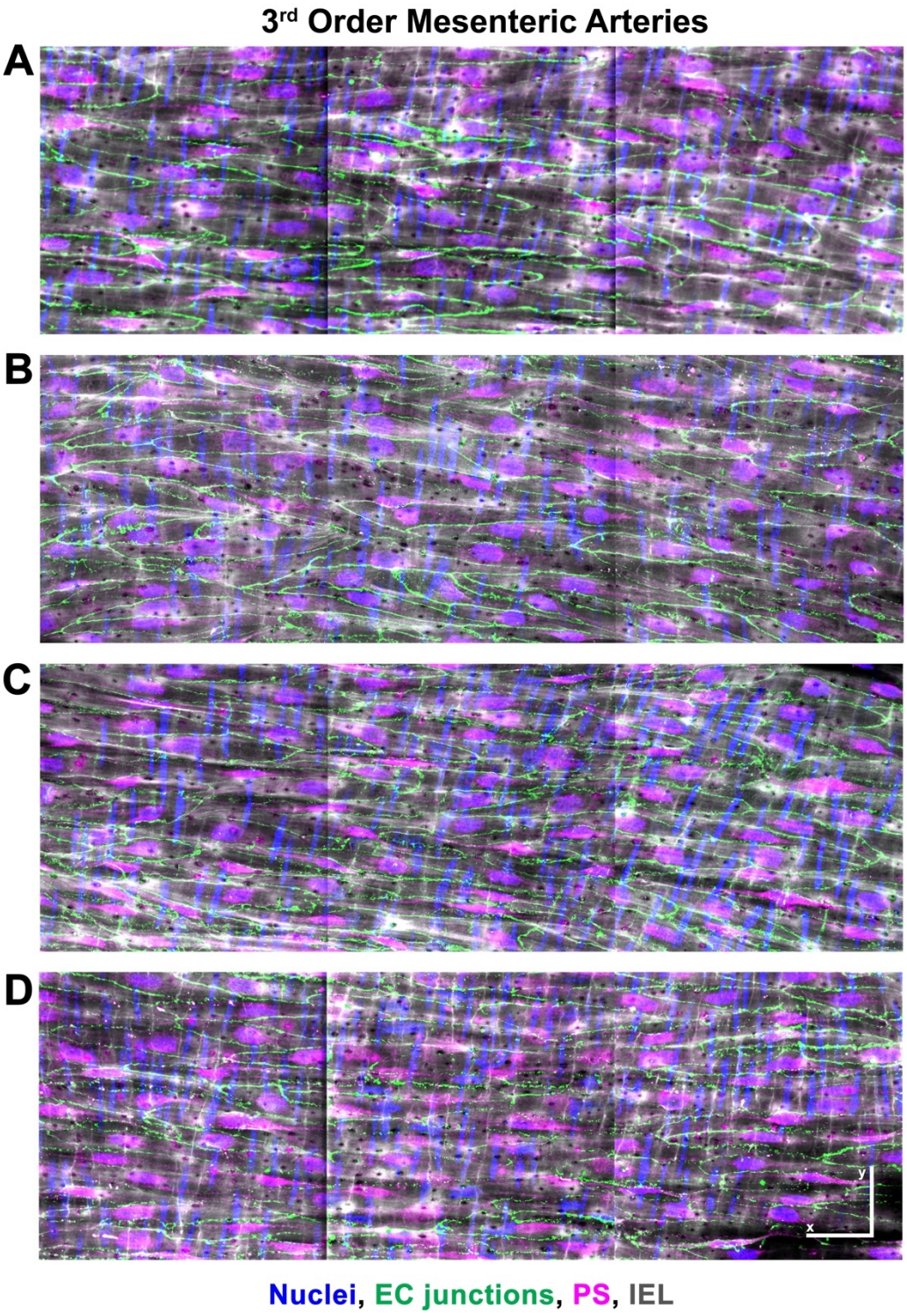

Figure 6. Stitched confocal images of third order mesenteric arteries prepared *en face*.

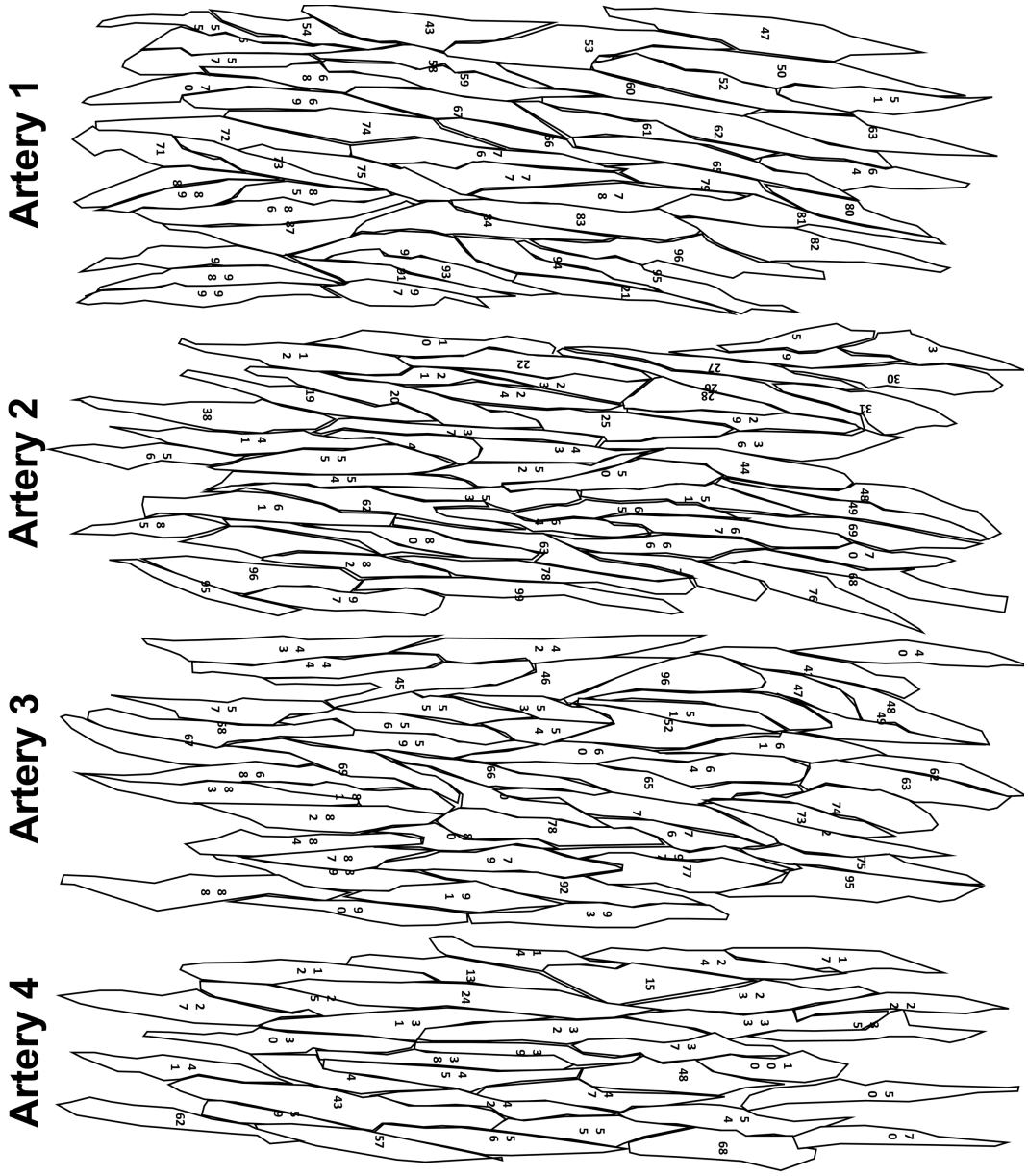

Figure 7. EC maps from stitched confocal images of third order mesenteric arteries prepared *en face*. Maps of ECs from multiple third order mesenteric arteries, where individual ECs are outlined in black. Claudin-5 staining was used to define EC borders. Borders were traced over and each EC given a number to track them for analysis. Only fully in view endothelial cells were considered. Images were taken with a 40x oil objective (1.8 zoom) on a Zeiss 880 LSM microscope. N=4 mice, n=4 arteries, n=205 ECs.

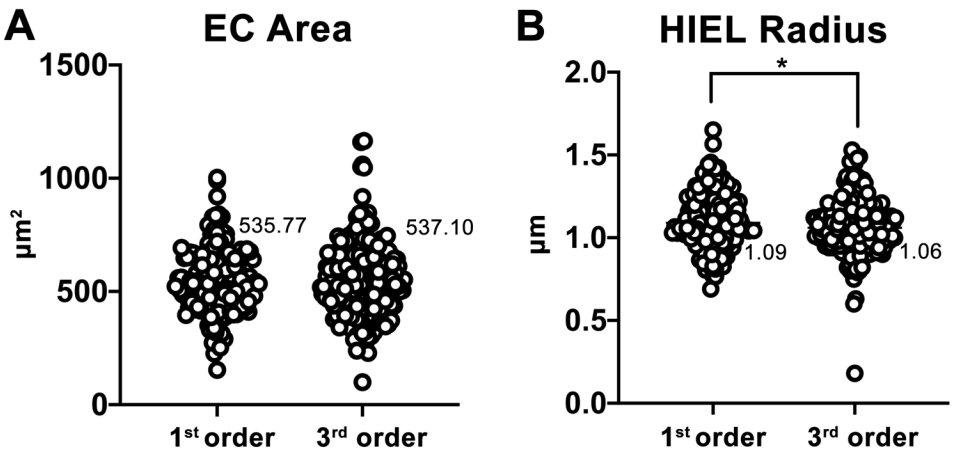

Figure 8. EC Area and HIEL radius, in first and third order mesenteric arteries. Data obtained from stitched confocal images comparing metrics from first and third order mesenteric arteries. The IEL was visualized with Alexa Fluor 488-linked hydrazide and interendothelial junctions were defined via claudin-5. **(A)** EC area comparing ECs from first and third order arteries. Area was measured by tracing over interendothelial junction staining in ImageJ. N=3 mice, n=3 arteries, n=155 ECs for first order mesenteric arteries, and N=4 mice, n=4 arteries, n=205 ECs for third order mesenteric arteries. (**B**) HIEL radius comparing first and third order arteries. Radius was measured via in-house Matlab analysis program. N=3 mice, n=3 arteries, n=155 ECs for first order mesenteric arteries, and N=4 mice, n=4 arteries, n=205 ECs for third order mesenteric arteries.

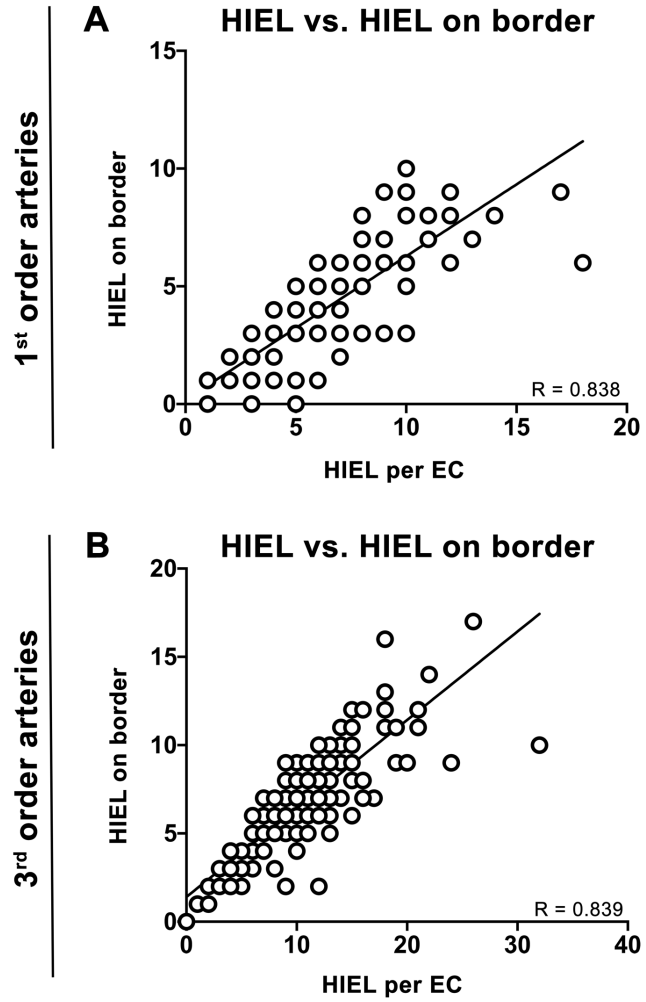

Figure 9. Correlation between the number of HIEL per EC and number of HIEL localized to the interendothelial junction. Stitched confocal images from (**A**) first order and (**B**) third order mesenteric arteries were used to analyze number and position of HIEL within individual ECs. Interendothelial junctions were defined via claudin-5 and IEL was visualized with Alexa Fluor 488-linked hydrazide. An HIEL was defined to be on border if it was within 1μm of claudin-5. Distance to claudin-5 was measured using the in-house Matlab analysis program. N=3 mice, n=3 arteries, n=155 ECs for first order mesenteric arteries, and N=4 mice, n=4 arteries, n=205 ECs for third order mesenteric arteries.

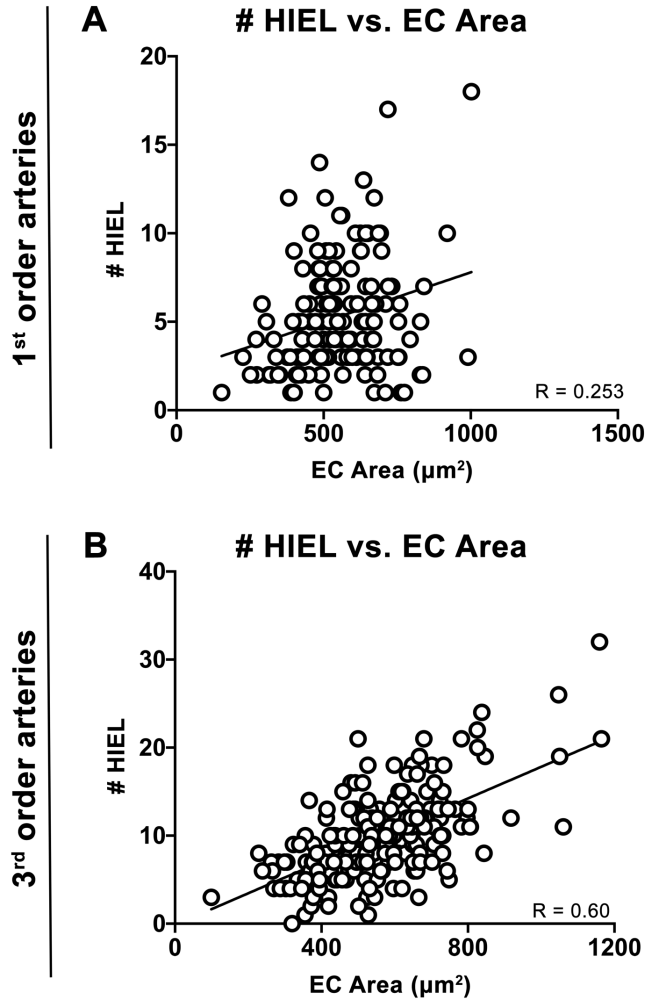

Figure 10. Correlation between the number of HIEL per EC and EC area. Stitched confocal images from (**A**) first order and (**B**) third order mesenteric arteries were used to analyze number of HIEL and the area of individual ECs (defined via claudin-5). The IEL was visualized with Alexa Fluor 488-linked hydrazide. EC area was measured by manual tracing in ImageJ. N=3 mice, n=3 arteries, n=155 ECs for first order mesenteric arteries, and N=4 mice, n=4 arteries, n=205 ECs for third order mesenteric arteries.

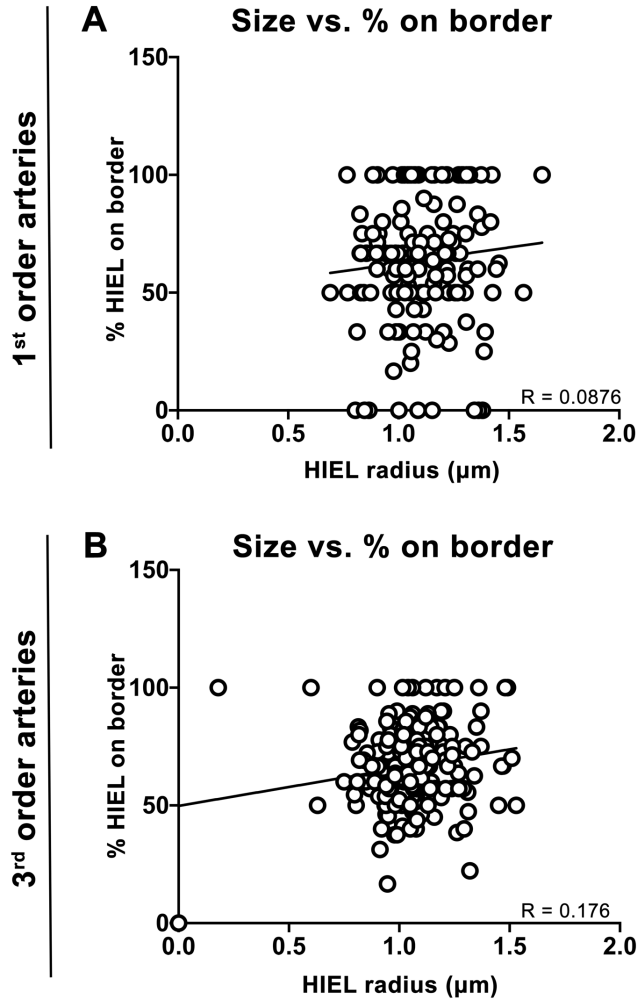

Figure 11. Correlation between the size of HIEL and percent HIEL localized to the interendothelial junction. Stitched confocal images from (**A**) first order and (**B**) third order mesenteric arteries were used to analyze number and position of HIEL within individual ECs. Interendothelial junctions were defined via claudin-5 and IEL was visualized with Alexa Fluor 488-linked hydrazide. An HIEL was defined to be on border if it was within 1µm of claudin-5. Distance to claudin-5 stain and HIEL radius were measured using the in-house Matlab analysis program. N=3 mice, n=3 arteries, n=155 ECs for first order mesenteric arteries, and N=4 mice, n=4 arteries, n=205 ECs for third order mesenteric arteries.

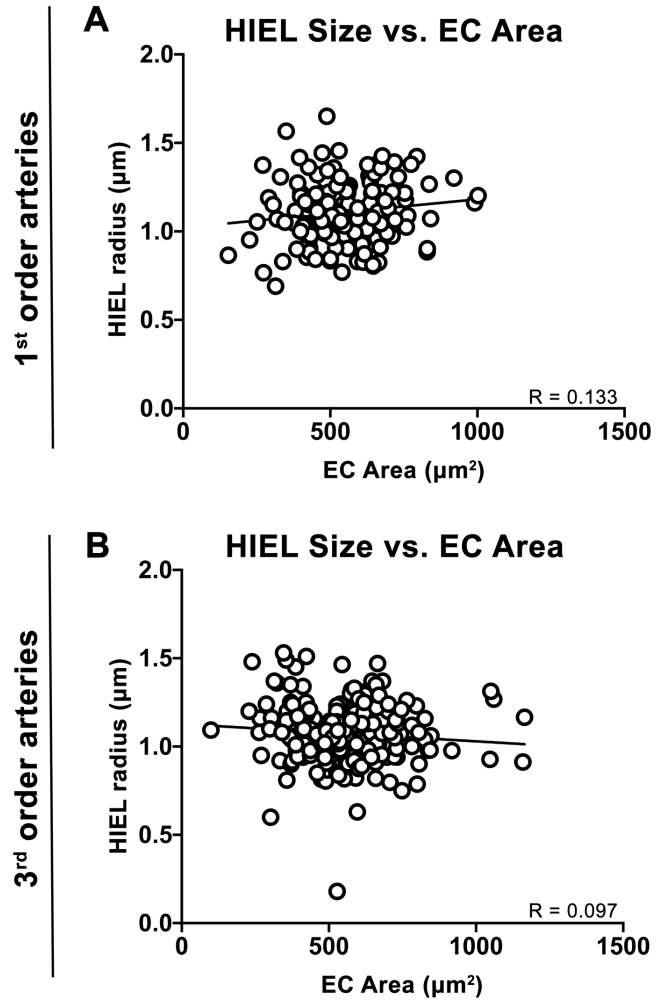

Figure 12. Correlation between HIEL size and EC Area. Stitched confocal images from (**A**) first order and (**B**) third order mesenteric arteries were used to analyze the size of HIEL and EC area. Interendothelial junctions were defined via claudin-5 and IEL was visualized with Alexa Fluor 488-linked hydrazide. HIEL radius measured using the in-house Matlab analysis program. EC Area was measured manually in ImageJ. N=3 mice, n=3 arteries, n=155 ECs for first order mesenteric arteries, and N=4 mice, n=4 arteries, n=205 ECs for third order mesenteric arteries.

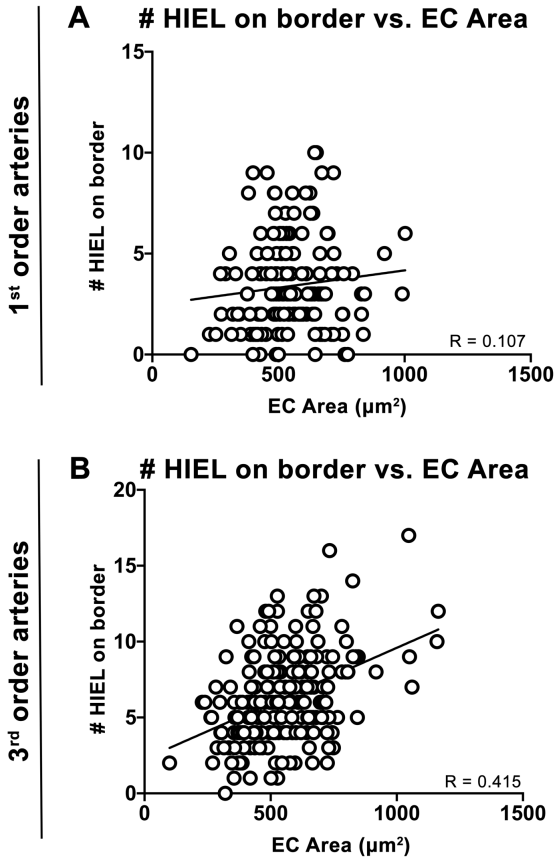

Figure 13. Correlation between the number of HIEL localized to the interendothelial junction and EC Area. Stitched confocal images from (**A**) first order and (**B**) third order mesenteric arteries were used to analyze number and position of HIEL within individual ECs. Interendothelial junctions were defined via claudin-5 and IEL was visualized with Alexa Fluor 488-linked hydrazide. An HIEL was defined to be on border if it was within 1μm of claudin-5 stain. Distance to claudin-5 stain and was measured using the in-house Matlab analysis program. EC Area was measured manually in ImageJ. N=3 mice, n=3 arteries, n=155 ECs for first order mesenteric arteries, and N=4 mice, n=4 arteries, n=205 ECs for third order mesenteric arteries.

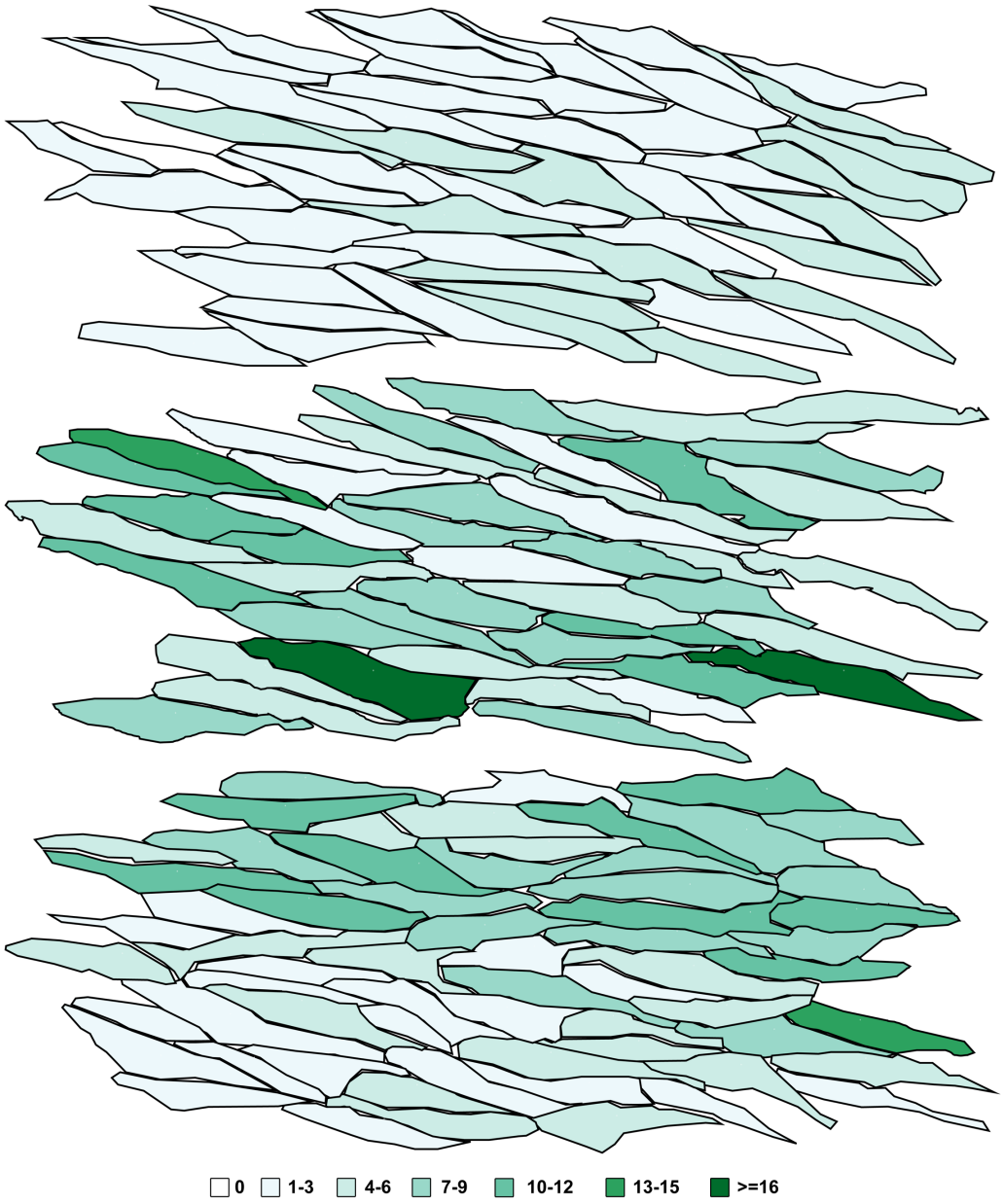

Figure 14. Number of HIEL per EC in first order mesenteric arteries prepared *en face*. Color-coded EC maps to visualize density of HIEL per EC in first order mesenteric arteries. Lighter green shades indicate lower HIEL while darker green shades indicate more HIEL are present within that EC. N=3 mice, n=3 arteries, n=155 ECs.

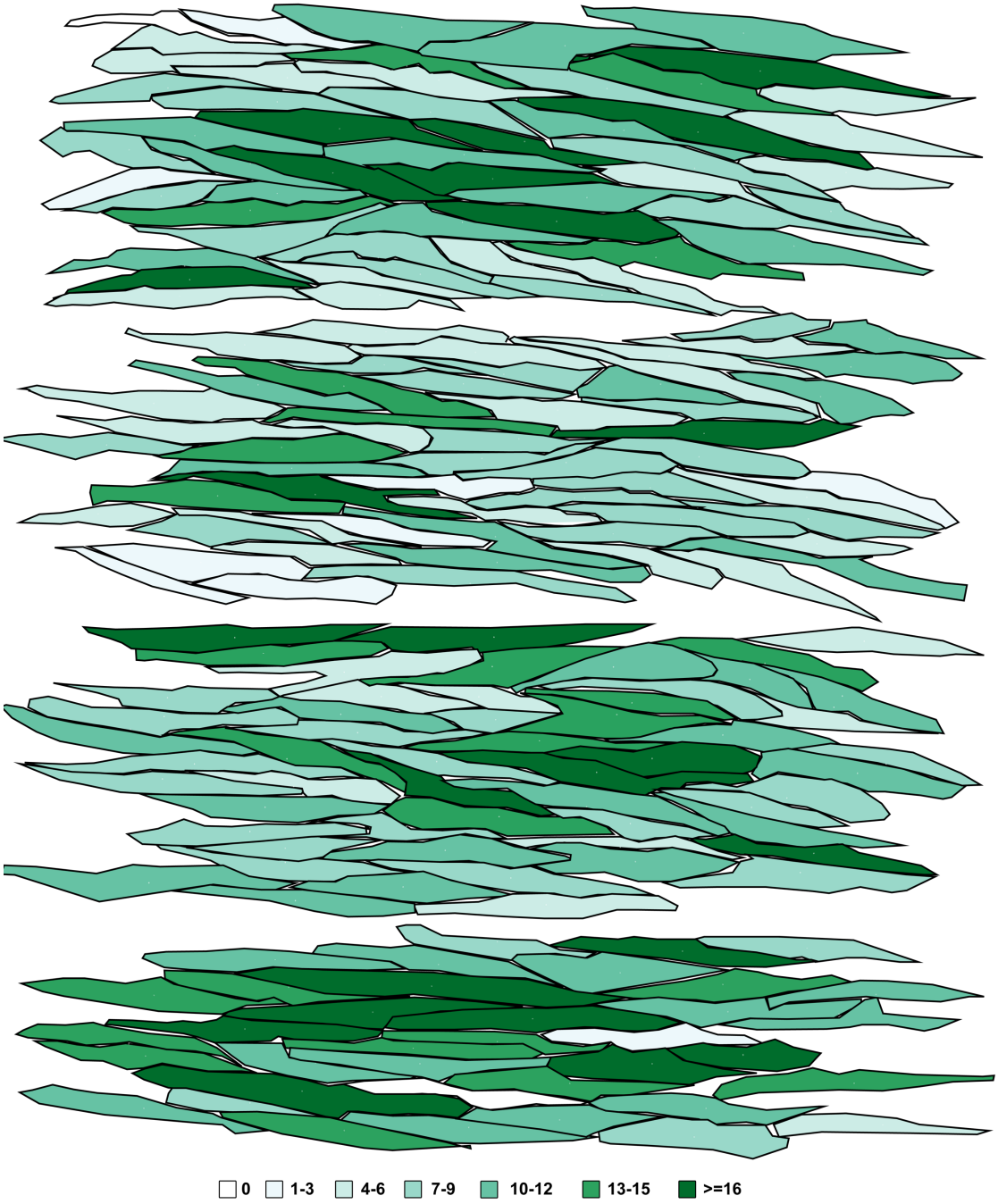

Figure 15. Number of HIEL per EC in third order mesenteric arteries prepared *en face*. Color-coded EC maps to visualize density of HIEL per EC in third order mesenteric arteries. Lighter green shades indicate lower HIEL while darker green shades indicate more HIEL are present within that EC. N=4 mice, n=4 arteries, n=205 ECs.

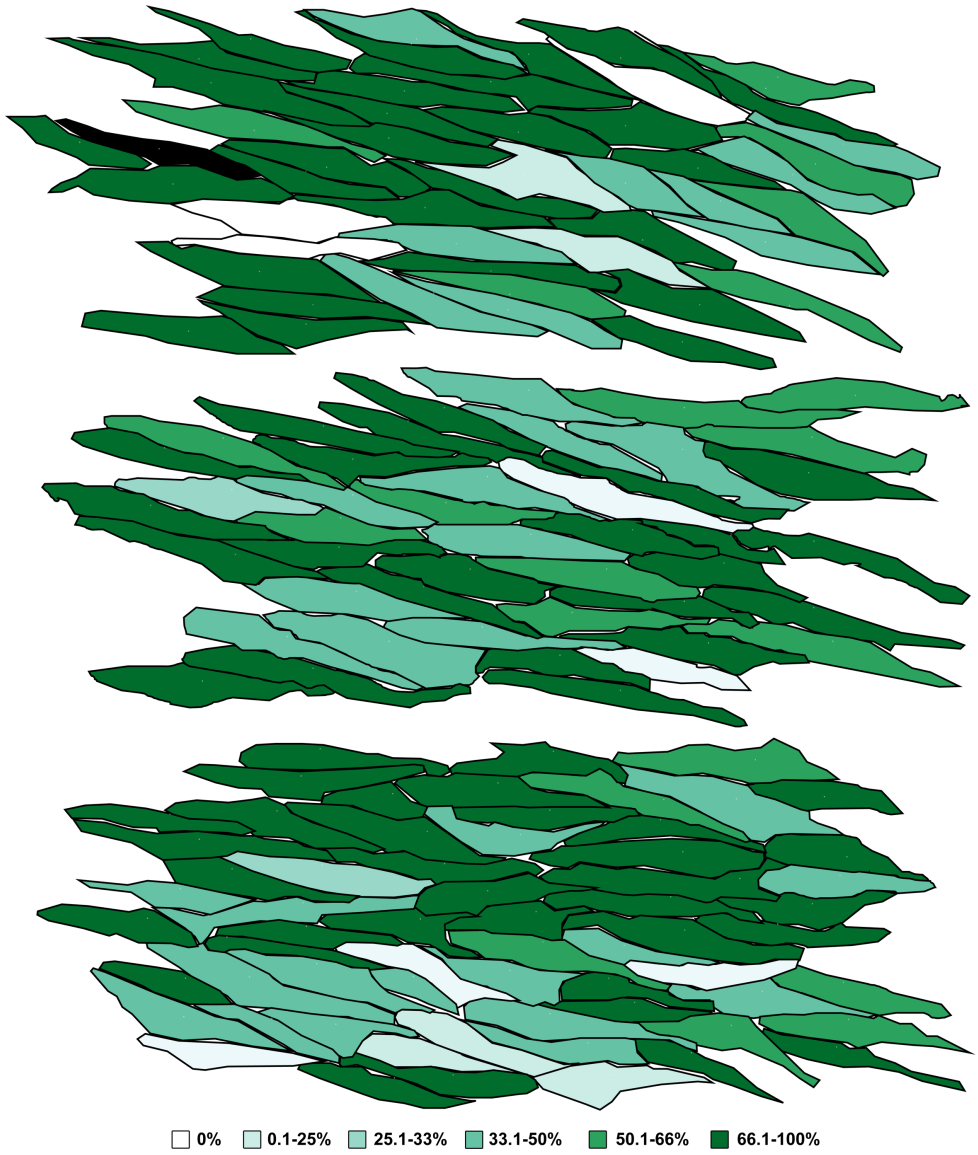

Figure 16. Percentage of HIEL within 1μm of interendothelial junction in first order mesenteric arteries prepared *en face*. Color-coded EC maps to show how HIEL are distributed within individual cells in first order mesenteric arteries. Lighter green shades indicate that the HIEL tend to be towards the middle of the cell whereas darker green shades indicate a localization towards interendothelial junctions. N=3 mice, n=3 arteries, n=155 ECs.

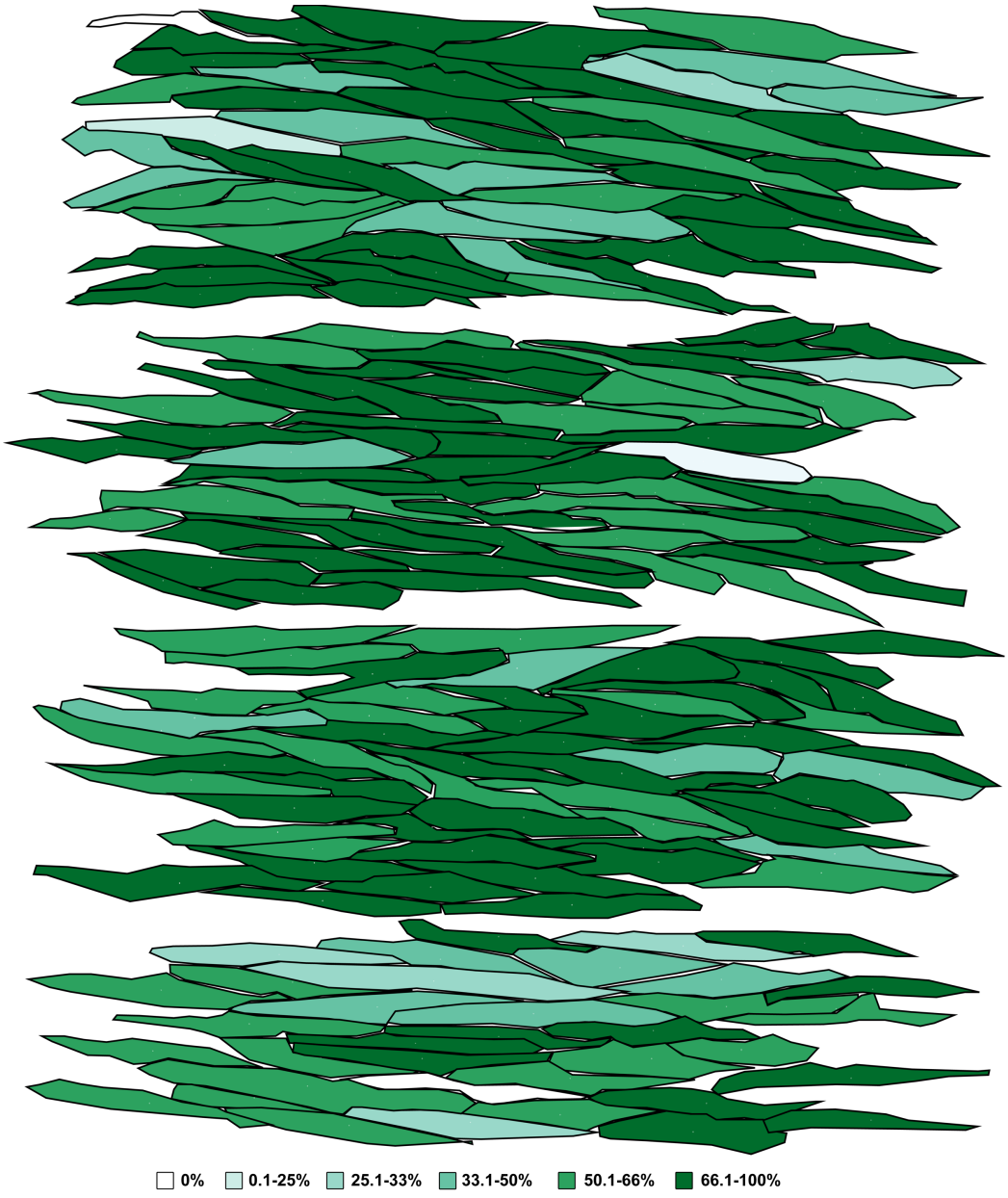

Figure 17. Percentage of HIEL within 1μm of interendothelial junction in third order mesenteric arteries prepared *en face*. Color-coded EC maps to how HIEL are distributed within individual cells in third order mesenteric arteries. Lighter green shades indicate that the HIEL tend to be towards the middle of the cell whereas darker green shades indicate a localization towards interendothelial junctions. N=4 mice, n=4 arteries, n=205 ECs.

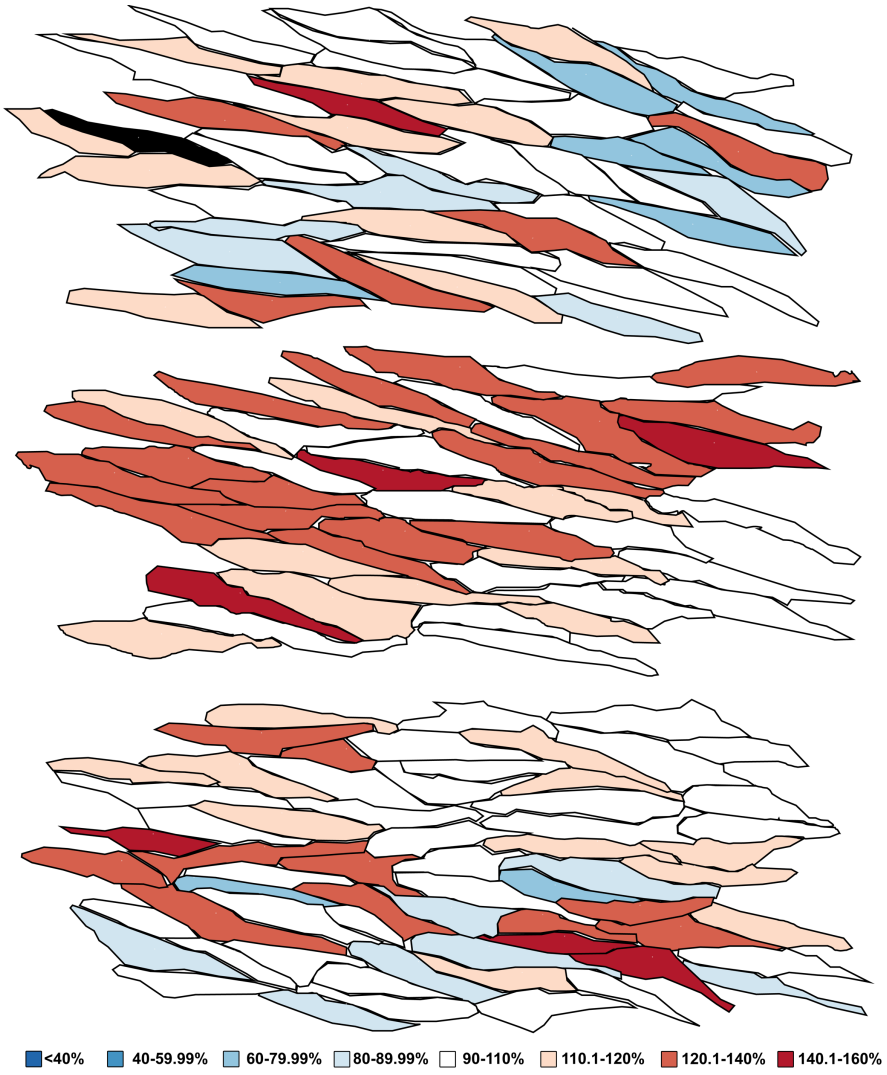

Figure 18. Average HIEL size within an EC compared to the average EC in first order mesenteric arteries prepared *en face*. Color-coded EC maps to visualize the average HIEL size within individual cells in first order mesenteric arteries. White ECs indicate that the HIEL within that cell are within the average range for that artery. ECs in cool, blue shades represent ECs with lower HIEL size compared to the artery average, and ECs in warm, red tones represent ECs with higher HIEL size compared to the artery average. N=3 mice, n=3 arteries, n=155 ECs.

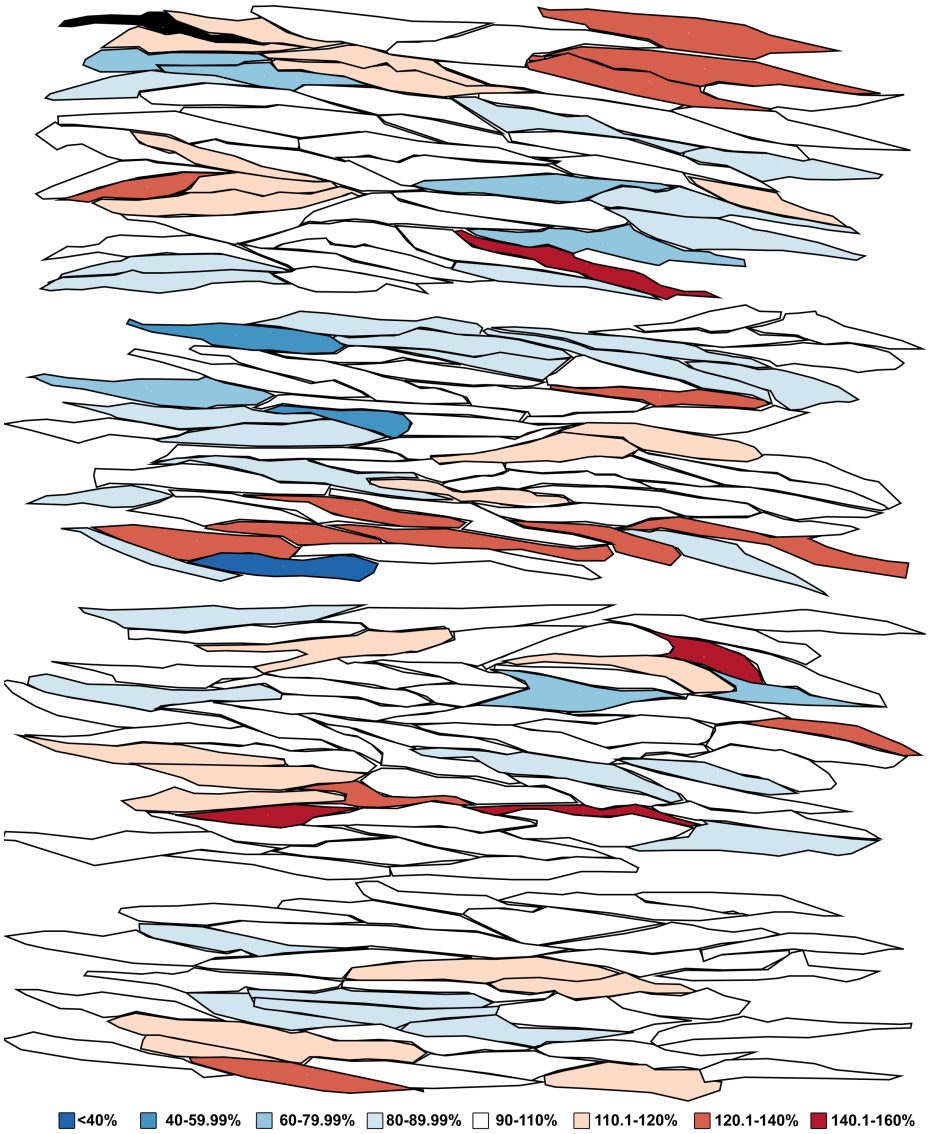

Figure 19. Average HIEL size within an EC compared to the average EC in third order mesenteric arteries prepared *en face*. Color-coded EC maps to visualize the average HIEL size within individual cells in third order mesenteric arteries. White ECs indicate that the HIEL within that cell are within the average range for that artery. ECs in cool, blue shades represent ECs with lower HIEL size compared to the artery average, and ECs in warm, red tones represent ECs with higher HIEL size compared to the artery average. N=4 mice, n=4 arteries, n=205 ECs.

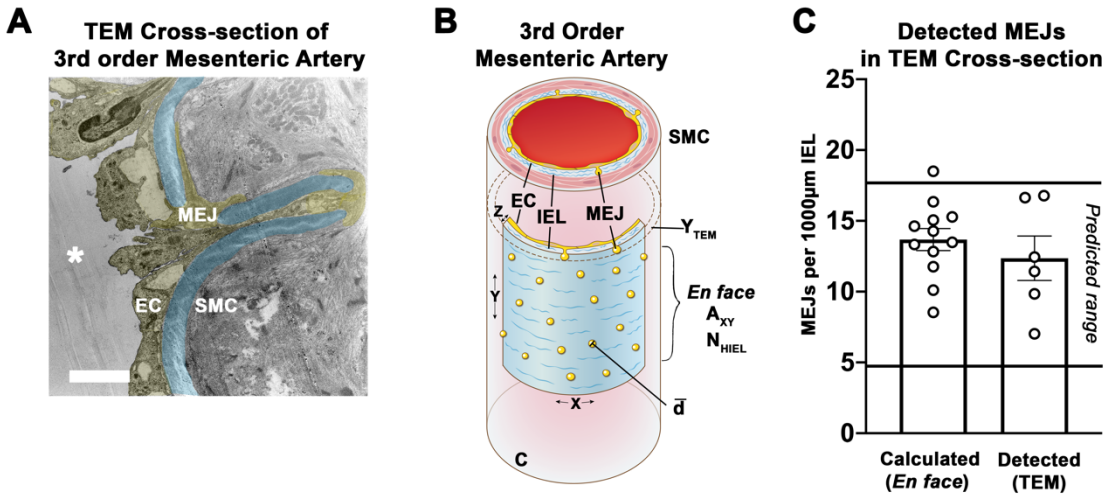

Figure 20. Every HIEL contains an MEJ. (**A**) Transmission electron microscopy image of an arterial cross-section at 2K magnification. IEL is pseudo-colored in blue and ECs/MEJs pseudo-colored in yellow. Scale bar 2μm. (**B**) Quantitation of *en face* HIEL from Matlab simulations that were used to predict if every HIEL contains an MEJ (also refer to **Tables 1-3** and **Chapter 4 Appendix**). Where **C** is the circumference of the artery, **d** is the diameter of HIEL, $\bar{\mathbf{A}}_{\mathbf{xy}}$ is the area of *en face* images, $\mathbf{N}_{\mathbf{HIEL}}$ is the average number of HIEL per image, $\mathbf{Y}_{\mathbf{TEM}}$ is the thickness of an individual TEM section, **X** is the width of an *en face* image, **Y** is the height of an *en face* image, and **Z** is the thickness of the arterial wall. (**C**) Quantification of HIEL per 1000μm measured in TEM cross-sections or back calculated from *en face* views. Note that both values are in predicted range. N=6 mice, n=6 arteries, n=3-5 TEM sections, and 570-964μm IEL length quantified per mouse.

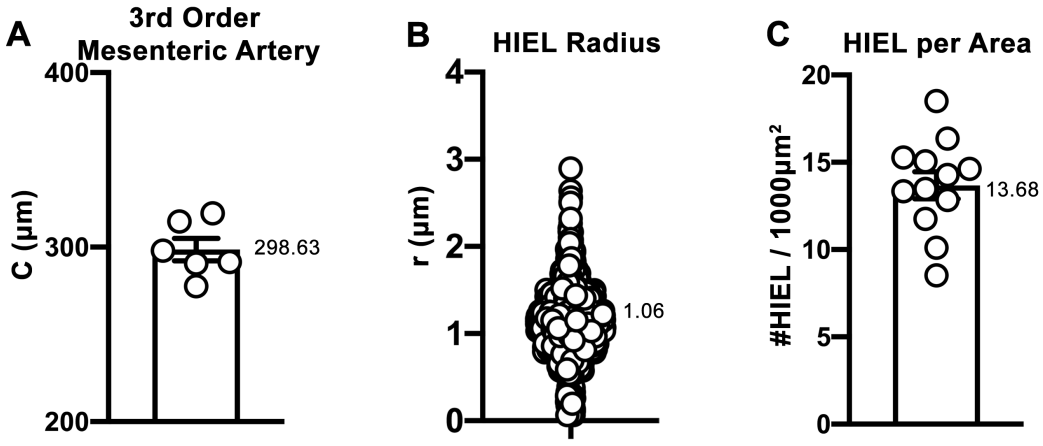

Figure 21. Quantitative data obtained from third order mesenteric artery *en face* preparations. (**A**) Circumference of third order mesenteric arteries measured as the width of the artery in an *en face* preparation. N=5 mouse, n=6 arteries. (**B**) HIEL radius measurements obtained from in-house Matlab program. N=6 mice, and n=10 arteries, n=22 ROIs, Area=$1.48x10^5 \mu m^2$, n=2166 HIEL. (**C**) HIEL per area taken from *en face* images used in Matlab analysis. Number of HIEL was determined via the in-house Matlab program. N=4 mice, n=4 arteries, n=12 ROIs, Area=$1.67x10^5 \mu m^2$.

Table 1. Summary of quantitative data obtained from third order *en face* images.

Variable	Value	Unit	Source	Description
C	298.6	μm	N=4, n=6 arteries	Circumference of 3rd order mesenteric arteries
C_{IEL}	298.6	μm	Assume that it is equal to C	Circumference of IEL
d	2.1	μm	N=5 mice, n=2166 HIEL	Average diameter of HIEL
$Å_{xy}$	13,942.9	μm^2		Area of en face images
$Ñ_{HIEL}$	190.7	HIEL / image	N=4, n=4 arteries, n=12 images	Average number of HIEL
ρ_{HIEL}	13.6	HIEL per $1000\mu m^2$	$(Ñ_{HIEL} / Å_{xy})$ **x** 1000 μm^2	Density of HIEL per 1000 μm^2

Table 2. Calculated parameters of arterial cross-sections imaged via TEM.

Variable	Value	Units	Source	Description
$\mathbf{Y_{TEM}}$	0.070	μm	Experimental parameter	Thickness of transverse TEM sections
$\mathbf{A_{TEM,1}}$	20.902	μm^2	$C_{\mathbf{IEL}}$ **x** Y_{TEM}	Artery area spanning $\mathbf{Y_{TEM}}$
$\mathbf{A_{TEM,\,d}}$	627.06	μm^2	$C_{\mathbf{IEL}}$ **x** d	Artery area spanning the length **d**
$\mathbf{L_{IEL}}$	1791.6	μm	6 **x** C_{IEL}	Length of IEL across 6 TEM sections
$\mathbf{HIEL_{TEM}}$	9	HIEL per A_{TEM}	(ρ_{HIEL} **x** $A_{TEM,d}$) / $1000\mu m^2$	Number of HIEL expected across $A_{TEM,d}$

Table 3. Case scenarios that consider the potential spatial distributions of HIEL.

Case Definition	Variable	Value	Units	Calculation	Description
Case1: Maximum case, assumes HIEL are evenly distributed	$D_{HIEL,\ 1}$	54	TEM detections	6* $HIEL_{TEM,6}$	HIEL detections over 6 sections for Case 1
Case 2: Assumes HIEL are randomly distributed	$D_{HIEL,\ 2}$	32		6* $HIEL_{TEM,6}$	HIEL detections over 6 sections for Case 2
Case 3: Minimum case, represents the rare case where each HIEL only appear on 1/6 of sections	$D_{HIEL,\ 3}$	9		6* $HIEL_{TEM,6}$	HIEL detections over 6 sections for Case 3
Normalized Case 1	$D_{HIEL,\ 1N}$	30	TEM detections per 1000µm IEL	$(D_{HIEL,\ 1})$ / (L_{IEL}) x 1000µm	HIEL detections over 6 sections for Case 1 normalized to IEL length
Normalized Case 2	$D_{HIEL,\ 2N}$	17.8		$(D_{HIEL,\ 2})$ / (L_{IEL}) x 1000µm	HIEL detections over 6 sections for Case 2 normalized to IEL length
Normalized Case 3	$D_{HIEL,\ 3N}$	5		$(D_{HIEL,\ 3})$ / (L_{IEL}) x 1000µm	HIEL detections over 6 sections for Case 3 normalized to IEL length

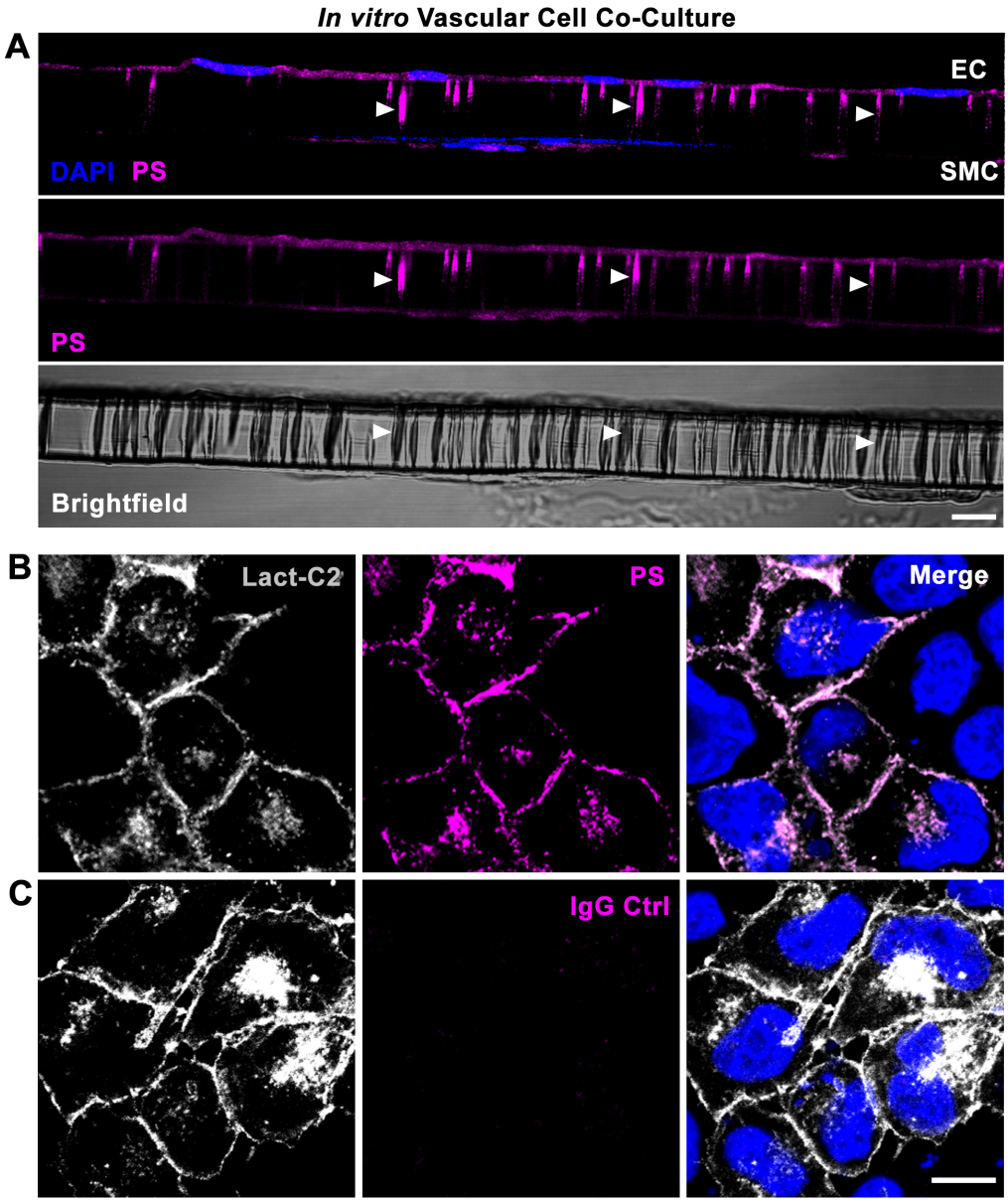

Figure 22. Validation of PS antibody. (A) Transverse cross-sections of an *in vitro* vascular cell co-culture model where EC and SMC are plated on either side of a Transwell. Nuclei (blue) are detected via DAPI and PS (magenta). Brightfield image of Transwell is shown in the bottom panel. Arrowheads indicates PS localization to *in vitro* MEJs. (**B**) HeLa cells transfected with Lact-C2-GFP plasmid (grey) and co-stained with PS antibody or (**C**) IgG control. Nuclei (blue) are detected via DAPI. Scale bars are 10μm.

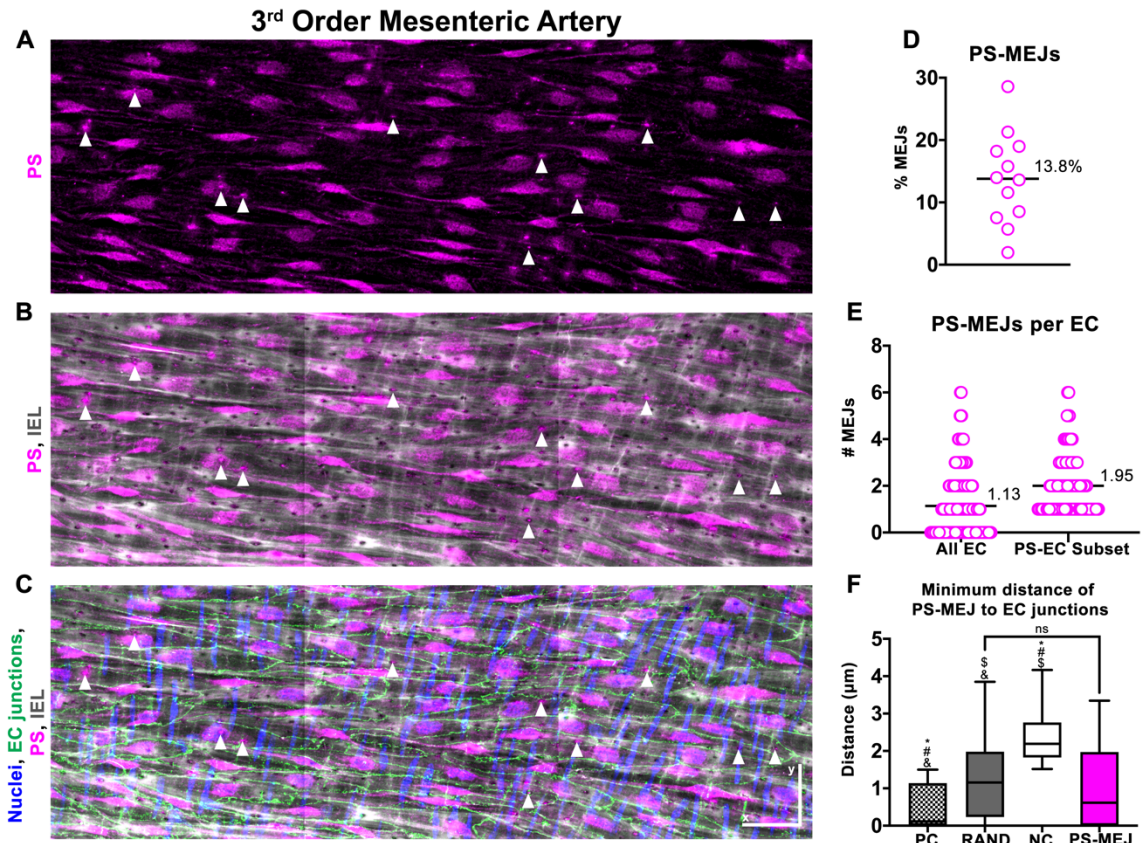

Figure 23. PS colocalizes with Kir2.1 in a subpopulation of MEJs. Representative stitched confocal image of a third order mesenteric artery showing (**A**) PS (magenta), (**B**) PS and IEL (grey) detected via Alexa Fluor 488-linked hydrazide, and (**C**) merge with nuclei (blue) detected via DAPI and interendothelial junctions (green) detected via claudin-5. Arrowheads indicate PS localized to MEJ. Scale bar is 30µm in both X and Y directions. **(D**) Percentage of MEJs that contain PS. (**E**) Number of MEJs containing PS per EC, where EC borders were defined via claudin-5 staining. N=4 mice, n=4 arteries, n=12 ROIs, and n=205 ECs. (**F**) Spatial analysis of PS-MEJ compared to positive control (PC), random (RAND), and negative control (NC) simulations. Brown-Forsythe and Welch ANOVA. # indicates a p <0.0001 significant difference from real-world HIEL distribution, *

indicates a p <0.0001 significant difference from random simulation distribution, $ indicates a p <0.0001 significant difference from PC simulation distribution, and & indicates a p <0.0001 significant difference from NC simulation distribution. N=3 mice, n=4 arteries, n=4 ROIs, n=66 PS-MEJs.

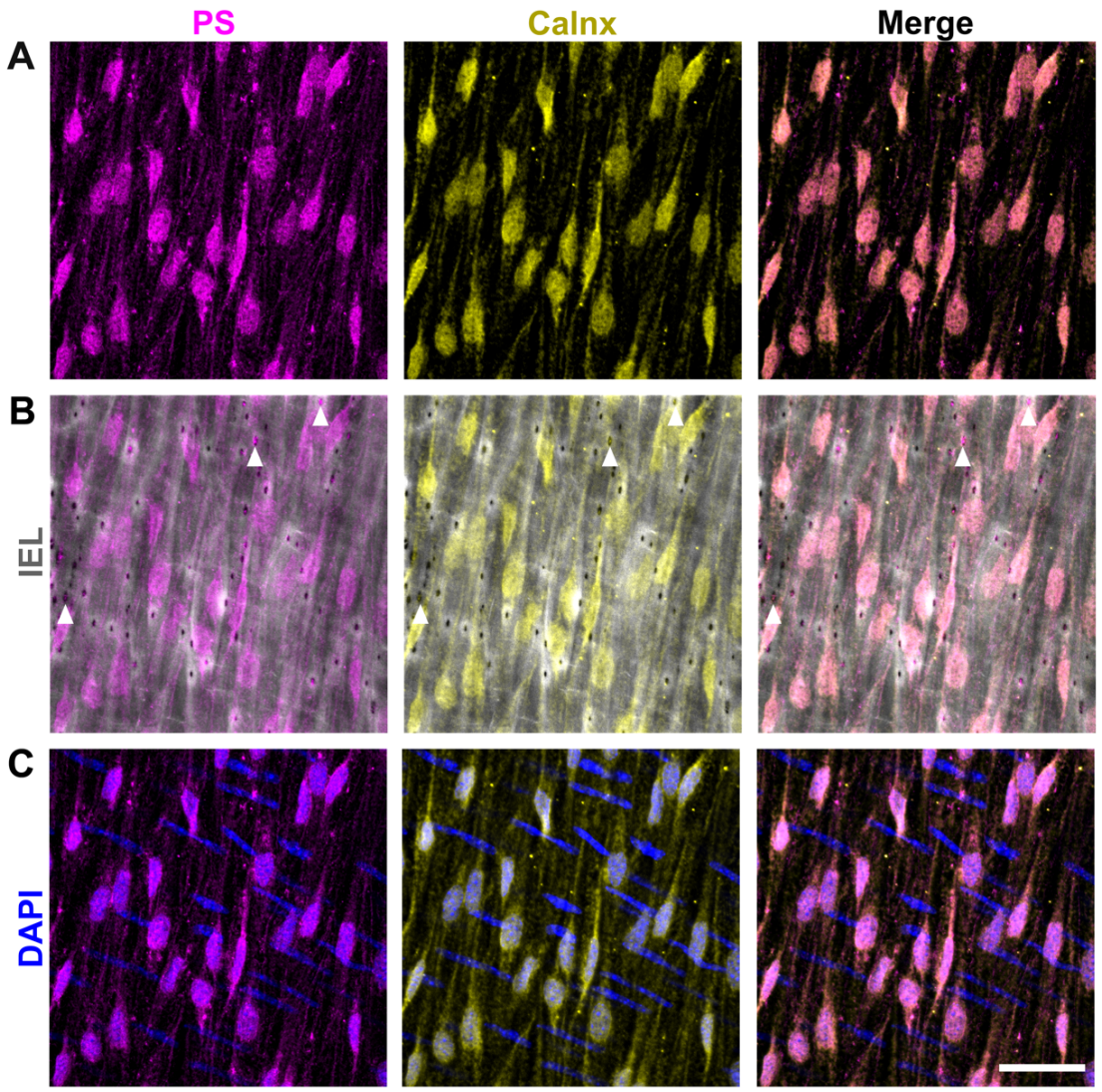

Figure 24. *En face* immunohistochemistry with PS and calnexin. Representative *en face* images from third order mesenteric arteries. (**A**) Panel demonstrating PS (magenta) and calnx (yellow) staining in separate channels or merged together. (**B**) PS, calnx, and merge staining overlayed on the IEL (grey) detected via Alexa Fluor linked hydrazide. Arrowheads indicate colocalization of PS and calnx to same HIEL. (**C**) PS, calnx, or merge overlayed with nuclei (blue), detected via DAPI. Scale bar is 30μm.

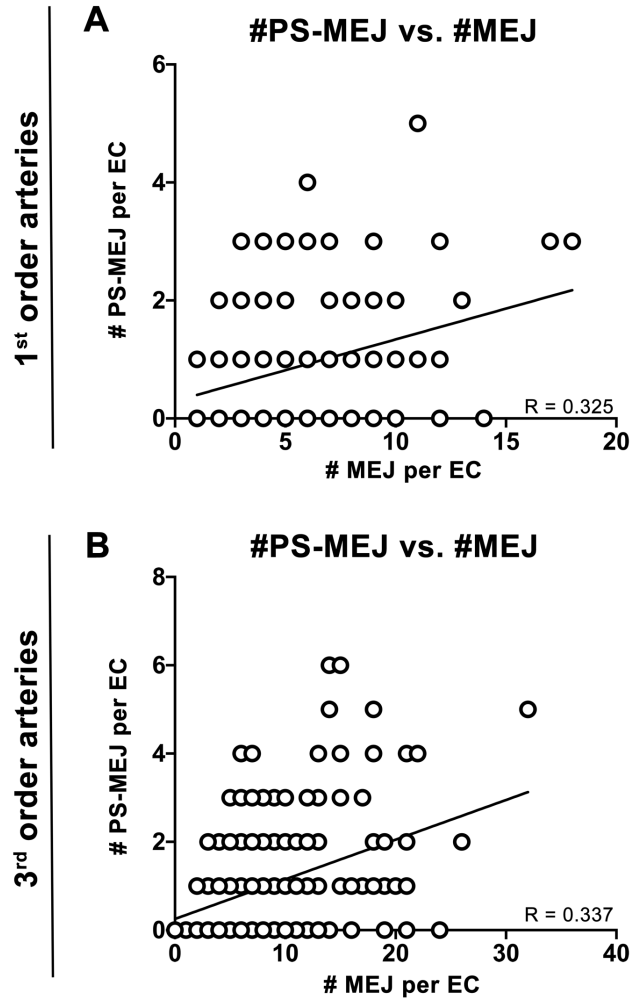

Figure 25. Correlation between the number of PS-MEJs per EC and #MEJs per EC. Stitched confocal images from (**A**) first order and (**B**) third order mesenteric arteries were used to analyze number of PS-MEJ and total MEJ within individual ECs (defined via claudin-5). The IEL was visualized with Alexa Fluor 488-linked hydrazide. N=3 mice, n=3 arteries, n=155 ECs for first order mesenteric arteries, and N=4 mice, n=4 arteries, n=205 ECs for third order mesenteric arteries.

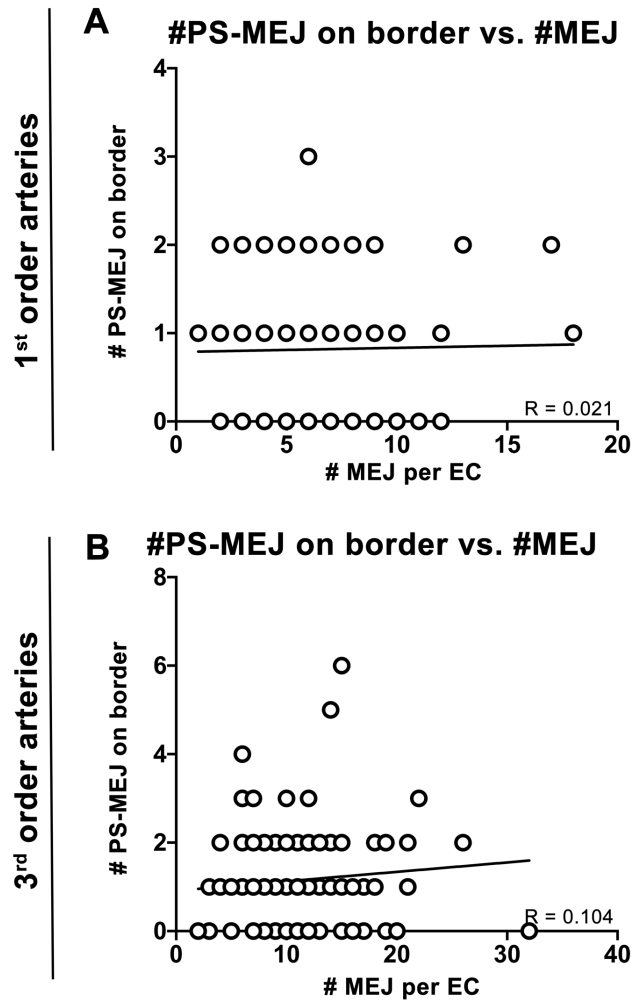

Figure 26. Correlation between PS-MEJ localization and number of MEJs per EC. Stitched confocal images from (**A**) first order and (**B**) third order mesenteric arteries were used to analyze PS-MEJ and total MEJs within 1μm of the interendothelial junction for individual ECs (defined via claudin-5). The IEL was visualized with Alexa Fluor 488-linked hydrazide. EC area was measured by manual tracing in ImageJ. Only ECs with at least one PS-MEJ were plotted. N=3 mice, n=3 arteries, n=81 ECs for first order mesenteric arteries, and N=4 mice, n=4 arteries, n=119 ECs for third order mesenteric arteries.

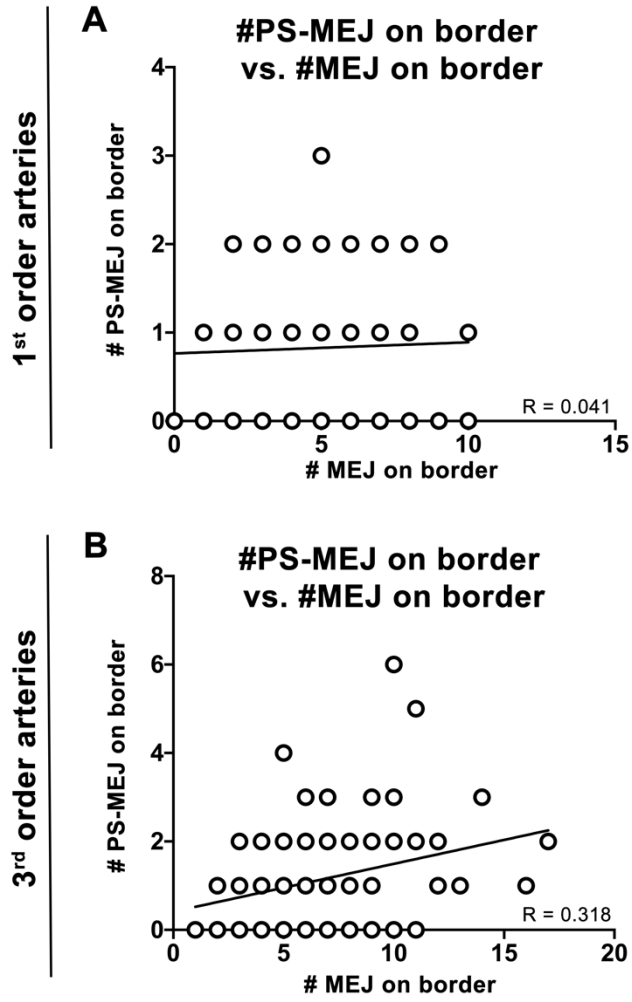

Figure 27. Correlation between PS-MEJ localization and MEJ localization. Stitched confocal images from (**A**) first order and (**B**) third order mesenteric arteries were used to analyze PS-MEJ and total MEJ localization within 1μm of the interendothelial junction for individual ECs (defined via claudin-5). The IEL was visualized with Alexa Fluor 488-linked hydrazide. EC area was measured by manual tracing in ImageJ. Only ECs with at least one PS-MEJ were plotted. N=3 mice, n=3 arteries, n=81 ECs for first order mesenteric arteries, and N=4 mice, n=4 arteries, n=119 ECs for third order mesenteric arteries.

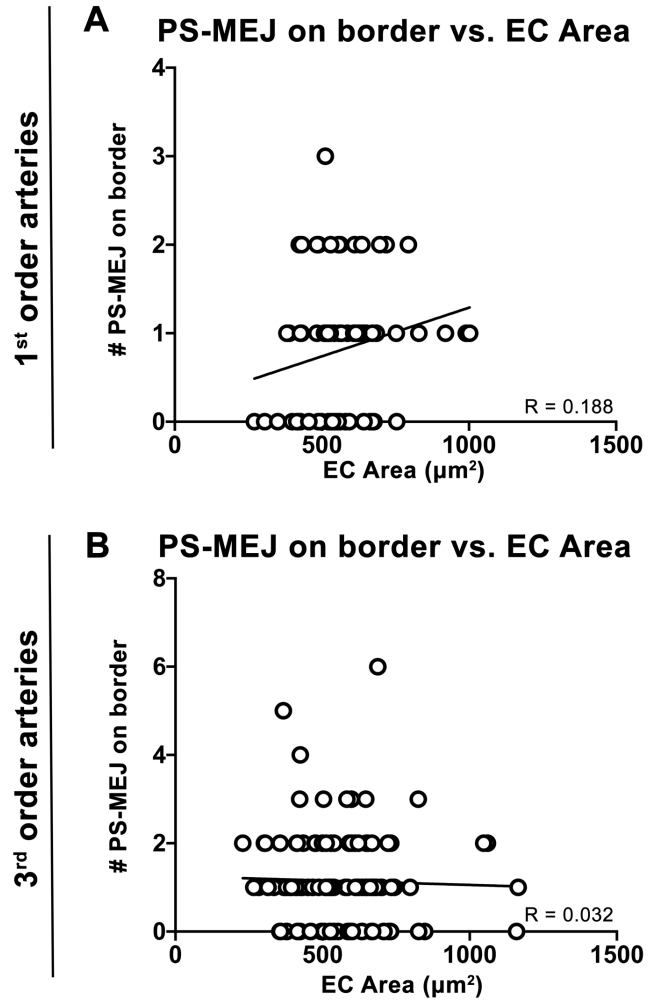

Figure 28. Correlation between PS-MEJ localization and EC area. Stitched confocal images from (**A**) first order and (**B**) third order mesenteric arteries were used to analyze PS-MEJ localization within 1μm of the interendothelial junction and EC area individual ECs (defined via claudin-5). The IEL was visualized with Alexa Fluor 488-linked hydrazide. EC area was measured by manual tracing in ImageJ. Only ECs with at least one PS-MEJ were plotted. N=3 mice, n=3 arteries, n=81 ECs for first order mesenteric arteries, and N=4 mice, n=4 arteries, n=119 ECs for third order mesenteric arteries.

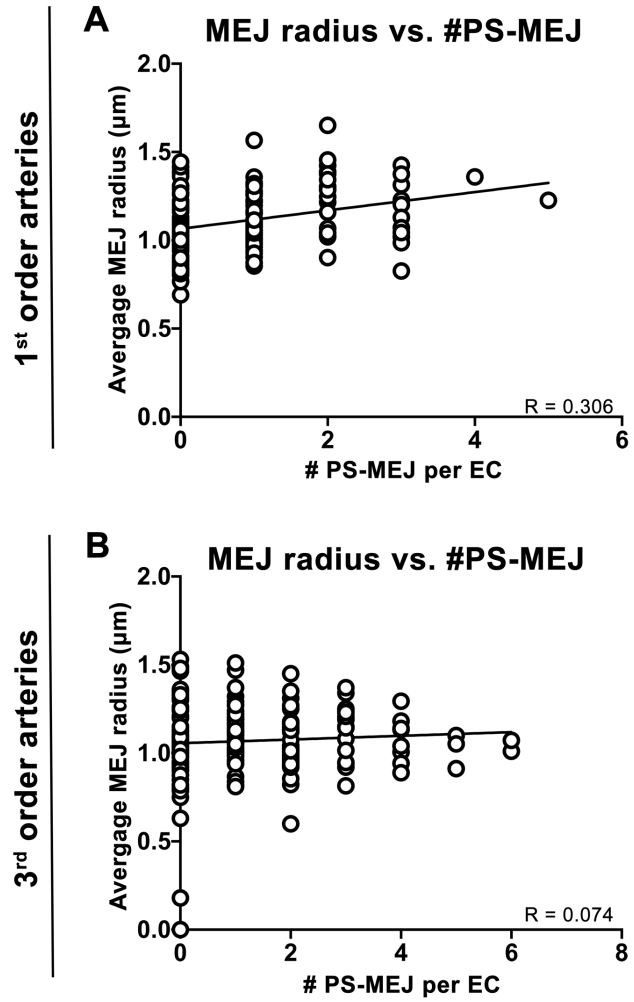

Figure 29. Correlation between the average MEJ size and number of PS-MEJs per EC. Stitched confocal images from (**A**) first order and (**B**) third order mesenteric arteries were used to analyze average MEJ size and number of PS-MEJ for each individual ECs (defined via claudin-5). MEJ size was determined via Matlab program. The IEL was visualized with Alexa Fluor 488-linked hydrazide. EC area was measured by manual tracing in ImageJ. Only ECs with at least one PS-MEJ were plotted. N=3 mice, n=3 arteries, n=81 ECs for first order mesenteric arteries, and N=4 mice, n=4 arteries, n=119 ECs for third order mesenteric arteries.

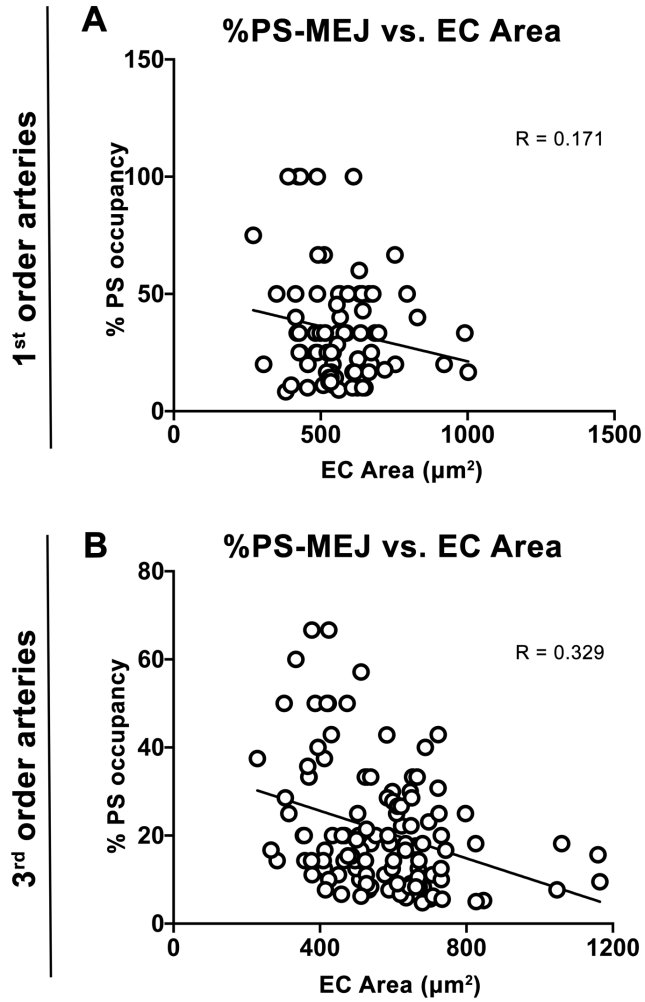

Figure 30. Correlation between the percentage of PS-MEJs per EC and EC area. Stitched confocal images from (**A**) first order and (**B**) third order mesenteric arteries were used to analyze percentage of PS-MEJ and EC area for each individual ECs (defined via claudin-5). The IEL was visualized with Alexa Fluor 488-linked hydrazide. EC area was measured by manual tracing in ImageJ. Only ECs with at least one PS-MEJ were plotted. N=3 mice, n=3 arteries, n=81 ECs for first order mesenteric arteries, and N=4 mice, n=4 arteries, n=119 ECs for third order mesenteric arteries.

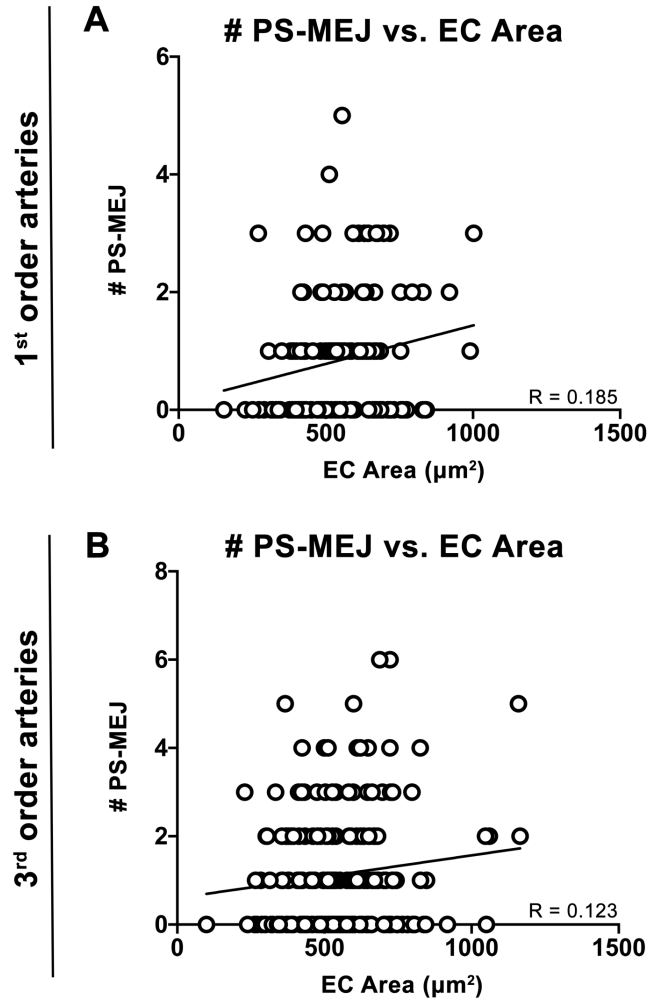

Figure 31. Correlation between the number of PS-MEJs per EC and EC area. Stitched confocal images from (**A**) first order and (**B**) third order mesenteric arteries were used to analyze number of PS-MEJ and EC area for each individual ECs (defined via claudin-5). The IEL was visualized with Alexa Fluor 488-linked hydrazide. EC area was measured by manual tracing in ImageJ. N=3 mice, n=3 arteries, n=155 ECs for first order mesenteric arteries, and N=4 mice, n=4 arteries, n=205 ECs for third order mesenteric arteries.

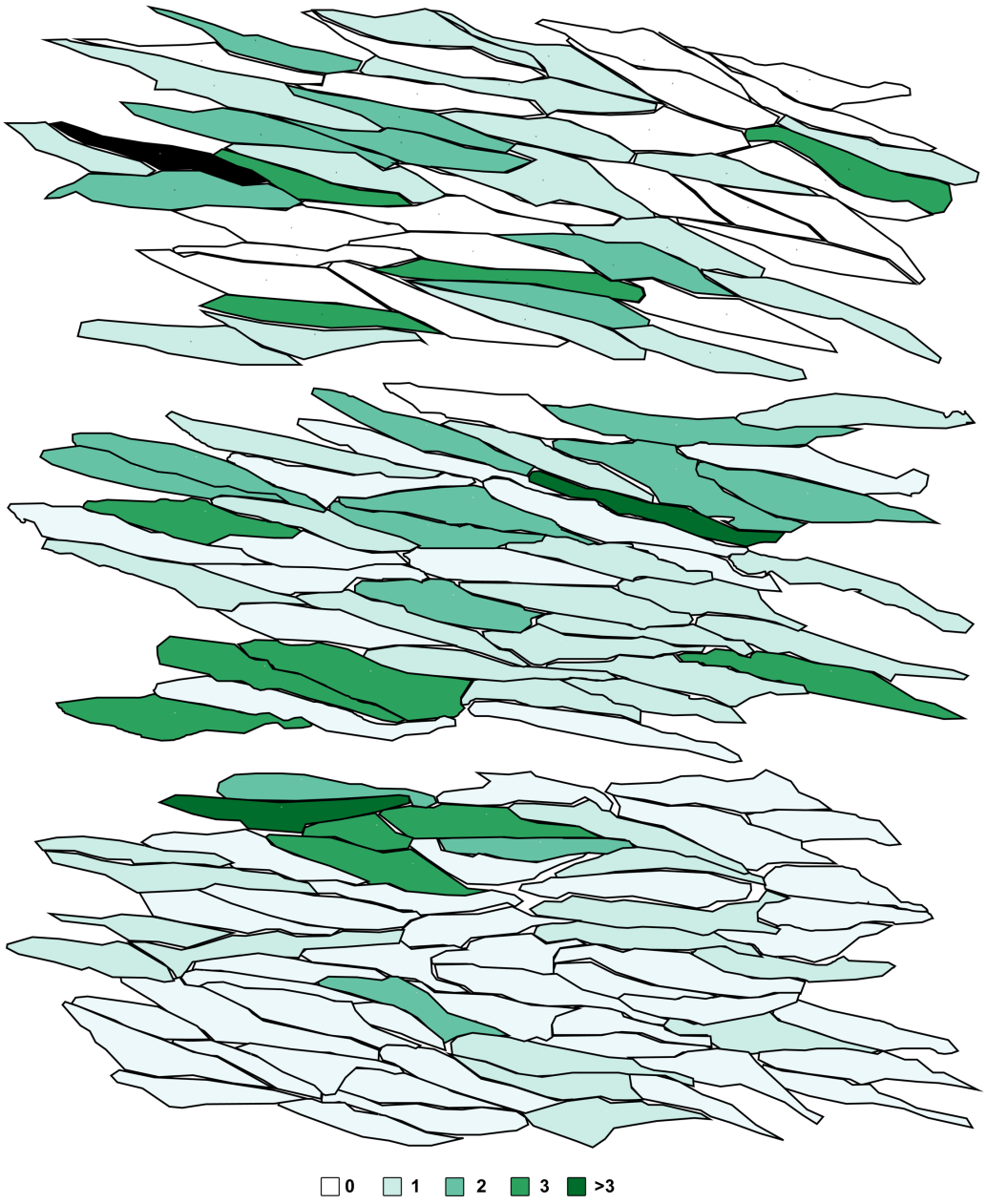

Figure 32. Number of PS-MEJ first order mesenteric arteries prepared *en face*. Color-coded EC maps to show how PS-MEJ are distributed within individual cells in first order mesenteric arteries. N=3 mice, n=3 arteries, n=155 ECs.

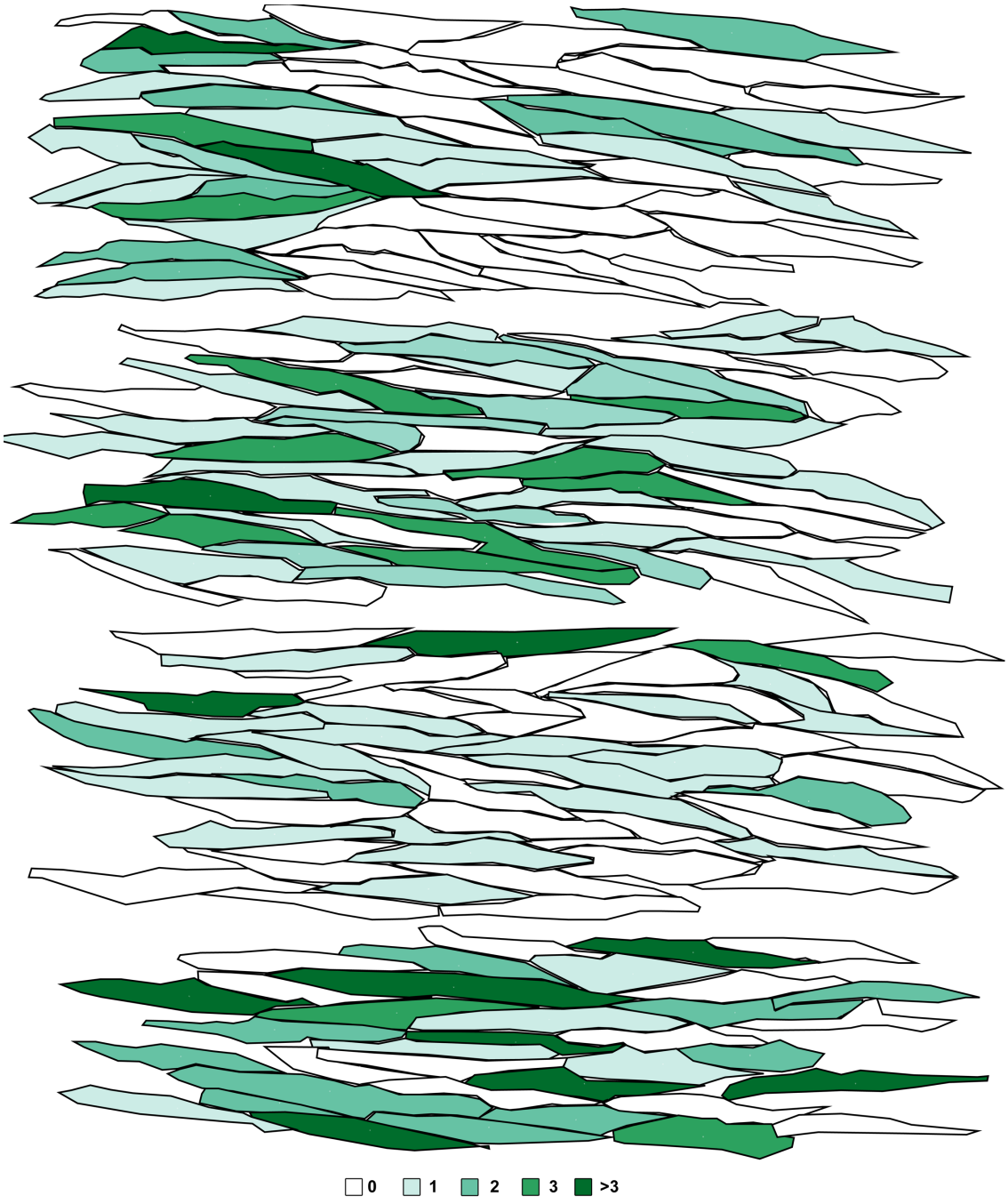

Figure 33. Number of PS-MEJ third order mesenteric arteries prepared *en face*. Color-coded EC maps to show how PS-MEJ are distributed within individual cells in third order mesenteric arteries. N=4 mice, n=4 arteries, n=205 ECs.

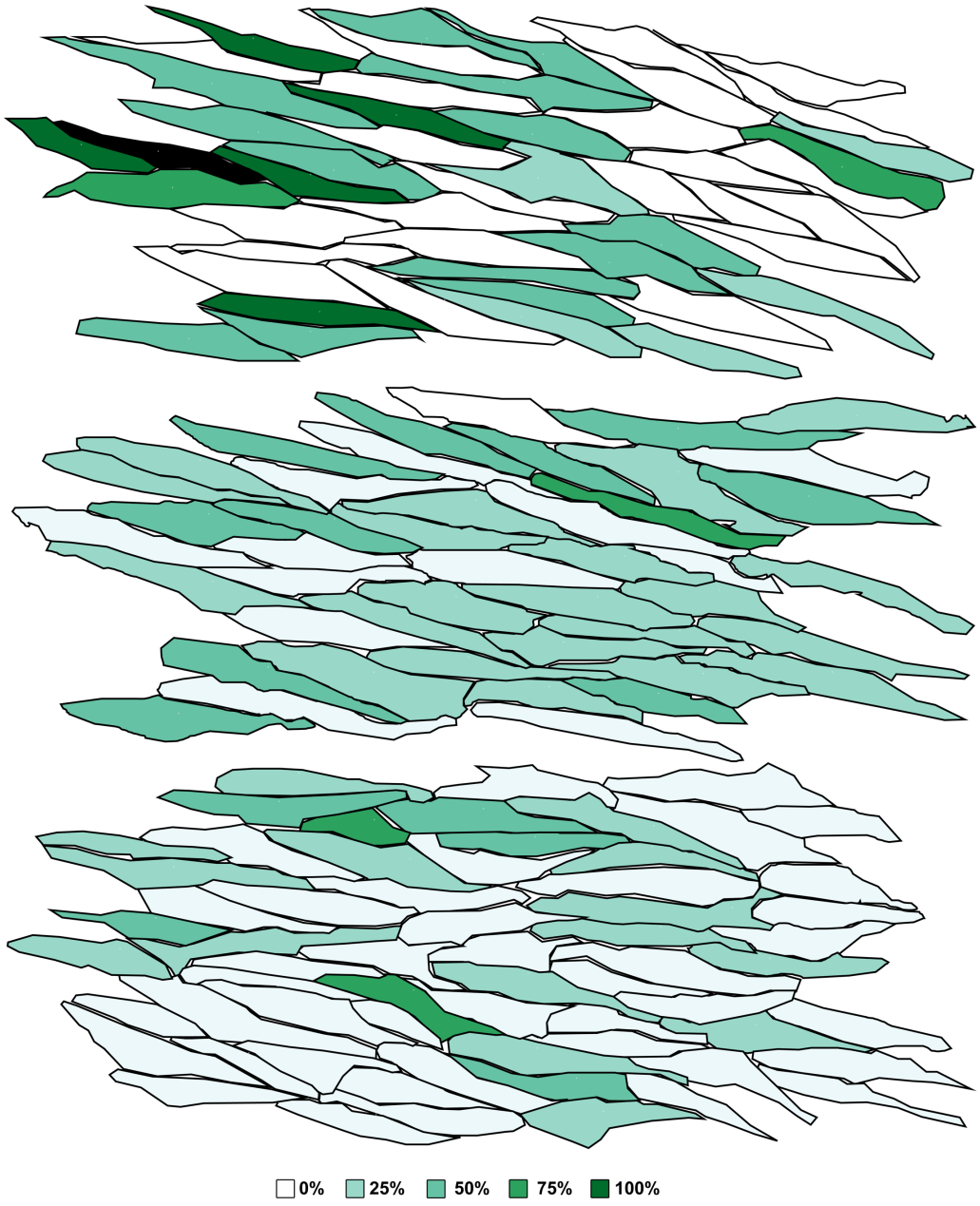

Figure 34. Percent PS-MEJ in first order mesenteric arteries prepared *en face*. Color-coded EC maps to show how percentage occupancy of PS in total MEJ is distributed within individual cells in first order mesenteric arteries. N=3 mice, n=3 arteries, n=155 ECs.

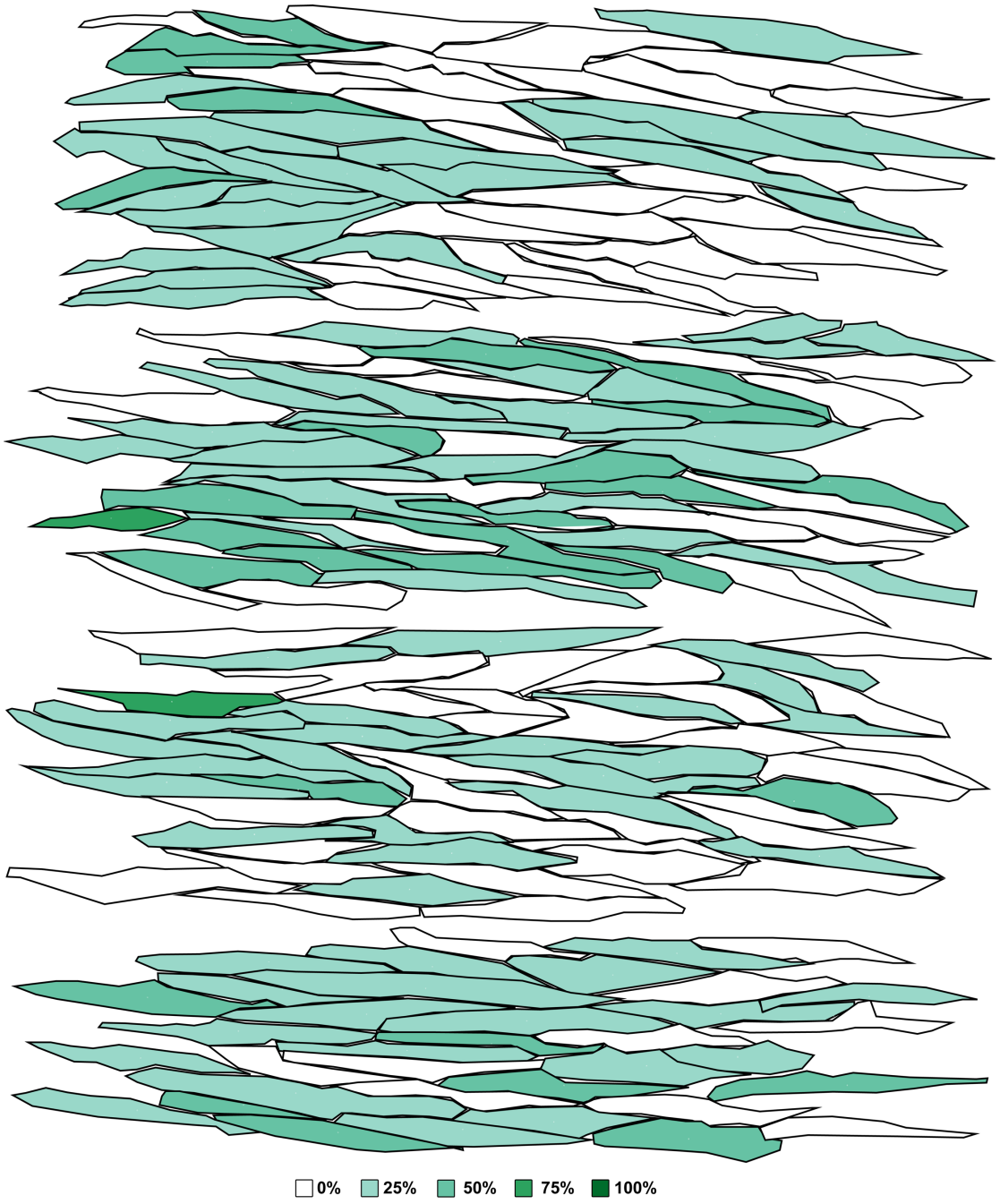

Figure 35. Percent PS-MEJ in first order mesenteric arteries prepared *en face*. Color-coded EC maps to show how percentage occupancy of PS in total MEJ is distributed within individual cells in first order mesenteric arteries. N=4 mice, n=4 arteries, n=205 ECs.

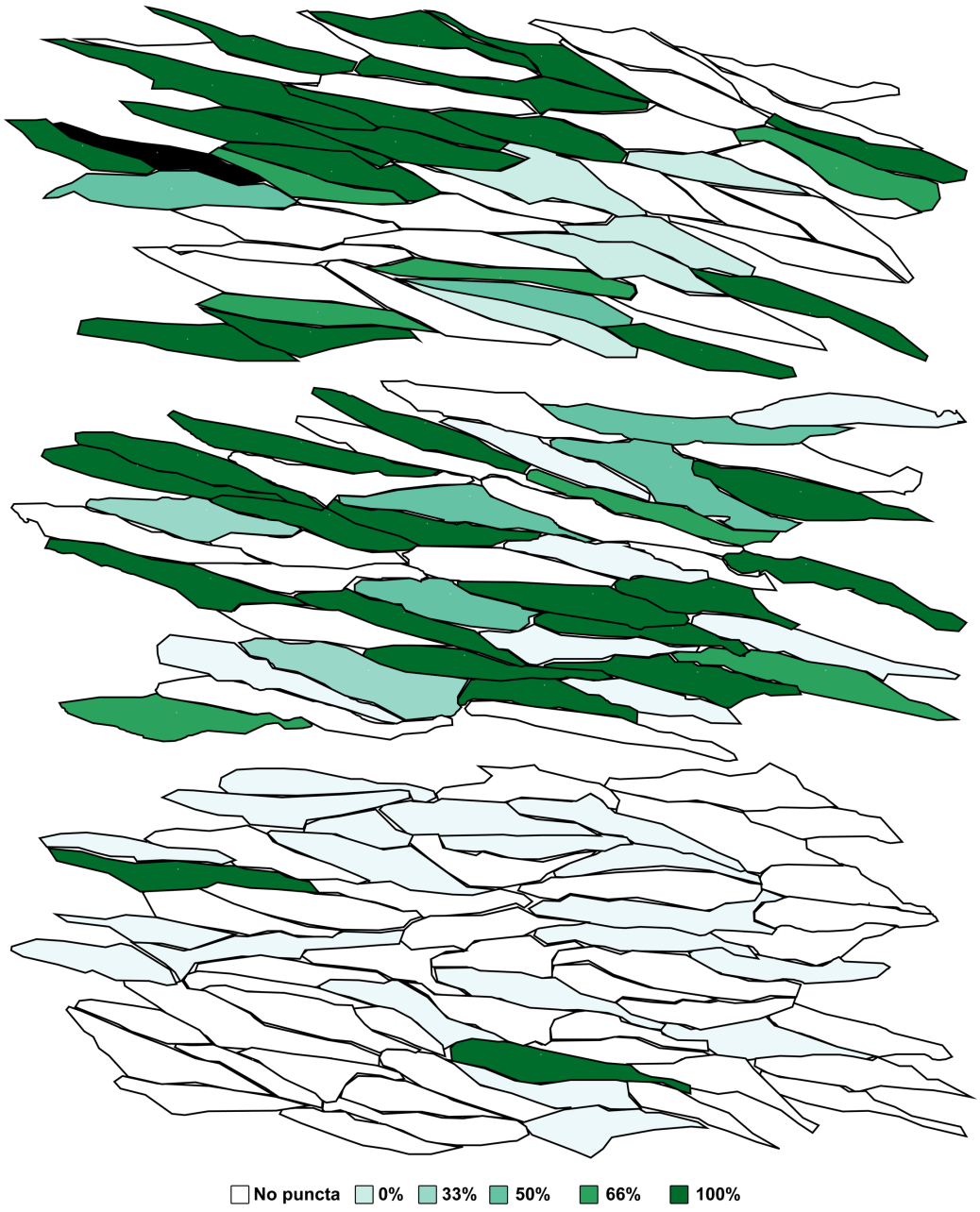

Figure 36. Percent PS-MEJ localized within 1μm of interendothelial junctions in first order mesenteric arteries prepared *en face*. Color-coded EC maps to visualize of PS-MEJ localization with respect to interendothelial junctions in first order mesenteric arteries. N=3 mice, n=3 arteries, n=155 ECs.

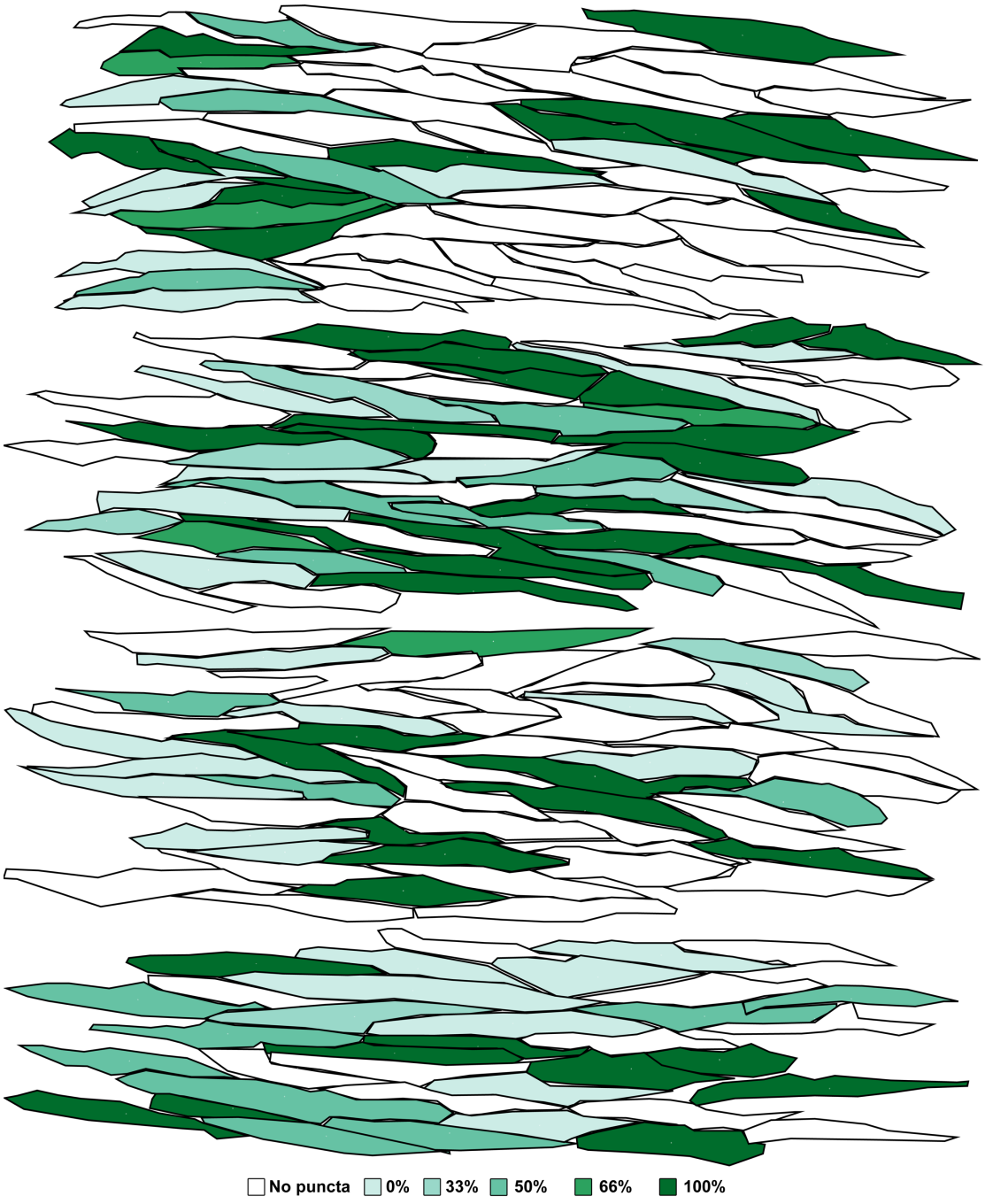

Figure 37. Percent PS-MEJ localized within 1μm of interendothelial junctions in third order mesenteric arteries prepared *en face*. Color-coded EC maps to visualize of PS-MEJ localization with respect to interendothelial junctions in third order mesenteric arteries. N=4 mice, n=4 arteries, n=205 ECs.

Table 4. Summary of en face stitch data for first and third order mesenteric arteries.

	1st order	3rd order	Units	Figures
HIEL per EC	5	9	HIEL per EC	Fig. 2
EC Area	535.77	537.10	μm^2	Fig. 8
Arterial Circumference	575.98	298.63	μm	Fig. 3, 21
HIEL per area	7.06	13.68	HIEL per $1000\mu m^2$	Fig. 3, 21
HIEL radius	1.09	1.06	μm	Fig. 3, 8, 21
HIEL vs. HIEL on border	0.838	0.839	R value	Fig. 9
HIEL vs. EC Area	0.253	0.601	R value	Fig.1, 3, 10
HIEL size vs. % on border	0.0876	0.176	R value	Fig. 11
HIEL size vs. EC Area	0.133	0.097	R value	Fig. 12
HIEL on border vs. EC Area	0.107	0.415	R value	Fig.13
PS-MEJ on border vs. MEJ	0.021	0.104	R value	Fig. 26

PS-MEJ on border vs. MEJ on border	0.041	0.318	R value	Fig. 27
PS-MEJ on border vs. EC Area	0.188	0.032	R value	Fig. 28
MEJ radius vs. PS-MEJ	0.306	0.074	R value	Fig. 29
%PS-MEJ vs. EC Area	0.171	0.329	R value	Fig. 30
PS-MEJ vs. EC Area	0.185	0.123	R value	Fig. 31

Part II: Proposed function of the PS-MEJ

PS localizes with Kir2.1 at the MEJ

Next, we sought to determine what proteins were localizing to the PS-MEJ subpopulation. Due to the function of caveolin-1 (Cav1) in regulating lipid environment, we hypothesized an enrichment of Cav1 protein specifically within PS-MEJs. *En face* staining reveals that while there is some potential overlap with Cav1 and PS (**Figure 38**), the Cav1 staining is ubiquitous throughout the endothelium and there are appear to be just as many MEJ containing PS or Cav1 alone as there are that contains both (n=1). Thus, any overlap between PS and Cav1 may be due to random localization. We therefore concluded that Cav1 does not contribute to the defining features and specificity of the PS-MEJ subpopulation.

Because it well known that lipid interactions with ion channels regulate channel activity (e.g.,(100, 102, 135, 202)), we wanted to investigate if PS could have a similar function. Recent *in silico* data suggests PS has a binding site on Kir2.1 (102), an important potassium channel involved in vasodilation.(21) This *in silico* study also demonstrated that PS can access and bind the PIP_2 binding site, a well-known activator of Kir2.1 channel activity (135, 202). Using *en face* IHC, we observed 83.33% of Kir2.1-MEJ puncta also contained PS (**Figure 39**). We verified Kir2.1 antibody specificity by transfecting HEK cells with a Kir2.1 plasmid (**Figure 41**). In contrast, Cx40, a component of gap junction formation at the MEJ (e.g.,(207)) localized with PS just 14.64% of the time. PS also did not localize with

Cx43 (**Figure 40**) (antibody confirmed in **Figure 42**). Thus, Kir2.1 is highly enriched in PS-MEJs, whereas Cx40 is segregated to non-PS MEJs.

The functional implication of the PS-Kir2.1 MEJ

The strong co-localization of Kir2.1 and PS at MEJs, with *in silico* data hypothesizing a binding site (102), led us to hypothesize that PS may regulate Kir2.1 function. We tested this by performing experiments on pressurized third order mesenteric arteries from adult C57Bl6 mice, and performing dose-response curves with NS309, a potent dilator that can activate Kir2.1(21). We observed a reduced dilatory capacity to NS309 in the presence of known Kir2.1 inhibitors BaCl (208) at 100μM (**Figure 43A**) and ML-133 at 3.6μM (**Figure 43B**). Next, we applied exogenous PS at 10μM to the arteries and observed a similar reduction in NS309-mediated vasodilation (**Figure 43C**), indicating that an enrichment of PS could have an inhibitory effect on Kir2.1 activity, in contrast to previous observations of PS supplementing channel activity. (104, 105) We confirmed that in this experimental setup PS could get to the MEJ (**Figure 44**). Importantly, the known K_{ir}2.1 inhibitors and PS did not influence smooth muscle function (**Figure 43D-F**; except for BaCl significantly inhibiting KCl constriction, likely due to off-target effects).

NS309 also activates IK_{Ca}, a potassium channel that is crucial for EDH-based vasodilation.(10, 21) Interestingly, application of exogenous PS to intact arteries inhibits vasodilation at higher NS309 doses compared to the Kir2.1-specific inhibitors, indicating that PS may also be inhibiting the activation of IK_{Ca}

channels at MEJs. We checked for co-localization of PS and IK_{Ca} at MEJs in the *en face* view (**Figure 45**), but the two were spatially separated to different MEJs (n=1). This initial data indicates that in the intact artery PS does not colocalize with IK_{Ca} to regulate its function, but that the addition of exogenous PS can block potassium flux in an *ex vivo* system.

The microscopy and functional data however still indicate that PS and Kir2.1 are localizing to the MEJs and there is an inhibition of Kir2.1 dilation upon exogenous PS application. We next sought to determine how PS was inhibiting Kir2.1 activity. There is strong evidence for PIP_2 mediated dilation of Kir2.1 in cerebral arteries (100). We sought to test the effect of PS on PIP_2-mediated dilation on arteries constricted to myogenic tone (**Figure 46C**). We also observed a consistent dilation to 10μM PIP_2 in pressurized third order mesenteric arteries (**Figure 46D**). Based on recent evidence that PS may compete for the PIP_2 binding site (102) and our data in **Figure 43**, we hypothesized that PS would block PIP_2-mediated vasodilation in these arteries. Indeed, we found that when we preincubated the arteries with 10μM exogenous PS for 30 minutes prior to adding PIP_2, the dilation was significantly decreased (**Figure 46D-E**), and the PIP_2 dilation was preserved when pre-treating the artery with PS vehicle alone (**Figure 46D**). The PIP_2 dilation was also blocked by well-described Kir2.1 inhibitors BaCl and ML-133, and the addition of PS alone did not result alter arterial diameter (**Figure 46D-E**). The residual dilation that occurs with a PS preincubation occurs at the same time as PIP_2 alone, indicating that some PIP_2 may still be able to compete for its binding site (**Figure 46F)**, although to a significantly lower extent (**Figure**

46D). Following a washout period at the end of the experiment, arteries were evaluated for EC health via dilation to 1μM NS309 (**Figure 46G**) and constriction to 30mM KCl (**Figure 46H**) in order to ensure measured differences in PIP_2 dilation were not due to arteries of compromised function. The sum of these results indicate that PS localizes to selective MEJs to regulate Kir2.1 function and subsequent vasodilation.

Since PS is blocking PIP_2-mediated vasodilation, we wanted to determine if PIP_2 was also concentrated to MEJs. Lipid mass spectrometry on in vitro indicates that diacylglycerol (DAG), a byproduct of phospholipase C cleavage of PIP_2, was detected and enriched within MEJs, but PIP_2 was not detected. (24) Using an antibody for PIP2, we saw that while there were punctate in the endothelium, the punctate did not overlap with the MEJ (**Figure 47**). Together with DAG enrichment at the MEJ, this suggests that PIP_2 at MEJs is rapidly cleaved by PLC to produce second messengers and activate downstream signaling pathways. Any remaining PIP_2 at the MEJ is likely prevented from increasing Kir2.1 activation due to the enrichment of PS, such that Kir2.1 mediated vasodilation does not have large fluctuations at homeostasis.

The MEJ is necessary for facilitating the PS-Kir2.1 interaction

Next, we sought to determine if the MEJ itself was the key driver in PS-Kir2.1 organization. To do this, we took advantage of floxed elastin mouse ($Eln^{fl/fl}$) on an endothelial cell-specific Cre (Cdh5-Cre) that had previously been shown to lack IEL in resistance arteries (209), and by extension possibly MEJs. These mice

had the correct elastin deletion and loss of IEL in resistance arteries (**Figure 48A-C**; **Figure 49A-C**) but not large arteries (**Figure 49D-G**). The disruption of IEL was also evident in the *en face* view with a 56.26% reduction in hydrazide area and the loss of observable HIEL (**Figure 48D-F**). Despite normal tight junction morphology (**Figure 48E**), the pattern of PS localization in endothelium is drastically changed, where it covers less surface area (**Figure 48I**), does not accumulate into large puncta (**Figure 48J**), and has decreased pixel intensity compared to controls (**Figure 48L-M**).

Despite this drastic change in PS and HIEL, the protein expression and function of $K_{ir}2.1$ as assessed by NS309-mediated dilation was unchanged in $Eln^{fl/fl}/Cre^{+}$ mice (**Figure 50A-B**). Given these two results, if the lack of PS organized at MEJs were important for Kir2.1-mediated dilation, application of PIP_2 would have increased dilation in $Eln^{fl/fl}/Cre^{+}$ arteries. $Eln^{fl/fl}/Cre^{-}$ arteries were used at 60mmHg based on their myogenic tone (**Figures 50C and 51**). This dilation was not different compared to arteries from C57BL6 mice at 60mmHg (**Figure 50C**). $Eln^{fl/fl}/Cre^{+}$ arteries exhibited a significant increase in PIP_2-mediated vasodilation which was inhibited after adding 10μM PS or 3.6μM ML-133 to the experimental setup (**Figure 50C**). Interestingly, arteries from $Eln^{fl/fl}/Cre^{+}$ had an increased time to maximum change in diameter (**Figure 50D-E**) compared to $Eln^{fl/fl}/Cre^{-}$ or C67Bl6 arteries, which is reflective of a continued dilation in $Eln^{fl/fl}/Cre^{+}$ arteries compared to a transient dilation in control experiments. A continued dilation coincides with the idea that PS is not spatially oriented to negatively regulate the PIP_2-mediated activation of Kir2.1 in EC-Eln KO arteries, thus resulting in an uncontrolled dilation.

After a washout period, EC and SMC health were evaluated with 1μM NS309 and 30mM KCl, respectively, to ensure differences in PIP_2 dilation were not due to compromised arterial health (**Figure 50F-G**).

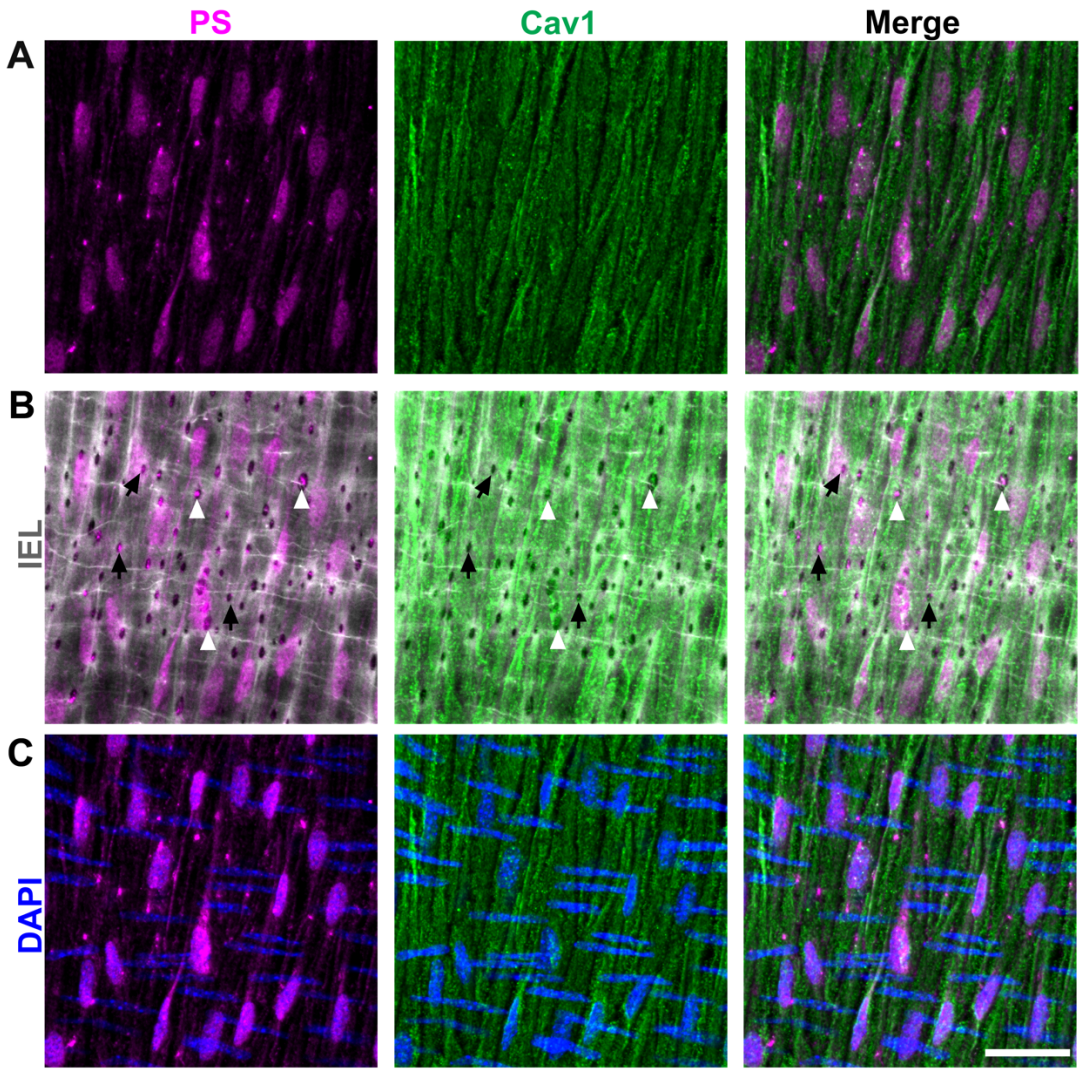

Figure 38. *En face* immunohistochemistry with PS and Cav1. Representative *en face* images from third order mesenteric arteries. (**A**) Panel demonstrating PS (magenta) and Cav1 (green) staining in separate channels or merged together. (**B**) PS, Cav1, and merge staining overlayed on the IEL (grey) detected via Alexa Fluor linked hydrazide. White arrowheads indicate colocalization of PS and Cav1 to same HIEL, while black arrows indicate localization of either PS or Cav1 to HIEL, but not both. (**C**) PS, Cav1, or merge overlayed with nuclei (blue), detected via DAPI. Scale bar is 30μm.

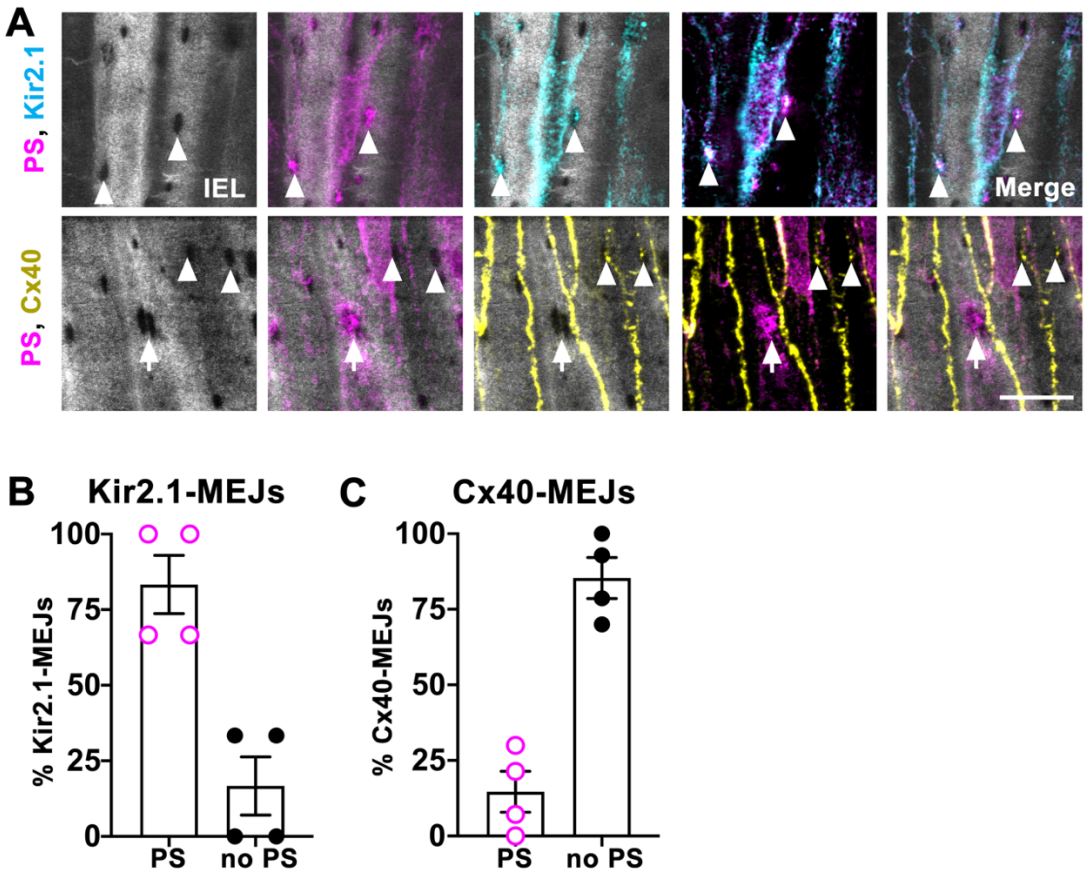

Figure 39. *En face* immunohistochemistry demonstrating specific co-localization of PS and Kir2.1 at MEJ. (**A**) *En face* images of third order mesenteric arteries with IEL (grey) detected via hydrazide, PS (magenta), $K_{ir}2.1$ (cyan), and Cx40 (yellow). (**B**) Analysis from in-house Matlab program that detects the incidence of PS and $K_{ir}2.1$ or (**C**) PS and Cx40 puncta at MEJ in *en face* images. Arrowhead indicates Kir2.1 and PS co-localization or only Cx40 localization to MEJ. Arrow indicates only PS localization to MEJ. N=4 mice, n=4 arteries per group.

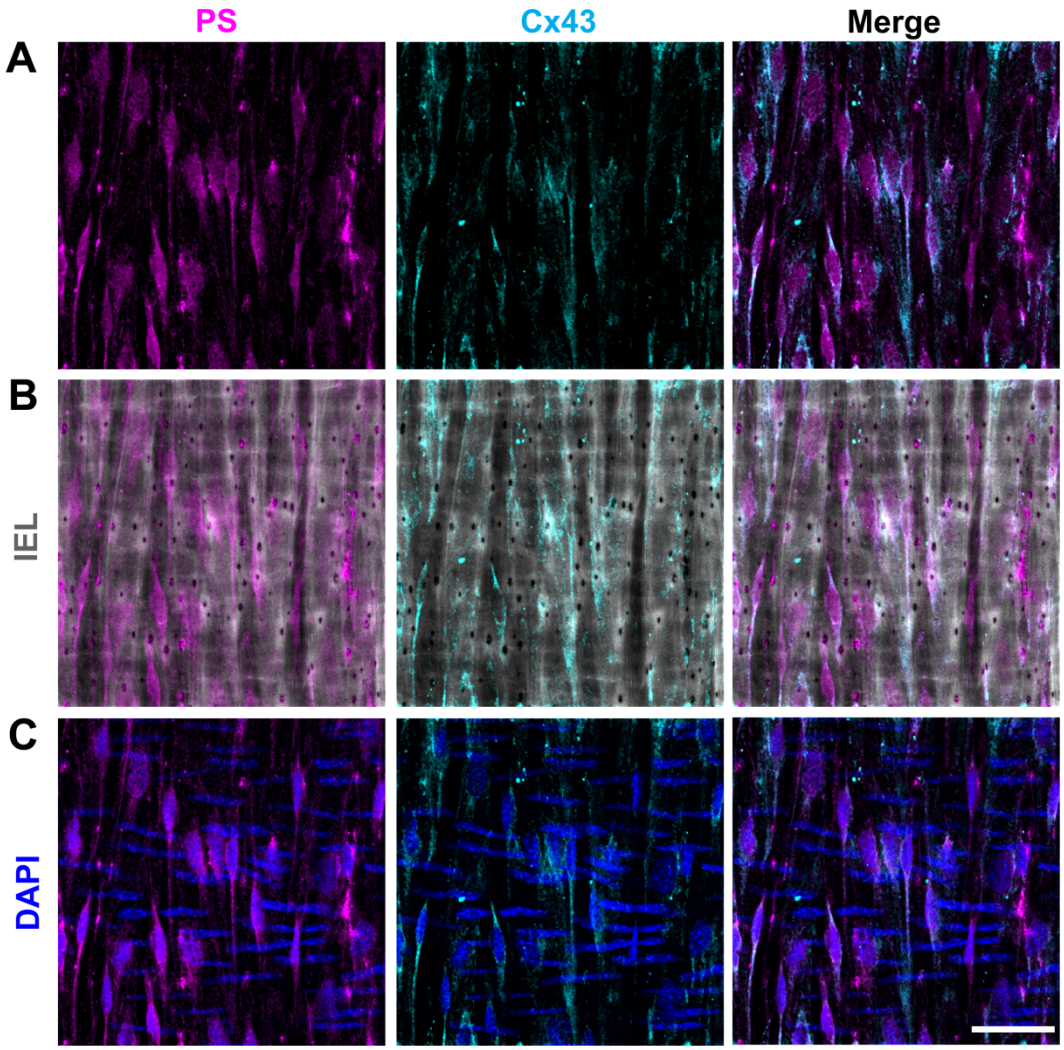

Figure 40. *En face* immunohistochemistry with PS and Cx43. (**A**) *En face* images of third order mesenteric arteries, showing PS (magenta), Cx43 (cyan), or merged. The same stains are also shown merged with (**B**) IEL (grey) detected via hydrazide, or (**C**) nuclei (blue) detected via DAPI. N=1 mouse, n=1 artery, n=1 image.

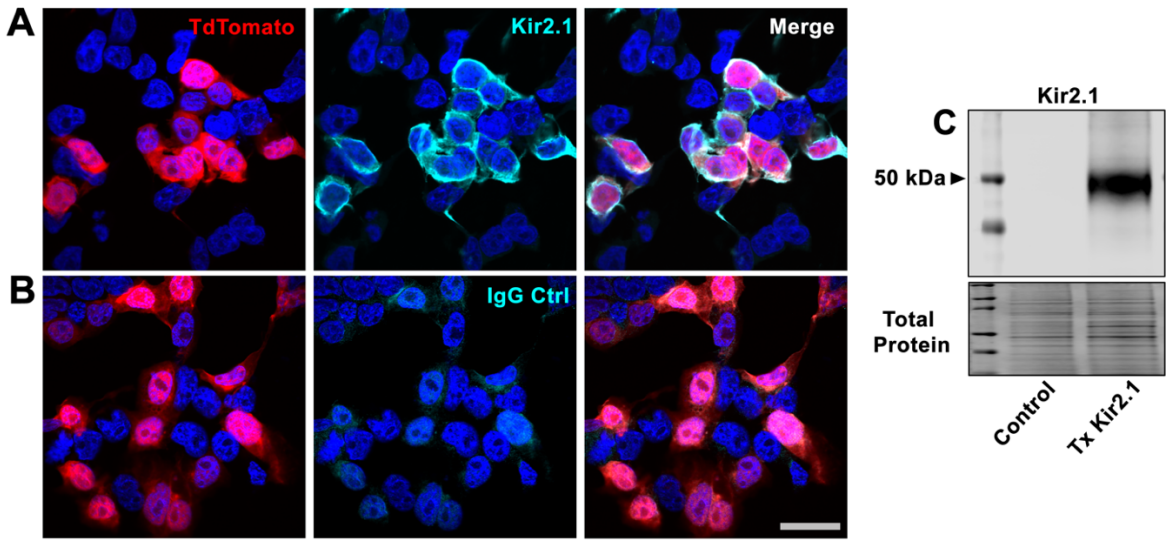

Figure 41. Validation of K_{ir}2.1 antibody. (**A**) HEK293T cells transfected with Kir2.1-T2A-tdTomato plasmid (red) and co-stained with PS antibody or (**B**) IgG control. Nuclei (blue) are detected via DAPI. Scale bar is 30μm. (**C**) Western blot detection of Kir2.1 protein in HEK293T cells that were untreated or transfected with Kir2.1-T2A-tdTomato plasmid. Total protein was used as a loading control.

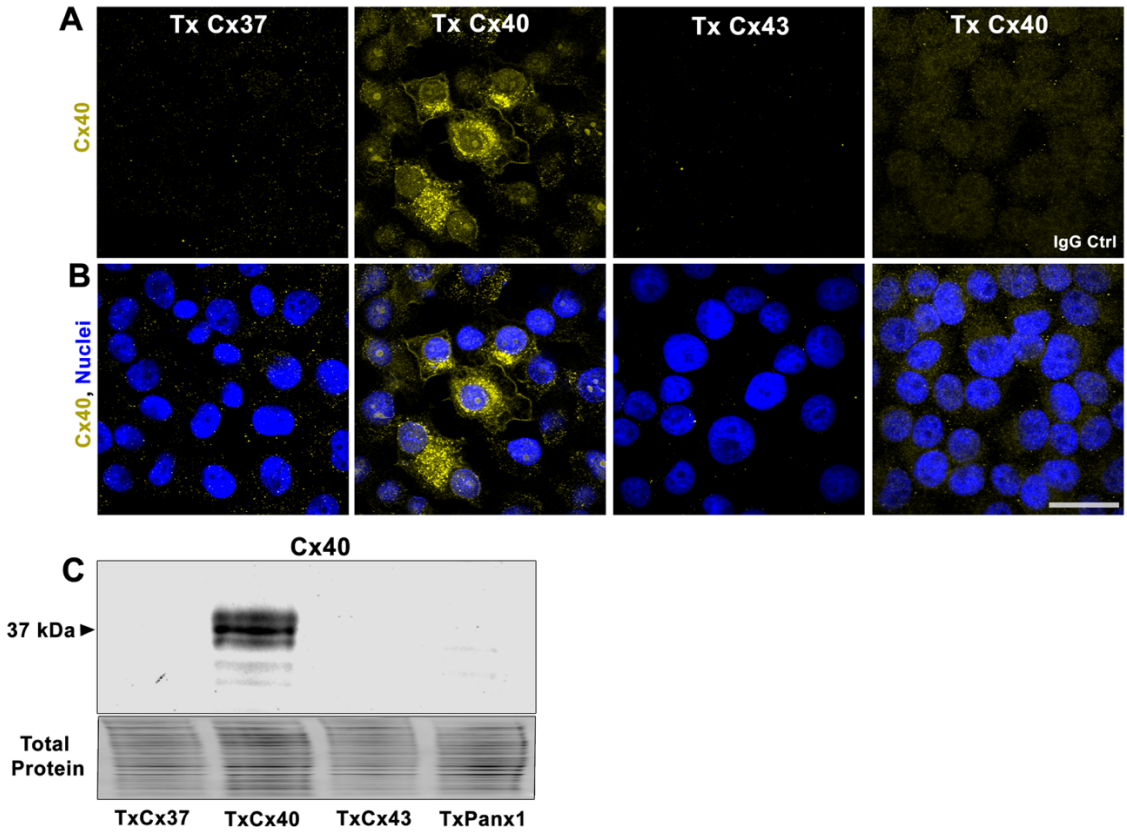

Figure 42. Validation of Cx40 antibody. (**A**) HeLa cells transfected with transfected with connexin plasmids (yellow): connexin 37 (Tx Cx37), connexin 40 (Tx Cx40), and connexin 43 (Tx Cx43). Cells were then stained using a Cx40 antibody or IgG control to evaluate antibody specificity for the isoform. Nuclei (blue) are detected via DAPI. Scale bar is 30μm. (**C**) Western blot detection of Cx40 protein in HeLa cells that were transfected with plasmids for Cx37, Cx40, Cx43, and Panx1. Total protein was used as a loading control.

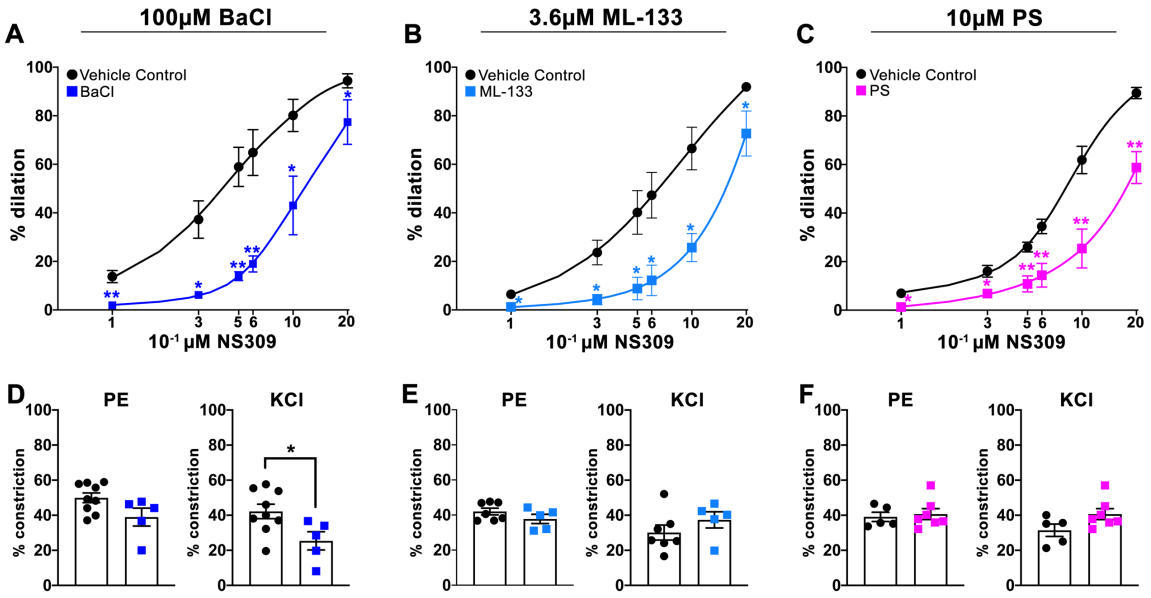

Figure 43. Exogenous PS blocks Kir2.1-mediated vasodilation. Dose response curves to NS309 on third order mesenteric arteries in the presence of (**A**) 100μm BaCl (**B**) 3.6μm ML-133, or (**C**) 10μm PS compared to vehicle controls of water, DMSO, and ethanol, respectively. (**D-F**) Percent constriction to PE or KCl in the presence of each $K_{ir}2.1$ inhibitor.

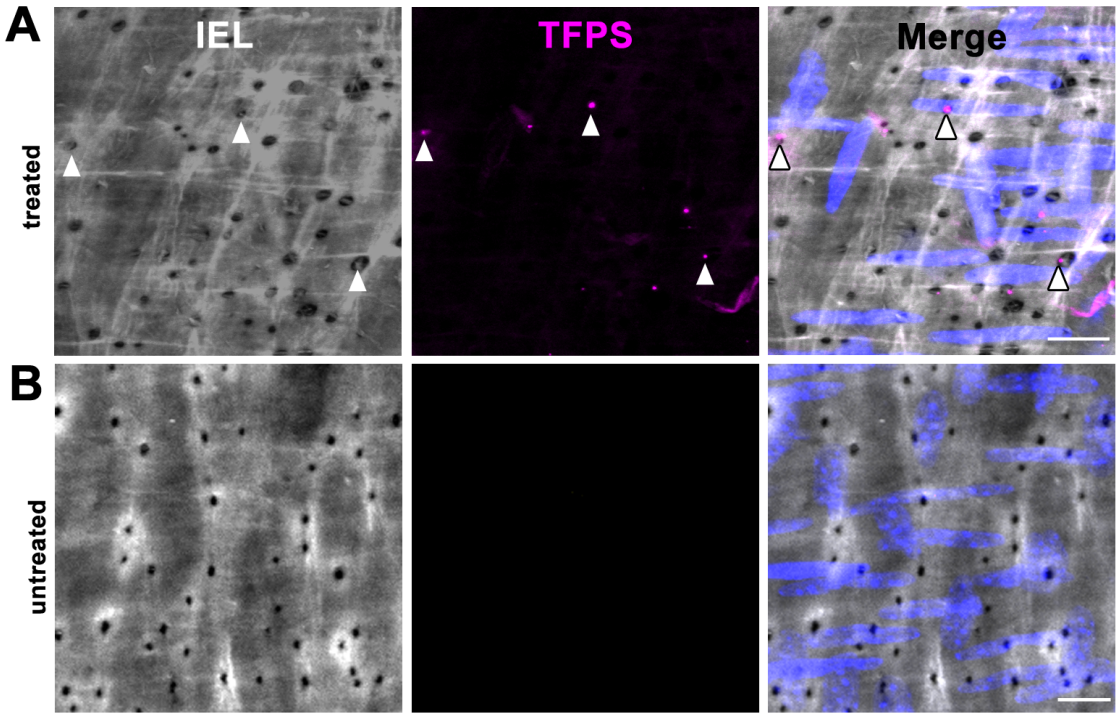

Figure 44. Exogenous application of TopFluor-PS localizes to the MEJ in intact third order mesenteric arteries. Live third order mesenteric arteries prepared *en face* after treatment with (**A**) 10μM TopFluor-PS in the bath solution of a pressure myography setup or (**B**) without treatment. Nuclei (blue) are detected via DAPI and IEL (grey) is detected via Alexa Fluor linked hydrazide. Arrowheads indicate TopFluor-PS localization to MEJ. Scale bars are 10μm.

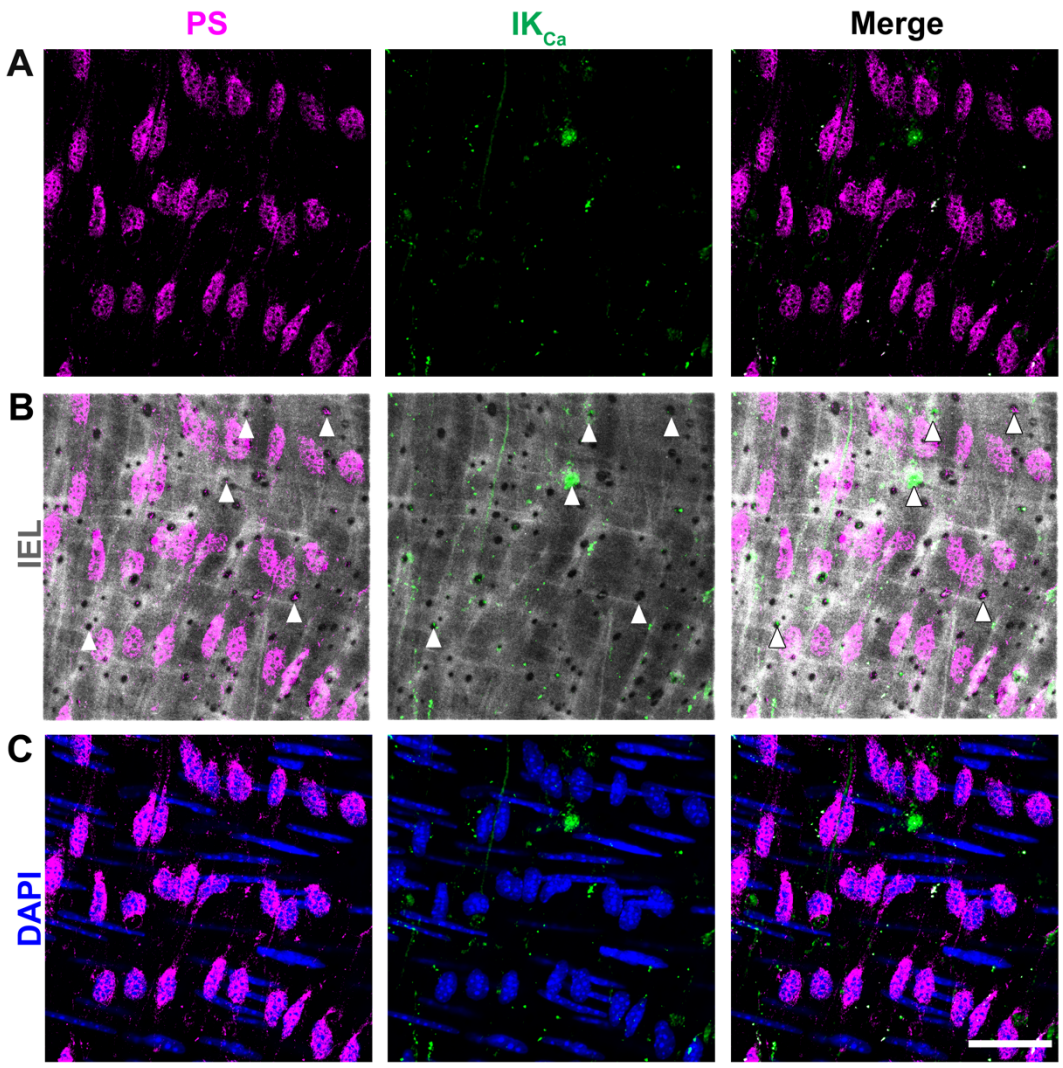

Figure 45. *En face* immunohistochemistry with PS and IK$_{Ca}$. Representative *en face* images from third order mesenteric arteries. (**A**) Panel demonstrating PS (magenta) and IK$_{Ca}$ (green) staining in separate channels. (**B**) PS, IK$_{Ca}$, and merge staining overlayed on the IEL (grey) detected via Alexa Fluor linked hydrazide. White arrowheads indicate spatial separation of PS and IK$_{Ca}$ to different MEJs (**C**) PS, IK$_{Ca}$, or merge overlayed with nuclei (blue), detected via DAPI. Scale bar is 30μm.

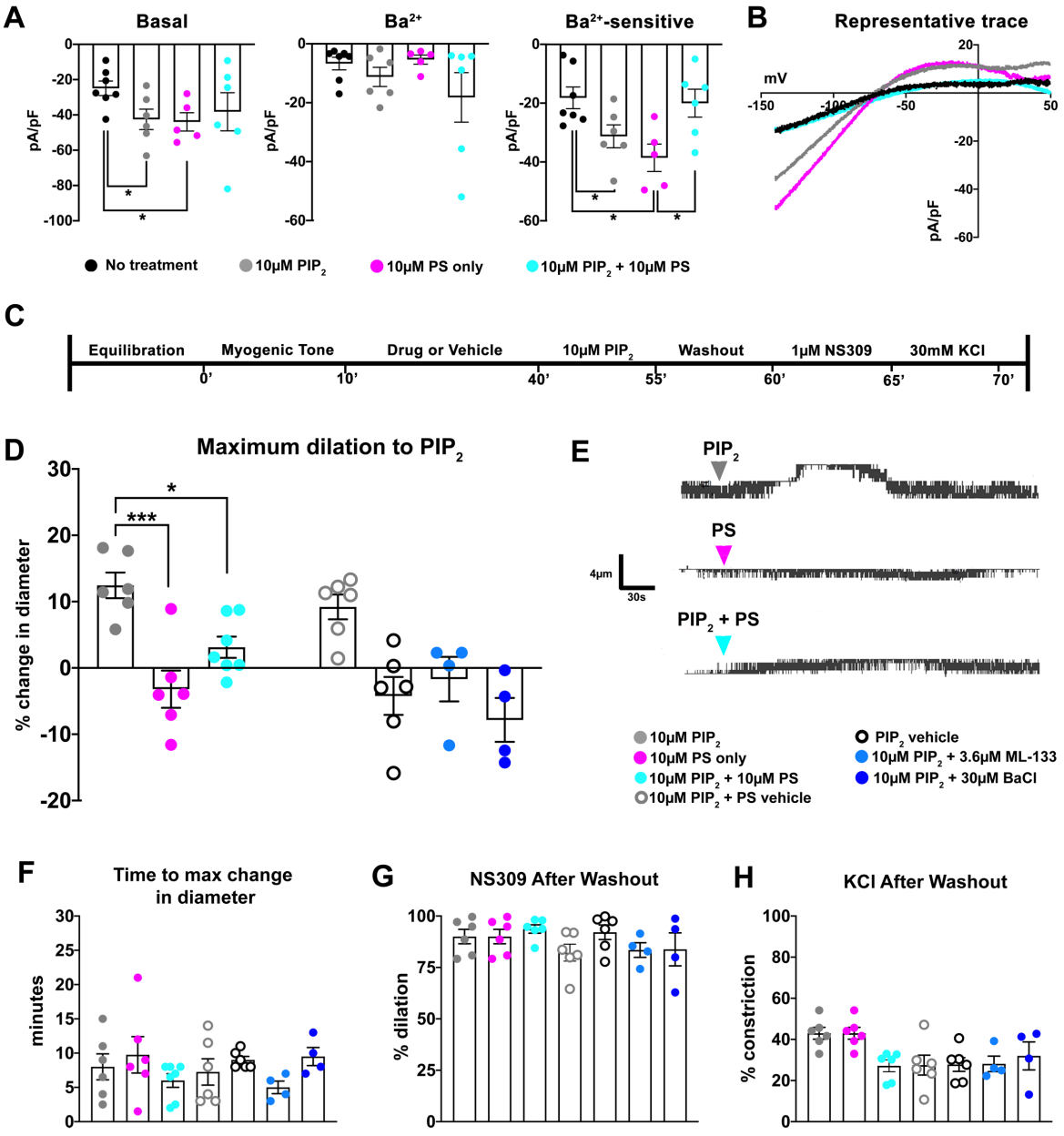

Figure 46. PIP_2 dilation in intact arteries is blocked by Kir2.1 inhibitors and PS. (**A**) Average whole cell Kir2.1 currents at -140mV in transfected HEK cells at baseline and with 100μM Ba^{2+}. Ba^{2+}-sensitive currents were calculated by subtracting Ba^{2+} current from basal current. (**B**) Representative traces of Ba^{2+}-sensitive currents. For all graphs: black is baseline, grey is treatment with 10μM PIP_2, magenta is treatment with 10μM PS, and cyan is treatment with 10μM PIP_2

+ 10μM PS. N=2-3 independent transfections and n=5-7 cells per group. Student's t-test. * indicates $p<0.05$. (**C**) Experimental timeline to assess PIP_2 dilation in intact arteries. Arteries are equilibrated to temperature and pressure until the development of myogenic tone. After 10 minutes of plateaued diameter, the drug or vehicle treatment was applied to the system for 30 minutes. Next, 10μm PIP_2 was applied to the system for 15 minutes. The maximum change in diameter within this period was recorded and used for analysis. Following a 5-minute washout, arterial function was assessed via 1μm NS309 and 30mM KCl. (**D**) Maximum change in diameter in each treatment group. Changes in diameter for PS were taken from the same experiments as 10μm PIP_2 + 10μm PS groups, where the maximum change in diameter was recorded within the 30-minute incubation prior to PIP_2 treatment. Student's t-test, where * $p<0.05$ and *** $p<0.001$. (**E**) Legend for the different groups where (**i**) 10μm PIP_2 is black circles, (**ii**) 10μm PS is magenta closed circles, (**iii**) 10μm PIP_2 + 10μm PS is magenta open circles, (**iv**) 10μm PIP_2 + PS vehicle is light grey circles, (**v**) 10μm PIP_2 + 10μm ML-133 is light blue circles, (**vi**) 10μm PIP_2 + 30μm BaCl is dark blue circles, and (**vii**) PIP_2 vehicle only is black open circles. Representative traces of inner diameter from pressure myography experiments demonstrating the effects of 10μm PIP_2, 10μm PS, or 10μm PIP_2 + 10μm PS on arterial diameter. (**F**) The timepoint at which maximum change in diameter is achieved for each group. (**G**) The dilation to 1μm NS309 following a 5-minute washout period to assess endothelial function in each experiment. (**H**) The constriction to 30mM KCl to assess smooth muscle cell function in each experiment. N=4-5 mice and n=4-7 arteries per group.

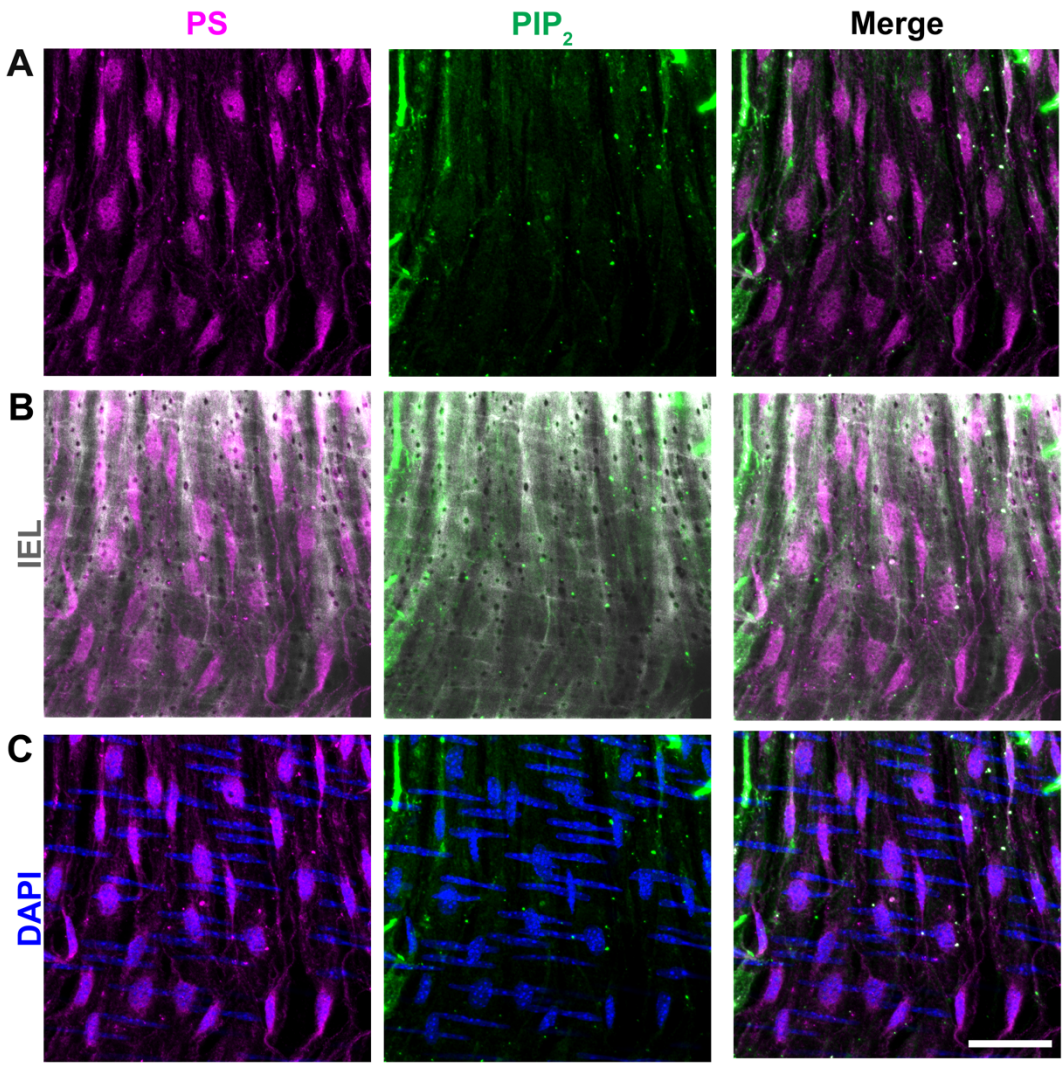

Figure 47. *En face* immunohistochemistry with PS and PIP_2. Representative *en face* images from third order mesenteric arteries. (**A**) Panel demonstrating PS (magenta) and PIP_2 (green) staining in separate channels or merged together. (**B**) PS, PIP_2, and merge staining overlayed on the IEL (grey) detected via Alexa Fluor linked hydrazide. (**C**) PS, PIP_2, or merge overlayed with nuclei (blue), detected via DAPI. Scale bar is 30μm.

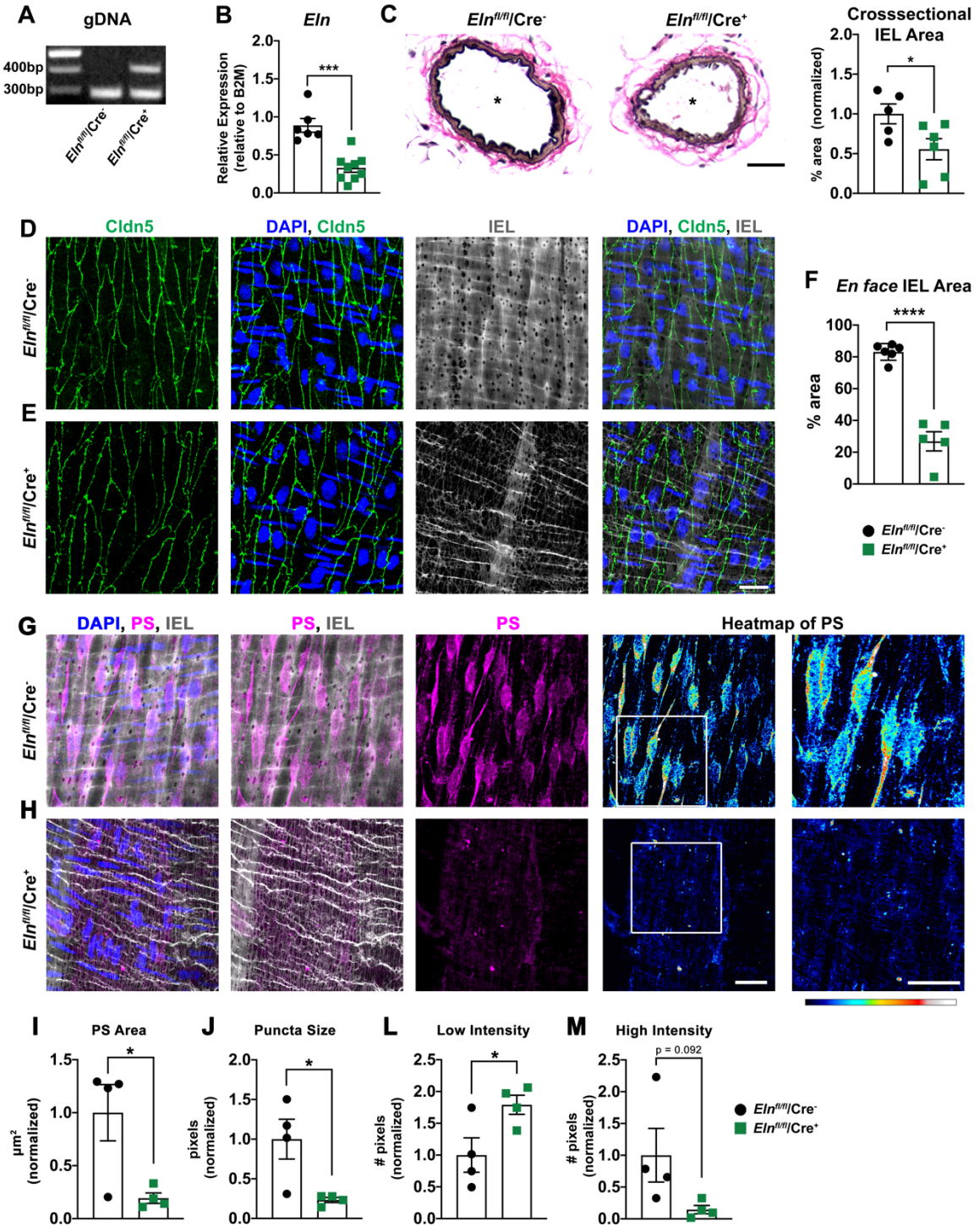

Figure 48. Eln$^{fl/fl}$/Cre^{+} mice have disrupted PS localization in endothelium. (**A**) Genomic DNA isolated from endothelial-rich lung tissue demonstrating the expected excision band of elastin in Eln$^{fl/fl}$/Cre^{+} tissue at 410bp. (**B**) qPCR on

mesenteric vasculature to assess the mRNA levels of *Eln* in both $Eln^{fl/fl}/Cre^{-}$ and $Eln^{fl/fl}/Cre^{+}$ tissue. (**C**) Cross-sections of third order mesenteric arteries that are stained with Verhoeff elastic stain (black) and counterstained with van Gieson (pink). * indicates lumen. Scale bar is 30μm. Percent area that is positive for elastin is quantified in the graph on the right. Student's t-test and * indicates $p < 0.05$. (**D**) *En face* immunohistochemistry on $Eln^{fl/fl}/Cre^{-}$ and (**E**) $Eln^{fl/fl}/Cre^{+}$ third order mesenteric arteries where interendothelial junctions (green) are detected via claudin-5, nuclei (blue) are detected via DAPI, and IEL (grey) is detected via and Alexa Fluor 488-linked hydrazide. Scale bar is 30μm. (**F**) Quantification of IEL area in *en face* views, expressed as a percentage of total image area. N=5 mice, n=6 arteries. Student's t-test and **** indicates $p < 0.0001$. (**G**) *En face* immunohistochemistry on $Eln^{fl/fl}/Cre^{-}$ and (**H**) $Eln^{fl/fl}/Cre^{+}$ third order mesenteric arteries where PS (magenta), nuclei (blue) are detected via DAPI, IEL (grey) is detected via Alexa Fluor 488-linked hydrazide. PS heatmaps were generated from Royal Lookup Tables in ImageJ, where low intensity signal is in cool tones (blue to aqua) and high intensity signal is warm tones (yellow to white). The white box on the heatmap indicates the zoomed in area shown on the right. Scale bars are 10μm. (**I**) Quantification of PS area, (**J**) puncta size, (**L**) low intensity pixels, and (**M**) high intensity pixels in PS *en face* images comparing $Eln^{fl/fl}/Cre^{-}$ and $Eln^{fl/fl}/Cre^{+}$ third order mesenteric arteries. N=3-4 mice, and n=4-5 arteries per group. Student's t-test and * indicates $p < 0.05$.

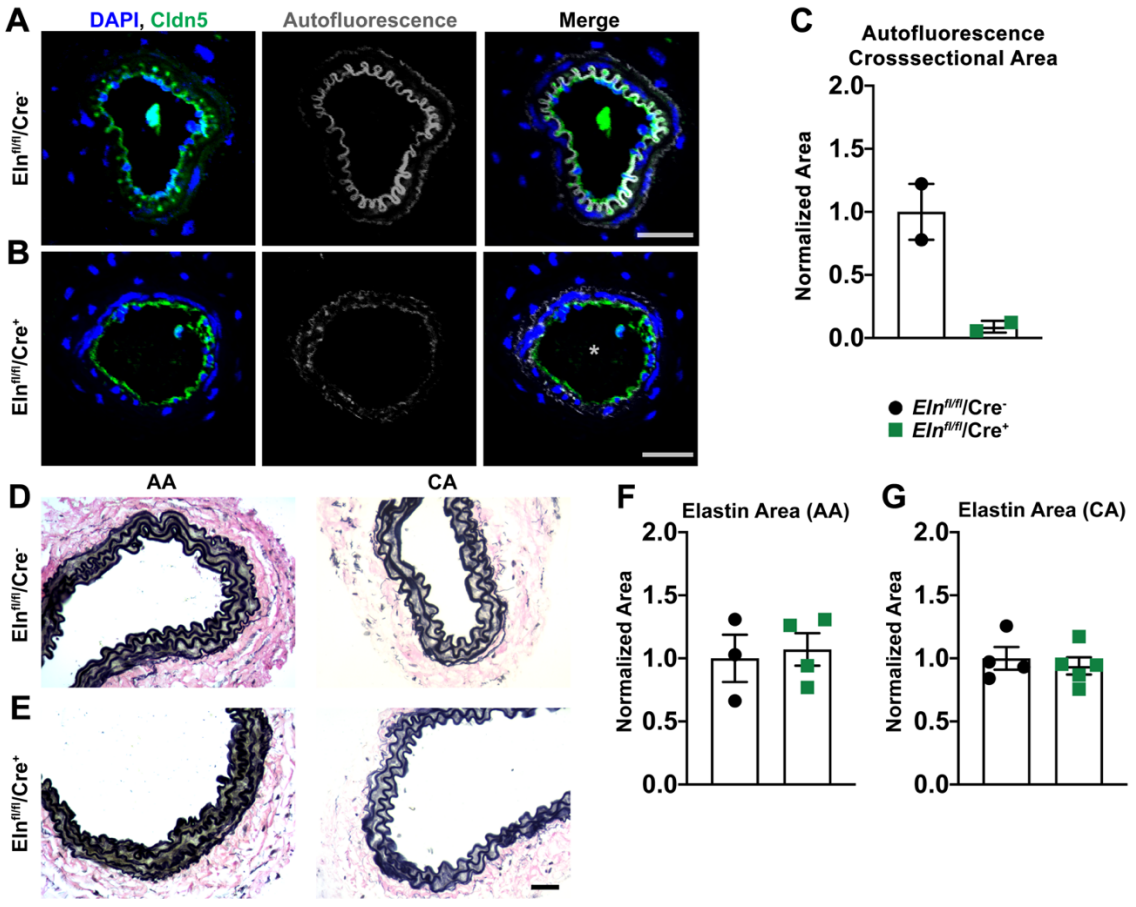

Figure 49. EC-specific knockout of elastin disrupts IEL in resistance arteries and not large conduit arteries. Representative images of cross-sections from third order mesenteric arteries taken from (**A**) $Eln^{fl/fl}/Cre^{-}$ and (**B**) $Eln^{fl/fl}/Cre^{+}$ mice where nuclei (blue) are detected via DAPI, IEL (grey) is detected via autofluorescence, and interendothelial junctions (green) are detected via claudin-5. Scale bar is 30μm. (**C**) Quantification of cross-sectional IEL area detected via autofluorescence. Representative images of cross-sections from the abdominal aorta (AA) and carotid artery (CA) of (**D**) $Eln^{fl/fl}/Cre^{-}$ and (**E**) $Eln^{fl/fl}/Cre^{+}$ mice. Scale bar is 30μm. Quantification of Verhoeff stain in (**F**) AA and (**G**) CA.

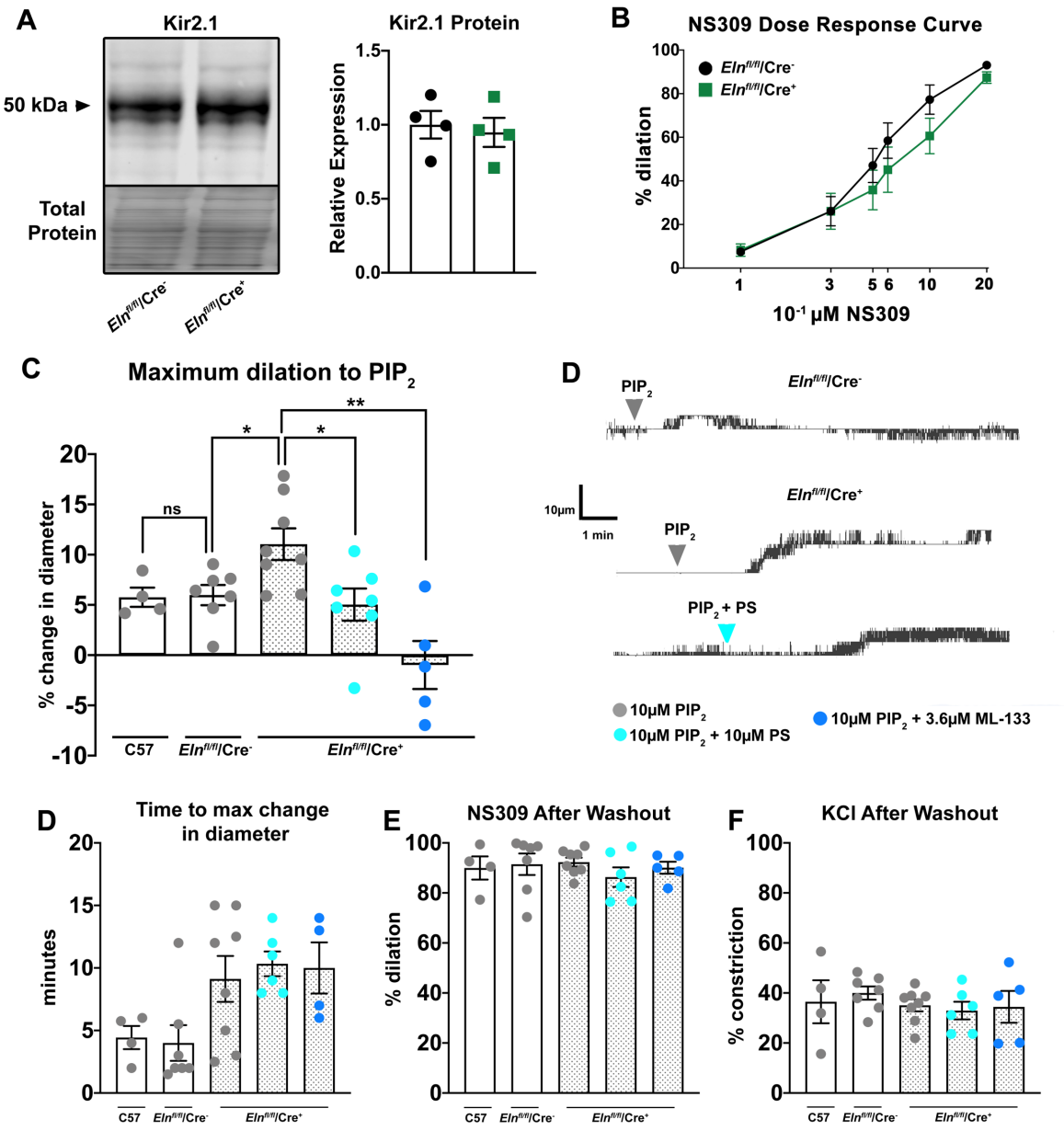

Figure 50. Eln$^{fl/fl}$/Cre^{+} mice have increased dilation to PIP$_2$. (**A**) Western blot on mesenteric vasculature to detect Kir2.1. Total protein was used as a loading control. Quantification was performed as a percent of total protein, then normalized with respect to control group. N=4 mice per group. (**B**) NS309 dose response curve on Eln$^{fl/fl}$/Cre^{-} and Eln$^{fl/fl}$/Cre^{+} third order mesenteric arteries. N=4 mice and n=8-11 arteries per group. (**C**) Dilation to PIP$_2$ experiments at 60mmHg. N=4-5 mice, n=4-

7 arteries per group. Student's t-test, where * indicates $p<0.05$ and ** indicates $p<0.01$. (**D**) Representative traces from pressure myography experiments demonstrating the dilation to PIP_2 in $Eln^{fl/fl}/Cre^{-}$ arteries and $Eln^{fl/fl}/Cre^{+}$ arteries with or without a 30-minute PS preincubation. (**E**) The timepoint at which maximum change in diameter is achieved for each group. (**F**) Dilation to 1μm NS309 following a 5-minute washout period to assess endothelial function in each experiment. (**G**) Constriction to 30mM KCl to assess smooth muscle cell function in each experiment.

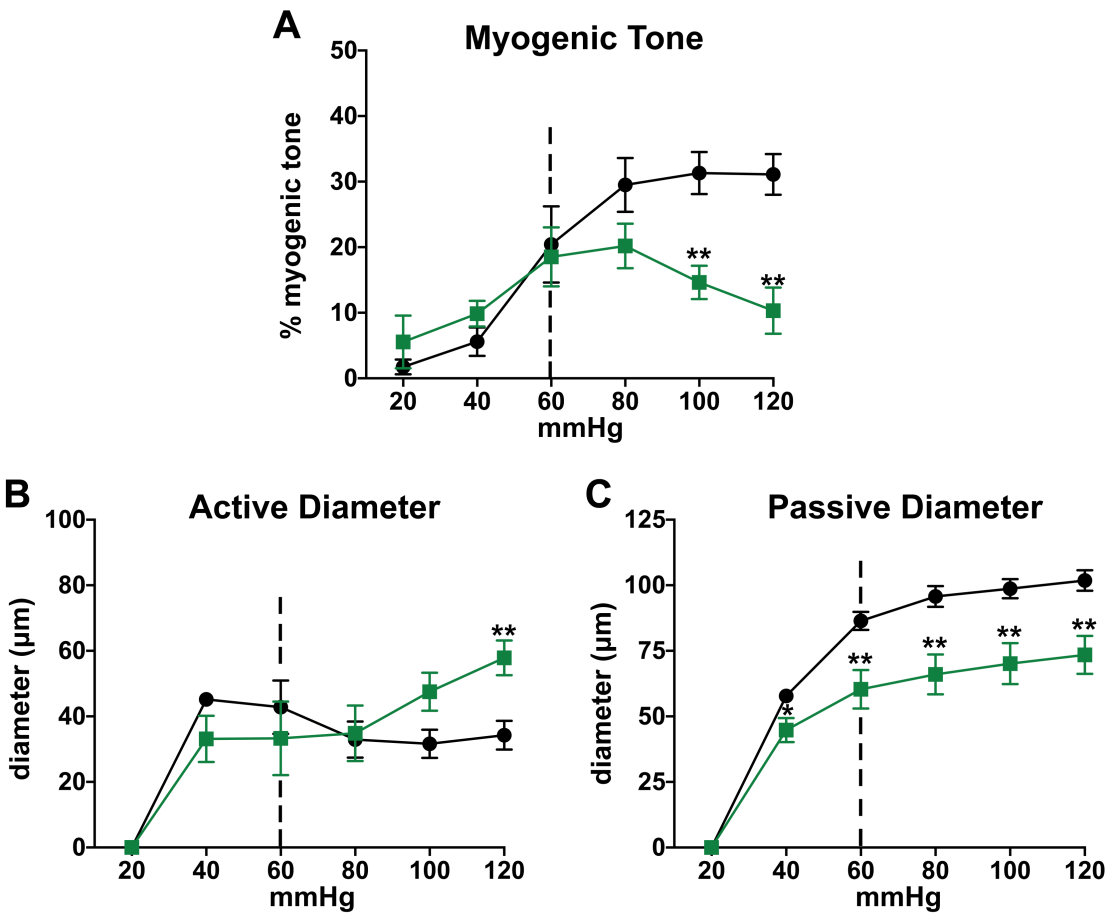

Figure 51. Determination of optimal pressure for myography experiments on EC-Eln KO mice. Pressure myography experiments on third order mesenteric arteries from $Eln^{fl/fl}/Cre^{-}$ and $Eln^{fl/fl}/Cre^{+}$ mice, where (**A**) is myogenic tone, (**B**) is the active diameter and (**C**) is the passive diameter. Dotted line indicates the optimal pressure for $Eln^{fl/fl}/Cre^{+}$ arteries. N=3 mice per group and n=4-6 arteries per group. Students t-test was performed at each pressure. * indicates $p<0.05$, and ** indicates $p<0.01$.

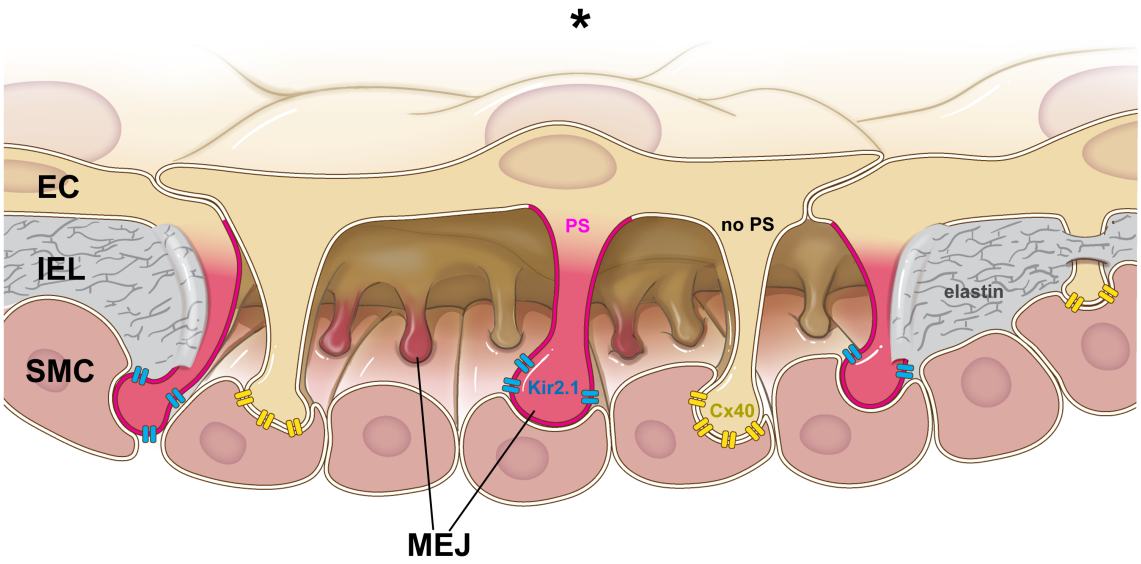

Figure 52. Heterogeneous lipid localization to MEJs results in functionally distinct subpopulations. A zoomed in look at MEJs in the arterial wall. ECs are at the top, SMCs are at the bottom, MEJs are between the two and are encased in IEL proteins such as elastin (grey). Kir2.1 channels (blue) localize to MEJs that are enriched with PS (magenta), while the gap junction protein Cx40 (yellow) localizes to MEJs that do not contain PS (beige). This demonstrates that subpopulations of MEJs exist within the artery and implies they have unique, specific functions. For clarity, the IEL is only shown at the edges of the image. * indicates lumen.

Discussion

HIEL spatial distribution in mesenteric arteries

The presence of MEJs in resistance arteries play a vital role in regulating signaling pathways to tightly control arterial diameter and thus peripheral resistance. This signaling domain is well studied and there are numerous proteins that are known to localize specifically to the MEJ, forming a specific signaling microdomain. Interestingly, we and others have demonstrated that these MEJ-localized proteins do not occupy every HIEL in *en face* views. (15, 23, 29, 38, 43, 199-201) I have demonstrated here that the localization of HIEL with respect to EC signaling domains exhibits a random spatial distribution, through analysis via an in-house Matlab program that leverages PC, NC, and RAND simulations (**Figures 1 and 3**). The in-house Matlab program considers a spatial pattern across an image and does not consider spatial orientation within individual ECs. Thus, in order to determine if there was a spatial distribution of HIEL in relation to individual ECs, we analyzed stitched confocal images that were stained for claudin-5 to detect interendothelial junctions as our method of defining individual cell borders.

Each arterial EC map does demonstrate some degree of similar ECs grouping together, although no patterns are consistent from artery to artery. For example, in the third order map of HIEL number per EC (**Figure 15, artery 4**), it is clear that ECs with a higher HIEL density are grouped together and separate from the ECs with lower HIEL density. This may also be the case when considering the results from the EC map that shows HIEL localization within ECs (**Figures 16 and**

17), which shows that ECs with >66.1% HIEL localized along the border, tend to group separately from ECs that contain HIEL in the middle of the cell.

Further, a large proportion of cells in each artery map are in the >66.1% HIEL localization category ECs (**Figures 16 and 17**). This brings up an interesting point given that Matlab analysis with respect to interendothelial junctions revealed a random localization. This is likely the case because of the large percentage range in the last category. Further, while the EC maps may offer explanations on spatial distributions of unique ECs, the in-house Matlab simulations are a more robust way of interpreting spatial localization in the endothelium because they include simulations that are repeated 1000 times per image. Thus, the conclusion from **Figures 16 and 17** should not be that HIEL tend to localize to the interendothelial junction, but should be used to evaluate if similar ECs tend to group together in the endothelium. Thus, the EC maps reveal that ECs of similar functions may group together spatially such that the endothelium can be considered as unique EC patches with heterogeneous roles, an idea that has been discussed in the literature. (210, 211)

This random distribution paired with demonstrated heterogenous protein localization to MEJs led us to ask whether or not every HIEL contained a physical cellular projection. Our TEM analysis revealed that every time an HIEL was detected, so was a cellular projection. Since the detection rate of HIEL in TEM was within the predicted range, we concluded that it is likely every HIEL contains an actual MEJ. This raises interesting questions about the heterogeneous protein

localization at the MEJ, and why segregated protein localization to unique MEJ subpopulations may benefit arterial function. (15)

Subpopulations of MEJs have distinct functions

The heterogeneous protein localization to MEJ is likely defined by the local lipid concentration rather than any unique spatial distribution throughout the endothelium (**Figures 1 and 3**). The lipids may contribute to protein trafficking or, may be colocalized with certain proteins to regulate their function. Here we have demonstrated that PS defines a functionally distinct subpopulation of MEJs where it localizes with and negatively regulates Kir2.1 through preventing PIP_2 activation, and is spatially separated from MEJs containing the gap junction protein Cx40 (**Figure 52**). It is likely that the primary function of PS-Kir2.1 MEJs is to generate vasodilatory hyperpolarization, which can be communicated to SMCs via nearby gap junction-MEJs. Segregating the generators and communicators of hyperpolarization to distinct subpopulations of MEJs (**Figure 52**) represents another mechanism of the tight regulation of resistance arterial diameter. The observation, coupled with the functional data herein, strongly suggests heterogenous MEJ populations may exist to carry out different functions, either direct heterocellular communication or to function in a vasodilatory capacity. Here we have defined a unique MEJ subpopulation, suggesting a role for PS in modulating PIP_2 activation of Kir2.1 within the artery.

Uncovering unique MEJ populations will continue to move the field forward in understanding how vasodilation is regulated in these arteries. One population

that has been described is the a-kinase anchoring protein 150 (AKAP150) localizes specifically with TRPV4 at MEJs, where AKAP150 is required for adequate activation of TRPV4 activation and vasodilation. (13) This co-localization at the MEJ is important for facilitating the EDH pathway. (97) In a separate study on rat resistance arteries, Cx37 and the IK_{Ca} colocalize in a subpopulation of MEJ, suggesting some potential for potassium channel and gap junction MEJ overlap. (15) Further spatial and functional analysis of the Cx37-IK_{Ca} would be necessary in order to fully understand the role for the co-localization, but we speculate that the Cx37-IK_{Ca} MEJ population identified in rat resistance arteries may exist in small groups of ECs and correlate with heterogenous responses of ECs to receptor agonism. (210) Interestingly, the Cx37-IK_{Ca} population is in contrast to the spatial separation of Kir2.1 and Cx40 that we demonstrate here. However, it is not surprising that there is a difference in colocalization with gap junctional MEJs between these two potassium channels because of the differences in regulation, activation, and potassium flux.

Further, it is likely that PS defines more than one MEJ subpopulation. We demonstrated that the majority of Kir2.1-MEJs also contain PS, however not every PS-MEJ contains Kir2.1. Another potential role for PS at the MEJ is to modulate IK_{Ca}. We show that addition of exogenous PS inhibits NS309-mediated dilation (**Figure 43**). In addition to inducing Kir2.1 activation, NS309 directly activates the IK_{Ca} channel that is localized to MEJs, (15, 21) where Kir2.1 activation occurs at lower doses, and IK_{Ca} activation at higher doses. (21) Our data in **Figure 43** shows that there is a larger inhibition of NS309-mediated vasodilation at the higher doses

compared to the inhibition in response to Kir2.1 specific inhibitors, implying PS may also be dampening IK_{Ca} activity. While I was not able to demonstrate a co-localization of PS and IK_{Ca} in an initial *en face* experiment (**Figure 45**), this co-stain should be repeated on more biological replicates. Lipid regulation of IK_{Ca} in endothelium, to our knowledge, is currently unexplored and our data indicates a potential role for PS regulating IK_{Ca} at the MEJ.

It is clear in our *en face* immunohistochemistry that PS localizes to the perinuclear region (**Figure 23**) suggesting localization in the endoplasmic reticulum (ER). Given the distinct subpopulation of MEJs that PS occupies, there is likely a specific mechanism of PS transport to facilitate accumulation in the MEJ. Energy driven lipid transport within a cell occurs via specific lipid transport proteins (LTP) at membrane contact sites, where two lipids are transported in opposite directions. A family of LTPs, called oxysterol-binding proteins (ORPs), have been implicated in the trafficking of PS to the plasma membrane. (175, 176, 212) It could be that the expression of an ORP in ECs drives deposition of PS to specific the MEJs. It is also well described that Kir2.1 is trafficked through the ER, and indeed, we see perinuclear staining in Kir2.1 *en face* preparations (**Figure 39**). (213, 214) Given the specific, targeted localization of Kir2.1 to PS-enriched MEJs, we speculate that PS may also function in trafficking Kir2.1 to these signaling microdomains.

Phosphatidylserine regulation of Kir2.1

Kir2.1 channel function is dependent on the presence of both PIP_2 and an anionic phospholipid. (104, 105) We have reproduced this data and shown that both PS and PIP_2 can activate the channel in an electrophysiology experiment. However, when added together, the lipids did not have an additive effect on channel activity, but rather did not increase current beyond baseline. In agreement with this finding, our pressure myography data indicates that addition of exogenous PS blocks PIP_2 activation of Kir2.1, suggesting that the role of PS at the MEJ may be primarily to dampen Kir2.1 channel activity as opposed to activating the channel. Our data also demonstrates that exogenous application of PS inhibits agonist-mediated Kir2.1 activation in intact arteries, also reinforcing the idea of PS as a negative regulator in these arteries. Since flux through the Kir2.1 channel hyperpolarizes the SMC membrane, PS localization with Kir2.1 at the MEJ likely dampens the K^+ flux through Kir2.1, to regulate the magnitude of relaxation and prevent overshooting a dilatory effect.

It has been demonstrated that relative concentrations of lipids can have differential effects on channel function, (104) and in MEJs where PS is localized, it is likely that the PS concentration is magnitudes higher than the local PIP_2 concentration, such that PIP_2 interactions with the channel are limited. Although the local concentration of PIP_2 at MEJs remains elusive, the half-life of PIP_2 at the MEJ is likely short given and the importance of IP_3 in heterocellular signaling to the SMC and the enrichment of diacylglycerol at the MEJ, the two products of PIP_2 cleavage by phospholipase C. (24, 41) An initial *en face* experiment using an

antibody for PIP2 supports this observation (**Figure 47**). Future studies should include repeating this *en face* stain for quantification and validating the antibody before drawing any conclusions. Thus, the PS localization to the MEJ may be antagonizing the PIP_2 requirement for channel opening, and may explain why in intact arteries PS blocks PIP_2 activation of Kir2.1. Together with the pressure myography results, it is evident that the balance between PS and PIP_2 within the membrane can have differential effects on the protein. We conclude a relatively higher PS concentration at the MEJ functions to negatively regulate Kir2.1 opening.

Our pressure myography data indicates that exogenous PS alone does not have an effect on arterial diameter, which is the opposite effect seen in electrophysiology experiments where PS activates the channel. A possible reason for the differential results of PS influence on Kir2.1 could be the differences in cellular lipid composition of HEK cells and intact arteries. (104) For example, the plasma membrane of ECs in intact arteries is complex, with signaling microdomains defined by protein and lipid composition. One example of this is the high density of caveolae in endothelium. (215) Caveolae are crucial for plasma membrane organization and are also enriched with cholesterol, with some studies also implicating specific localization of PS and PIP_2 to caveolae. (180, 194) It could be that there is some interplay between PS and cholesterol, a known depressor of Kir2.1 activity (96, 98, 99), in intact arteries that prevents PS alone from having a dilatory effect. Indeed, this could be another mechanism by which cholesterol prevents Kir2.1 activation. It is highly likely that caveolae are present within this

population given the high density of caveolae in the endothelium (**Figure 38**). In the future, the interplay between cholesterol, PS, and PIP_2 at the MEJ should be investigated in the context of Kir2.1 and other ion channels.

The role of MEJ in facilitating phosphatidylserine regulation of Kir2.1

We also demonstrate the inhibitory effect of PS on PIP_2 activation using arteries from a mouse model with HIEL morphology and thus MEJ formation ($Eln^{fl/fl}/Cre^{+}$). In this mouse, the PS localization within the intact resistance arterial endothelium is completely disrupted (**Figure 48**), covering less surface area and demonstrating reduced accumulation into punctate (reduced high intensity signal). Notably, Kir2.1 protein expression is unchanged, yet $Eln^{fl/fl}/Cre^{+}$ arteries exhibited an increased dilation to PIP_2, which was brought back down to control levels by adding back PS to the artery. These results support our findings that PS negatively regulates PIP_2-mediated Kir2.1 vasodilation. Based on the result that the PIP_2 dilation can be recovered to control levels with the addition of PS or ML-133 (a known Kir2.1 inhibitor), we attribute the increase dilation to the increased access of PIP_2 to Kir2.1. This increased dilation is likely due to the disrupted PS localization in the endothelium rather than a direct result of reduced elastin protein, which is cogent with Kir2.1 not demonstrating any known adhesion properties or being regulated by ECM proteins. However, there are some studies that link integrin signaling to ion channel function (216) and in particular, increasing current through Kir2.1. (217) Integrin signaling is likely decreased in $Eln^{fl/fl}/Cre^{+}$ arteries since there is a reduction of integrin substrate (ECM proteins). Thus, integrins are

likely not at play here since we see an increase in PIP_2-mediated dilation. We therefore do not attribute the increase in PIP_2 dilation to reduced Kir2.1-elastin interactions or a reduced Kir2.1-integrin signaling axis.

Lastly, the $Eln^{fl/fl}/Cre^{+}$ mouse model has broader implications for studying the functional importance of elastin on the formation of the anatomical structure of the MEJ and the protein/lipid trafficking that is necessary to form this functional signaling microdomain. In the future, the anatomical structure of MEJs in these resistance arteries should be investigated through transmission electron microscopy. It is possible that there are fewer individual MEJs, where each one occupies a larger area of heterocellular contact. If this is the case, the MEJ may not be no longer identified as a "microdomain" within the cell which may alter the spatial distribution of transcription, translation, and trafficking of proteins. It is also possible that disruption or downregulation of an ORP may be responsible for the disruption of PS localization.(175, 218) Since the MEJ is a crucial regulator of vasodilation in resistance arteries, any alterations in protein trafficking could also have implications in signaling pathways that contribute to total peripheral resistance.

Limitations of this work

I present evidence of a novel lipid regulation mechanism in intact arteries and proposes a new role for PS regulation of Kir2.1 function. My interpretation of PS negatively regulating PIP_2 mediated activation assumes that local PIP_2 concentration at the MEJ is orders of magnitude lower compared to PS. It is a

technical challenge to establish the local lipid concentration of PIP_2 at the MEJ; it was not detected in lipid mass spectrometry of *in vitro* MEJs, but rather, a product of its cleavage, DAG, was found to be enriched at MEJ compared to EC or SMC. (24) This suggests to us that the half-life of PIP_2 at the MEJ is short lived because its cleavage products are needed for downstream vasodilatory signaling. (24, 41)

I also present convincing evidence of lipid regulation of Kir2.1 by using an $Eln^{fl/fl}/Cre^{+}$ mouse model. However, it should be noted that this is the first study to investigate endothelial function on these mice. While ECs appear to function normally (**Figure 50B**), their myogenic tone (**Figure 51**) is significantly altered at higher pressures with deviation from controls beginning at 80mmHg, a pressure that is within normal physiological range. This suggests a possible alteration of other pathways within the arterial model.

Appendix

Sanger sequencing alignment Lactadherin-C2 plasmid

```
Program: BLASTN
Query: None ID: lcl|Query_10757(dna) Length: 763
Subject:None ID: lcl|Query_10759(dna) Length: 5194

Sequences producing significant alignments:
                                                                                Scientific
Per.   Acc.
Description                                                                     Name
Ident  Len        Accession
None provided
100.00 5194       Query_10759

Alignments:
>
Sequence ID: Query_10759 Length: 5194
Range 1: 619 to 1361

Score:1373 bits(743), Expect:0.0,
Identities:743/743(100%),  Gaps:0/743(0%), Strand: Plus/Plus

Query  21    AGCTGGTTTAGTGAACCGTCAGATCCGCTAGCGCTACCGGTCGCCACCATGGTGAGCAAG  80
             ||||||||||||||||||||||||||||||||||||||||||||||||||||||||||||
Sbjct  619   AGCTGGTTTAGTGAACCGTCAGATCCGCTAGCGCTACCGGTCGCCACCATGGTGAGCAAG  678

Query  81    GGCGAGGAGCTGTTCACCGGGGTGGTGCCCATCCTGGTCGAGCTGGACGGCGACGTAAAC  140
             ||||||||||||||||||||||||||||||||||||||||||||||||||||||||||||
Sbjct  679   GGCGAGGAGCTGTTCACCGGGGTGGTGCCCATCCTGGTCGAGCTGGACGGCGACGTAAAC  738

Query  141   GGCCACAAGTTCAGCGTGTCCGGCGAGGGCGAGGGCGATGCCACCTACGGCAAGCTGACC  200
             ||||||||||||||||||||||||||||||||||||||||||||||||||||||||||||
Sbjct  739   GGCCACAAGTTCAGCGTGTCCGGCGAGGGCGAGGGCGATGCCACCTACGGCAAGCTGACC  798

Query  201   CTGAAGTTCATCTGCACCACCGGCAAGCTGCCCGTGCCCTGGCCCACCCTCGTGACCACC  260
             ||||||||||||||||||||||||||||||||||||||||||||||||||||||||||||
Sbjct  799   CTGAAGTTCATCTGCACCACCGGCAAGCTGCCCGTGCCCTGGCCCACCCTCGTGACCACC  858

Query  261   CTGACCTACGGCGTGCAGTGCTTCAGCCGCTACCCCGACCACATGAAGCAGCACGACTTC  320
             ||||||||||||||||||||||||||||||||||||||||||||||||||||||||||||
Sbjct  859   CTGACCTACGGCGTGCAGTGCTTCAGCCGCTACCCCGACCACATGAAGCAGCACGACTTC  918

Query  321   TTCAAGTCCGCCATGCCCGAAGGCTACGTCCAGGAGCGCACCATCTTCTTCAAGGACGAC  380
             ||||||||||||||||||||||||||||||||||||||||||||||||||||||||||||
Sbjct  919   TTCAAGTCCGCCATGCCCGAAGGCTACGTCCAGGAGCGCACCATCTTCTTCAAGGACGAC  978

Query  381   GGCAACTACAAGACCCGCGCCGAGGTGAAGTTCGAGGGCGACACCCTGGTGAACCGCATC  440
             ||||||||||||||||||||||||||||||||||||||||||||||||||||||||||||
Sbjct  979   GGCAACTACAAGACCCGCGCCGAGGTGAAGTTCGAGGGCGACACCCTGGTGAACCGCATC  1038

Query  441   GAGCTGAAGGGCATCGACTTCAAGGAGGACGGCAACATCCTGGGGCACAAGCTGGAGTAC  500
             ||||||||||||||||||||||||||||||||||||||||||||||||||||||||||||
Sbjct  1039  GAGCTGAAGGGCATCGACTTCAAGGAGGACGGCAACATCCTGGGGCACAAGCTGGAGTAC  1098

Query  501   AACTACAACAGCCACAACGTCTATATCATGGCCGACAAGCAGAAGAACGGCATCAAGGTG  560
             ||||||||||||||||||||||||||||||||||||||||||||||||||||||||||||
Sbjct  1099  AACTACAACAGCCACAACGTCTATATCATGGCCGACAAGCAGAAGAACGGCATCAAGGTG  1158

Query  561   AACTTCAAGATCCGCCACAACATCGAGGACGGCAGCGTGCAGCTCGCCGACCACTACCAG  620
             ||||||||||||||||||||||||||||||||||||||||||||||||||||||||||||
Sbjct  1159  AACTTCAAGATCCGCCACAACATCGAGGACGGCAGCGTGCAGCTCGCCGACCACTACCAG  1218

Query  621   CAGAACACCCCCATCGGCGACGGCCCCGTGCTGCTGCCCGACAACCACTACCTGAGCACC  680
             ||||||||||||||||||||||||||||||||||||||||||||||||||||||||||||
Sbjct  1219  CAGAACACCCCCATCGGCGACGGCCCCGTGCTGCTGCCCGACAACCACTACCTGAGCACC  1278

Query  681   CAGTCCGCCCTGAGCAAAGACCCCAACGAGAAGCGCGATCACATGGTCCTGCTGGAGTTC  740
             ||||||||||||||||||||||||||||||||||||||||||||||||||||||||||||
Sbjct  1279  CAGTCCGCCCTGAGCAAAGACCCCAACGAGAAGCGCGATCACATGGTCCTGCTGGAGTTC  1338

Query  741   GTGACCGCCGCCGGGATCACTCT  763
             |||||||||||||||||||||||
Sbjct  1339  GTGACCGCCGCCGGGATCACTCT  1361
```

Sanger sequencing alignment for Cx37 plasmid

```
Sequence ID: Query_37397 Length: 1617
Range 1: 38 to 1043

Score:1784 bits(966), Expect:0.0,
Identities:990/1008(98%),  Gaps:4/1008(0%), Strand: Plus/Plus

Query  50    CTGCAGAGAGAGGCCCTGGAAACATGGGCGACTGGGGCTTCCTGGAGAAGTTGCTAGACC  109
             ||||||||||||||||||||||||||||||||||||||||||||||||||||||||||||
Sbjct  38    CTGCAGAGAGAGGCCCTGGAAACATGGGCGACTGGGGCTTCCTGGAGAAGTTGCTAGACC  97

Query  110   AGGTCCAGGAACACTCGACCGTGGTGGGCAAGATCTGGTTAACGGTGCTCTTCATCTTCC  169
             ||||||||||||||||||||||||||||||||||||||||||||||||||||||||||||
Sbjct  98    AGGTCCAGGAACACTCGACCGTGGTGGGCAAGATCTGGTTAACGGTGCTCTTCATCTTCC  157

Query  170   GCATCCTCATCCTGGGGCTGGCTGGCGAGTCGGTGTGGGGCGACGAGCAGTCTGATTTTG  229
             ||||||||||||||||||||||||||||||||||||||||||||||||||||||||||||
Sbjct  158   GCATCCTCATCCTGGGGCTGGCTGGCGAGTCGGTGTGGGGCGACGAGCAGTCTGATTTTG  217

Query  230   AGTGTAACACAGCCCAGCCGGGCTGCACCAACGTCTGCTATGACCAGGCCTTCCCCATCT  289
             ||||||||||||||||||||||||||||||||||||||||||||||||||||||||||||
Sbjct  218   AGTGTAACACAGCCCAGCCGGGCTGCACCAACGTCTGCTATGACCAGGCCTTCCCCATCT  277

Query  290   CCCACATCCGATACTGGGTGCTGCAGTTCCTCTTCGTCAGCACACCCACCCTGATCTACC  349
             ||||||||||||||||||||||||||||||||||||||||||||||||||||||||||||
Sbjct  278   CCCACATCCGATACTGGGTGCTGCAGTTCCTCTTCGTCAGCACACCCACCCTGATCTACC  337

Query  350   TGGGCCACGTCATCTACCTGTCTCGGCGGGAAGAGCGGTTGCGGCAGAAAGAGGGAGAGC  409
             ||||||||||||||||||||||||||||||||||||||||||||||||||||||||||||
Sbjct  338   TGGGCCACGTCATCTACCTGTCTCGGCGGGAAGAGCGGTTGCGGCAGAAAGAGGGAGAGC  397

Query  410   TCCGGGCGCTGCCATCCAAGGACCTACATGTAGAGCGGGCACTGGCTGCCATCGAACATC  469
             ||||||||||||||||||||||||||||||||||||||||||||||||||||||||||||
Sbjct  398   TCCGGGCGCTGCCATCCAAGGACCTACATGTAGAGCGGGCACTGGCTGCCATCGAACATC  457

Query  470   AGATGGCCAAGATCTCGGTGGCAGAGGACGGTCGTCTTCGGATTCGTGGGGCGCTCATGG  529
             ||||||||||||||||||||||||||||||||||||||||||||||||||||||||||||
Sbjct  458   AGATGGCCAAGATCTCGGTGGCAGAGGACGGTCGTCTTCGGATTCGTGGGGCGCTCATGG  517

Query  530   GTACCTATGTGGTCAGCGTGCTGTGTAAGAGTGTGCTGGAGGCAGGCTTCCTCTATGGCC  589
             ||||||||||||||||||||||||||||||||||||||||||||||||||||||||||||
Sbjct  518   GTACCTATGTGGTCAGCGTGCTGTGTAAGAGTGTGCTGGAGGCAGGCTTCCTCTATGGCC  577

Query  590   AGTGGCGCCTCTATGGCTGGACCATGGAGCCGGTGTTTGTGTGCCAGCGTGCGCCCTGCC  649
             ||||||||||||||||||||||||||||||||||||||||||||||||||||||||||||
Sbjct  578   AGTGGCGCCTCTATGGCTGGACCATGGAGCCGGTGTTTGTGTGCCAGCGTGCGCCCTGCC  637

Query  650   CCCACATCGTGGACTGCTATGTCTCTCGACCCACTGAGAAGACTATCTTCATCATCTTCA  709
             ||||||||||||||||||||||||||||||||||||||||||||||||||||||||||||
Sbjct  638   CCCACATCGTGGACTGCTATGTCTCTCGACCCACTGAGAAGACTATCTTCATCATCTTCA  697

Query  710   TGCTGGTGGTAGGAGTCATCTCCCTGGTGCTCAACCTGCTGGAGCTGGTTCACCTGCTGG  769
             |||||||||||||||||||||||||||||||||||||||||||||||||||||||||| |
Sbjct  698   TGCTGGTGGTAGGAGTCATCTCCCTGGTGCTCAACCTGCTGGAGCTGGTTCACCTGCT-G  756

Query  770   TGTCGGTGTGTCAGCCGGGAGATAAAGGCACGAAGGGACCACGACGCCCGCCCGGCCCAG  829
             ||||||||||||||||||||||||||||||||||||||||||||||||||||||||||||
Sbjct  757   TGTCGGTGTGTCAGCCGGGAGATAAAGGCACGAAGGGACCACGACGCCCGCCCGGCCCAG  816

Query  830   GGCAGTGCCTCAGACCCTTACCCTGAACAGGTTTTCTTCTACCTCCCCANGGGGCGAGGG  889
             ||||||||||||||||||||||||||||||||||||||||||||||||  |||||||||
Sbjct  817   GGCAGTGCCTCAGACCCTTACCCTGAACAGGTTTTCTTCTACCTCCCCAT-GGGCGAGGG  875

Query  890   ACCCTCTTCCCCACCGTGTCCCACCTACAACGGGCTCTCATCCACTGAGCAGAACTGGGC  949
             ||||||||||||||||||||||||||||||||||||||||||||||||||||||||||||
Sbjct  876   ACCCTCTTCCCCACCGTGTCCCACCTACAACGGGCTCTCATCCACTGAGCAGAACTGGGC  935

Query  950   CAACTTGACCACAGANNANAGACTGACCTCTTCCAGACCTCCCCCATTTGTAAACACAGC  1009
             ||||||||||||||  | ||||||||||||||||||||||||||||||||||||||||||
Sbjct  936   CAACTTGACCACAGAGGAGAGACTGACCTCTTCCAGACCTCCCCCATTTGTAAACACAGC  995

Query  1010  TCCCCNGGGNGNNNGAAAGTCCCCNANNNNCCC--ACAGCTCTGCATC  1055
             ||||| ||| |   |||||||||| |    |||  ||||||||||||
Sbjct  996   TCCCCAGGGTGGCCGAAAGTCCCCTAGCCGCCCCAACAGCTCTGCATC  1043
```

Sanger sequencing alignment for Cx40 plasmid

```
>M. musculus gene for connexin40
Sequence ID: X61675.1 Length: 1218
Range 1: 97 to 1037

Score:1620 bits(877), Expect:0.0,
Identities:916/943(97%),  Gaps:8/943(0%), Strand: Plus/Plus

Query  121   CCTCGGTCTCCTACTCTTGGCAAGATGGGTGACTGGAGCTTCCTGGGGGAGTTCCTGGAG  180
Sbjct  97    ............................................................  156

Query  181   GAGGTCCACAAGCACTCCACAGTCATCGGCAAGGTCTGGCTCACTGTCCTGTTCATTTTC  240
Sbjct  157   ............................................................  216

Query  241   CGCATGCTGGTCCTGGGCACCGCTGCTGAGTCCTCCTGGGGAGATGAGCAGGCCGACTTC  300
Sbjct  217   ............................................................  276

Query  301   CGGTGCGATACCATTCAGC----NTGCCAAAATGTCTGCTATGACCAAGCCTTCCCCATC  356
Sbjct  277   ....................CTGGT.....................................  336

Query  357   TCCCACATTCGTTATTGGGTACTGCAGATCATCTTTGTGTCCACGCCTTCTCTAGTGTAC  416
Sbjct  337   ............................................................  396

Query  417   ATGGGCCATGCCATGCACACTGTGCGCATGCAGGAAAAGCAGAAATTGCGGGATGCTGAG  476
Sbjct  397   ............................................................  456

Query  477   AAAGCTAAAGAGGCCCACCGCACTGGTGCCTATGAGTACCCAGTAGCCGAAAAGGCCGAG  536
Sbjct  457   ............................................................  516

Query  537   CTGTCCTGCTGGAAAGAAGTAGATGGGAAGATTGTCCTCCAGGGCACCCTACTCAACACC  596
Sbjct  517   ............................................................  576

Query  597   TATGTCTGCACCATTCTGATCCGCACCACCATGGAGGTGGCCTTCATCGTAGGCCAGTAC  656
Sbjct  577   ............................................................  636

Query  657   CTCCTCTATGGGATCTTCCTGGATACCCTGCATGTCTGCCGCAGGAGTCCCTGTCCCCAC  716
Sbjct  637   ............................................................  696

Query  717   CCAGTCAACTGTTATGTTTCGAGGCCCACGGAGAAGAATGTCTTCATTGTCTTTATGATG  776
Sbjct  697   ............................................................  756

Query  777   GCTGTGGCTGGACTGTCTCTGTTTCTCAGCCTGGCTGAACTCTACCACCTGGGCTGGAAG  836
Sbjct  757   ............................................................  816

Query  837   AAGATCCGACAGCGCTTTGGCAAGTCACGGCAGGGTGTGGACAAGCACCAGCTGCCTGGN  896
Sbjct  817   ............................................................C  876

Query  897   CCTCCCACCAGCCTCGTCCAGAGCCTCACTCCTCCCCCTGACTTC-ATCAGTGCCTAAAG  955
Sbjct  877   ..........................................A.................  936

Query  956   AACAGCTCCGGAGAGAANTNCTTCAGCGACTTCAGTAATANCNTNN-CTCCCGGAANNAT  1014
Sbjct  937   ................A.T.....................A.A.GGG.........GA..  996

Query  1015  CCAGANGCTNNTGGNNNCTGGGGNANNNGCCAAACCAGNAGCA  1057
Sbjct  997   .....C...C-...CCA......A.GT-..........G....  1037
```

Sanger sequencing alignment for Cx43 plasmid

```
>Mus musculus gap junction protein, alpha 1 (Gja1), mRNA
Sequence ID: NM_010288.3 Length: 3105
Range 1: 33 to 926

Score:1375 bits(744), Expect:0.0,
Identities:843/896(94%),  Gaps:6/896(0%), Strand: Plus/Plus

Query  157   GCTTTTACGAGGTATCAGCACTTTTCTTTCATTGGGGGGAAGGCGTGAGGAAAGTACCAA  216
              |||||||||||||||||||||||||||||||||||||||| |||||||||||| |||||||| |
Sbjct  33    GCTTTTACGAGGTATCAGCACTTTTCTTTCATTGGGGGAAAGGCGTGAGGGAAGTACCCA  92

Query  217   ACAGCAGCAGACTTTTAAACTTTAAACAGACAGGTCTGAGAGCCTGAACTCTCATTTTTC  276
              ||||||||||||||| |||||||||||||||||||||||||||| ||||||||  |||||
Sbjct  93    ACAGCAGCAGACTTTGAAACTTTAAACAGACAGGTCTGAGAGCCCGAACTCTC-CTTTTC  151

Query  277   CTTTGACTTCAGCCTCCAAGGAGTTCCACCAACTTTGGC--G-CGNNTTCACTTTCATTA  333
              ||||||||||||||||||||||||||||||| |||||||  | ||  |||||||||||||
Sbjct  152   CTTTGACTTCAGCCTCCAAGGAGTTCCACCA-CTTTGGCGTGCCGGCTTCACTTTCATTA  210

Query  334   AGTGAAAGAGAGGTGCCCAGACATGGGTGACTGGAGTGCCTTGGGGAAGCTTCTGGACAA  393
              |||||||||||||||||||||||||||||||||||||||| |||||||||||||| |||||||
Sbjct  211   AGTGAAAGAGAGGTGCCCAGACATGGGTGACTGGAGCGCCTTGGGGAAGCTGCTGGACAA  270

Query  394   GGTCCAAGCCTACTCCACCGCTGGAGGGAAGGTGTGGCTGTCAGTGCTCTTCATATTCAG  453
              |||||||||||||||| || |||||||||||||||||||| |||||||||||| ||||||
Sbjct  271   GGTCCAAGCCTACTCCACGGCCGGAGGGAAGGTGTGGCTGTCGGTGCTCTTCATTTTCAG  330

Query  454   AATCCTGCTCCTGGGGACAGCTGTTGAGTCAGCTTGGGGTGATGAACAGTCTGCCTTTCG  513
              |||||||||||||||||||| |||||||||||||||||||||||||||||||||||||||
Sbjct  331   AATCCTGCTCCTGGGGACAGCGGTTGAGTCAGCTTGGGGTGATGAACAGTCTGCCTTTCG  390

Query  514   CTGTAACACTCAACAACCTGGCTGCGAAAACGTCTGCTATGACAAGTCCTTCCCCATCTC  573
              |||||||||||||||| || || |||||| |||||||||||||||||||||||||||||||
Sbjct  391   CTGTAACACTCAACAACCCGGTTGTGAAAATGTCTGCTATGACAAGTCCTTCCCCATCTC  450

Query  574   TCACGTGCGCTTCTGGGTCCTTCAGATCATATTCGTGTCTGTGCCCACCCTCCTGTACTT  633
              |||||||||||||||||||||||||||||||||||||||||||||||| ||||||||||||
Sbjct  451   TCACGTGCGCTTCTGGGTCCTTCAGATCATATTCGTGTCTGTGCCCACACTCCTGTACTT  510

Query  634   GGCCCATGTGTTCTATGTGATGAGGAAGGAAGAGAAGCTAAACAAGAAAGAAGAGGAGCT  693
              ||| || |||||||||||||||| |||||||||||| |||||||||||||||||||||||
Sbjct  511   GGCTCACGTGTTCTATGTGATGAGAAAGGAAGAGAAGCTGAACAAGAAAGAAGAGGAGCT  570

Query  694   CAAAGTGGCCCAGACTGACGGGGTCAACGTGGAGATGCACCTGAAGCAGATTGAAATCAA  753
              ||||||||| ||||| |||||||||||||||||||||||||||||||||||||||||||||
Sbjct  571   CAAAGTGGCGCAGACCGACGGGGTCAACGTGGAGATGCACCTGAAGCAGATTGAAATCAA  630

Query  754   GAAGTTCAAGTACGGGATTGAAGAGCACGGCAAGGTGAAAATGAGGGGCGGCTTGCTGAG  813
              |||||||||||| |||||||||| |||||||||||||| |||||| || ||| |||||||
Sbjct  631   GAAGTTCAAGTATGGGATTGAAGAACACGGCAAGGTGAAGATGAGAGGTGGCCTGCTGAG  690

Query  814   AACCTACATCATCAGCATCCTCTTCAAGTCTGTCTTCGAGGTGGCCTTCCTGCTCATCCA  873
              |||||||||||||||||||||||||||||||||||||||||||||||||||||||| |||||
Sbjct  691   AACCTACATCATCAGCATCCTCTTCAAGTCTGTCTTCGAGGTGGCCTTCCTGCTGATCCA  750

Query  874   GTGGNACATCTATGGGTTCAGCTTGAGCGCGGTCTACACCTGCAAGANAGATCCCTGCCC  933
              |||| |||||||||||||| |||| |||||||||||||||||||| ||||||||||||
Sbjct  751   GTGGTACATCTATGGGTTCAGCCTGAGTGCGGTCTACACCTGCAAGAGAGATCCCTGCCC  810

Query  934   CCACCAGGTAGACTGCTTCCTCTCACGTCCCACGGAN-AAACCATCTTCATCATCTTCAT  992
              ||||||||| |||||||||||||||||||||||||  |||||||||||||||||||||||
Sbjct  811   CCACCAGGTGGACTGCTTCCTCTCACGTCCCACGGAGAAAACCATCTTCATCATCTTCAT  870

Query  993   GCTGGNGGNNTCCTNGGNGTCTCTCGCTTTGAACATCATTGAGCTCTTCTACGTCT  1048
              ||||| ||  |||| || |||||||||| |||| |||||||||||||||| ||||
Sbjct  871   GCTGGTGGTGTCCTTGGTGTCTCTCGCTCTGAATATCATTGAGCTCTTCTATGTCT  926
```

Predicting the incidence of myoendothelial junctions in transmission electron microscopy cross-sections

First, we can consider basic descriptive data obtained from the *en face* images (**Table 1**) including the circumference of the artery (**C**, Supp Fig2A) the average diameter of HIEL (**d**, Supp Fig2B), and spatial density of HIEL ($\boldsymbol{\rho_{HIEL}}$, Supp Fig2C), which is calculated by dividing the number of HIEL in an image ($\boldsymbol{\tilde{N}_{HIEL}}$) by the image area ($\boldsymbol{\tilde{A}_{xy}}$). $\boldsymbol{\tilde{N}_{HIEL}}$ and **d** were quantified via the in-house Matlab program, and **C** was measured as the width of the artery when prepared *en face*. For this calculation, we assume that the measured circumference of the artery is equivalent to the circumference of the IEL ($\boldsymbol{C_{IEL}}$).

Next, we considered the transverse view of the artery when prepared for TEM imaging (**Table 2**). The TEM section is a thin cross section sliced from a third order mesenteric artery where the thickness of an individual section is $\boldsymbol{Y_{TEM}}$. Since our quantification of HIEL thus far is from the *en face* view, we wanted to ask the question of how much IEL surface area would be represented in one TEM section in order to predict the density of HIEL. A single TEM cross-section corresponds to an *en face* surface area of 20.902μm^2, which was calculated by multiplying the thickness of a TEM section by the circumference of the artery ($\boldsymbol{A_{TEM,1} = Y_{TEM} * C_{IEL}}$). An important note is that **d** is much larger than $\boldsymbol{Y_{TEM}}$, such that the average HIEL will span 30 TEM sections ($\boldsymbol{d / Y_{TEM}}$). For conceptual clarity, we will consider 6 TEM sections equally spaced apart along artery length **d**, which corresponds to an IEL surface area of 627.06μm^2 ($\boldsymbol{A_{TEM,\,d} = C_{IEL}\ x\ d}$), and an IEL length of 1791.6μm

($\mathbf{L_{IEL} = 6 * C_{IEL}}$). Using ρ_{HIEL} and $\mathbf{A_{TEM,\,d}}$, we calculated that we would detect a total of 9 unique HIEL across artery length **d** ($\mathbf{HIEL_{TEM}} = (\rho_{HIEL} \mathbf{\times A_{TEM,\,d}}) \mathbf{/\ 1000\mu m^2}$).

The final variable we considered in our prediction is the spatial distribution of holes throughout the IEL. For this, we considered three cases of distribution (**Table 3**): (1) uniform distribution (maximum detection), (2) random distribution, and (3) sparse distribution (minimum detection). Using ρ_{HIEL} and $\mathbf{A_{TEM,\,d}}$, we calculated that we would detect a total of 9 unique HIEL across artery length **d** ($\mathbf{HIEL_{TEM}} = (\rho_{HIEL} \mathbf{\times A_{TEM,\,d}) / 1000\mu m^2}$).

For Case 1, we considered 6 TEM sections over artery length **d** and assumed that each of the 9 HIEL were exactly aligned with the start and end of the sectioned area, such that the HIEL distribution is uniform, such that the number of HIEL detections by the microscope user is 54 (9 total HIEL, appearing once on each of the 6 sections). However, due to the nature of TEM, the entire cross-sectional area cannot be imaged due to visibility blockages by grid lines, indicating that all 54 HIEL cannot be imaged by the user, even if they were present. In order to account for this technical challenge, the predicted number of HIEL detections can be normalized to the length of IEL in the TEM image. This normalization process results in a numerical value with the units of HIEL per length of IEL. **Thus, if HIEL are uniformly distributed, then we expect 30 HIEL per 1000μm IEL length** (54 HIEL / 1791.6μm IEL length x 1000μm IEL).

However, based on the Matlab simulations (**Figure 1**), we have shown that HIEL are randomly distributed. We therefore incorporated a random distribution of HIEL into our prediction. Thus, instead of assuming each HIEL would have 6

detections across each of the 6 sections, we assumed that each HIEL had a different number of detections due to a random alignment with the beginning and end of the length sectioned area. The random distribution of detections was considered as follows**:** 2 HIEL with 6 detections each (12 detections), 1 HIEL with 5 detections each (5 detections), 2 HIEL with 4 detections each (8 detections), 1 HIEL with 3 detections each (3 detections), 1 HIEL with 2 detections each (2 detections), and 2 HIEL with 1 detection each (2 detections), bringing the total to 32 detections. Using the same normalization process as described above, we determined that **if HIEL are randomly distributed, we expect 17.5 HIEL per 1000μm length of IEL (**32 HIEL / 1791.6μm IEL length x 1000μm IEL).

Due to the random distribution of HIEL, there are some areas of IEL that have relatively few holes. Thus, a third case is considered to reflect a sparse distribution scenario. In this minimum case scenario, each of the 9 HIEL are only aligned with 1 TEM section and thus is only detected once during imaging. For 9 HIEL considered across 6 sections, with each HIEL appearing in only 1 section, there are 9 total detections. Normalizing these to the IEL within TEM images as for the previous two scenarios, **5 HIEL are expected per 1000um length of IEL** (12 HIEL / 1791.6μm IEL length x 1000μm IEL).

There are areas in the internal elastic lamina that are more sparse with HIEL, and since we have demonstrated that the HIEL are randomly distributed, we conclude that **the predicted range of HIEL density in the TEM images is 5-17.8 HIEL per 1000μm IEL analyzed**.

Representative Myogenic Tone Trace for $Eln^{fl/fl}/Cre^{-}$

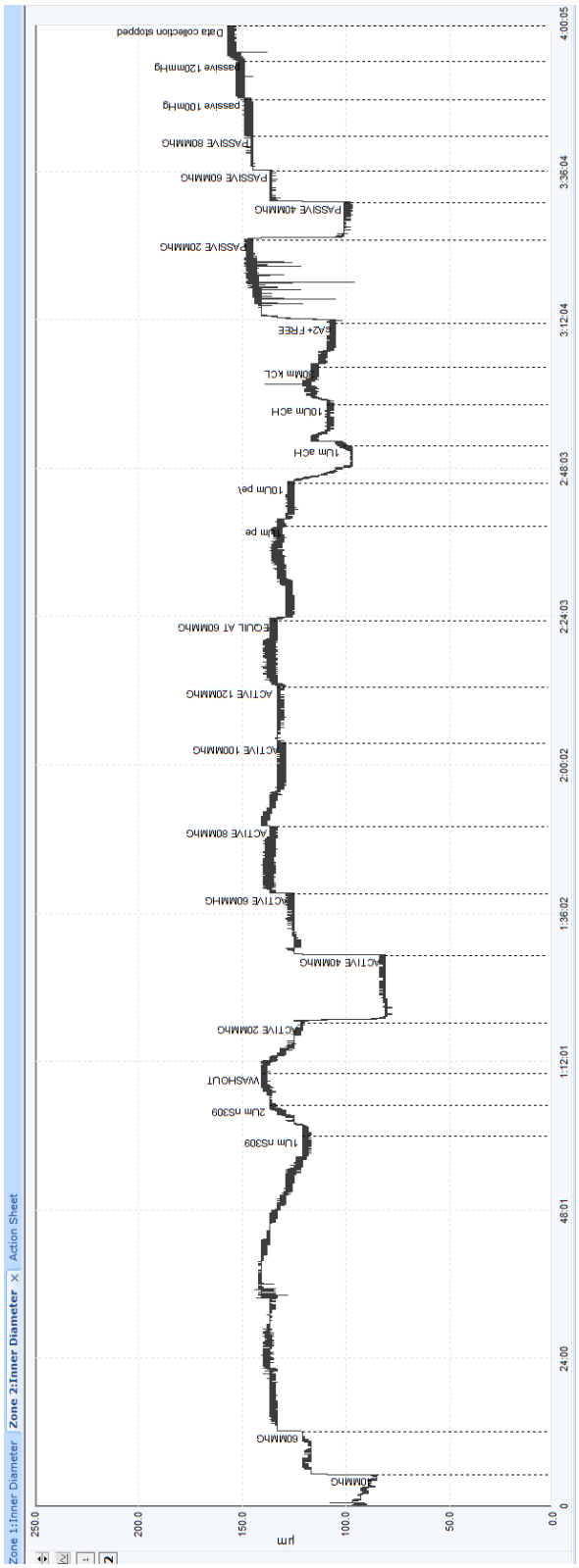

Representative Myogenic Tone Trace for $Eln^{fl/fl}/Cre^{+}$

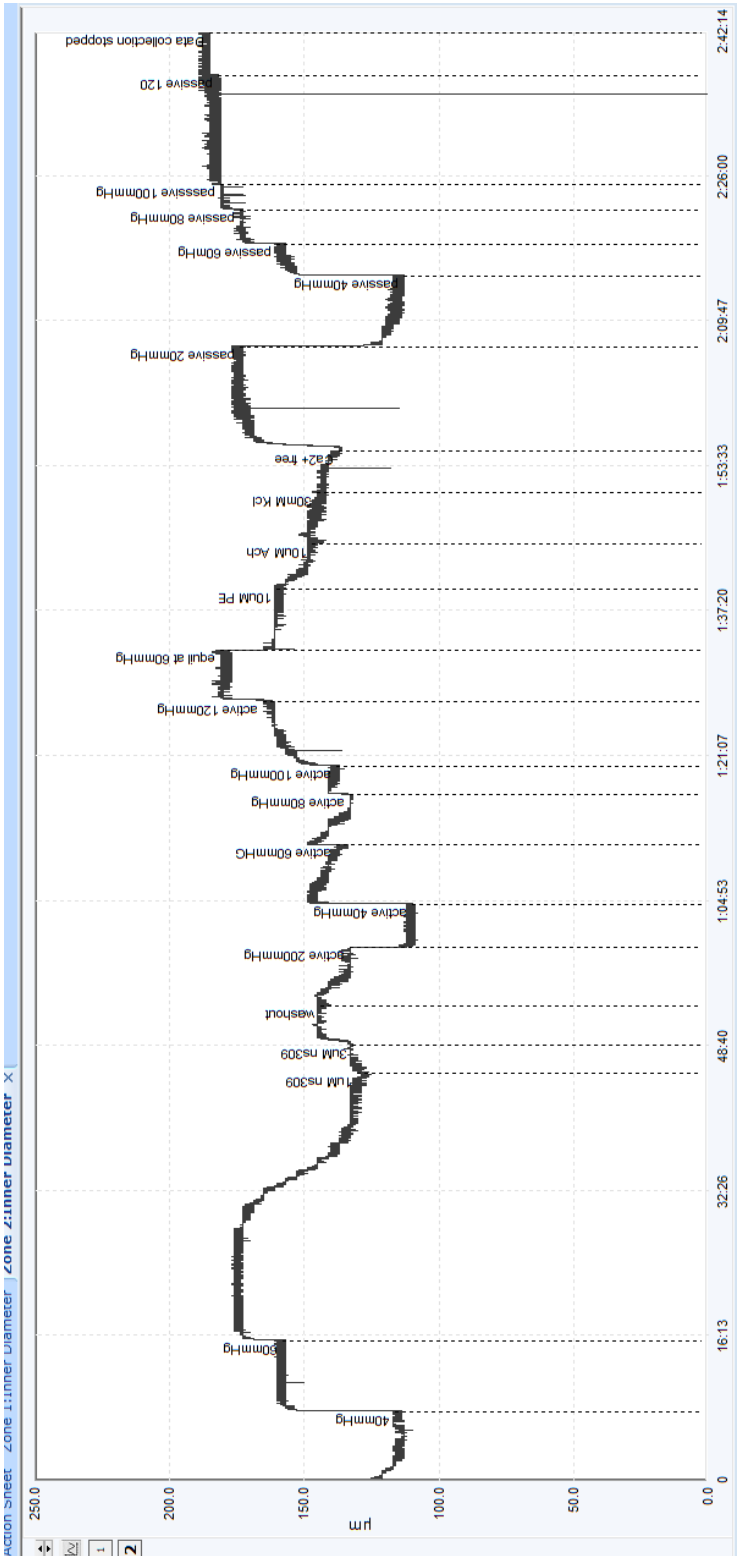

Chapter 4. The internal elastic lamina regulates vasodilation

Abstract

The MEJ is a crucial regulator of total peripheral resistance and thus blood pressure. This anatomical signaling microdomain is defined as an EC extension that makes contact with SMCs by protruding through holes in the matrix layer that separates the two cell types, termed the internal elastic lamina (IEL). The holes in the IEL increase as arterial diameter decreases and is correlated with the mechanism of vasodilation. In larger, conduit arteries where there are no HIEL, nitric oxide is the primary vasodilator. NO can diffuse across the IEL and to the several layers of smooth muscle in the large arteries. In contrast, smaller resistance arteries have a high density of HIEL and a predominate EDH-based vasodilation profile, which can be attributed to the protein localization to this signaling microdomain. Hemoglobin alpha (Hba) is an MEJ-resident protein that significantly contributes to the predominance of EDH-based signaling in resistance arteries by complexing with endothelial nitric oxide synthase (eNOS) and chelating any NO produced by the enzyme.

A recent study investigated the contributions of both SMC and EC to IEL formation in both large and small arteries. Interestingly, ECs were the major contributor to IEL formation in small resistance arteries, where $Eln^{fl/fl}/Cre^{+}$ (on a Cdh5 Cre) mice demonstrated a fragmented IEL in cross-section TEM views. **We therefore wanted to investigate the impact on canonical HIEL and MEJ**

formation in these arteries. Alexa Fluor-488 linked hydrazide was used to detect IEL. In knockout arteries, hydrazide signal was reduced by 56.26% with a complete ablation of canonical sites of MEJ formation. **Thus, I hypothesized that the localization of the MEJ-resident protein Hba would be disrupted in these arteries.** Indeed, Hba in $Eln^{fl/fl}/Cre^{+}$ arteries covered more surface area with a reduced amount of high intensity puncta, indicating a more diffuse localization in the endothelium. Western blot analysis on the mesenteric vasculature also shows a reduction in Hba protein. This new localization pattern and reduction in protein in turn decreased the amount of Hba-eNOS interactions in the endothelium as demonstrated by decreased PLA puncta in en face preparations.

Next, we tested if this reduced interaction had a functional consequence on the vasodilatory profile. We pressurized third order mesenteric arteries to 60mmHg, which was determined to be the ideal pressure for this transgenic mouse (Figure X), and evaluated vasodilation via an acetylcholine (Ach) dose response curve. At baseline conditions, Ach-based vasodilation was similar between wildtype and knockout arteries, with $Eln^{fl/fl}/Cre^{+}$ arteries exhibiting a slight reduction in dilation (significantly different at only 1 of 8 doses). When 30μM of the NOS inhibitor L-NAME was added to the system, wildtype arteries did not demonstrate a reduction in Ach, which is an expected result based on the predominate EDH pathway in these arteries. However, $Eln^{fl/fl}/Cre^{+}$ arteries did exhibit a significant reduction in Ach-mediated vasodilation when L-NAME was present in the system, indicating an increased reliance on NO-based vasodilation.

Further, SMC function is reduced in $Eln^{fl/fl}/Cre^{+}$ mice, with a significant reduction in constriction to both PE and KCl. We hypothesized that SMC contractile machinery may be expressed at lower levels in these mice. However, mRNA levels of Acta2 indicate no significant differences. Integrins may also be behind the reduced smooth muscle cell function. Integrins bind to extracellular matrix and are important in for communicating inside-out and outside-in signaling. Without the matrix layer present it is likely that integrin signaling is disrupted in these animals.

Despite all of these vascular deficiencies, the $Eln^{fl/fl}/Cre^{+}$ mice have normal blood pressure. We hypothesize that the animal is compensating for the vascular deficiencies through increased fluid retention or kidney function, and that mechanism has yet to be determined.

Introduction

Some sections adapted from (* indicates co-first authorship):

Wolpe AG*, Ruddiman CA*, Hall PJ, Isakson BE. Polarized Proteins in Endothelium and Their Contribution to Function. J Vasc Res. 2021;58(2):65-91. doi: 10.1159/000512618. Epub 2021 Jan 27. PMID: 33503620; PMCID: PMC7954879. * indicates co-authorship

The internal elastic lamina

In immediate contact with the abluminal EC surface is an ECM layer termed the internal elastic lamina (IEL) that separates ECs from SMCs. When viewed in a cross-section, is a wavy, dense layer, (38, 39) and in large conduit arteries, these laminae are also present between the multiple SMC layers.(10) When viewed *en face*, the IEL of resistance arteries, but not conduit arteries, have a high proportion of circular shaped holes in the IEL (HIEL), where extracellular matrix proteins are absent. (10, 38, 76, 219) (10, 38, 76) As discussed throughout this thesis, these fenestrations facilitate the heterocellular communication that is vital to regulating vasodilation and vasoconstriction pathways in resistance arteries, through allowing highly specific signaling microdomains to form called MEJs. (9, 10, 12, 13, 23, 24,

38, 40, 41, 97) This layer also serves as an adhesion substrate for integrins that are localized to the endothelial abluminal surface, which participate in a number of important processes such as angiogenesis.(220-222) Later in this section, I will highlight the function of integrins in the vasculature.

The IEL layer consists of collagen IV, elastin, lamin-8/10, nidogen, and heparan sulfate proteoglycans; (73, 223-226) however, the composition is not uniform across vascular bed or vessel size. (73, 225, 227, 228) (Please see **Chapter 5** for the mass spectrometry results that identify potentially unique ECM proteins in mesenteric arteries.) For example, conduit arteries, often referred to as elastic arteries due to their high elastin content, function to absorb the force generated by the heart.(225, 228, 229) Elastin in resistance arteries, although not as prevalent, (228) still demonstrates important functionality in bearing longitudinal stress, rather than circumferential stress (as in conduits). (73, 224) The cell type that produces the elastin that gets deposited in the IEL is SMC in conduit arteries versus EC in resistance arteries .(209)

In vitro work demonstrates secretion of other extracellular matrix proteins and suggests a collaborative effort between the endothelial and smooth muscle cells in forming the IEL. (209, 223) For example, endothelial derived extracellular matrix proteins include fibronectin (230) and elastin, (231-233) while collagen I and III are secreted from the smooth muscle cell layer and are regulated by NO. (234) In injury or inflammation, additional matrix proteins such as fibrinogen or fibronectin are secreted. (235, 236) However, it is unclear whether these proteins identified *in vitro* are deposited in the IEL of intact vessels, become part of the adventitia, or

are released into the circulation. For example, collagen I is more prevalent in the adventitia rather than the IEL of cremaster arterioles. (73)

Elastin

Elastin is a durable, insoluble ECM protein with an incredible half-life of 70 years. (237, 238) The traditional “elastin” that we talk about is actually the product of crosslinked tropoelastin, a soluble protein between 60-70kDa rich in lysine and proline residues. (239, 240) In humans, there is one gene that encodes tropoelastin, *Eln*, and the numerous splice variants leads to the generation of 13 mature tropoelastin isoforms. (241) The protein sequence of tropoelastin is relatively low in complexity and alternates between hydrophobic and cross-linking domains. The hydrophobic domains can vary in length but generally consist of valine, proline, glycine and alanine. (238, 242) Interactions between glycine and proline within these domains contributes to the flexible and recoiling nature of tropoelastin. (243) Cross-linking domains contain a high percentage of lysines. After tropoelastin is outside of the cell, the enzyme lysyl oxidase will crosslink tropoelastin. Lysyl oxidase deaminates the lysine and the resultant aldehyde group can react with other highly reactive aldehydes or unaltered lysines to form crosslinks. There are different types of lysyl oxidases that can crosslink either collagen or elastin, or both, and have relatively different functions across different tissues. (244, 245) Crosslinked tropoelastin (elastin) now uses microfibrils as a scaffold to assemble into mature elastic fibers which happens exclusively in

gestation and postnatal development. There are no new fibers that are formed in the adult. (246)

Microfibrils consist of fibrillins, microfibril associated glycoproteins (MAGPs), fibulins, and elastin microfibril interface located protein (EMILIN)-1, (247) and provide a structural scaffold for tropoelastin crosslinking and elastin molecular alignment. The major component of the microfibril is comprised of fibrillins, a large, cysteine-rich protein (~350kDa) with 3 identified isoforms (fibrillin-1, fibrillin-2, and fibrillin-3). (248) Fibrillins can interact with integrins and heparin sulfate proteoglycans through their Arg-Gly-Asp binding motif and heparin binding domains, respectively, and thus are not only important for elastic fiber assembly but also participate in cellular signaling. (245) Homozygous global knockout mice of fibrillin-1 gene die shortly after birth from vascular and pulmonary complications, highlighting the role of this microfibril protein in vascular development. (249) MAGPs are small proteins (~20kDa) that bind to tropoelastin and fibrillins; however, they may not be necessary for normal elastic fiber assembly. (245, 250-252) Fibulins are variable in size and range from 50-200kDa (253), with five members in the family (fibulin-1 through -5), where fibulin-4 and fibulin-5 have been described to either bind to tropoelastin or localize to microfibrils. (254) Lastly, EMILIN-1 is ~100kDa protein that, as the name implies, localizes between the microfibrils and crosslinked tropoelastin (elastin), and it has been shown to bind with elastin and fibulin-5 in *in vitro* assays. (245, 255) Elastic fiber structure in mice lacking EMILIN-1 show a separated elastin-microfibril interface as expected, and exhibited a hypertension phenotype similar to heterozygous elastin global

knockout mice. The vascular phenotypes were reversed through genetic heterozygous deletion of TGF-β. (256, 257)

Degradation of elastin

Membrane metalloproteinases (MMPs) are calcium- and zinc-dependent endoproteases that degrade ECM proteins such as collagens, proteoglycans, fibronectin. These are important for facilitating vascular remodeling as in development and pregnancy. The different isoforms are heterogeneously distributed throughout the body and have different substrate specificities. (258) MMP-2, -7, -9, -12, and -14 are able to degrade both tropoelastin and elastin. (259) This family of enzymes contains a propeptide domain, catalytic domain, a linker peptide, and a hemopexin domain. The propetide domain chelates the Zn^{2+} binding site thus keeping the enzyme in a latent form. This domain must be cleaved to activate the catalytic domain, which contains a Zn^{2+} binding motif to accommodate two ions, and also bind Ca^{2+} ions for stability. The hemopexin domain is thought to contribute to substrate specificity across the MMP family. (260) MMPs can be secreted by EC, SMC, or macrophages in the vasculature, and can be pathogenic. (261) For example, MMP secretion can contribute to the development of atherosclerosis through facilitating SMC migration and neointimal formation. (261, 262)

Vascular phenotypes of elastin deficiency in mice

Elastin is a crucial component of the circulatory system and it is the main contributor to the distensibility of blood vessels in large arteries. The ECM arrangement in blood vessels is organized into laminae that are between layers of cells. This organization facilitates the distensibility of arteries, especially conduit arteries that are situated in close proximity to the heart where the force of flow is highest. In studies using global elastin homozygous knockout mice, the pups only survive for a few days after birth, where ultimately their death is due luminal obstruction by SMCs. (263) This suggests that elastin is also an important regulator of luminal integrity through restricting migration of SMCs. This concept is also demonstrated in atherosclerosis where MMPs are heavily secreted and ECM organization is disrupted. (261, 262) Global heterozygous elastin knockout mice have a normal lifespan; however, they are hypertensive, with elevated systolic and diastolic pressures that contribute to a MAP that is 25-30 mmHg higher compared to controls. (256) There are contributions from both increased arterial stiffness and increased cardiac output in these mice that contribute to hypertension. (256, 264) This highlights the role of elastin in regulating the homeostasis of the cardiovascular system.

The laminae within the arteries are structurally and functionally important for a successful cardiovascular system, and the cells that produce the laminae are different depending on location in the vascular tree, specifically related to arterial diameter. (209) Large conduit arteries are located in close proximity to the heart and contain several SMC layers, with elastic laminae situated between them in

addition to the IEL, which is the lamina that separates SMC from EC. In a constitutive SMC-specific elastin knockout mouse model, laminae organization, formation, and composition are disrupted. In heterozygous knockouts, there is an increase in laminae, but an overall decrease in compliance of the artery. This suggests that the artery attempts to compensate for the decrease in elastin production through making more laminae layer. These mice have a normal lifespan and are normotensive. In the homozygous knockout, most mice die within three weeks of life and have severe vascular deformities. In the ascending aorta, lamina formation is severely disrupted and SMC layers toward the lumen of the vessel represents a random orientation. In contrast, as artery size decreases and distance from the heart increases, there are fewer SMC and only two laminae in the wall, the IEL and the external elastic lamina (EEL). In a constitutive EC-specific elastin knockout mouse model, the IEL was severely disrupted in small resistance arteries and preserved in larger arteries. (209) Altogether, these results indicate that elastin deposition is primarily mediated by SMC in larger arteries and EC in smaller arteries.(209)

Materials and Methods

For additional methodology, please see Chapter 3 Materials and Methods.

Proximity Ligation Assay Experiment and Analysis

DuoLink reagents were used for proximity ligation assays (PLA) (Sigma, DUO92002, DUO92004, DUO92008). Third order mesenteric arteries were prepared *en face* and Sylgard squares were placed in individual wells of a 24-well dish. Arteries were permeabilized for 40 minutes using 0.2% NP40/PBS at RT with medium shaking. Sylgard squares were transferred to microscope slides and placed in a humidity chamber. Block by pipetting a drop DuoLink Blocking Solution onto the Sylgard square and place in a 37°C incubator for 100 minutes. At the end of the blocking period, blocking solution was gently removed by tapping the microscope slide on the lab bench, and quickly add the primary antibody solution to the artery (1:20 dilution in the DuoLink Antibody Diluent) for an overnight incubation at 4°C. The next day, complete 2x 5-minute washes with Wash Buffer A with no agitation. For DuoLink PLA probe incubation step, apply the plus and minus probes at a 1:5 dilution each to each artery. For example, 8μl of minus probe, 8μl of plus probe, and 24μl of antibody diluent. Pipette this 40μl up and down and then apply 20μl to each artery. Incubate the arteries with this solution for 1 hour at 37°C in a humidity chamber. Wash 2x Wash Buffer A at RT with no agitation. For the ligation step, dilute Ligase 1:40 in ligation buffer and apply to the artery for 45 minutes at 37°C. Next, wash the slides 2x 5 minutes with Wash Buffer

A at RT with no agitation. For the amplification step, apply the diluted polymerase 1:80 in Amplification Buffer and incubate slides in humidity chamber for 100 minutes at 37°C. Last, complete 2x 10-minute 1x Wash Buffer B and end with a 0.01x Wash Buffer B. Mount *en face* samples as normal and image on a confocal microscope. Visit Sigma's product website to see a full protocol.

Acetylcholine Dose Response Curves

Please see "**General Pressure Myography" in Chapter 3** for more details. Arteries were cannulated on a DMT pressure myography rig and equilibrated to 60mmHg and 37°C over a 20-minute period. Arteries were pre-constricted to 1μM PE. Ach dose response curve was begun after a diameter plateau period of 5 minutes (D_{PE}). At the end of the experiment, EC health was evaluated via 1μM NS309 and 30mM KCl. Ca2+-free Krebs-HEPES was circulated for 10 minutes at the end of the experiment to get the maximum diameter (D_{MAX}). Percent dilation was calculated as the percent increase in diameter from PE pre-constriction: (D_{Ach} – D_{PE}) / (D_{MAX}-D_{PE}) *100. For Ach experiments with 30μM L-NAME (100mM stocks in diH_2O stored at -20C, Sigma, 5751), the inhibitor was circulated in the bath for 15 minutes prior to PE constriction. Ach is stored as 50μl aliquots at 1M, and is serially diluted prior to experiment for delivering doses. See **Tables 1 and 2** below.

Table 1. Serial dilutions for Ach or PE.

Tube	Drug	dH_2O	$[\ ]_f$ in tube
-1	50µL of 1M	450µL	0.1 M
-2	50µL of -1	450µL	0.01 M
-3	50µL of -2	450µL	0.001 M
-4	50µL of -3	450µL	0.0001 M
-5	50µL of -4	450µL	0.00001 M
-6	50µL of -5	450µL	0.000001 M
-7	50µL of -6	450µL	0.0000001 M
-8	50µL of -7	450µL	0.00000001 M

Table 2. Volume of serial dilutions to pipette into a 10ml system to deliver specific doses of Ach or PE.

Final [Drug] in beaker	add to beaker
$1x10^{-10}$	100µL of -8 (serial dilution tubes)
$1x10^{-9}$	90µL of -7
$1x10^{-8}$	90µL of -6
$3x10^{-8}$	20µL of -5
$1x10^{-7}$	70µL of -5
$3x10^{-7}$	20µL of -4
$1x10^{-6}$	70µL of -4
$3x10^{-6}$	20µL of -3
$1x10^{-5}$	70µL of -3
$1x10^{-4}$	90µL of -2
$1x10^{-3}$	90µL of -1

Measurements on histological sections

Histological sections were cut and stained with Masson's Trichrome or Picosirus red at the UVA Histology Core. Images were taken on a brightfield microscope using a 40X objective. Image analysis was done in ImageJ. The colors of the original image were then separated by "Masson Trichrome stain" color deconvolution (Image → Color → Color Deconvolution → Masson Trichrome). The green (externa) and red (media) images were saved for further analysis while the

dark blue was discarded. The saved images were converted to a black and white mask, and the threshold of green and red were automatically determined by the imagej software (Process → Binary → Convert to Mask).

ROIs were constructed around the red externa and green media in the processed images to exclude noise signal not from the vessel when collecting measurements. Measurements were taken after setting the measurement scale to 92 pixels/20 microns for a 20X image (or 184 pixels/20 microns for a 40X image). Only the stained area of the ROI is collected and recorded for both Masson Trichrome stain colors. To verify that ONLY the Masson Trichrome stained area is collected in the ROI measurement, a new control ROI was built including an empty portion of the image (no stain). The area resulted in a measurement of $0\mu m^2$. Circumference measurements were performed manually in ImageJ.

qPCR

Mesenteric vasculature was trimmed of connective tissue, snap frozen in liquid nitrogen, and stored in -80°C. RNA isolation from tissue was achieved using a Aurum Total RNA Fatty and Fibrous Tissue Kit (BioRad, 7326870). RNA yields were between 40-200 ng/μl. cDNA synthesis was next performed using SuperScript IV Reverse Transcriptase (Thermofisher, 18090050). Total well volume is 20μl with equal amounts of cDNA for each sample loaded in 8μl, and master mix as 12μl and containing: (1) Taqman gene expression master mix (Thermofisher, 4369016), (2) probe of interest, and an (3) in-well control (Taqman probe Mm00437762_m1 B2M VIC PL, Thermofisher, 4448485). Each sample was

loaded in triplicate. Protocol was run using a Biorad Thermal Cycler using a standard protocol for 40 cycles. $\Delta\Delta C_T$ quantification method.

List of probes used for qPCR: ***Eln*** (Taqman probe Mm00514670_m1 Eln FAM-MGB, Thermofisher, 4453320), ***Acta2*** (Taqman Probe: Mm00725412_s1 Acta2 FAM-MGB,Thermofisher, 4331182), ***Fto*** (Taqman Probe: Mm00488755_m1 Fto FAB-MGB, Thermofisher, 4331182), ***Itgav*** (Taqman Probe: Mm00434486_m1 Itgav FAM-MGB, Thermofisher, 4331182), ***Itgb3*** (Taqman Probe: Mm00443980_m1 Itgb3 FAM-MGB, Thermofisher, 4331182), ***Nos3*** (Taqman Probe: Mm00435217_m1 Nos3 FAM-MGB, Thermofisher, 4331182).

Blood pressure measurements

Blood pressure measurements were collected from live, mice via implanted radiotelemetery for a period of five continuous days. Systolic, diastolic, mean arterial pressure (MAP), and heart rate (HR) were analyzed for inactive and active periods as well as 24-hour period.

Collection of blood from mice

Mice were dosed with metofane until loss of toe pinch reflex. The peritoneum was opened up and the diaphragm and ribs were cut and clamped back to expose the beating heart. A 27G needle was connected to a 1ml syringe and flushed with 1M EDTA. The needle was used to puncture the left ventricle where slow pressure was applied to the syringe plunger in order to draw blood into the syringe. Depending on blood test, 250-500μl are collected. Blood samples

were sent to UVA blood lab along with appropriate paperwork to be processed. Results were faxed to lab the next day.

Results

Part I: Vasodilation pathway shift in arteries lacking conical sites for MEJ formation

In Chapter 3, I demonstrate that $Eln^{fl/fl}/Cre^{+}$ mesenteric arteries have a significantly reduced IEL area in both cross-section and *en face* views (**Chapter 3: Figure 48C-F, Figure 49A-C**) that is specific to small resistance arteries (**Chapter 3: Figure 49D-G**). This disruption in the IEL is also present in the thoracodorsal artery (TDA) (**Figure 1**). Since the spatial distribution of PS was disrupted in these arteries (**Chapter 3: Figure 48G-M**), I hypothesized that other MEJ-localized components would also be disrupted, like alpha globin. The protein expression of alpha globin is significantly reduced in mesenteric lysate, and it is no longer polarized to high intensity punctate in the *en face* view (**Figure 2**). The function of alpha globin in the resistance artery endothelium is to bind to and regulate the function of eNOS; thus, I evaluated the extent of alpha globin interactions with eNOS via proximity ligation assay (PLA) in intact third order mesenteric arteries prepared *en face*. Each punctate in a PLA image represents a protein-protein interaction where the two proteins being evaluated are within 40nm of each other. PLA puncta are reduced in arteries from $Eln^{fl/fl}/Cre^{+}$ mice (**Figure 3**). In order to test if this reduced interaction had a functional effect on the vasodilation in intact arteries, I assessed the dilatory capacity to acetylcholine (Ach) in the presence or absence of the NOS inhibitor L-NAME (**Figure 4**). The $Eln^{fl/fl}/Cre^{+}$ arteries had a 61.59% contribution of NO to the dilation elicited by Ach, whereas the $Eln^{fl/fl}/Cre^{-}$ arteries had a -34% contribution of NO. The vasodilation experiments were

performed at 60mmHg based on the myogenic tone of the $Eln^{fl/fl}/Cre^{+}$ arteries (**Chapter 3: Figure 51**). Despite this increased reliance on NO-based signaling, the mRNA expression of EDH-associated potassium channels were unchanged in $Eln^{fl/fl}/Cre^{+}$ mesenteric lysate (**Figure 5**).

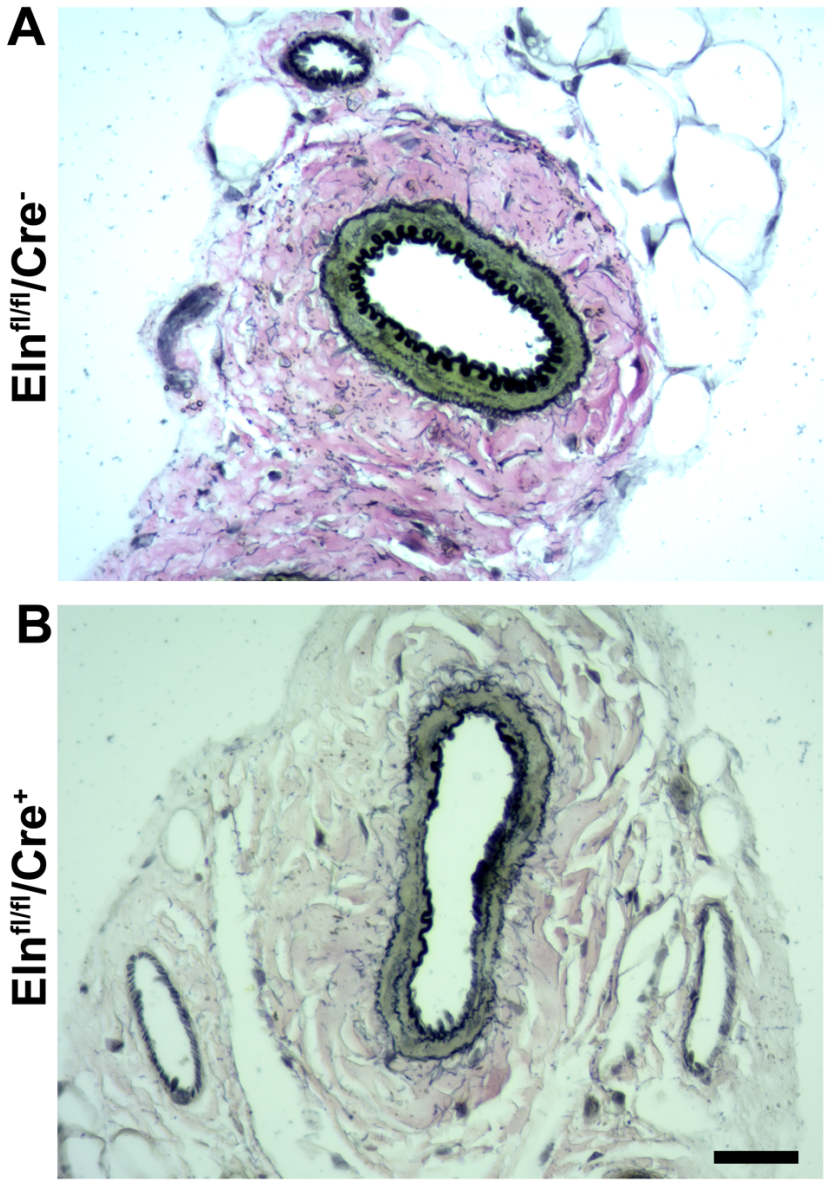

Figure 1. Verhoeff van Gieson histological stain on cross-sections of the thoracodorsal artery. Cross-sections of the thoracodorsal artery from (**A**) $Eln^{fl/fl}/Cre^{-}$ and (**B**) $Eln^{fl/fl}/Cre^{+}$ mice stained with Verhoeff (black) for elastin and van Gieson (pink) counterstain. N=1 per group. Scale bar is 30μm.

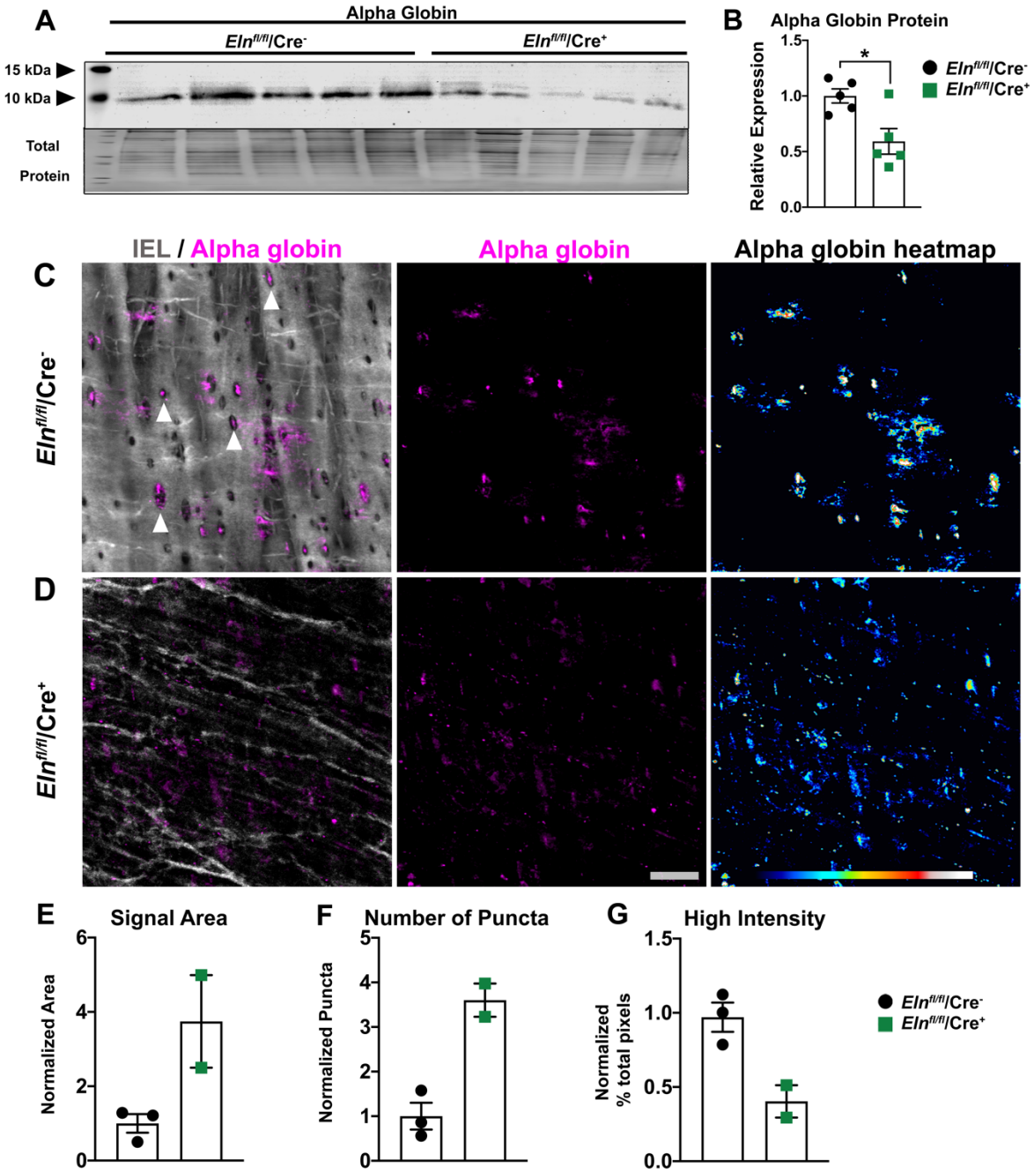

Figure 2. Alpha globin loses its polarized localization to the MEJ without an intact IEL. (**A**) Western blot using mesenteric lysates from $Eln^{fl/fl}/Cre^{-}$ and $Eln^{fl/fl}/Cre^{+}$ mice and stained with an alpha globin antibody (Abcam, ab92492). Total protein was used as a loading control and for quantification. (B) Quantification of alpha globin levels in $Eln^{fl/fl}/Cre^{-}$ and $Eln^{fl/fl}/Cre^{+}$ mesenteric lysate.

N=5 mice per group. Student's t-test and * indicates p = 0.0145. **(C)** *En face* view of third order mesenteric arteries in $Eln^{fl/fl}/Cre^{-}$ and (**D**) $Eln^{fl/fl}/Cre^{+}$ mice. Arteries are stained for alpha globin (magenta), and IEL (hydrazide, grey). Image J was used to produce a heatmap (right column), which displays the signal intensity of alpha globin ranging from low (blue) to high (white). (**E**) The area that alpha globin positive staining covers per image is higher in $Eln^{fl/fl}/Cre^{+}$ mice, along with **(F)** the overall number of puncta. **(G)** Analysis of heatmap pixel intensity demonstrates that $Eln^{fl/fl}/Cre^{+}$ mice have fewer high intensity puncta. N=2-3 mice per group. Scale bar is 10μm.

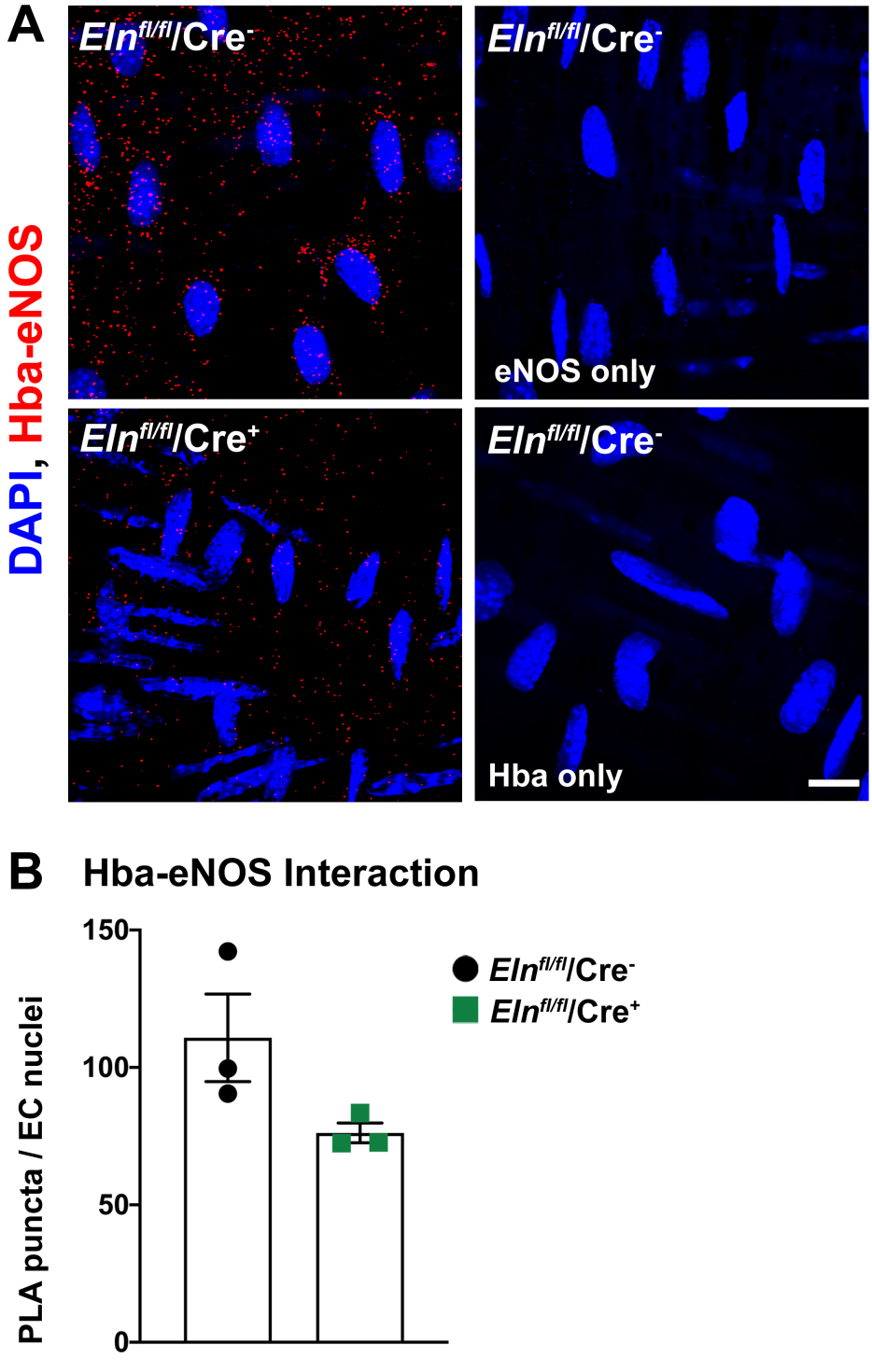

Figure 3. (A) *En face* preparations of third order mesenteric arteries that show a proximity ligation assay (PLA) between alpha globin and eNOS in both $Eln^{fl/fl}/Cre^{-}$

and $Eln^{fl/fl}/Cre^{+}$, and representative images of negative controls where only one primary antibody was applied. Both **(B)** Quantification of PLA puncta per endothelial nuclei in $Eln^{fl/fl}/Cre^{-}$ and $Eln^{fl/fl}/Cre^{+}$ arteries. PLA puncta were identified via automatic thresholding. N=1 mouse per group, n=3 arteries. Scale bars are 10μm.

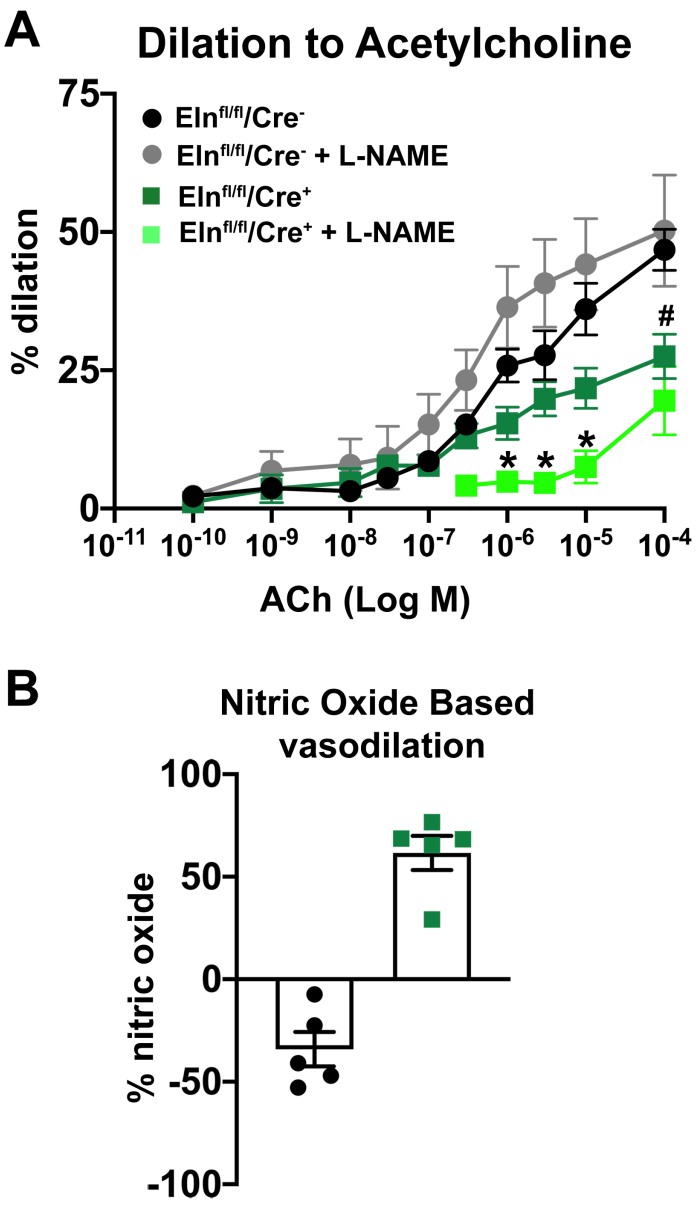

Figure 4. (A) Acetylcholine (Ach) dose response curves were performed on third order mesenteric arteries from $Eln^{fl/fl}/Cre^{-}$ and $Eln^{fl/fl}/Cre^{+}$ mice at 60mmHg. Arteries were pre-constricted to 1-2μM PE prior to starting the Ach Curve. $Eln^{fl/fl}/Cre^{+}$ mice show a reduced capacity to vasodilate to Ach at baseline. Ach curves were also performed in the presence of 30μM L-NAME. Control arteries do not show a reduction in vasodilation in the presence of L-NAME, while $Eln^{fl/fl}/Cre^{+}$ arteries

show a decrease. **(B)** Quantification of the NO component of dilation in control and knockout mice. Each data point represents the calculated difference between the average values for vehicle control and L-NAME groups at each dose. N=3-5 mice per group. Students t-test performed for each dose. # indicates significant difference to $Eln^{fl/fl}/Cre^{-}$ control curve, * indicates significant difference to $Eln^{fl/fl}/Cre^{+}$ control curve.

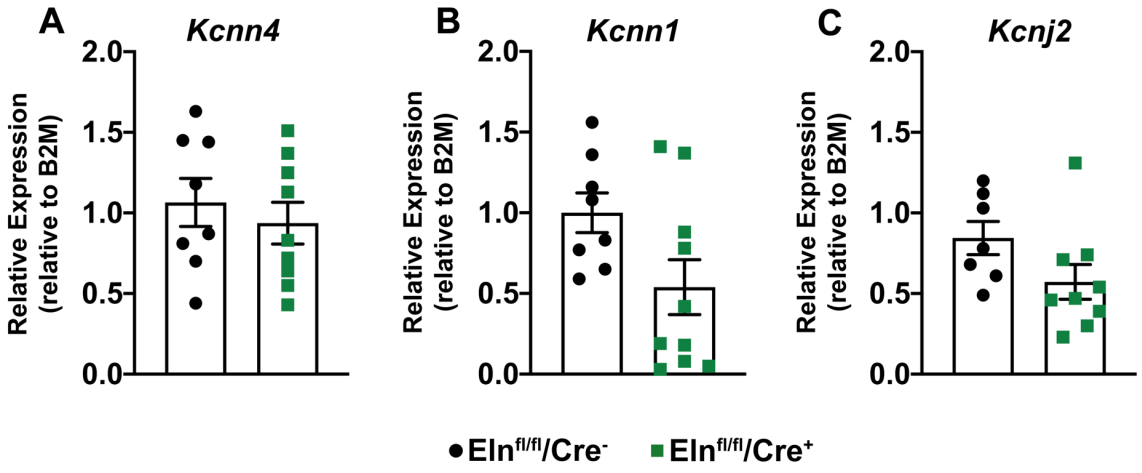

Figure 5. mRNA expression of EDH-associated potassium channels. qPCR results on mesenteric lysate to evaluate the relative mRNA expression of (**A**) *Kcnn4* (IK_{Ca}), (**B**) *Kcnn1* (SK_{Ca}), or (**C**) *Kcnj2* (Kir2.1). N=8-10 mice per group. Student's t-test.

Part II: SMC constriction is reduced in knockout arteries

In addition to the shift in vasodilation pathway, the $Eln^{fl/fl}/Cre^{+}$ arteries exhibited a reduced capacity to constrict to both PE and KCl (**Figure 6**). Histological sections from aorta, carotid, and third order mesenteric arteries were stained with Masson's Trichrome (**Figure 7**) or Picosirius Red (**Figure 8**) to visualize thickness of arterial walls. Masson's Trichrome images were used for quantification such that tunica media (red) could be measured separately from tunica externa (blue) (**Figure 9**). While there were some unexpected differences in thickness in the larger arteries, there were no significant differences in wall thickness or specifically tunica media thickness in the third order mesenteric arteries. This indicates that the reduced ability to constrict is likely not due to reduced SMC thickness in the vascular wall. Initial qPCR results indicate that this reduced contraction is also not due to a reduction of SMC actin or integrin signaling (**Figure 10**). However, these genes were positively correlated with the amount of Eln mRNA in the mesenteric RNA samples (**Figures 11-14**).

Despite the vascular deficiencies within these mice, the blood pressure is normal (**Figure 15**). Blood measurements to evaluate kidney function indicate that kidney function is normal as well, suggesting if any change in BP is caused by elastin deficiency in resistance arteries, that the kidney is not compensating for the deviation from homeostatic BP (**Figure 16**). Lastly, complete blood count (CBC) results do not indicate any major abnormalities in these mice in terms of RBC and WBC characteristics (**Figures 17-18**).

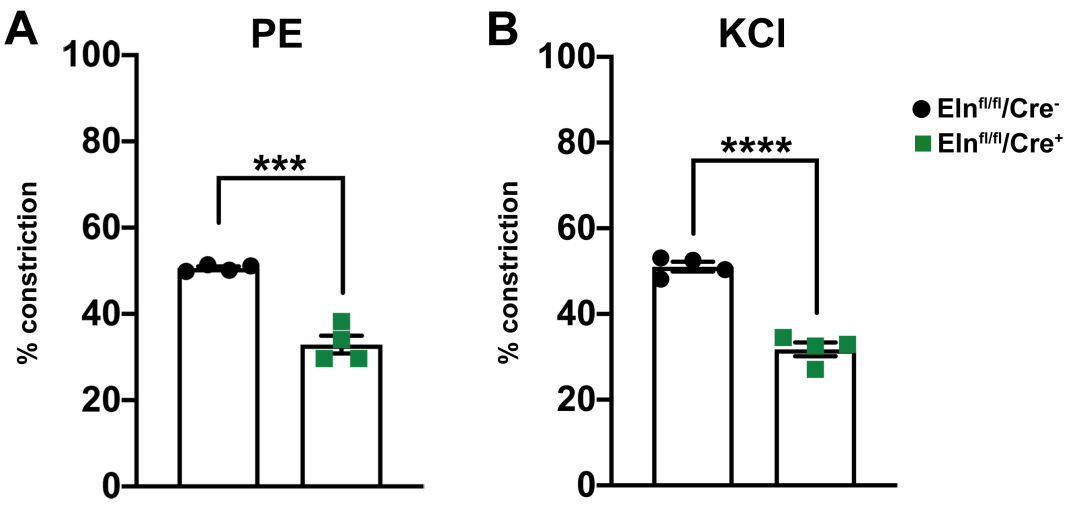

Figure 6. Eln$^{fl/fl}$/Cre^{+} arteries demonstrate decreased constriction. Third order mesenteric arteries constricted with (**A**) 1-2μM PE or **(B**) 30mM KCl. These data were collected in the same experiment as Ach dilation. N=3-5 mice per group. Students t-test. *** indicates p=0.0001 and **** indicates p<0.0001.

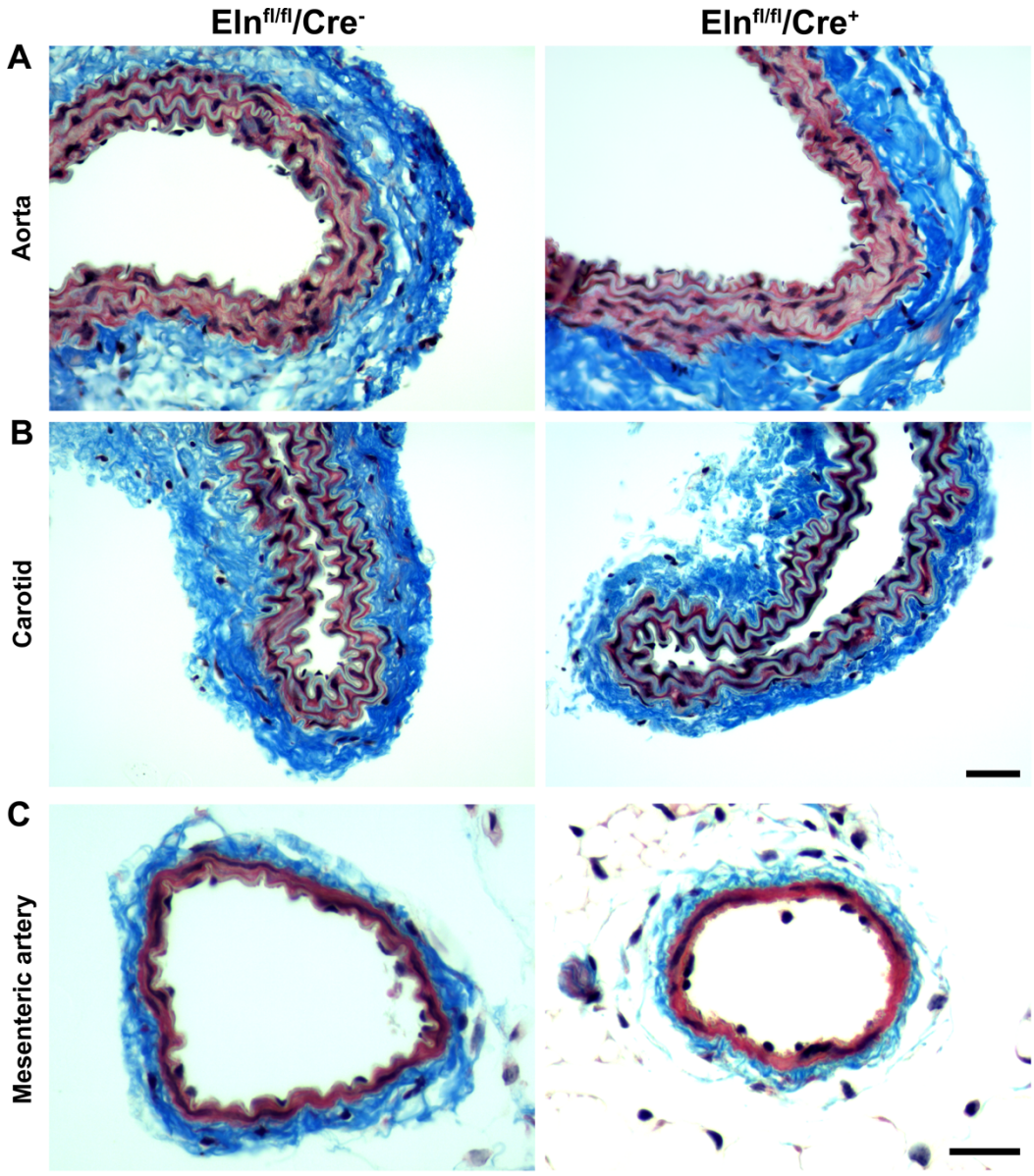

Figure 7. Masson's Trichrome stain. Cross-sections from (**A**) abdominal aorta, (**B**) left carotid artery or (**C**) third order mesenteric artery taken from $Eln^{fl/fl}/Cre^{-}$ and $Eln^{fl/fl}/Cre^{+}$ mice and stained with Masson's trichrome stain, where blue is collagen, pink is cytoplasm, and dark brown is nuclei. Taken with a 40X objective. Mesenteric artery images are cropped and enlarged for visualization. Scale bars are 30μm.

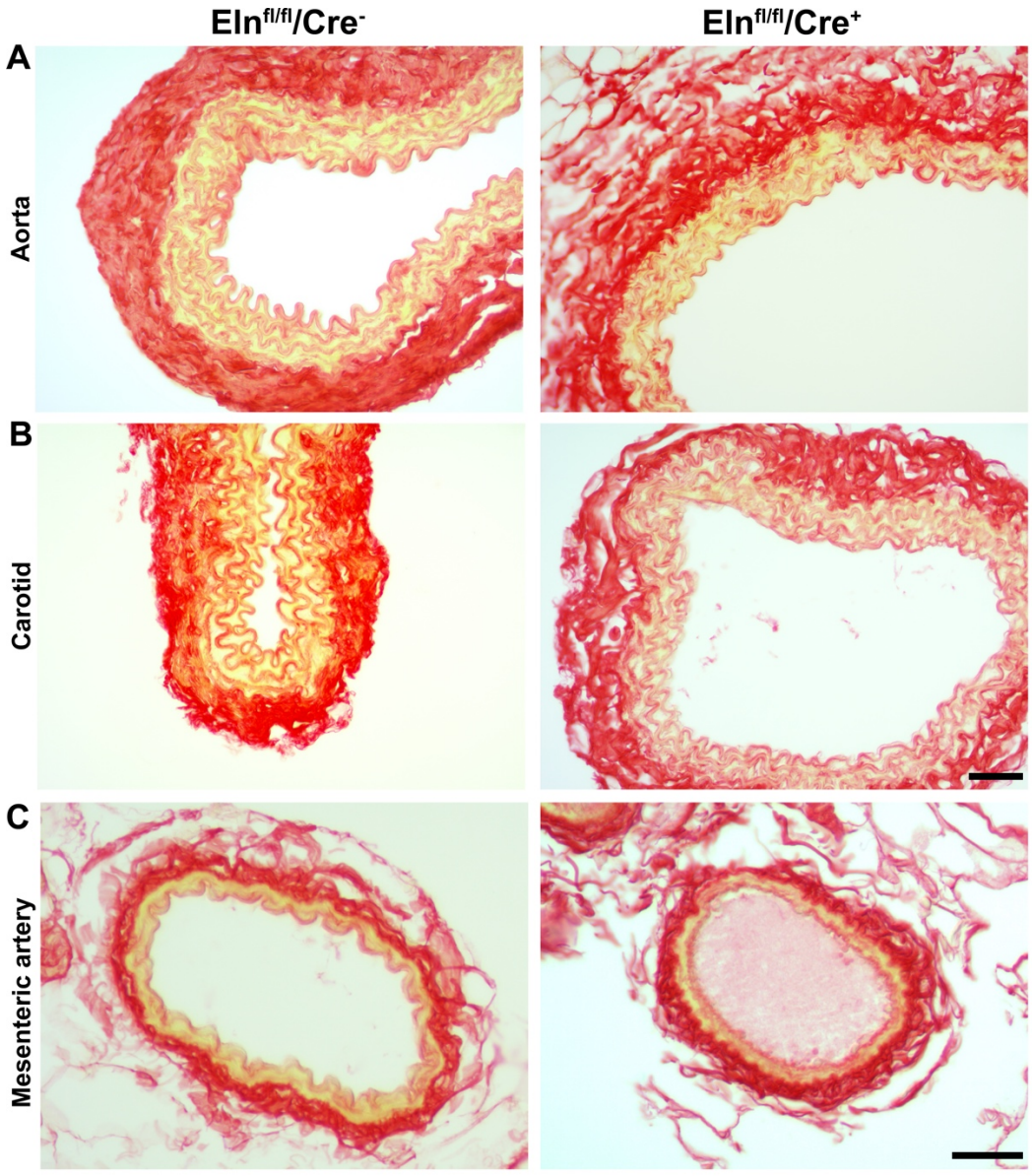

Figure 8. Picosirius Red stain. Cross-sections from (**A**) abdominal aorta, (**B**) left carotid artery or (**C**) third order mesenteric artery taken from $Eln^{fl/fl}/Cre^{-}$ and $Eln^{fl/fl}/Cre^{+}$ mice and stained with Picosirus Red, where nuclei, cytoplasm, and muscular fibers are in yellow and collagen is in red. Taken with a 40X objective. Mesenteric artery images are cropped and enlarged for visualization. Scale bars are 30μm.

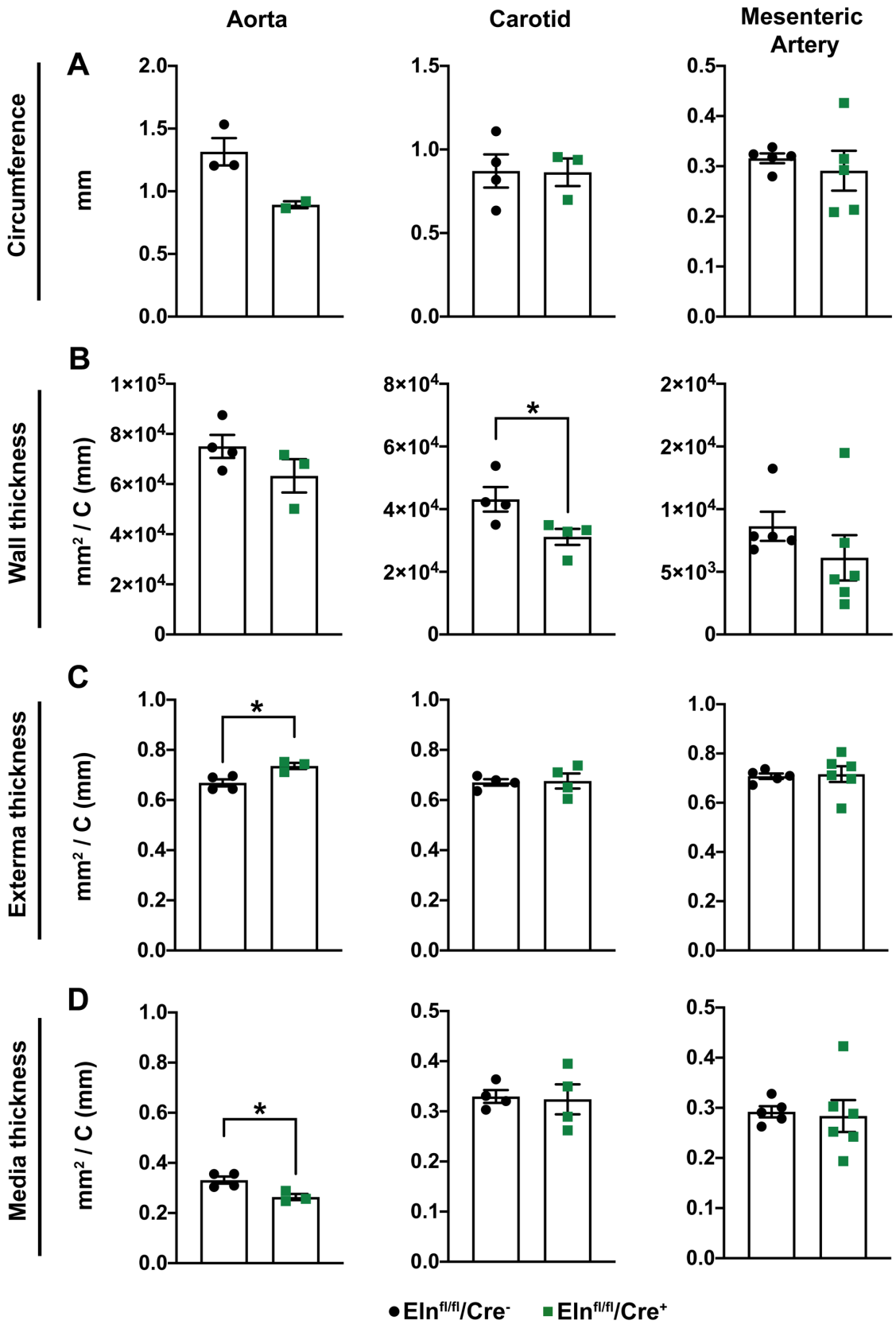
Aorta
Carotid
Mesenteric Artery
A
Circumference
mm
2.0
1.5
1.0
0.5
0.0
1.5
1.0
0.5
0.0
0.5
0.4
0.3
0.2
0.1
0.0
B
Wall thickness
mm² / C (mm)
1×10⁵
8×10⁴
6×10⁴
4×10⁴
2×10⁴
0
8×10⁴
6×10⁴
4×10⁴
2×10⁴
0
*
2×10⁴
2×10⁴
1×10⁴
5×10³
0
C
Exterma thickness
mm² / C (mm)
1.0
0.8
0.6
0.4
0.2
0.0
*
1.0
0.8
0.6
0.4
0.2
0.0
1.0
0.8
0.6
0.4
0.2
0.0
D
Media thickness
mm² / C (mm)
1.0
0.8
0.6
0.4
0.2
0.0
*
0.5
0.4
0.3
0.2
0.1
0.0
0.5
0.4
0.3
0.2
0.1
0.0
Eln^fl/fl/Cre⁻
Eln^fl/fl/Cre⁺

Figure 9. Wall thickness measurements from histological sections. Histological sections stained from $Eln^{fl/fl}/Cre^{-}$ and $Eln^{fl/fl}/Cre^{+}$ mice stained with Masson's Trichrome were used to measure the (**A**) circumference, (**B**) wall thickness, (**C**) tunica externa thickness, and (**D**) tunica media thickness through automatic thresholding in ImageJ. Images where tunica media and externa could not be differentiated in automatic thresholding were excluded. N=3-6 mice per group. Student's t-test. * indicates $p<0.05$.

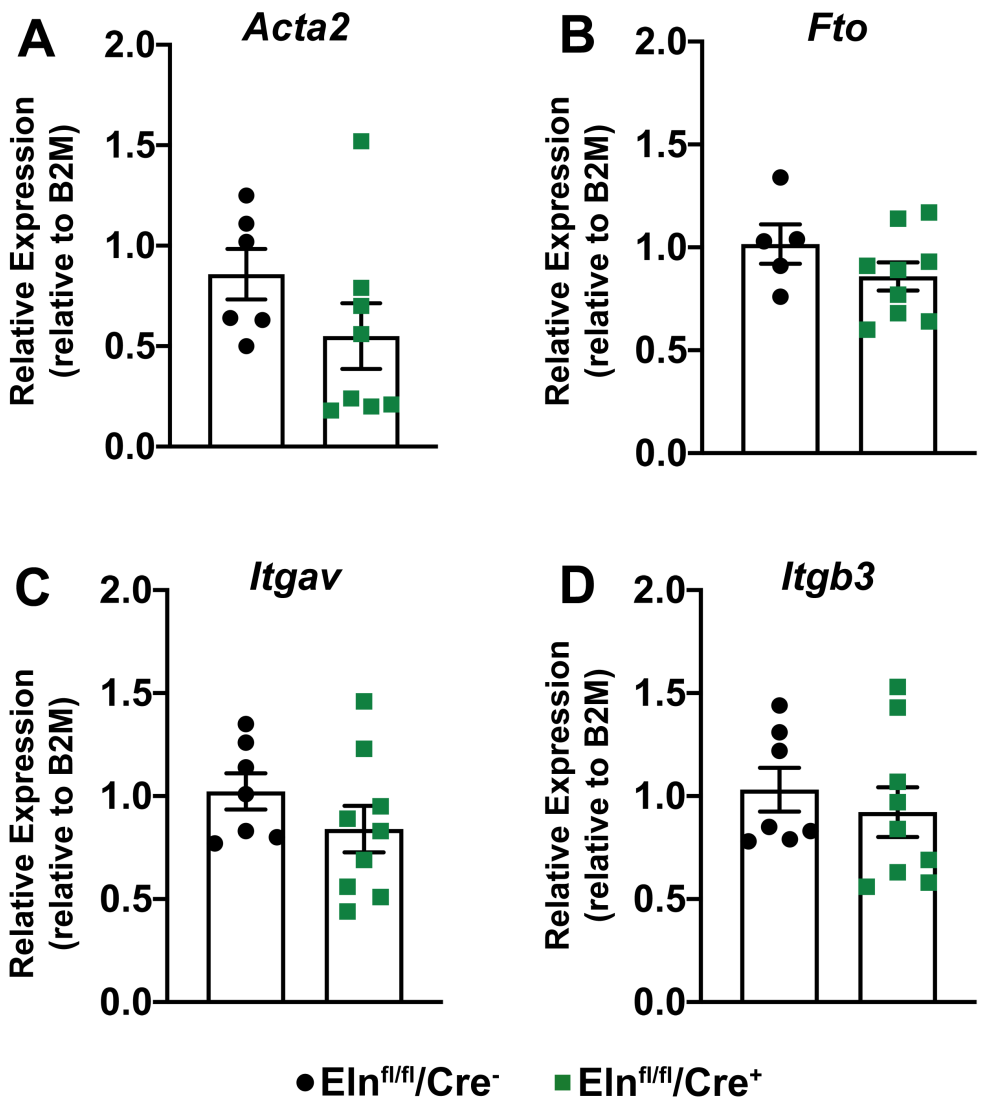

Figure 10. mRNA expression of EDH-associated potassium channels. qPCR results on mesenteric lysate to evaluate the relative mRNA expression of (**A**) *Kcnn4* (IK_{Ca}), (**B**) *Kcnn1* (SK_{Ca}), or (**C**) *Kcnj2* (Kir2.1). N=8-10 mice per group. Student's t-test.

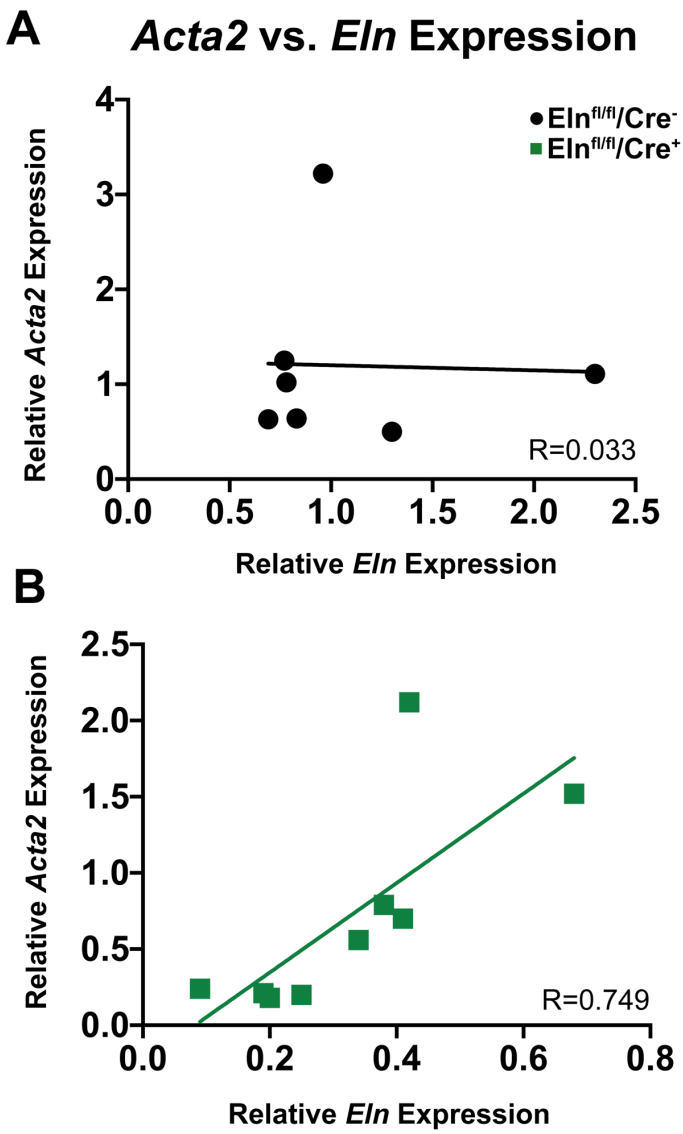

Figure 11. Correlation of *Acta2* and *Eln* mRNA expression. qPCR results on mesenteric lysate to evaluate the relative mRNA expression of *Acta2* versus *Eln* in (**A**) $Eln^{fl/fl}/Cre^{-}$ and (**B**) $Eln^{fl/fl}/Cre^{+}$ mice. N=8-10 mice per group.

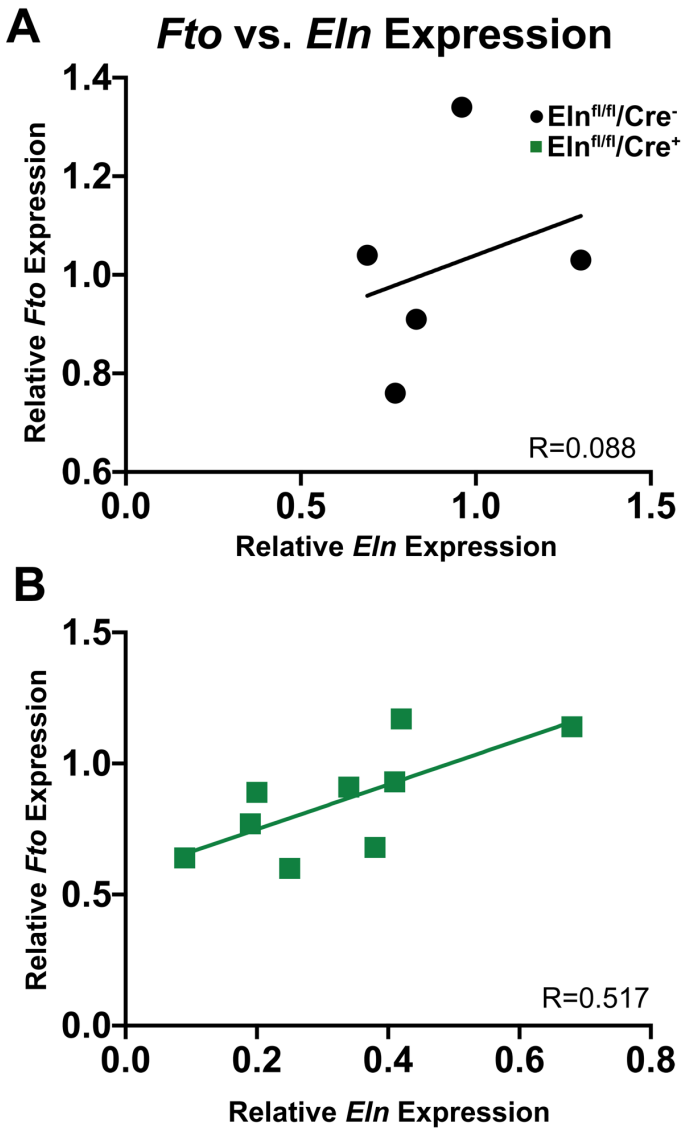

Figure 12. Correlation of *Fto* and *Eln* mRNA expression. qPCR results on mesenteric lysate to evaluate the relative mRNA expression of *Fto* versus *Eln* in (**A**) $Eln^{fl/fl}/Cre^{-}$ and (**B**) $Eln^{fl/fl}/Cre^{+}$ mice. N=8-10 mice per group.

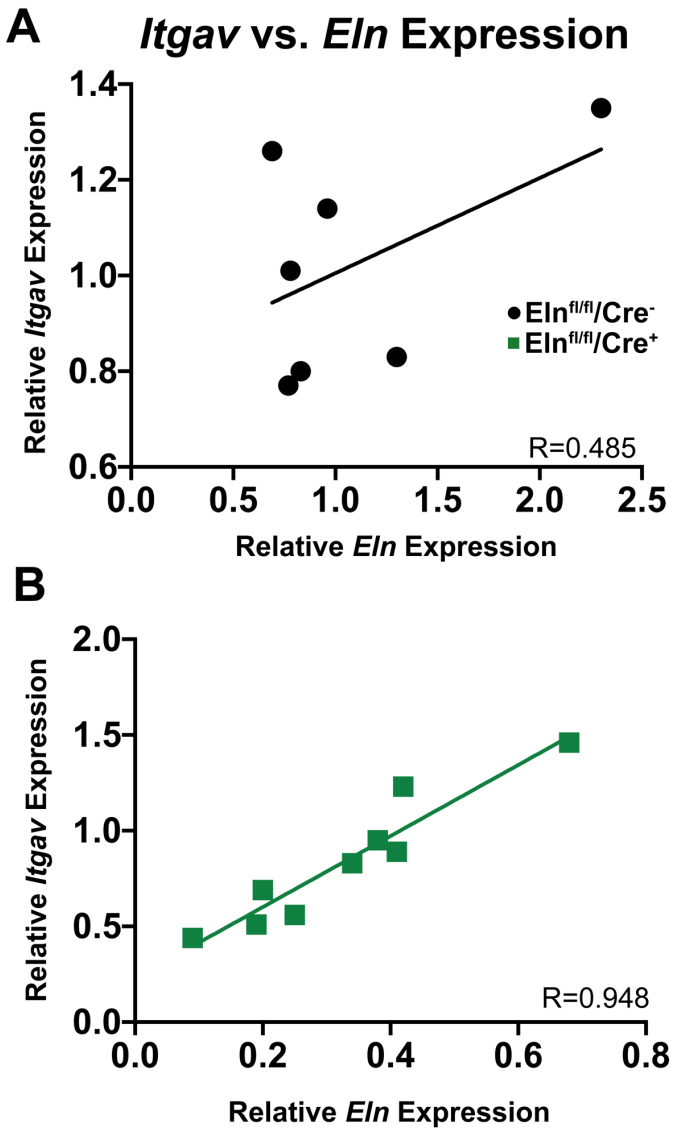

Figure 13. Correlation of *Itgav* and *Eln* mRNA expression. qPCR results on mesenteric lysate to evaluate the relative mRNA expression of *Itgav* versus *Eln* in (**A**) $Eln^{fl/fl}/Cre^{-}$ and (**B**) $Eln^{fl/fl}/Cre^{+}$ mice. N=8-10 mice per group.

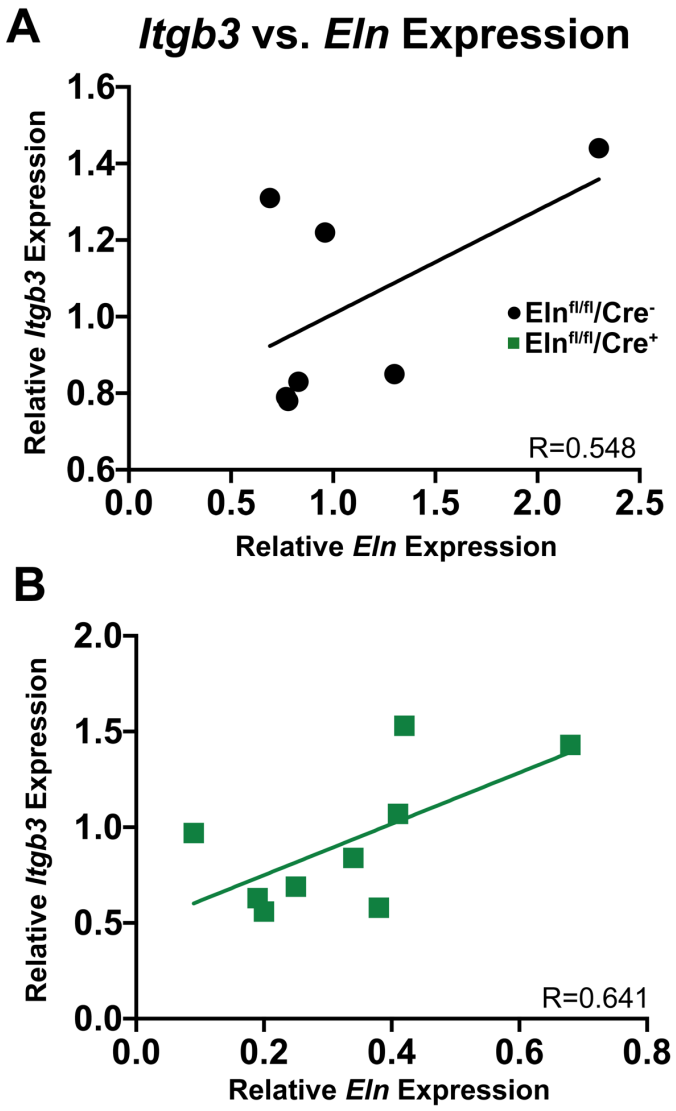

Figure 14. Correlation of *Itgb3* and *Eln* mRNA expression. qPCR results on mesenteric lysate to evaluate the relative mRNA expression of *Itgb3* versus *Eln* in (**A**) $Eln^{fl/fl}/Cre^{-}$ and (**B**) $Eln^{fl/fl}/Cre^{+}$ mice. N=8-10 mice per group.

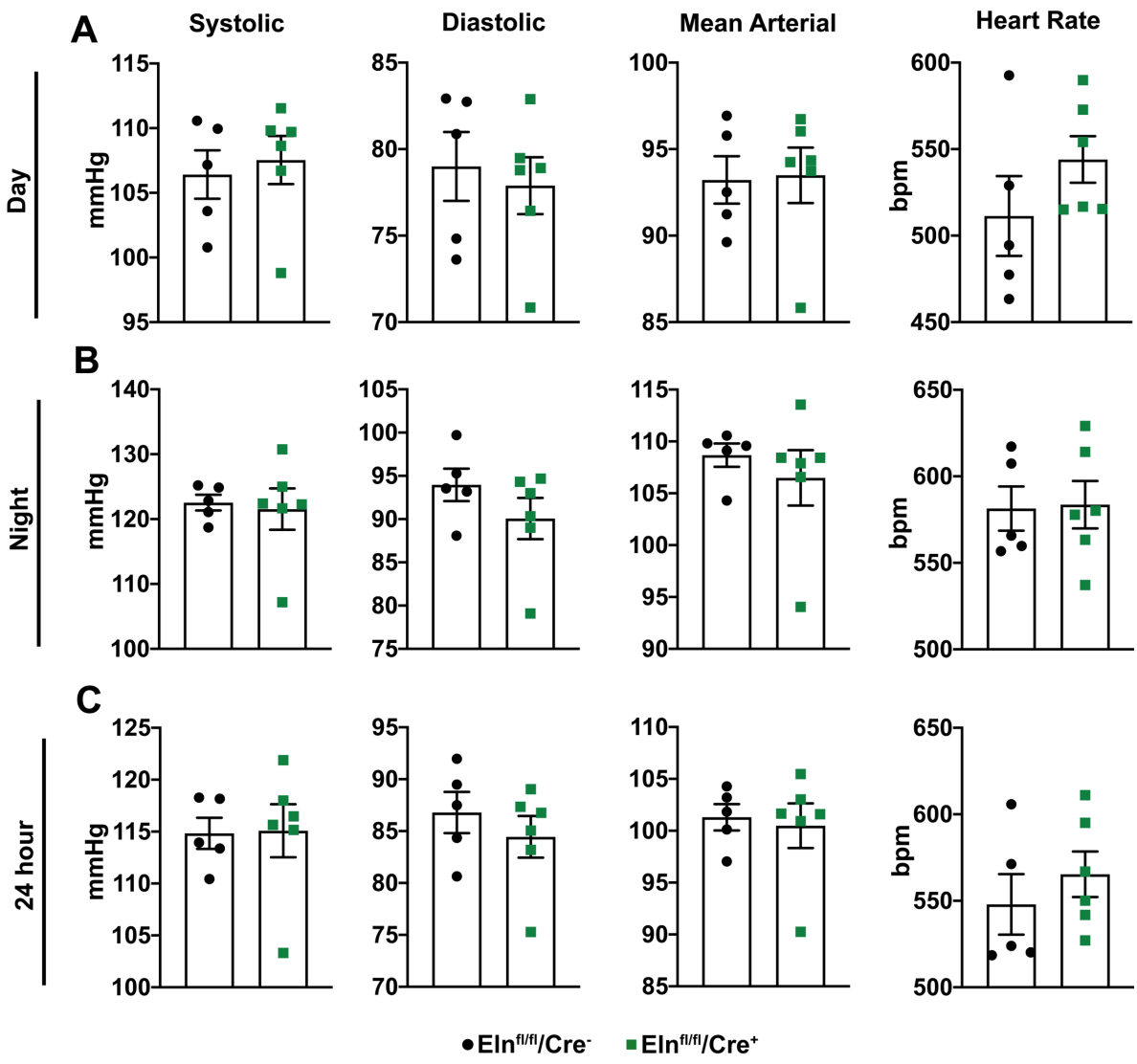

Figure 15. Radiotelemetery blood pressure measurements in Eln$^{fl/fl}$/Cre^{-} and Eln$^{fl/fl}$/Cre^{+} mice. Systolic, diastolic, mean arterial pressures are shown in (mmHg) and heart rate in beats per minute (bpm), with analysis of values during (**A**) day, (**B**) night, or (**C**) averaged over the entire recording period. Values are an average of a 5-day baseline. N=5-6 mice per group.

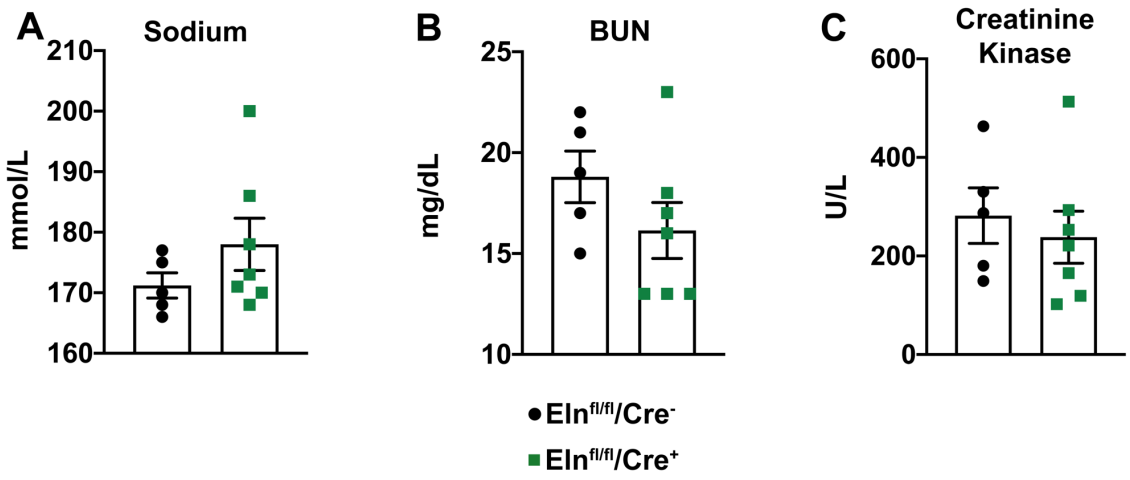

Figure 16. Blood measurements to evaluate kidney function. Measurements of (**A**) sodium, (**B**) blood urea nitrogen (BUN), or (**C**) creatinine kinase from $Eln^{fl/fl}/Cre^{-}$ and $Eln^{fl/fl}/Cre^{+}$ blood. N=5-7 mice per group.

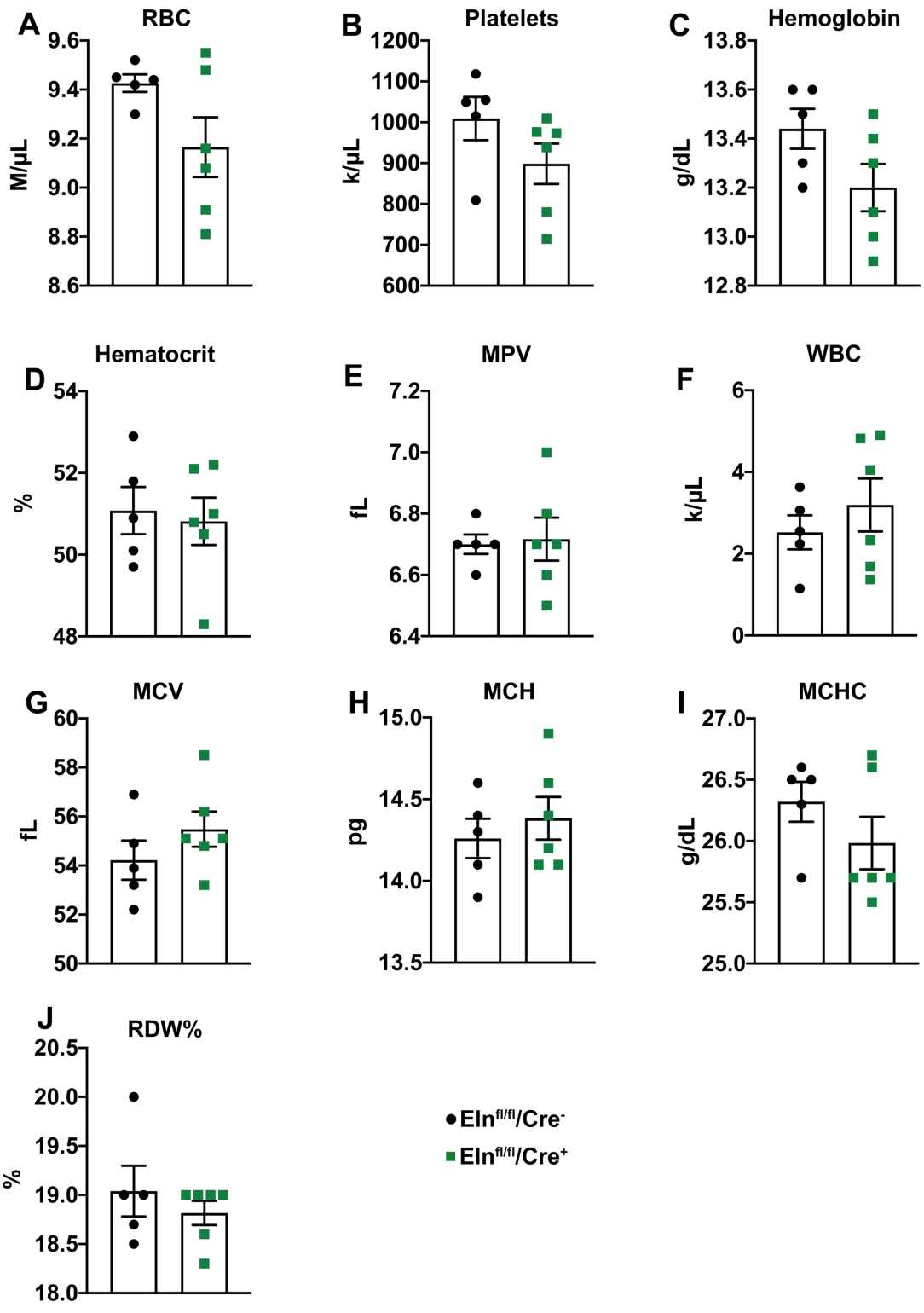

Figure 17. Readouts of complete blood count from Eln$^{fl/fl}$/Cre^{-} and Eln$^{fl/fl}$/Cre^{+} mice. Values for (**A**) Red blood cells, (**B**) platelets, (**C**) hemoglobin, (**D**) hematocrit,

(**E**) mean platelet volume, (**F**) white blood cells, (**G**) mean corpuscular volume, (**H**) mean corpuscular hemoglobin, (**I**) mean corpuscular hemoglobin concentration and (**J**) red cell distribution width. N=5-6 mice per group.

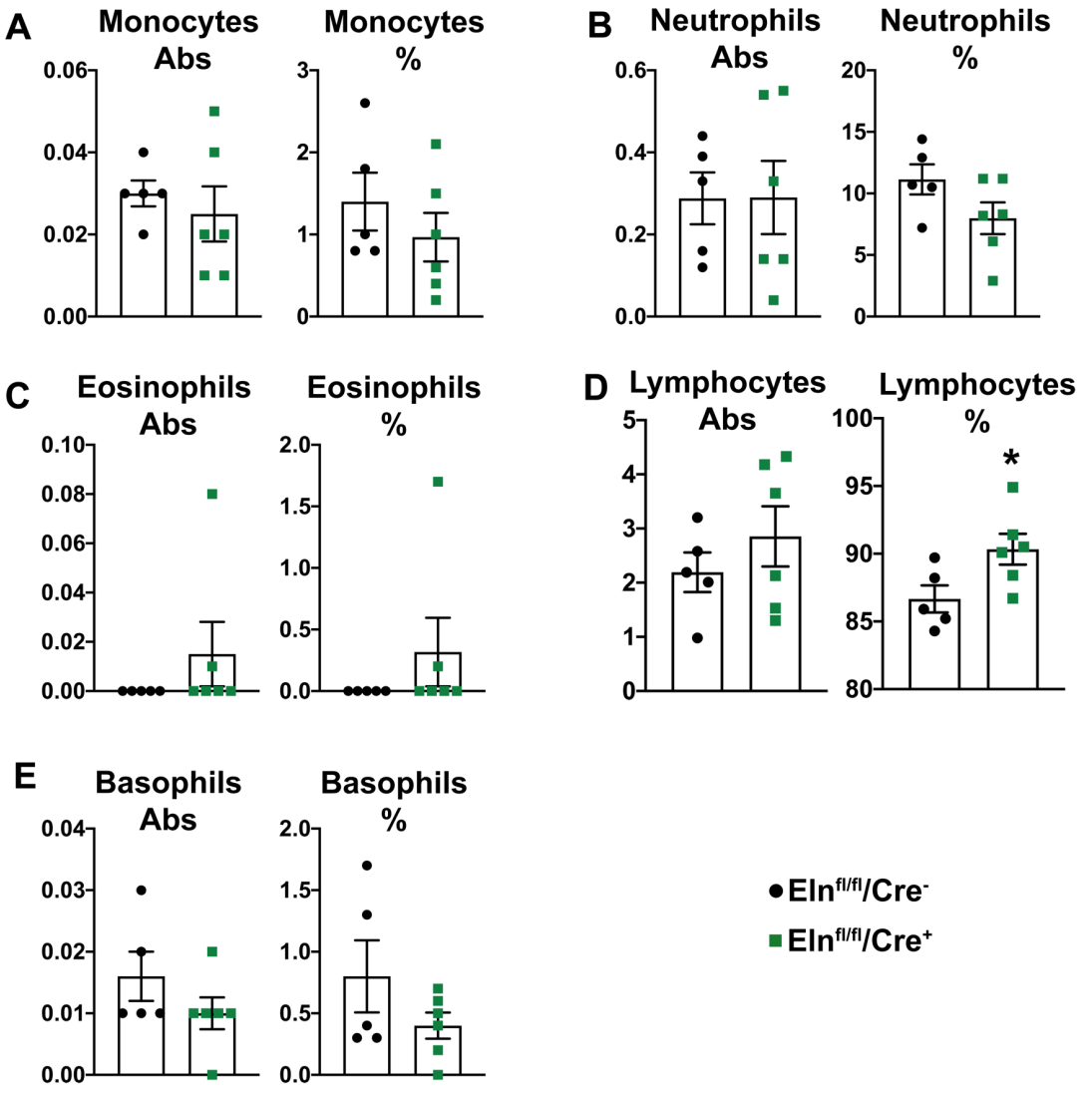

Figure 18. White blood cell distribution in $Eln^{fl/fl}/Cre^{-}$ and $Eln^{fl/fl}/Cre^{+}$ mice. Absolute values and percentage of all WBC for (**A**) monocytes, (**B**) neutrophils, (**C**) eosinophils, (**D**) lymphocytes, and (**E**) basophils. N=5-6 mice per group.

Discussion

Vasodilation in $Eln^{fl/fl}/Cre^{+}$ is predominately NO-based

In **Chapter 3** I introduced a mouse model where elastin is constitutively deleted from ECs and results in a disrupted IEL with loss of canonical sites of MEJ formation in third order mesenteric arteries (**Chapter 3: Figures 48 and 49**), and in this chapter I show evidence of IEL disruption in the TDA, a resistance artery in skeletal muscle. (82) The expression and distribution of an MEJ-localized protein, alpha globin was disrupted in these arteries that do not contain canonical MEJs, which led reduced interactions of alpha globin with eNOS, a major function of alpha globin in resistance arteries (**Figures 2 and 3**). Pressure myography data evaluating the dilation to Ach revealed that the contribution of NO-based signaling was significantly increased in arteries lacking EC elastin, confirming the expected functional consequence for the reduced alpha globin-eNOS interaction. (38, 39) mRNA levels of EDH-associated potassium channels are not changed in $Eln^{fl/fl}/Cre^{+}$ mice (**Figure 5**), and the dilation to EDH-associated agonist NS309 is not significantly changed in $Eln^{fl/fl}/Cre^{+}$ arteries (**Chapter 3: Figure 50B**). The increased reliance on NO vasodilation suggests vasodilation through the EDH pathway would be reduced, yet these data do not indicate a reduced component from the EDH pathway. Future studies should include Ach curves with the EDH inhibitors apamin, TRAM-34, and indomethacin on resistance arteries in order to further test this hypothesis, and should evaluate the protein levels of key EDH mediators, such as IK_{Ca}, TRPV4, and Cx40.

These data are complementary to the data in **Chapter 2** where inducing the formation of MEJs in a conduit artery shifts the vasodilatory mechanisms in the artery. When MEJs are induced in the carotid artery, the vasodilation mechanism swtiches from NO-based to primarily EDH-based, and when canonical MEJ sites are disrupted, there is an increase in NO-based vasodilation to Ach. I have demonstrated disruption of protein and lipid polarization to the MEJ in this mouse model in the $Eln^{fl/fl}/Cre^{+}$ resistance arteries (present chapter and **Chapter 3**); thus, these mice could serve as a tool for investigating additional protein-protein and protein-lipid interactions facilitated by the MEJ. For example, it is likely that the AKAP150-TRPV4 interaction (13) at MEJs is disrupted in this mouse model, which would further implicate the anatomical structure of the MEJ as a prerequisite for protein-protein interactions.

$Eln^{fl/fl}/Cre^{+}$ blood pressure is normal

Arteries from $Eln^{fl/fl}/Cre^{+}$ mice also demonstrate impaired constriction to both PE and KCl (**Figure 6**), which is not due to decreases in media thickness measured from histological cross-sections of arteries (**Figure 7-9**). Due to the variability that can be associated with differences in sectioning tissue, these observations should be confirmed on a TEM ultrastructural level where individual SMC can be identified. TEM analysis of SMC function may also reveal other structural differences, such as decreased SMC-SMC interactions or decreased SMC-ECM interactions, which may could be informative in understanding the impaired contraction phenotype. An initial qPCR screen of contractile machinery

and integrins demonstrate that mRNA regulation is unchanged in these categories (**Figure 10**). However, there are strong positive linear correlations between the relative expression of these genes and relative expression of *Eln* (**Figures 11 and 14**). Future studies should screen additional genes associated with SMC contraction such as *Mhy11*. Integrins associated with SMC contraction should also be investigated. For instance, the decreased expression of these integrins could reduce SMC attachment to ECM and inhibit flux through signaling pathways that promote SMC contraction.

Despite these significant alterations in EC and SMC function, blood pressure measurements taken from alive, freely moving mice indicate there are no changes in baseline BP in $Eln^{fl/fl}/Cre^{+}$ mice (**Figure 15**). We hypothesized that there would be a decreased baseline BP due to the impaired SMC contraction and increased NO production. Since BP were normal, we hypothesized that the kidneys were compensating by increasing BP, and we screened kidney function through a blood panel (**Figure 16**) and there are no significant changes between the two groups. However, there is a trending increase in blood sodium levels which could indicate compensatory salt retention by the animal to maintain higher blood volume and counteract the predicted hypotension (**Figure 16A**). Future studies should involve weighing age- and sex-matched $Eln^{fl/fl}/Cre^{-}$ *and* $Eln^{fl/fl}/Cre^{+}$ mice while controlling for water and food consumption to evaluate if $Eln^{fl/fl}/Cre^{+}$ weigh more.

CBC results indicate Eln as a potential regulator of bone marrow cell differentiation

Basic readouts from CBC tests comparing $Eln^{fl/fl}/Cre^{-}$ and $Eln^{fl/fl}/Cre^{+}$ do not show any significant differences (**Figure 17**); however, there are some trends related to RBC and hemoglobin that are worth discussing, especially since the protein expression of alpha globin in the mesenteric vasculature is significantly decreased (**Figure 2A-B**). The total RBC count is trending lower (**Figure 17A**) and MCV, the average size of RBC, is trending increased (**Figure 17G**). These two results are the inputs of hematocrit (**Figure 17D**), which does not trend in either direction. Together these suggest that overall there are fewer RBC larger in size. The relative range of RBC size between the two groups does not have a trend in either direction (**Figure 17J**). The hemoglobin in the blood and normalized to a group of RBC are both decreased (**Figure 17C** and **Figure 17I**), while the hemoglobin per RBC does not trend in either direction (**Figure 17H**). Overall this could indicate an anemic phenotype in mice that do not produce EC elastin that is exacerbated under stressors such as exercise. Indeed, genetic modification of ECs in the microenvironment of bone marrow in mice has been demonstrated to result in anemia. (265)

RBC and platelet counts are trending down while overall WBC counts have an upward trend in $Eln^{fl/fl}/Cre^{+}$ mice. This could be indicative of differential regulation of bone marrow production of erythrocytes and leukocytes. The only statistically significant result from the CBC data is an increased lymphocyte percentage relative to total WBC in the count. The absolute value of lymphocytes,

although not significant, shows a strong upward trend in $Eln^{fl/fl}/Cre^{+}$ mice. Generally, an upregulation of WBC is indicative of an infection or acute myeloid leukemia. However, these disorders likely have statistically significant increases in WBC much more drastic than the trends here. Further, it is unlikely the mice have contracted an infection due to their clean room housing. The mice also do not appear to be sick or have an altered lifespan.

Chapter 5. IEL composition and stability of HIEL

Abstract

TEM evidence indicates HIEL remain open structures in the absence of EC projections. This raises questions regarding the stability of the HIEL within the ECM layer and suggests there is an intrinsic property of the IEL that prevents recoiling and collapsing of HIEL. In this chapter, I use a mass spectrometry approach to evaluate differential protein composition across third order mesenteric arteries and third order mesenteric veins, in an attempt to identify ECM protein in the resistance artery IEL that contributes to the stability of HIEL. A large majority of proteins detected were cytoskeletal components and SMC proteins, whereas canonical MEJ-localized proteins were not detected, indicating that lowly expressed proteins are not likely to appear on the screen. Nonetheless, differentially expressed ECM proteins were identified, including collagen 14a1 and collagen 12a1. Initial *en face* IHC was not successful in localizing Coll14a1 or Coll12a1 within the arterial wall.

Introduction

Some sections adapted from (* indicates co-first authorship):

Wolpe AG*, Ruddiman CA*, Hall PJ, Isakson BE. Polarized Proteins in Endothelium and Their Contribution to Function. J Vasc Res. 2021;58(2):65-91. doi: 10.1159/000512618. Epub 2021 Jan 27. PMID: 33503620; PMCID: PMC7954879.

In Chapter 3, I outline experiments that demonstrate the role of PAI-1 in MEJ formation. The effect of PAI-1 on HIEL formation is transient, with a maximum HIEL density achieved at day 7 and a wash out effect by day 21. This suggests that PAI-1 is involved in contributing to the stability of HIEL, but how it is doing that is still elusive. PAI-1 as it has been suggested to bind to ECM proteins to prevent proteolytic degradation, (266) and perhaps PAI-1 is binding to a particular ECM protein immediately surrounding the HIEL to contribute to its stability. It is known that in general the IEL layer consists of collagen IV, elastin, lamin-8/10, nidogen, and heparan sulfate proteoglycans; (73, 223-226) and the composition is not uniform across vascular bed or vessel size. (73, 225, 227, 228) To our knowledge, an experiment has not been done that identifies the relative percentage of these

ECM proteins in the IEL of resistance arteries, but a closer look at more lowly expressed ECM proteins could be informative on identifying a candidate that PAI-1 may be binding to in order to promote HIEL stability and thus MEJ formation. It could also reveal unique ECM proteins within mesenteric arteries that themselves promote stability of HIEL openings, by being enriched in the immediate surrounding area of HIEL (independent of PAI-1 binding). To take a closer look at this, we performed mass spectrometry on third order mesenteric arteries and veins.

Materials and Methods

See Chapter 3 for *en face IHC* methodology.

Monitoring HIEL dynamics in intact arteries

Third order mesenteric arteries were cannulated on a pressure myograph designed for a confocal microscope (referred to as Marie's rig in the Isakson Lab). The pressurized artery was visualized using an Olympus FV3000 with a 40X water immersion objective. Z-stacks were obtained using the resonant scanner once every 10 minutes and were processed using deconvolution to obtain high resolution. HIEL were manually identified in tracked across images using Image J.

Mass spectrometry

Third order mesenteric arteries and veins were dissected out at an equal length and homogenized in Krebs buffer. Samples were kept at -80°C for a few days before bringing to the UVA mass spectrometer core. Raw data is available as a Scaffold viewer file (.sf3) on Claire Ruddiman's hard drive.

Results

It is unknown if MEJ and their prerequisite HIEL are temporally dynamic and are capable of forming and retracting over time. In an effort to study HIEL temporal dynamics, pressurized, third order arteries were imaged on a confocal microscope with a water immersion lens (Olympus FV3000, **Figure 1**). The artery was imaged using autofluorescence at baseline, and once every 10 minutes over the course of the hour to track HIEL over time. From this pilot experiment, it was determined that 30.6% of HIEL identified at baseline were not identified at some point throughout the imaging process and 12% had ambiguity during the imaging process. Altogether, 53.6% of HIEL initially detected disappeared during some time points (and later reappeared) or had some ambiguity in their presence. This difficulty in detection was likely due to artery movement in the pressurized system and some photobleaching when imaging the autofluorescence. Thus, this method was not successful in reliably tracking individual HIEL in a large artery, so no conclusions could be made about temporal dynamics of HIEL using this method (**Figure 2**).

In Chapter 4, I demonstrated that every HIEL contains an MEJ via a TEM based approach (**Chapter 3, Figure 20**). In an effort to determine the relationship between the presence of an EC projection in HIEL and the stability of HIEL were, I repeated this TEM analysis on denuded arteries (no ECs), and found the same number of cellular projections in denuded arteries as compared to their intact counterparts, indicating that the stability of an HIEL is not dependent on the presence of a cellular projection (**Figure 3**).

Thus, it is unclear what may contribute to the stability of an HIEL. One possibility is an enrichment of ECM proteins surrounding HIEL to make the openings more rigid and less likely to recoil in the event of an EC denudation. In fact, in *en face* views of the IEL (**Figure 4**), it is apparent that some HIEL have a brighter hydrazide signal surrounding them; thus, I hypothesized that a unique ECM protein was being deposited around HIEL for stability. To identify potential candidates, I sent third order mesenteric arteries and veins, which do not have the same IEL morphology as arteries (**Figure 5**), to be analyzed via mass spectrometry for differential protein enrichment analysis.

There were 930 unique proteins detected (90% confidence level) each with at least 1 spectra that mapped back to the protein identified. In total, 14099 total spectra (0.21% decoy FDR) were identified across both samples. First, I checked for the detection of known EC proteins in my sample (**Table 1**), and although low total spectra counts (TSC), PECAM-1, eNOS, and ACE, among others were detected. The low TSC on EC proteins may be due to the overabundance of SMC and cytoskeletal components, categories which had the highest TSC across all detected proteins (**Tables 2 and 3**). The majority of MEJ-localized proteins, representing a small population of all EC proteins, were not detected in the arterial sample (**Table 4**).

A total of 20 unique ECM proteins were detected via mass spectrometry, and 10 of them were unique collagen isoforms (**Table 5**). The TSC for surprisingly low for Col4a1 and Col4a2, the former of which was only detected in venous sample. Col6a1 and Col6a3 had relatively high TSC and there was approximately

equivalent detection in both the artery and vein. Col1a1 and Col1a2 were identified as being enriched in the venous samples. The collagen isoforms Col12a1 and Col14a1 were identified as potential ECM proteins that were unique to the arterial sample as potential protein that surrounds HIEL to contribute to the stability. Two different antibodies per isoform were tested on *en face* preparations to determine if there was localization near HIEL (**Figures 6 and 7**); however, antibody signal appeared nonspecific in most cases despite testing antibodies from different companies, experimenting with different fixation methods (4% PFA vs 1:1 methanol:acetone), and testing on different micro-vessels: intact arteries, denuded arteries, and intact mesenteric veins. The image of Col14a1 fixed with 4% PFA and detected via the Thermofisher antibody (**Figure 7A**) indicates there could be some expression of this isoform within ECs, but it is unclear if deposition into the IEL occurs. Lastly, in addition to collagen isoforms, fibrinogen, nidogen, and heparan sulfate proteoglycans (hpsg) were also detected as expected in these samples.

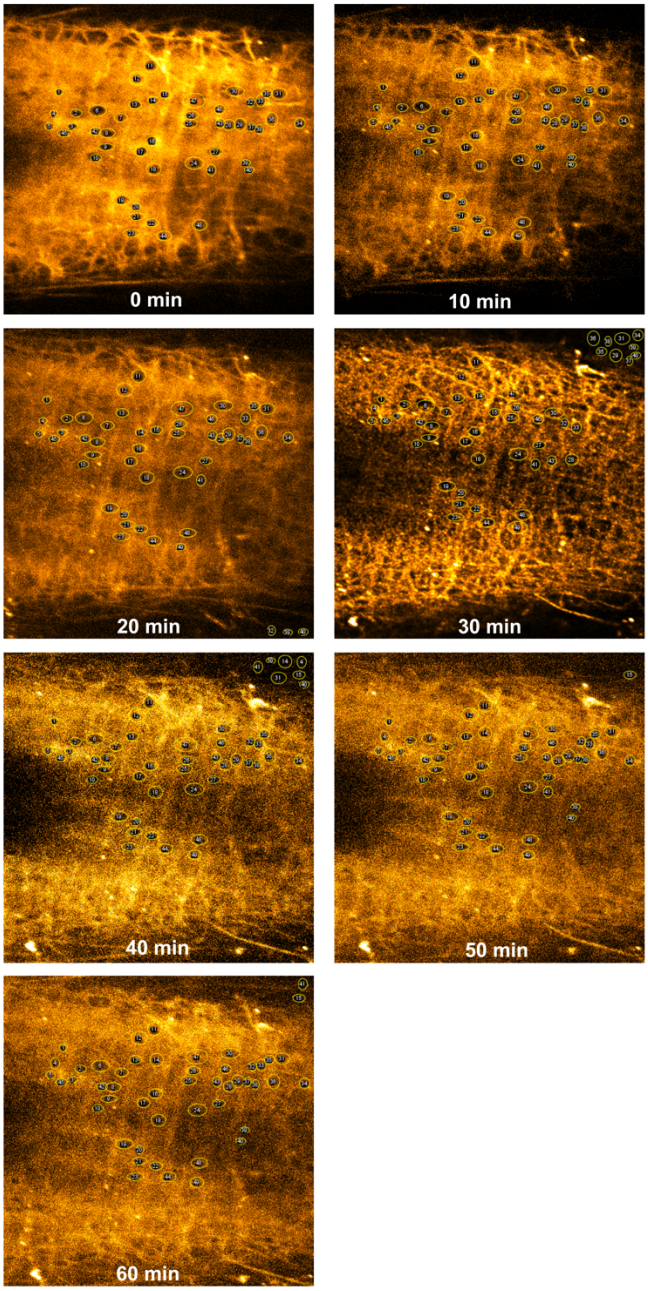

Figure 1. Autofluorescence of live pressurized arteries over one hour. One area of an intact third order mesenteric artery was imaged on an Olympus Fluoview 3000 with a water immersion lens every 10 minutes. HIEL were tracked from each timepoint to the next.

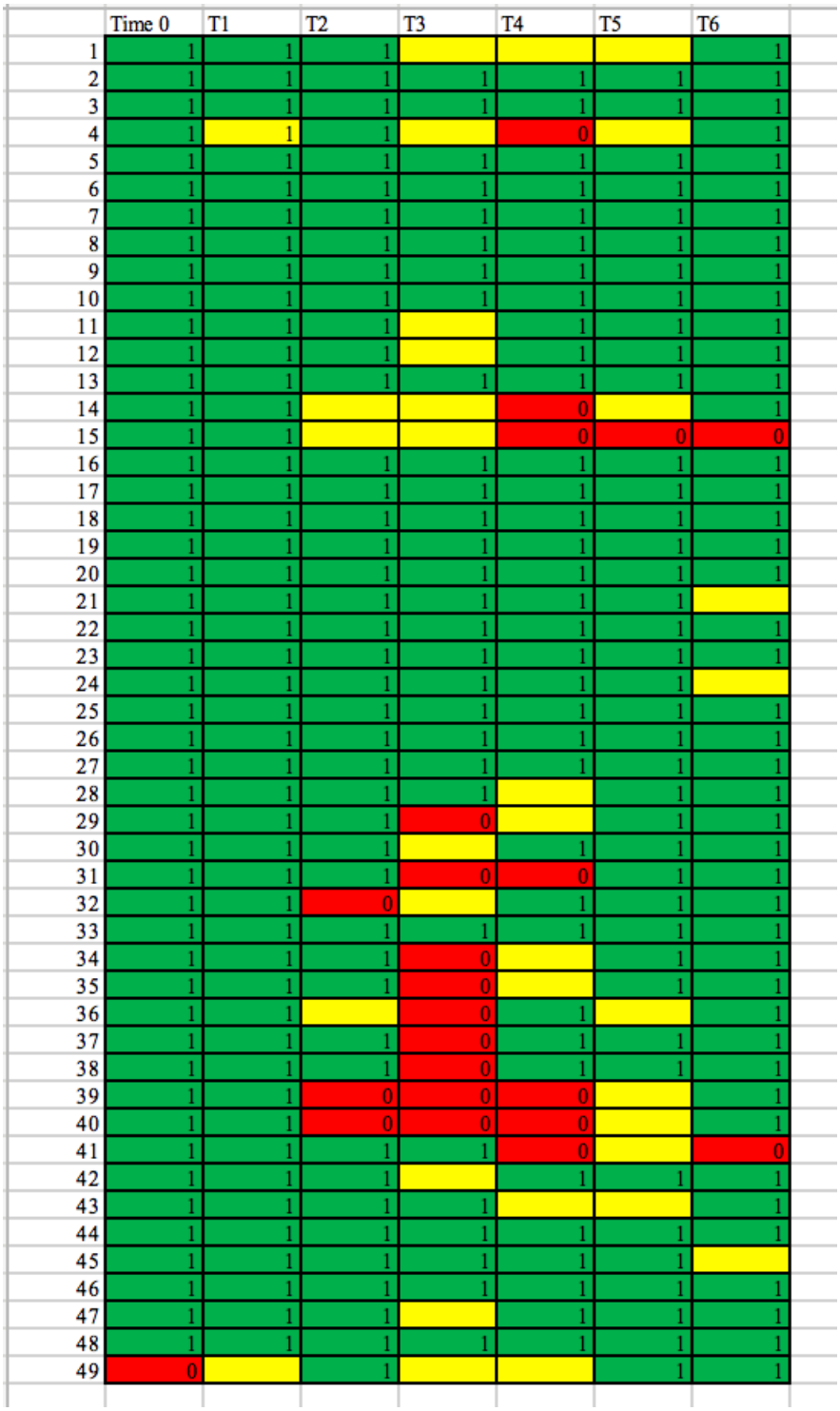

	Time 0	T1	T2	T3	T4	T5	T6
1	1	1	1				1
2	1	1	1	1	1	1	1
3	1	1	1	1	1	1	1
4	1	1	1		0		1
5	1	1	1	1	1	1	1
6	1	1	1	1	1	1	1
7	1	1	1	1	1	1	1
8	1	1	1	1	1	1	1
9	1	1	1	1	1	1	1
10	1	1	1	1	1	1	1
11	1	1	1		1	1	1
12	1	1	1		1	1	1
13	1	1	1	1	1	1	1
14	1	1			0		1
15	1	1			0	0	0
16	1	1	1	1	1	1	1
17	1	1	1	1	1	1	1
18	1	1	1	1	1	1	1
19	1	1	1	1	1	1	1
20	1	1	1	1	1	1	1
21	1	1	1	1	1	1	
22	1	1	1	1	1	1	1
23	1	1	1	1	1	1	1
24	1	1	1	1	1	1	
25	1	1	1	1	1	1	1
26	1	1	1	1	1	1	1
27	1	1	1	1	1	1	1
28	1	1	1	1		1	1
29	1	1	1	0		1	1
30	1	1	1		1	1	1
31	1	1	1	0	0	1	1
32	1	1	0		1	1	1
33	1	1	1	1	1	1	1
34	1	1	1	0		1	1
35	1	1	1	0		1	1
36	1	1		0	1		1
37	1	1	1	0	1	1	1
38	1	1	1	0	1	1	1
39	1	1	0	0	0		1
40	1	1	0	0	0		1
41	1	1	1	1	0		0
42	1	1	1		1	1	1
43	1	1	1	1			1
44	1	1	1	1	1	1	1
45	1	1	1	1	1	1	
46	1	1	1	1	1	1	1
47	1	1	1		1	1	1
48	1	1	1	1	1	1	1
49	0		1			1	1

Figure 2. Detection of HIEL in pressurized, intact arteries over one hour. Visual summary of HIEL tracking from images in Figure 1, where 48 HIEL were

identified in the baseline image. Each column represents the image taken at the next timepoint in the experiment. Green indicates successful detection of that HIEL, yellow indicates ambiguity in detection, and red indicates not detected.

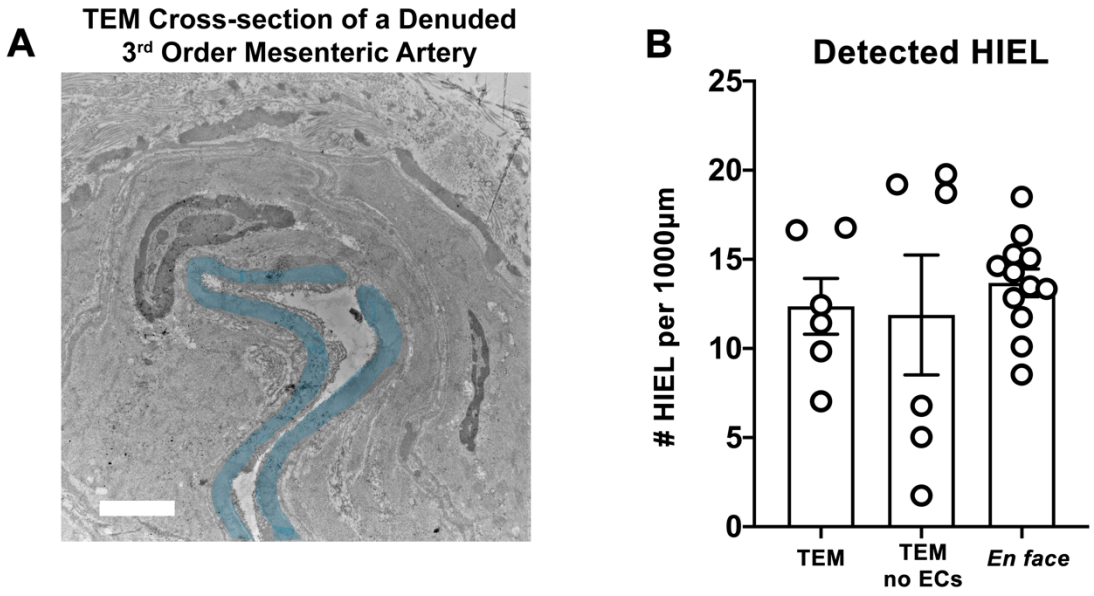

Figure 3. HIEL detection in denuded third order mesenteric arteries. (**A**) Transmission electron microscopy image of a denuded third order mesenteric arterial cross-section at 4K magnification. IEL is pseudo-colored in blue. Scale bar 2.5µm. (**B**) Quantification of HIEL per 1000µm measured in TEM cross-sections or back calculated from *en face* views. For denuded TEM, N=6 mice, n=6 arteries, n=3-7 TEM sections, and 533-607µm IEL length quantified per mouse. For intact TEM, N=6 mice, n=6 arteries, n=3-5 TEM sections, and 570-964µm IEL length quantified per mouse. For *en face*, N=4 mice, n=4 arteries, n=12 ROIs, Area=$1.67 \times 10^5 \mu m^2$. Statistical test.

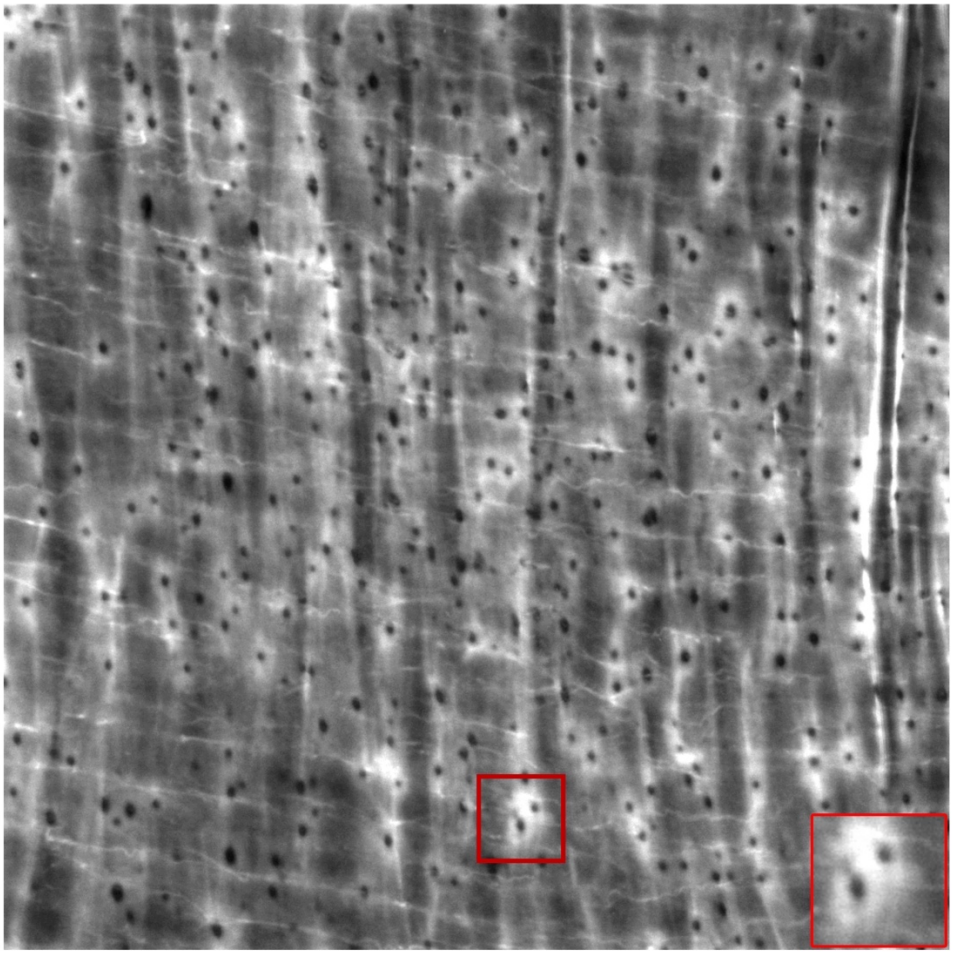

Figure 4. *En face* view of IEL from a third order mesenteric artery. The IEL was detected using Alexa Fluor linked hydrazide. Red box is a zoomed in view of two HIEL that have brighter hydrazide signal surrounding them compared to the rest of the image.

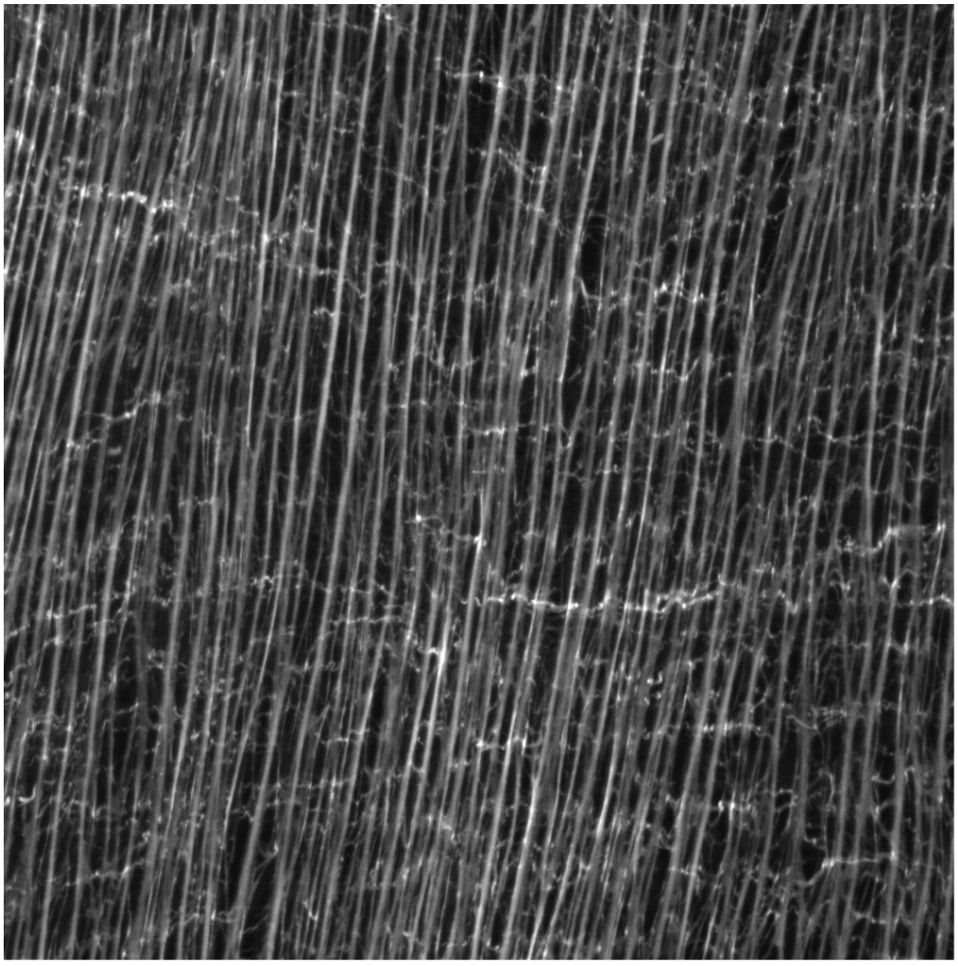

Figure 5. *En face* view of IEL from a mesenteric vein. The IEL was detected using Alexa Fluor linked hydrazide.

Protein	Fold Change	Artery TSC	Vein TSC
ACE	0.0	1	0
Akap12	1.2	2	2
Calnexin	2.4	2	4
Calreticulin	0.9	19	14
Cav1	13	1	11
eNOS	0.0	1	0
PECAM-1	0.7	5	3
Phosphotyrosine phosphatase	0.0	2	0
Cluster of vWF	17	3	42
vWF A domain	2.4	1	2

Table 1. EC proteins detected. Higher fold change values indicate enrichment in venous sample. TSC is total spectra count.

Protein	Fold Change	Artery TSC	Vein TSC
Acta1	0.8	460	299
Caldesmon	0.9	50	37
Calponin-1	1.0	51	41
Desmokoyin	1.7	76	105
Filamin	0.9	252	188
Myosin 6	1.5	87	111
Myosin 11	1	392	325
Myosin light chain kinase	0.5	64	27
Transgelin	0.6	199	94
Tropomyosin $\alpha 1$-chain	1.1	85	81
Tropomyosin β-chain	0.9	99	73

Table 2. SMC proteins detected. Higher fold change values indicate enrichment in venous sample. TSC is total spectra count.

Protein	Fold Change	Artery PD	Vein PD
Alpha actinin 1	0.5	137	56
Tubulin β5	0.8	141	99
Vimentin	1.3	260	279

Table 3. Cytoskeletal proteins detected. Higher fold change values indicate enrichment in venous sample. TSC is total spectra count.

Protein	Fold Change	Artery TSC	Vein TSC
Cx37	N/A	ND	ND
Cx40	N/A	ND	ND
Cx43	N/A	ND	ND
IK_{Ca}	N/A	ND	ND
IP3R	N/A	ND	ND
PAI-1	N/A	ND	ND
SK_{Ca}	N/A	ND	ND
TRPV4	N/A	ND	ND

Table 4. Proteins not detected. Known proteins that are functionally crucial for mesenteric arterial function that were not detected in the mass spectrometry sample readouts. TSC is total spectra count.

Protein	Fold Change	Artery TSC	Vein TSC
Col1a1	4.2	2	7
Col4a1	INF	0	2
Col6a1	1.3	18	20
Col12a1	0.0	1	0
Col14a1	0.0	21	0
Col18a1	0.7	5	3
Col1a2	6.0	5	25
Col4a2	3.6	1	3
Col6a2	1.8	6	9
Col6a3	1.9	45	70
Cspg4	0	6	0
Elastin	0.9	4	3
Fibrinogen α-chain	4.5	4	15
Fibrinogen β-chain	11	2	19
Fibrinogen γ-chain	11	2	19
Fibrillin-1	2.1	17	20
Fibronectin	INF	0	3
Hpsg2	1.5	19	24
Nidogen	1.5	13	16
Cluster of Nidogen	INF	0	7

Table 5. Matrix proteins detected. Higher fold change values indicate enrichment in venous sample. TSC is total spectra count.

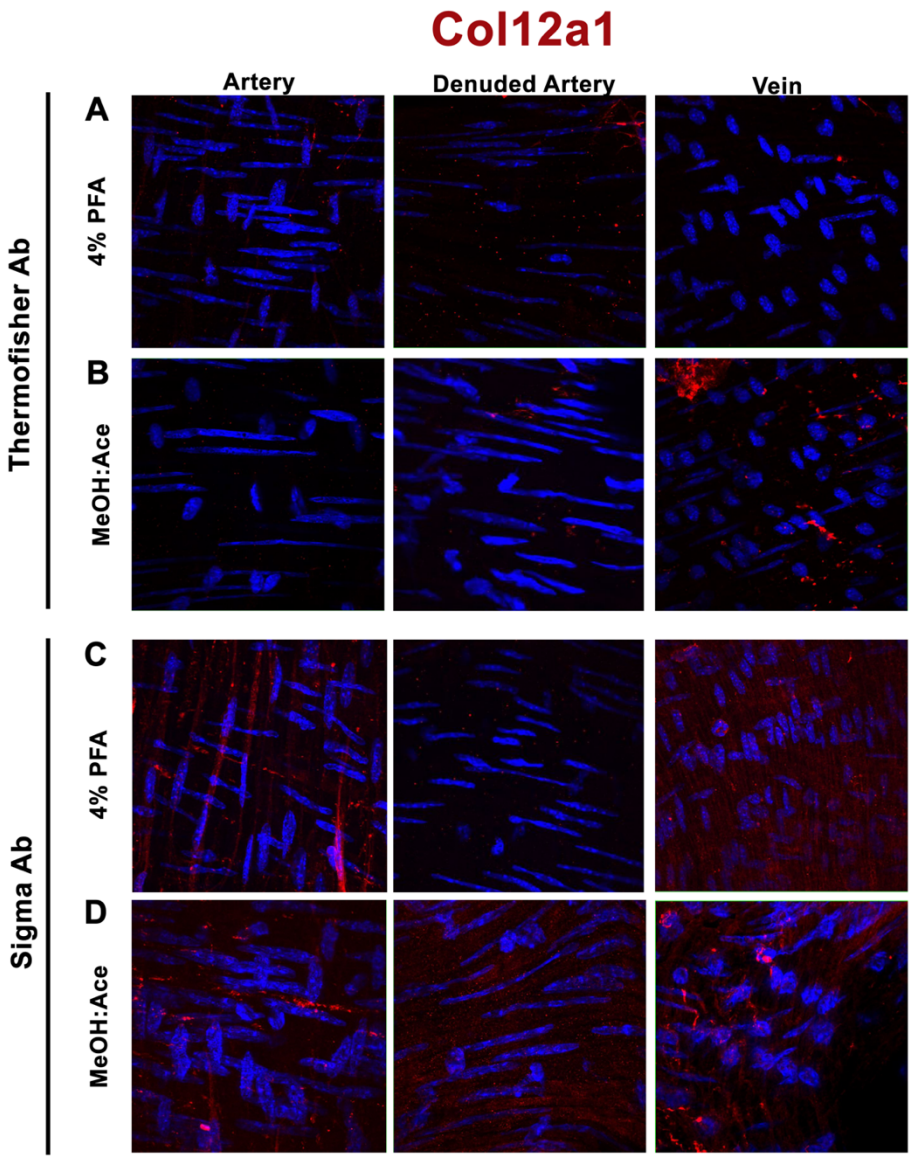

Figure 6. *En face* detection of Col12a1. An antibody from Thermofisher (Cat #, PA5-38890) was used to detect Col12a1 in intact or denuded third order mesenteric arteries and mesenteric vein that were fixed with either (**A**) 4% PFA or (**B**) a 1:1 mixture of icecold methanol to acetone. An antibody from Sigma (Cat #, HPA009143) was used to detect Col12a1 in intact or denuded third order mesenteric arteries and mesenteric vein that were fixed with either (**C**) 4% PFA or (**D**) a 1:1 mixture of ice-cold methanol to acetone.

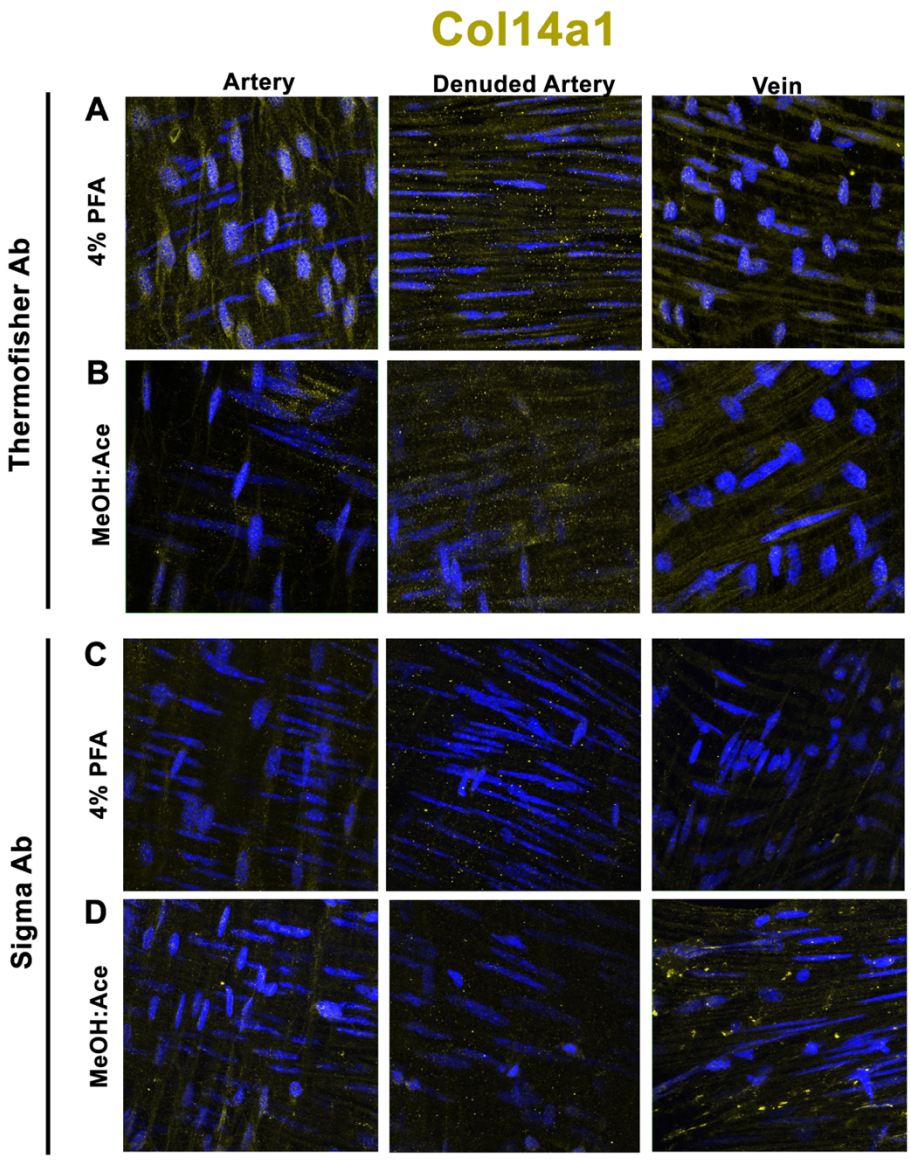

Figure 7. *En face* detection of Col14a1. An antibody from Thermofisher (Cat #, PA5-49916) was used to detect Col14a1 in intact or denuded third order mesenteric arteries and mesenteric vein that were fixed with either (**A**) 4% PFA or (**B**) a 1:1 mixture of icecold methanol to acetone. An antibody from Sigma (Cat #, SAB4503061) was used to detect Col14a1 in intact or denuded third order mesenteric arteries and mesenteric vein that were fixed with either (**C**) 4% PFA or (**D**) a 1:1 mixture of ice-cold methanol to acetone.

Discussion

The same length of third order mesenteric artery and vein were sent to mass spec for analysis, where the amount of protein detected was 11μg and 6μg, respectively. This alone is an interesting finding in that there is approximately double the amount of protein in an equal length of artery compared to vein. This is likely due to the increased amount of SMC in the arterial sample compared to the vein sample (**Tables 2, 3**). Because of this, EC proteins may appear more enriched in the venous samples compared to SMC-rich arterial samples. Thus, any enrichment of non-SMC proteins in venous sample should be followed up by additional experimentation such as IHC experiments, western blot, or additional mass spectrometry analysis. This also applies to any ECM proteins identified as enriched in the venous sample.

Despite the overabundance of SMC diluting detection of other proteins in the sample, there were still two collagens of interest that were detected in the arterial and not the venous sample, Col14a1 and Col12a1. My initial experiments were not able to show localization of these collagen isoforms to the IEL (**Figures 6 and 7**). A reason for this could be lack of antigen accessibility by the antibody. Future experiments should reinvestigate these collagen isoforms and include an antigen retrieval step, similar to what would be performed in paraffin sections, in the IHC protocol. Another possibility is that there is an accumulation of an abundant collagen isoform or elastin that is surrounding the HIEL, and that it is not a lowly expressed isoform.

Chapter 6. Attempt at making a pan-connexin antibody

Abstract

Vascular connexins localize to the MEJ and facilitate EDH-based vasodilation. Given the heterogeneity of proteins that localize to the MEJ, it is unclear if every MEJ contains gap junctions that can communicate hyperpolarization through direct access to the adjacent SMC cytoplasm. The major isoforms of connexins in the vasculature are CX37, Cx40, and Cx43. Since commercial antibodies are only validated to identify individual isoforms, an immunohistochemical approach to understanding what proportion of MEJs contain gap junctions is technically challenging due to the limitation of how many different fluorescent channels can be detected in a single image. In order to approach this question, in this chapter, I present an approach at creating an antibody that can label all vascular connexin isoforms, or a “pan-connexin” antibody. The antigen is a 54 amino acid peptide that contains the N-terminal sequences of Cx37, Cx40, and Cx43. I first determine the specificity of commercial connexin antibodies using HeLa cells transfected with respective plasmids, and demonstrate there is some cross-reactivity among the commercial antibodies. I then test the custom pan-connexin antibodies on HeLa cells and show that it recognizes a non-specific, ER-localized epitope. Lastly, the staining pattern of pan-connexin antibodies does not resemble expected connexin labeling in third order mesenteric arteries prepared *en face*. Therefore, the custom pan-connexin antibody was not successful.

Introduction

Some sections adapted from (* indicates co-first authorship):

Wolpe AG*, Ruddiman CA*, Hall PJ, Isakson BE. Polarized Proteins in Endothelium and Their Contribution to Function. J Vasc Res. 2021;58(2):65-91. doi: 10.1159/000512618. Epub 2021 Jan 27. PMID: 33503620; PMCID: PMC7954879.

Connexins are enriched at the MEJ and also regulate vasodilation and vasoconstriction pathways. In small arterioles, connexin 37, 40, and 43 are most prevalent (Cx37, Cx40, Cx43, respectively), (15, 29) with connexin 40 exhibiting arterial specificity in mice.(53) When assembled as hexamers, connexins form gap junctions that physically link the cytoplasm of two cells. Heterocellular communication occurs through gap junctions to facilitate EDH (32) and myoendothelial feedback. (41, 58, 59) Myoendothelial feedback is critical in regulating the degree of constriction elicited through α-adrenergic activation on SMCs. This feedback occurs when the inositol 1,4,5-trisphosphate (IP_3) generated in VSMC diffuses through myoendothelial gap junctions, where it then activates vasodilatory signaling in ECs as negative feedback regulation. (41, 60-63) When

Cx40 gap junctions are blocked by loading inhibitory antibodies, this negative regulation is lost, illustrating the functional importance of gap junctions within this microdomain. (32) The localization of gap junctions to the abluminal surface of the endothelium, and within the MEJ signaling microdomains, is essential in modulating vasodilatory signaling.(10)

Materials and Methods

Please refer to Chapter 3 for additional methods such as *en face* IHC.

Antibodies and plasmids

The following connexin plasmids were a kind gift of Janis Burt: pcDNA3.1 hygro mouse Cx37, pcDNA3.1 puro mouse Cx40, and pcDNA3 neo mouse Cx43. pcDNA3.1 Panx1 was cloned in house. Antibodies used were rabbit anti phosphatidylserine (Biomatik, CA30389), mouse anti KCNJ2 (Sigma, SAB5200027), rb anti connexin 37 (Thermofisher 40-4300, preferred), mouse anti connexin 40 (Thermofisher, 37-890, preferred), rb anti connexin 40 (Thermofisher, 36-400), mouse connexin 43 (Sigma, C8093), rb anti connexin 43 (Sigma, C6219, preferred), rb anti pannexin 1 (Sigma, HPA016930), and Alexa-Fluor linked hydrazide 488 (Thermofisher, A10436) or 647 (Thermofisher, A20502).

Transfections for immunohistochemistry

HeLa cells were transfected using nucleofection (Lonza, VCA-1001) where $1x10^6$ cells were transfected with 0.50µg plasmid and split across two wells of a 12-well dish. Cells were fixed with 4% PFA for 10 minutes at 4°C, washed with PBS 3x5 minutes, then blocked for one hour with 1% fish skin gelatin, 0.20% Triton-X 100, 0.50% BSA, and 5% animal serum in PBS. Primary antibody was diluted in blocking solution at a 1:100 concentration overnight at 4°C. The next day, following 3x 5-minute PBS washes, secondary antibody incubations were

performed at a concentration of 1:500 for 1 hour. After secondary incubations, samples were washed once with PBS for 10 minutes, then incubated with DAPI at a concentration of 1:5000 for 10 minutes in PBS, and washed again for 10 minutes with DAPI prior to mounting the coverslips onto microscope slides. Images were obtained using an Olympus FV1000 confocal microscope.

Results

In an attempt to determine what percentage of total MEJs contain a gap junction, we designed an antigen that contains the N-terminal sequences of the vascular connexins (**Figure 1**), with the goal of the subsequent antibody detecting all vascular connexins in an artery. For this reason, we refer to this custom antibody as the “pan”-connexin antibody. The antigen also had sequence similarity with non-vascular connexins (**Table 1**). Antibody production was performed by Thermofisher, where each of the two goats received 8 injections of antigen over the course of two and a half months (**Figure 2**).

To determine the specificity of pan-connexin antibody, we wanted to compare staining patterns to commercial antibodies. First, HeLa cells were transfected with plasmids for mouse isoforms of Cx37, Cx40, and Cx43, and also with a non-connexin four-transmembrane protein Panx1 (**Figure 3**). Each plasmid transfection was stained with commercial antibodies for Cx37, Cx40, Cx43, and Panx1. The connexin 40 antibody was specific to its isoform with no detectable fluorescent signal in cells transfected with Cx37, Cx43 or Panx1. The Cx43 and Panx1 antibodies were able to detect transfected cells with respective plasmids, but also had large amounts of low intensity signal throughout the field of view that is not seen in IgG controls. The Cx43 commercial antibody also may detect Cx37 (**Figure 3A**).

Commercial connexin antibodies were then tested on intact third order mesenteric arteries prepared *en face* to evaluate spatial patterns in the arterial wall (**Figures 4-6**). When Cx40 and Cx37 antibodies are used in the same experiment,

Cx40 detects signal along the interendothelial junction, and Cx37 shows up in the perinuclear region with a small amount along the interendothelial junction (**Figure 4**). However, when Cx37 is co-stained with Cx43, there is an increased Cx37 signal along the interendothelial junction compared to a co-stain with Cx40 (**Figure 5**). Cx43 largely appears in the perinuclear region and also in some punctate, although rarely localizing to the MEJ (**Figure 5**). Lastly, in a Cx40 and Cx43 co-stain, Cx40 localizes to the interendothelial junction and Cx43 to the perinuclear region (**Figure 6**).

After determining commercial antibody specificity and *en face* spatial patterns of the vascular connexins, we next proceeded to do the same experiments with the two custom antibodies from goats 1 and 2 (Pan1 or Pan2). The specificity for both Pan1 and Pan2 were evaluated in experiments where HeLa cells were transfected with plasmids for mouse isoforms of Cx37, Cx40, and Cx43, and also with a non-connexin four-transmembrane protein Panx1 (F**igure 7**). The results indicate that the Pan1 antibody, at two different concentrations, detects something in the perinuclear region of Cx37, Cx40, and Cx43 transfected cells compared to IgG and secondary only controls. However, the Pan1 antibody also detects similar signal in cells transfected with Panx1, indicating that the signal detected is not specific to connexins. The second custom antibody, Pan2, did not detect similar signal in transfected cells, except for some low intensity signal in the Panx1 transfected cells (**Figure 7D**).

Next, the spatial pattern of these custom antibodies were evaluated in *en face* views, along with PS (an MEJ marker that I describe extensively in **Chapter**

3) (**Figures 8 and 9**). The custom antibody from Goat 1 localizes to the perinuclear region, similar to transfected cell experiments, and also has some punctate in MEJs. However, there is no signal present at the interendothelial junctions, a major site of localization for connexins in the vascular wall (**Figure 8**). The antibody from Goat 2 did have some signal in the perinuclear region, unlike the HeLa transfected experiments. However, again, there is no signal either in the MEJ or at the interendothelial junction, indicating that these custom antibodies do not accurately detect connexins in the intact artery. The lack of specificity for connexin antibodies was also confirmed via western blot experiments on transfected HeLa lysates (**Figure 10**).

Antigen(54aa): N-term Cx40, N-term Cx43, N-term Cx37

GDWSFLGEFLEEVHKHSTGDWSALGKLLDKVQAYSTGDWGFLEKLLDQVQEHST

Figure 1. Antigen sequence for custom pan-connexin antibody.

Activity Schedule Download

Date	Day	Activity	Description
06/03/20	0	Injection	Initial Inoculation
06/03/20	0	Bleed	Pre-Bleed
06/08/20	5	Processed	Processed
06/17/20	14	Injection	Boost
07/01/20	28	Injection	Boost
07/15/20	42	Plasmapherisis	Test Bleed
07/20/20	47	Processed	Processed
07/29/20	56	Injection	Boost
07/29/20	56	Plasmapherisis	Test Bleed
08/03/20	61	Processed	Processed
08/12/20	70	Injection	Boost
08/26/20	84	Injection	Boost
08/26/20	84	Plasmapherisis	Test Bleed
08/31/20	89	Processed	Processed
09/09/20	98	Injection	Boost
09/23/20	112	Injection	Boost
09/23/20	112	Plasmapherisis	Test Bleed
09/28/20	117	Processed	Processed
09/30/20	119	Ship	Ship to customer

Figure 2. Production schedule for custom antibodies.

Mouse Protein	% Identity	Sequence (N-terminus)	Sequence Match
Cx 26	53%		38-DWGFLEKLLDQVQEHST-54 38-DWG_L+_+L__V_+HST-54
Cx 30.3	47%		38-DWGFLEKLLDQVQEHST-54 38-+WGFL+_+L__V_++ST-54
Cx 37	100%	MGDWGFLEKLLDQVQEHSTV	37-GDWGFLEKLLDQVQEHST-54 37-GDWGFLEKLLDQVQEHST-54
Cx 40	100%	MGDWSFLGEFLEEVHKHST	1-GDWSFLGEFLEEVHKHST-18 1-GDWSFLGEFLEEVHKHST-18
Cx 43	100%	MGDWSALGKLLDK	19-GDWSALGKLLDKVQAYST-36 19-GDWSALGKLLDKVQAYST-36
Cx 45	69%		3-WSFLGEFLEEVHKH-16 3-WSFL____LEE+H_HST-16
Cx 47	69%		3-WSFLGEFLEEVHKH-16 3-WSFL____LEE+H_HST-16
Cx 50			1-GDWSFLGEFLEEVHKHST-18 1-GDWSFLG__LEEV++HST-18

Table 1. Predicted percent identity with custom antigen.

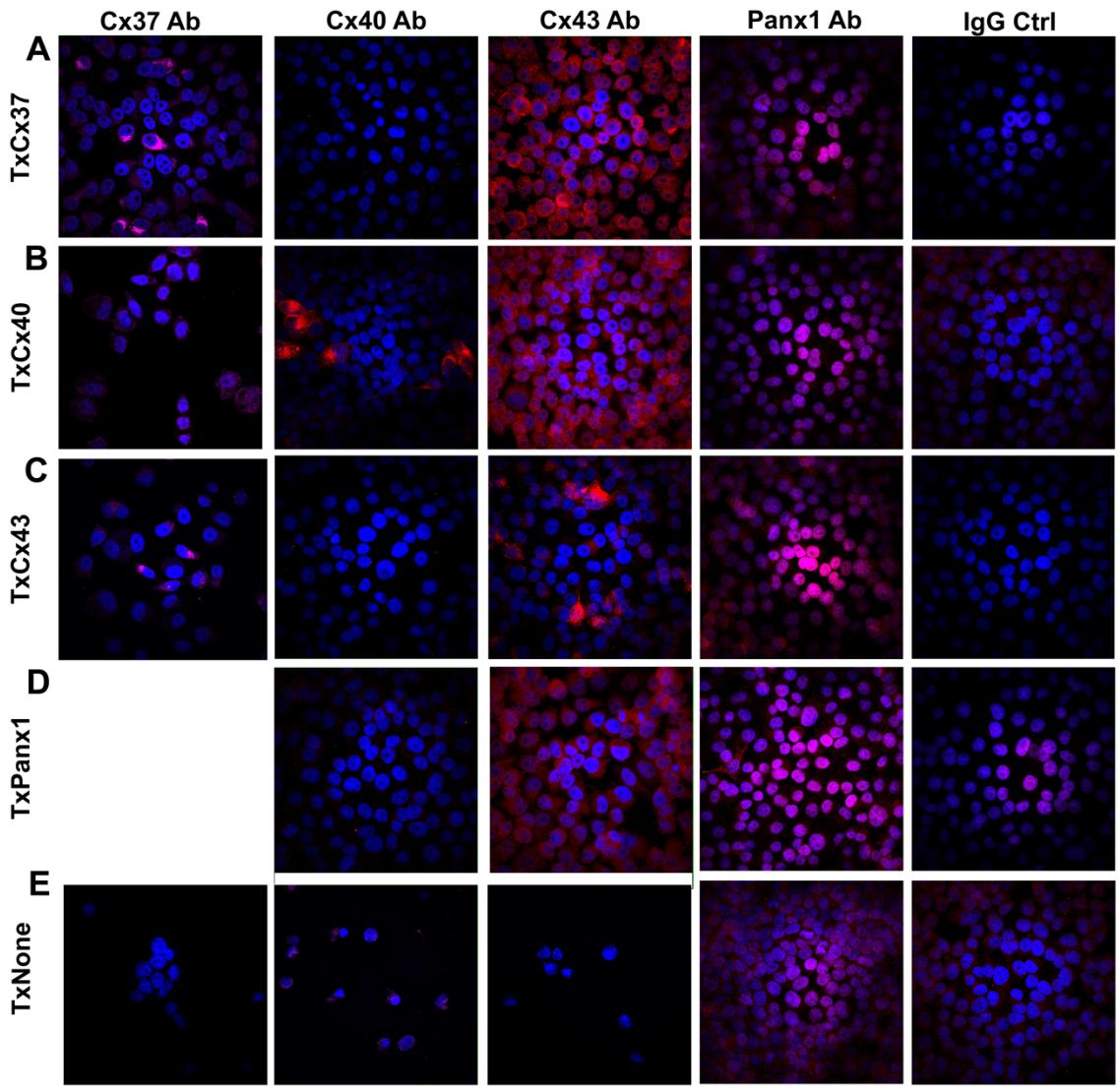

Figure 3. Validation of commercial connexin antibodies. HeLa cells transfected with (**A**) mCx37, (**B**) mCx40 (mouse anti Cx40 ab), (**C**) mCx43 (mouse anti Cx43 antibody), (**D**) Panx1, or (**E**) No plasmid, and stained with Cx37, Cx40, Cx43, or Panx1 commercial antibodies, or an IgG control for the host species of the primary antibody that matches the transfected plasmid in that row.

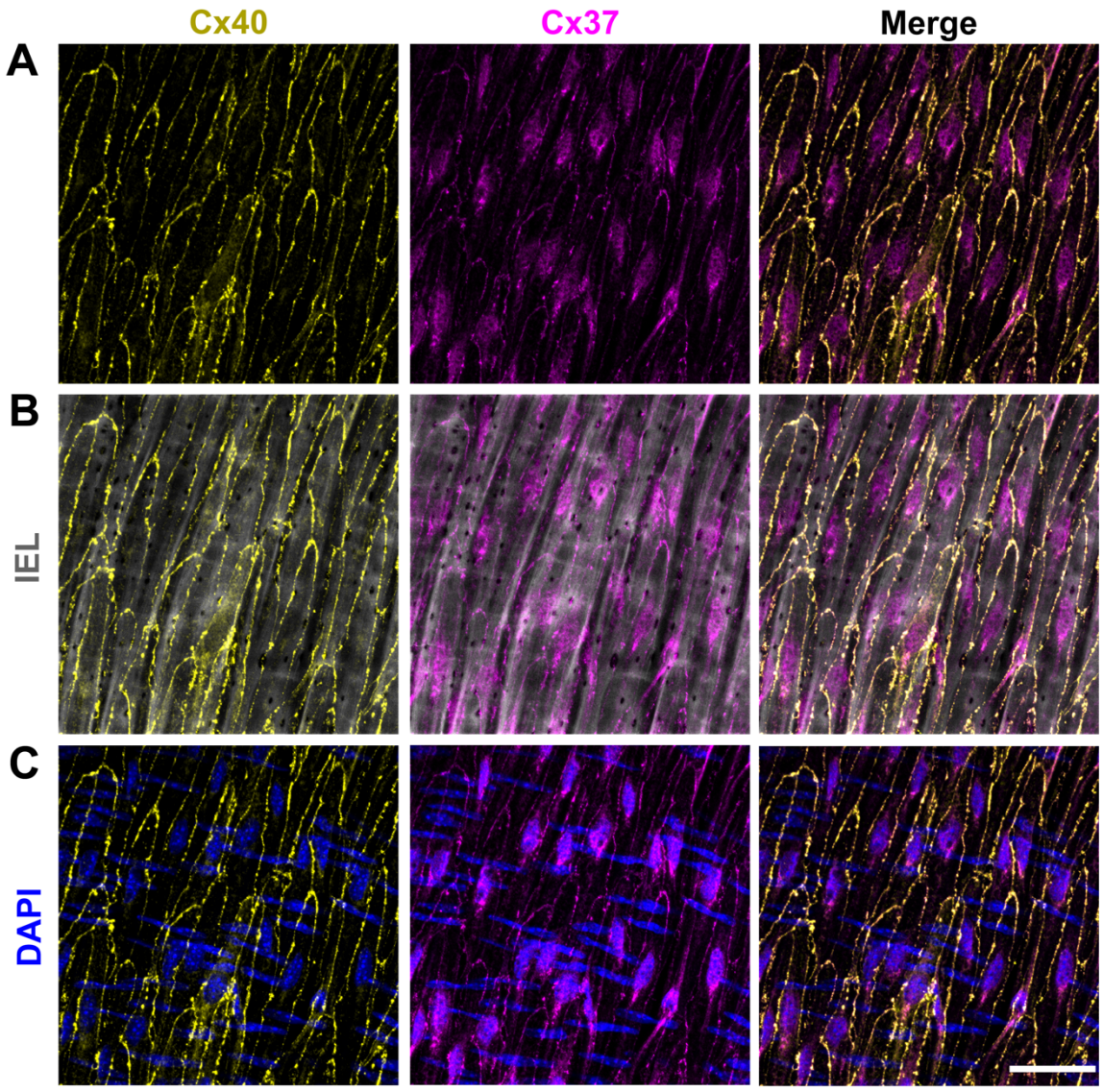

Figure 4. *En face* immunohistochemistry of Cx37 and Cx40 with commercial antibodies. (**A**) Cx40 (yellow), Cx37 (magenta), or merged. (**B**) Cx40, Cx37, or both merged with IEL (grey) detected via Alexa Fluor hydrazide. (**C**) Cx40, Cx37, or both merged with nuclei (blue) detected via DAPI. Scale bar is 30μm.

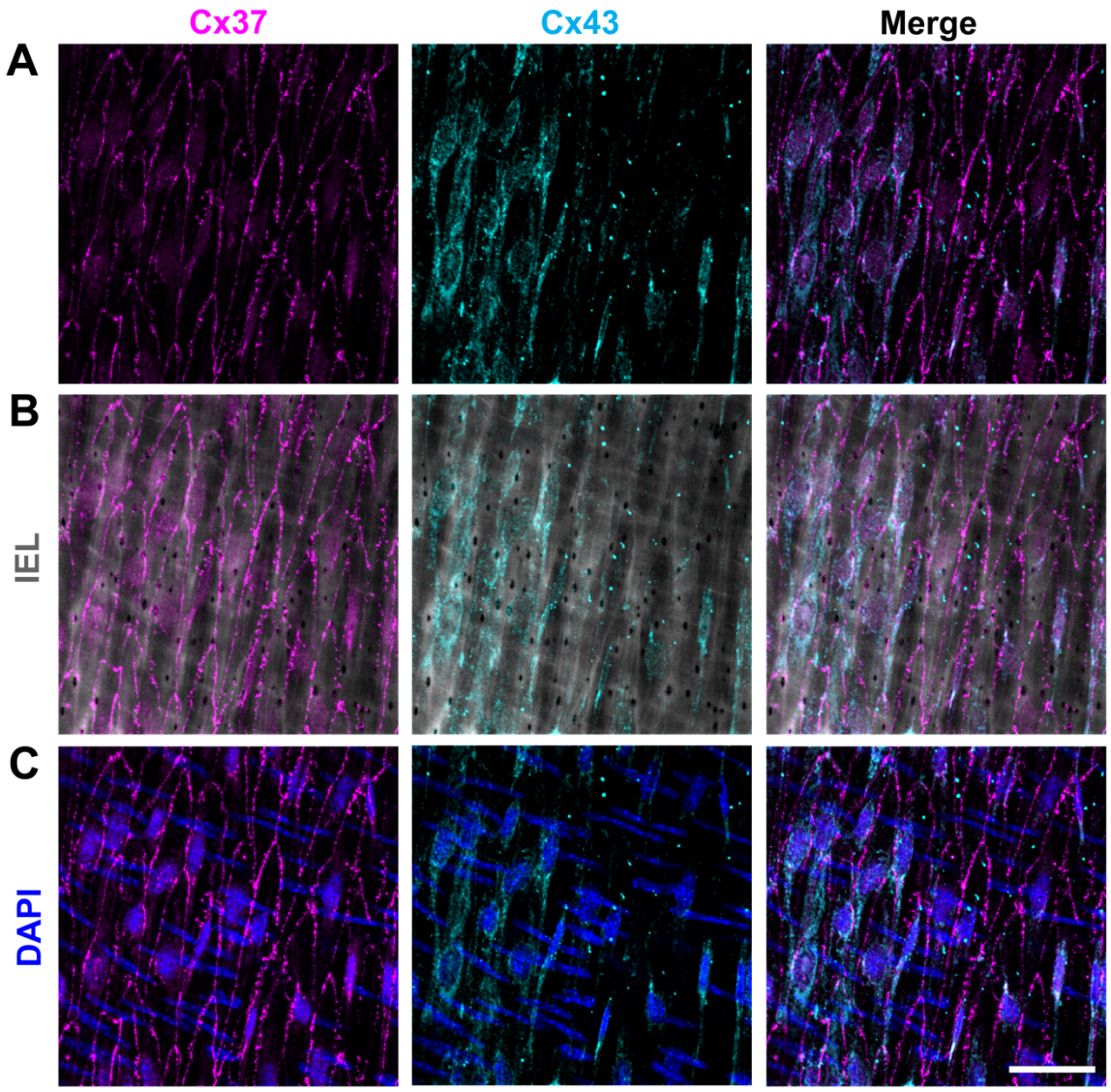

Figure 5. *En face* immunohistochemistry of Cx37 and Cx43 with commercial antibodies. (**A**) Cx37 (magenta), Cx43 (cyan), or merged. (**B**) Cx37, Cx43, or both merged with IEL (grey) detected via Alexa Fluor hydrazide. (**C**) Cx37, Cx43, or both merged with nuclei (blue) detected via DAPI. Scale bar is 30μm.

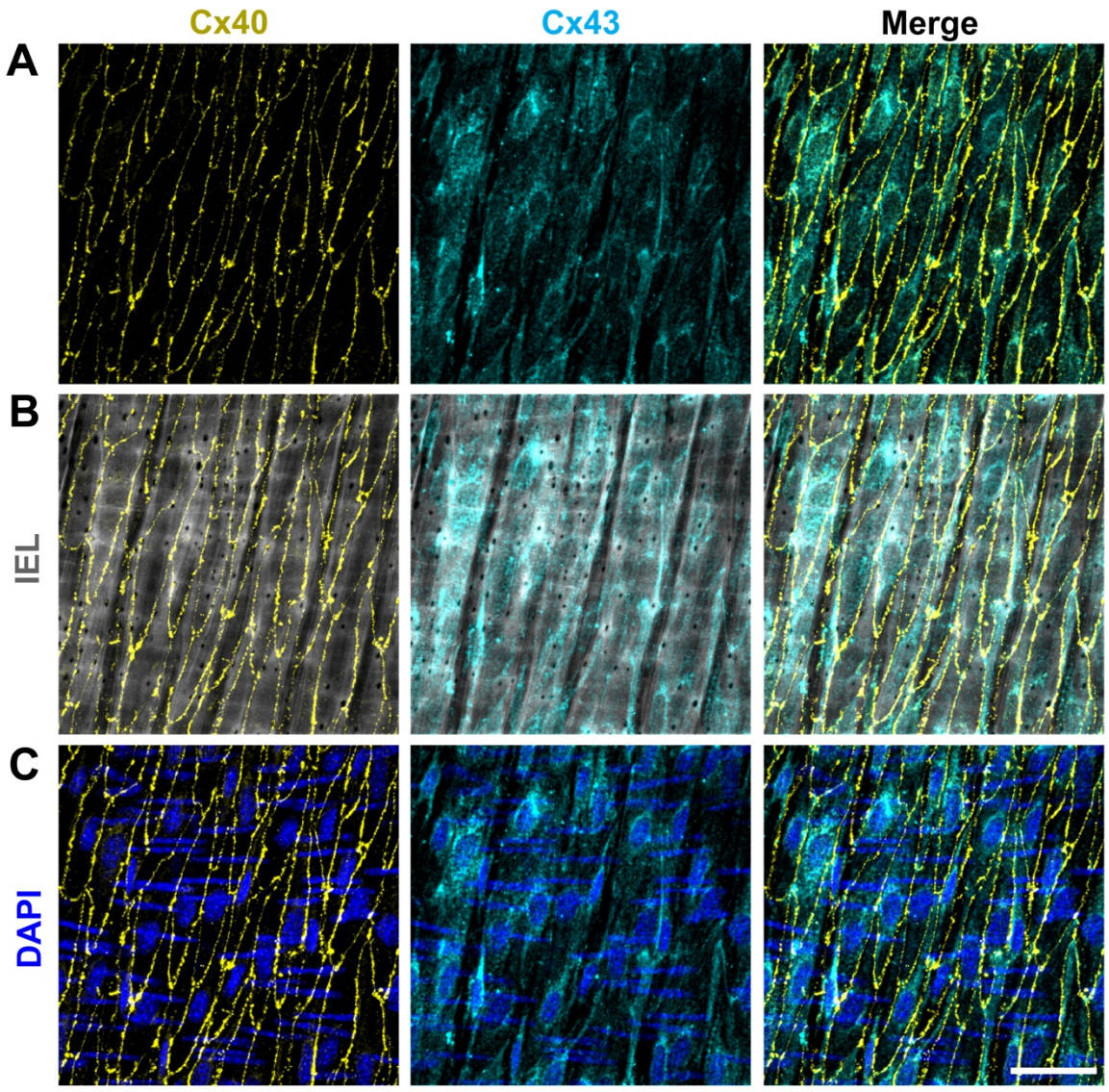

Figure 6. *En face* immunohistochemistry of Cx40 and Cx43 with commercial antibodies. (**A**) Cx40 (mouse anti Cx40, yellow), Cx43 (rabbit anti connexin 43 cyan), or merged. (**B**) Cx40, Cx43, or both merged with IEL (grey) detected via Alexa Fluor hydrazide. (**C**) Cx40, Cx43, or both merged with nuclei (blue) detected via DAPI. Scale bar is 30μm.

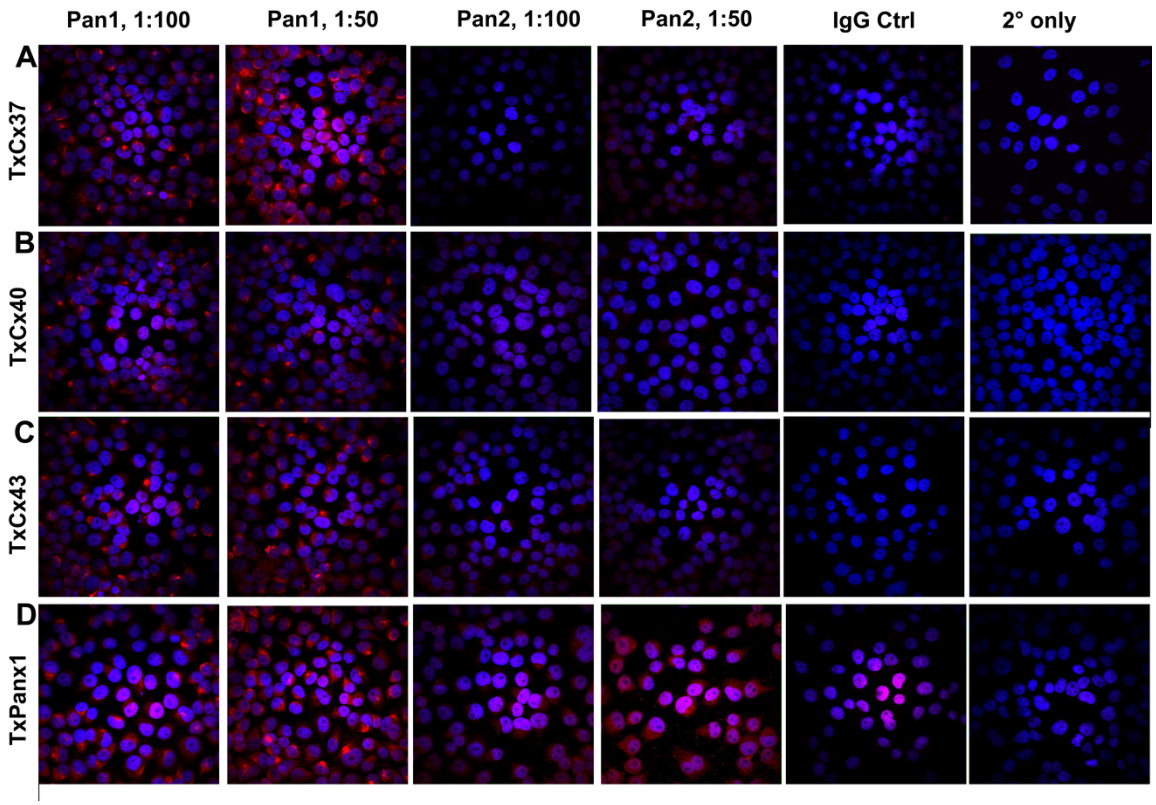

Figure 7. Validation of pan connexin custom antibodies in transfected HeLa cells. HeLa cells transfected with (**A**) mCx37 (mouse anti Cx40), (**B**) mCx40 (mouse anti connexin 40), (**C**) mCx43 (rabbit anti Cx43), (**D**) Panx1, and stained with custom antibodies from Goat 1 and 2 (Pan1 or Pan2) at two different concentrations (1:100 or 1:50), goat IgG, or secondary antibody only.

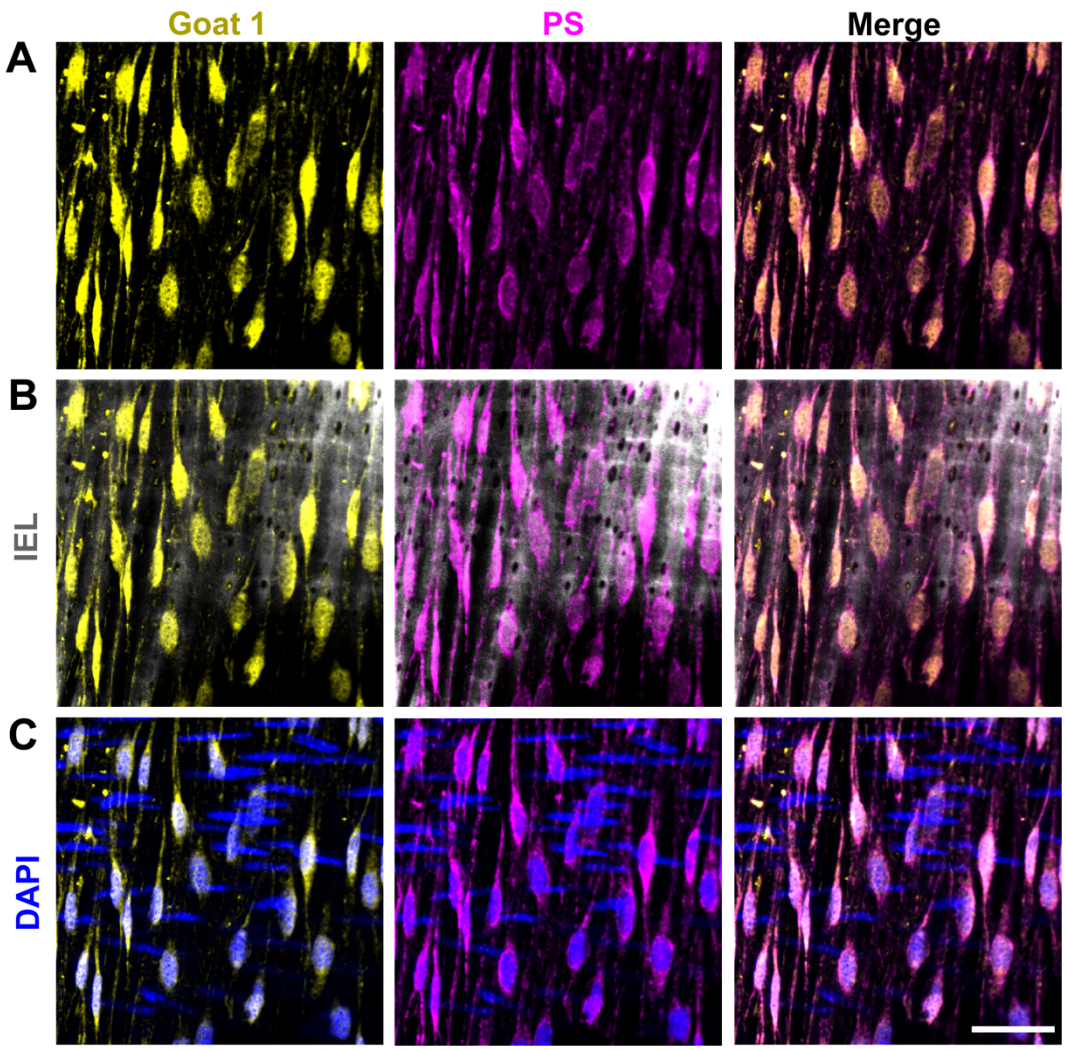

Figure 8. *En face* immunohistochemistry of custom antibody from Goat 1 and PS. (**A**) Custom antibody from Goat 1 (yellow), PS (magenta), or merged. (**B**) Custom antibody from Goat 1, PS, or both merged with IEL (grey) detected via Alexa Fluor hydrazide. (**C**) Custom antibody from Goat 1, PS, or both merged with nuclei (blue) detected via DAPI. Scale bar is 30μm.

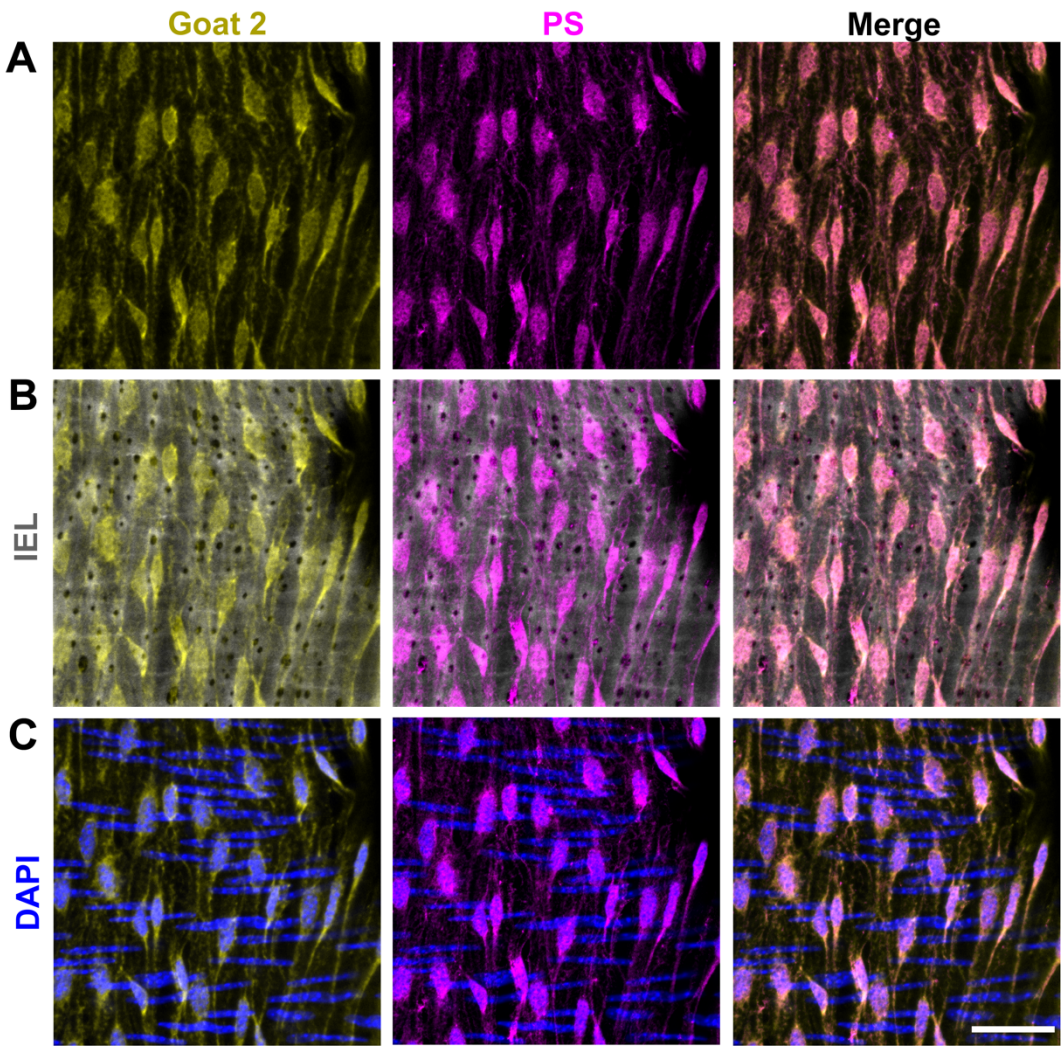

Figure 9. *En face* immunohistochemistry of custom antibody from Goat 2 and PS. (**A**) Custom antibody from Goat 2 (yellow), PS (magenta), or merged. (**B**) Custom antibody from Goat 2, PS, or both merged with IEL (grey) detected via Alexa Fluor hydrazide. (**C**) Custom antibody from Goat 2, PS, or both merged with nuclei (blue) detected via DAPI. Scale bar is 30μm.

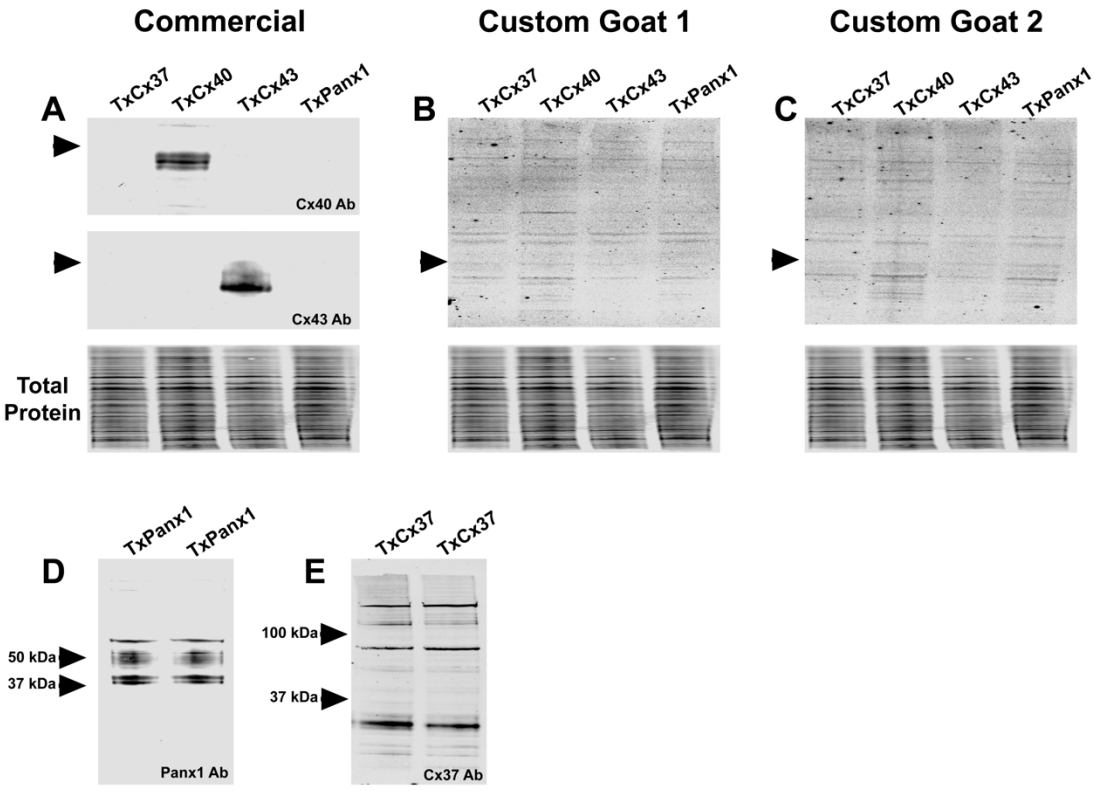

Figure 10. Western blots on transfected HeLa lysates to assess antibody specificity. Lysates from HeLa cells transfected with mCx37, mCx40, mCx43, or Panx1, and probed with (**A**) commercial Cx40 or Cx43 antibodies at 1:100, (**B**) custom antibody from Goat 1 at 1:50 concentration or (**C**) custom antibody from Goat 2 at 1:39 concentration (to match protein concentration of Goat 1 antibody). Total protein shown as loading controls. (**A-C**) were done on the same blot. Arrowheads indicate molecular weight marker of 37kDa. (**D**) HeLa lysate transfected with Panx1 and probed with commercial antibody. (**E**) HeLa lysate transfected with Cx37 and probed with commercial antibody.

Discussion

The custom antibody from Goat 1 likely identifies an endoplasmic reticulum specific sequence rather than a subset of connexins. In the transfected HeLa cell experiments, there is localization to the perinuclear region in very distinct circular puncta that could either be ER or Golgi based. The positive signal detected in cells transfected with Panx1 indicates that this signal is not specific to connexins, and that it would likely show up in any transfected cell where there is an abundance of protein being trafficked through the ER and Golgi. Similarly, in *en face* images with Goat 1, there is perinuclear staining that colocalizes with perinuclear PS staining, indicating that there is some ER localization to this fluorescent signal. This would also make sense with the punctate that are in MEJs, since there is an ER presence at the MEJ (**Chapter 3 Figure 24**).(44) However, this ER based signal is likely still nonspecific, as there is not a unique banding pattern identifiable on the western blot for this antibody.

The custom antibody from Goat 2 did not have similar results to Goat 1, as there was not a detectable signal in transfected HeLa experiments. There was faint perinuclear staining *en face*, but at a lower intensity compared to Goat1, and no localization to the MJ. Thus, the signal in *en face* images could have been nonspecific ad the custom antibody from Goat 2 likely does not detect anything. The western blot results also show nonspecific bands from the Goat 2 antibody, although, again, at a lower signal intensity compared to Goat 1.

The failure of this custom antibody to detect vascular connexins is likely due to the length the antigen. The goal was to have each goat produce antibodies for

each connexin N-terminal region such that the final product was a polyclonal mix that would be able to simultaneously detect the vascular connexins. However, the produced antibodies were nonspecific to connexins, likely due to the length of the designed antigen, of which a recommended length is 20 amino acids. Ideally, all three vascular isoforms should be detected through a “pan” vascular connexin antibody. However, in my preparations, the localization frequency of Cx43 to the MEJ is far lower compared to the other two isoforms. A future antigen may only include sequence identification for Cx37 and Cx40. The N-terminal region of Cx40 and Cx37 share 56% identity, but perhaps there is another region in the proteins that is more highly conserved that would be successful in detecting these two isoforms.

Lastly, the localization pattern of Cx37 changes based on what is co-stained with (**Figures 4 and 5**) indicating there is likely some steric hindrance at play for antigen sites when used in combination with the Cx40 commercial connexin antibodies. This is similar to results seen in en face preparations of the rat aorta, where the localization pattern of connexins changes based on what other primary antibody is included in the experiment.(267)

This presents a challenge to determine connexin occupancy of MEJs if the commercial antibodies cannot be used for an accurate co-staining experiment. In order to try to answer this question, I would recommend that future experiments do calculate the percent occupancy of Cx37 and Cx40 MEJs in independent staining experiments to estimate the percentage of MEJs containing an MEJ. Due to the likelihood of heteromeric connexons forming in the endothelium and at

MEJs, this method of quantification would result in an overestimation of the number of MEJ containing functional gap junctions.

Appendix

Custom antibodies were created with Thermofisher. Custom antibody ID 1VD2880. Final products were shipped to us on 09/03/2020. Person of contact was Lauren Carlson-Dexter.

All connexin plasmids were a gift of Janis Burt. Sanger sequencing results for these plasmids are in the Chapter 3 Appendix.

Chapter 7. Future Directions

Myoendothelial junction heterogeneity and PS regulation of Kir2.1

Are HIEL random with respect to SMC signaling domains?

In Chapter 4 I have demonstrated extensively that HIEL are randomly distributed with respect to EC signaling domains. However, it could be that there is a spatial pattern with respect to SMC signaling domains, which would require additional image analysis. A pattern with respect to SMC could represent another level of control for the heterocellular contact that controls the arterial diameter in resistance arteries in that the SMC may be directing the formation of the MEJs. The only known regulator of MEJ formation is PAI-1, but the molecular mechanisms still remain to be elucidated. (10, 36) SMCs may be involved in directing MEJ formation, perhaps through localized expression of MMPs that degrade ECM proteins in the IEL. There could also be some factors released by the SMC to promote EC extensions through HIEL. These contributions have yet to be determined and a spatial pattern in relation to SMC signaling domains could help reveal a potential role for SMC in MEJ formation.

What is driving the deposition of PS into MEJs?

Lipids are synthesized in the ER and transported to the Golgi for further processing prior to being shuttled to the PM. In order to go between these

organelles and eventually make it to the lipid bilayer boundary of the cell, lipids are transported between membranes through simple diffusion, vesicular transport, or via lipid transfer proteins (LTP) located at membrane contact sites (MCS). These LTPs have a hydrophobic binding pocket that allow transport of lipids through the cytosolic environment.(268)

The oxysterol-binding protein-related proteins (ORPs) is a family of LTPs with 12 different isoforms in mammals. (269-272) ORPs contain two major domains, the pleckstrin homology (PH) domain which binds to PI4P on the Golgi,(273) and the highly conserved OSBP-related ligand-binding domain (ORD) that creates the hydrophobic pocket for lipid binding.(274) The OR domain contains a FFAT sequence that can interact with VAP proteins on the ER, which is one of the mechanisms that facilitates communication between different organelle membranes.(275)

ORPs transport two species of lipids in opposite directions. The forward movement of one lipid is supported by the energy that is generated from the phosphoinositide species that is counter-transported, where a phosphate group is cleaved for energy.(276) Often this phosphoinositide species is phosphatidylinositol 4-phosphate (PI4P), a phosphoinositide with a single phosphate group. PI4P is synthesized by PI4P kinases, which localize to plasma membrane, trans Golgi network, endosomes and late endosomes, making this lipid widely available at various organelles throughout the cell.(212) In contrast, PIP_2 is highly concentrated at the plasma membrane.(277) PI4P phosphatases, such as the Sac phosphatase domain family, localize to the ER and degrade PI4P leading

to a low concentration of this phosphoinositide at the ER. This concentration gradient of PI4P promotes the lipid counter-transport carried out by ORPs because PI4P is follows its chemical gradient.(278)

The specific localization of PS to a subpopulation of MEJs suggests that its trafficking to those signaling microdomains is an intentional process rather than the result of simple diffusion. Our lab has demonstrated that the endoplasmic reticulum is present within MEJs,(37) and our microscopy suggests PS is heavily synthesized in the ER of these ECs, which we demonstrate via a calnexin-PS co-stain (**Figure 24**). This potential ER-PM membrane contact site at the MEJ may contain an LTP to facilitate transport of lipids from the ER to the PM. Future studies should investigate ORP localization in endothelium, given that a number of ORP isoforms have been implicated in regulating the transport of PS,(175, 176) and being functionally relevant in endothelium.(279) If a particular ORP isoform does localize to MEJs or is heavily expressed in cells with a high PS-MEJ percentage, then an EC-specific, inducible knockout mouse model could be created to deplete that isoform from endothelial cells. I would expect that the disruption of PS transport to the MEJ would result have functional consequences in terms of arterial tone. In a pressure myography experiment to measure dilation to exogenous PIP_2 application, I would expect that the results would be similar to arteries from EC-Eln KO mice (**Figure 50**). This uncontrolled dilation could also lead to an imbalance of SMC constriction and thus difficulty in achieving myogenic tone.

Lastly, it is known that Kir2.1 is also trafficked through the ER. (213, 214) Future studies should also investigate if PS contributes to the specific localization

of Kir2.1 to the MEJ. This could be another level of regulation that PS exerts over the function of Kir2.1. Since the MEJ is not a structure seen in normal cell culture, this idea would have to be tested in cells first. Both PS and Kir2.1 could be transfected into the cell with a fluorescent tag, and their localization could be trafficked over time to investigate if PS and Kir2.1 traffic to the same membrane sites. The potential regulation of PS on Kir2.1 transport to the plasma membrane is likely independent of a direct interaction with the ER exit sequence of Kir2.1, which exerts a net negative charge. (213, 214)

Further investigation of PIP_2 dilation in arteries

The evidence I present here suggests that the PIP_2 dilation is due to Kir2.1, since this dilation is inhibited in the presence of Ba^{2+} or ML-133 (**Figure 46**). There are additional experiments that would add confidence to this observation. The first would be do add the known Kir2.1 inhibitors, Ba^{2+} or ML-133, along with PS to evaluate if there is an additive inhibition on NS309 or PIP_2-mediated vasodilation. I do not expect an additive effect that is significantly different, but I do think it makes sense that the results from two inhibitors would result in lower dilation than just one since these inhibitors likely act through different mechanisms.

The second experiment would be to evaluate the PIP_2 dilation on mice deficient in Kir2.1. Ideally, this would be on inducible, EC specific Cre mouse such that effects of channel loss during development or in other tissues would not affect dilation. I would expect there to be a significant reduction in the ability of PIP_2 to induce a dilation in intact arteries. However, if dilation did occur, it would be

interesting to investigate if another channel is activated by PIP_2 in these tissues, such as the IK_{Ca} channel.

The IK_{Ca} channel is also crucial in EDH-based vasodilation, and like Kir2.1 (**Figure 39**), also localizes to MEJs. Exogenous PS inhibits NS309 mediated vasodilation (**Figure 43**), which is also a potent activator of IK_{Ca}. To my knowledge, lipid regulation of this channel is unexplored. It would be interesting to investigate if PIP_2 also activates this channel. I would use a similar experimental setup to test the dilation of PIP_2 in the presence of the specific IK_{Ca} inhibitor, TRAM-34. In **Figure 45**, IK_{Ca} and PS do not localize to the same MEJs. However, this is one experiment and there are not many MEJs populated with IK_{Ca} in the field of view as previous reports have indiciated.(15) Therefore, this experiment should be repeated in more arteries to fully establish the spatial relationship between PS and IK_{Ca}. The localization of SK_{Ca} and PS could also be investigated to help explain the reduction in NS309 dilation at higher doses. Although this localization is not expected to be at the MEJ, since SK_{Ca} primarily localizes to the interendothelial junctions. (15)

Effects of MEJ lipid environment on Kir2.1 function

In order to evaluate how the local lipid concentration of the MEJ impacts Kir2.1 channel activity, whole cell patch clamp experiments on native endothelial cells from resistance arteries should be performed. Native ECs from $Eln^{fl/fl}/Cre^{+}$ should also be evaluated for basal Kir2.1 currents and compared to that taken from wildtype mice. I predict that basal currents of Kir2.1 in $Eln^{fl/fl}/Cre^{+}$ arteries would be

higher compared to littermate controls, since PS is not localized to MEJs to negatively regulate Kir2.1 activity (**Figures 48 and 50**).

Further, it is still a question why PS alone does not induce vasodilation in intact arteries compared to results in electrophysiology where PS can increase Kir2.1 currents (**Figure 46**). The differential results here across experiments could be due to the distinct lipid environments of the HEK cells versus intact arteries. As discussed in the introduction of this section, the ECs of intact arteries have defined signaling microdomains and a high density of caveolae present, which are heavily enriched with caveolae. It is likely that caveolae, microdomains enriched with cholesterol, are also present at the PS-Kir2.1 MEJs due to the high density of these microdomains in endothelium, and I have some preliminary evidence indicating some overlap in *en face* immunohistochemistry images (**Figure 38**). Indeed, there are several studies indicating that cholesterol and PS influence each other's trafficking and localization within the endothelium, and they are both implicated in regulating Kir2.1 activity. (177) (99, 102, 185)

The presence of cholesterol enrichment at MEJs could prevent the exogenous PS adequate access to its binding sites thus preventing any conformational changes that would result in a vasodilation response. In contrast, this rigidity may not present the same access issues for PIP_2 since it is a much smaller lipid. In the electrophysiology experiments, the HEK cells are not as enriched with caveolae and they are transfected with Kir2.1 channel, where they express Kir2.1 at a level orders of magnitude higher than native endothelium. This alone indicates that each Kir2.1 channel is incorporated into the plasma membrane slightly differently and

gives PS the opportunity to interact with Kir2.1 channels that are not a part of lipid rafts. This interpretation also opens the question of how PS is able to inhibit PIP_2-mediated vasodilation if cholesterol is preventing it from accessing the lipid binding sites (**Figure 46**). It could be that the head group of PS is till able to interact with or around the lipid binding site in such a way that steric hindrance alone is preventing PIP2 from being able to access, without the PS-Kir2.1 interaction being sufficient to induce a conformational change that leads to channel opening in the local lipid environment.

This rigidity of cholesterol preventing PS activation in intact arteries can be tested experimentally. Methyl-β-cyclodextrin (MβCD) can deplete cholesterol in cells. I predict treating arteries with MβCD prior to exogenous PS application can result in vasodilation. In **Figure 46**, the PS application to the intact arteries does not have an effect. However, there is one artery that did exhibit dilation to PS. It could be the case that the cholesterol content in that artery was reduced allowing PS to have access to the channel. This may represent another mechanism by which cholesterol inhibits Kir2.1-mediated vasodilation.(98, 99)

The interpretation of PS inhibiting PIP_2-meditated activation of Kir2.1 is that it is oversaturating the channel and specifically binding to PIP_2 binding site such that PIP_2 cannot access the its binding site to facilitate channel opening. These binding sites for PIP_2 are positively charged lysines at the primary binding site (K219 and K220) and a crucial lysine at the secondary lipid binding site for PS binding (K62). (102, 104) There are also additional positive residues at the primary lipid binding site. In the intact artery setup, cholesterol is likely restricting access to the smaller

secondary binding site, but PS may still be able to access one of the many positive residues in the primary lipid binding site, where PIP_2 prefers to bind, thus preventing PIP_2 binding by directly occupying its binding site or via steric hindrance.

To determine the mechanism by which PS is preventing PIP_2 from binding to Kir2.1, ideally Kir2.1 channels containing specific mutations for positively charged residues should be created and transfected into HEK cells. However, this becomes a complicated experiment because mutating any residue within the PIP_2 binding pocket will not only effect PS inhibitory binding but also PIP_2 binding, making any results difficult to interpret. For studying channel function in vivo, mutagenesis of certain sites would be the most viable option. Thus, the tools needed to test these hypotheses in an intact animal are not yet available. However, the specific residues at play can still be investigated in cells through tethering positive residues in the PIP_2 binding site to the membrane to simulate PS binding, and then repeat electrophysiology studies in the presence of PIP_2 and PS.(143, 280) In this scenario, I hypothesize that tethering a particular residue to the membrane would block PIP_2 binding from its site.

The morphology and composition of the IEL dictates arterial function

In both Chapters 2 and 4 I demonstrate that the morphology of the IEL dictates arterial function: inducing HIEL formation in conduit arteries promotes a shift to EDH-based vasodilation while eliminating HIEL through decreased elastin deposition in resistance arteries promotes a shift to NO-based signaling. Another way to antagonize this pathway to understand the role of MEJs in vasodilatory signalign is to induce ECM deposition in the $Eln^{fl/fl}/Cre^{+}$ mice, and study the change in vasodilation, morphological changes to the IEL, and protein localization in an *en face* view of the endothelium. Long term oral administration of minoxidil restored vascular compliance in mice with chronic vascular stiffness, (281) and is currently in clinical trials for the treatment of Williams Syndrome, a disease associated with elastin deficiency. (282) I hypothesize that minoxidil treatment on $Eln^{fl/fl}/Cre^{+}$ would partially restore the canonical IEL morphology of resistance arteries and partially correct protein and lipid localization in the endothelium. This could help evaluate if the MEJ is a necessary prerequisite in determining protein polarization within the endothelium. If hemoglobin alpha protein levels are normalized to control levels after minoxidil treatment, this would indicate that the IEL influences the translation of EC proteins.

Long term administration of minoxidil in wildtype mice may promote retraction of MEJs and reduce the number of HIEL in a resistance artery, and could help further define the relationship between MEJs and endothelial protein localization. As I have demonstrated in **Chapter 2** and **Chapter 4**, this protein

localization has functional consequences. Thus, I hypothesize that arteries from these mice would shift to NO-based signaling, consistent with the theme that IEL morphology is correlated with vasodilation pathways. In this mouse model, I predict a thicker IEL with reduced incidence of HIEL and MEJs; thus, I predict disrupted protein localization.

While I have demonstrated the IEL in resistance arteries does not have canonical sites of MEJ formation, or HIEL, it is still an outstanding question how heterocellular contact is different at the ultrastructural level. Future studies should include evaluating the extent of heterocellular contact via TEM. I predict that there are fewer individual sites of contact with increase surface contact area. This altered, larger area of heterocellular contact may no longer be recognized as a signaling microdomain and could in part explain why protein and lipid localization is so disrupted within the endothelium.

As mentioned in the discussion of Chapter 4, the specific contribution of EDH-based vasodilation should be investigated using specific pharmacological inhibitors to interrogate that pathway in an Ach dose response curve experiment. Based on the evidence in **Chapter 4 Figures 2-4**, I predict that there will be less vasodilation attributed to the EDH pathway and Ach dose response curves with inhibitors will be at comparable levels compared to control curves. However, if the contribution of EDH is unchanged in $Eln^{fl/fl}/Cre^{+}$ resistance arteries, and there is a reduction in Ach-based vasodilation in the presence of these specific pharmacological inhibitors, then there may be another explanation for the increase in NO. The increased NO signaling could also be related to increased oxidative

stress or production of free radicals. Future studies should evaluate the production of reactive oxygen species in these arteries, through measurements on histological sections or in blood. Another method to test the contribution of NO signaling in resistance arteries is to monitor the blood flow using a doppler in live, anesthetized mice, with a total of four groups, both genotypes and treated with or without L-NAME in the drinking water. The hypothesis is that $Eln^{fl/fl}/Cre^{+}$ treated with L-NAME will have reduced blood flow compared to littermate controls also treated with L-NAME. The results from this study could also help to clarify the role of increased NO production in these mice.

It is unclear why the SMC in these arteries exhibit less vasoconstriction to phenylephrine or KCl. As mentioned in the discussion, investigation into expression of other proteins involved in SMC contraction should be pursued along with other integrin candidates, such as $\alpha 8\beta 1$, (283) that may be downregulated. Another explanation for reduced contraction is decreased SMC innervation. This could be tested with a tyrosine hydroxylase (TH) IHC on intact third order mesenteric arteries. If there were a reduction in TH staining, this may indicate that the SMC are not well adapted to respond to alpha adrenergic stimulation, thus explaining reduced constriction to PE (**Chapter 4, Figure 6**). However, this would result in further questions about the role of EC-derived elastin in directing the innervation of various tissues.

In Chapter 4, I show that the vasodilation pathway of ECs is altered in the absence of EC-derived elastin, and that SMC contraction is impaired. Remarkably, BP is unchanged in these mice (**Chapter 4, Figure 15**). Initial blood results indicate

that kidney function may be compensating for the hypothesized hypotension (**Chapter 4, Figure 16**). Another axis that should be considered is an upregulation of renin in the circulation, by testing the concentration of renin in blood plasma from both genotypes.

A final thought on tropoelastin

Homozygous global deletion of tropoelastin leads to death within a few days of birth due to SMC luminal occlusion of the aorta. (263) This phenotype is so severe that it may be masking another important developmental role for tropoelastin. In addition to the well-known fate of tropoelastin in forming mature elastic fibers, tropoelastin may also act as a transcriptional activator since levels in $Eln^{fl/fl}/Cre^{+}$ mice trend downwards in nearly every gene evaluated (**Figures 5 and Figures 10-14**). This would indicate trophoblastic as a master regulator of proper embryonic development. A single cell RNAseq experiment on ECs isolated from pups at birth could reveal how EC-derived elastin affects the transcription of genes at the beginning of postnatal development, and could reveal another physiological role for tropoelastin before being incorporated into mature elastic fibers.

Chapter 8. Protocols

Acetylcholine dose response curve

Volume of system = 7.5ml drug beaker + 2.5 ml bath/tubing = 10ml

1. Pressure up to 20 mmHg for 5 min
2. Pressure up to 40 mmHg for 5 min
3. Pressure up to 60 mmHg for 5 min
4. Pressure up to 80 mmHg for 20 min
5. 1μM PE pre- constriction for ~10 min
    a. 1μl of the -2 tube into 7.5ml of the drug beaker (final concentration of 1μM in 10ml)
    b. If no constriction, add 1μl incrementally. For mesenteric arteries, max 3μM. For larger arteries, like the carotid, use 10μM dose.
    c. Record measurement after inner diameter plateaus for 5 mins
    d. There is also the option to constrict to myogenic tone here. I recommend a diameter plateau of 10 minutes before beginning the dose response curve.
6. $1x10^{-9}$ Ach (~ 5% dilation)
    a. 90μl of -7 tube
7. $1x10^{-8}$ Ach
    a. 90μl of -6 tube
8. $3x10^{-8}$ Ach
    a. 20μl of -5 tube
9. $1x10^{-7}$ Ach
    a. 70μl of -5 tube
10. $3x10^{-7}$ Ach
    a. 20μl of -4 tube
11. $1x10^{-6}$ Ach (biggest jump in dilation)
    a. 70μl of -4 tube

12. $3x10^{-6}$ CCh
    a. 20μl of -3 tube
13. $1x10^{-5}$ Ach
    a. 70μl of -3 tube
14. $1x10^{-4}$ Ach
    a. 90μl of -2 tube
15. $1x10^{-3}$ Ach (60% dilation)
    a. 90μl of -1 tube
16. 1μM NS309: 100% dilation
    a. 1μl of 10mM stock into 7.5ml of the drug beaker (final concentration of 1μM in 10ml)
    b. If no constriction, add 1μl incrementally. For mesenteric arteries, max 3μM.
    c. Record measurement after inner diameter plateaus for 5 mins
17. 30mM KCl: ~50% constriction
    a. 300μl of 1mM KCl into the drug beaker
    b. Record measurement after inner diameter plateaus for 5 mins
18. Ca^{2+} free: 100% dilation (should be as high as 1μM NS309 or diameter at 80mmHg)
    a. Wash in an open system for 5 min, then wash in a closed system for 15 min.

Notes:

- Record inner diameter 5 minutes after each dose.
- For accurate measurements, it is important to make sure pressure does not change

NS309 dose response curve

1. Pressure up to 20 mmHg for 5 min
2. Pressure up to 40 mmHg for 5 min
3. Pressure up to 60 mmHg for 5 min
4. Pressure up to 80 mmHg for 20 min
5. 1μM PE pre- constriction for ~10 min
    a. 5μl of the -2 tube into 47.5ml of the drug beaker (final concentration of 1μM in 50ml)
    b. If no constriction, add 5μl incrementally. For mesenteric arteries, max 3μM. For larger arteries, like the carotid, use 10μM dose.
    c. Record measurement after inner diameter plateaus for 5 mins.
    d. There is also the option to constrict to myogenic tone here. I recommend a diameter plateau of 10 minutes before beginning the dose response curve.
6. Begin NS309 curve and record the average diameter over 7 minutes for each dose.
7. 0.10μM NS309
    a. 0.50μl 10mM stock in 50ml
8. 0.30μM NS309
    a. 1μl 10mM stock in 50ml
9. 0.50μM NS309
    a. 1μl 10mM stock in 50ml
10. 0.60μM NS309
    a. 0.50μl 10mM stock in 50ml
11. 1 μM NS309
    a. 2μl 10mM stock in 50ml
12. 2 μM NS309
    a. 5μl 10mM stock in 50ml
13. 30mM KCl: ~50% constriction
    a. 300μl of 1mM KCl into the drug beaker

b. Record measurement after inner diameter plateaus for 5 mins

14. Ca^{2+} free: 100% dilation (should be as high as 1μM NS309 or diameter at 80mmHg)
    a. Wash in an open system for 5 min, then wash in a closed system for 15 min.

Myogenic tone pressure myography

1) Equilibrate artery to pressure from 20-80mmHg in 20mmHg increments with a 5 minute incubation at each pressure
2) Allow the artery to develop myogenic tone
3) Once tone has stabilized, test EC function with 1-3 μM of NS309. Begin with 1 μM, and add 1μM incrementally if needed.
4) Wash out NS309 and watch for the return of myogenic tone
5) Begin the active curve
    a. Slowly drop the pressure down to 20mmHg and equilibrate for 5 minutes
    b. Increase the pressure by 20mmHg from 20mmHg-120mmHg.
    c. Record the plateaued diameter, 5-10 minutes for each pressure
6) Slowly drop pressure down to 80mmHg to equilibrate for 5-10 minutes at normal pressure
7) Assess SMC function by dosing with 10μM PE. Record diameter after plateau.
8) Assess EC function by dosing with 10μM Ach. Record diameter after plateau.
9) Assess SMC function by dosing with 30mM KCl. Record diameter after plateau.
10) Circulate Ca2+ free buffer in an open system for 5 minutes, and circulate for another 15 minutes.
11) Begin the passive curve
    a. Slowly drop the pressure down to 20mmHg and equilibrate for 5 minutes
    b. Increase the pressure by 20mmHg from 20mmHg-120mmHg.
    c. Record the plateaued diameter, 5-10 minutes for each pressure
12) Myogenic tone was calculated as $((D_{ACT}-D_{PASS})/D_{PASS})*100$.
13) For active and passive curves, the percent change in diameter relative to the diameter at 20mmHg was calculated as $((D_X-D_{20})/D_{20})*100$, where D_X is diameter at any pressure and D_{20} is the diameter at 20mmHg.

General *en face* protocol

1. Sac mouse and clear away fat from several vessels
2. Take vessels out, move to Sylgard square, and secure a tungsten pin in each end
3. Fix vessels in 4% PFA for 15 min at 4°C (or 1:1 MeOH:Acetone on ice for 5-10 minutes)
4. Wash 3x 20 min with PBS
5. Cut vessel *en face*. (Note: Vessel sits in Krebs w/ 2mM Ca^{2+} at 4°C until all vessels are completed)
6. Permeabilize for 30 min with 0.2% NP40/PBS with medium shake
7. Block for 1 hour in 400μl of 0.2% NP40/PBS with 5% serum (of animal secondary antibody is raised in or 10% BSA)
8. Add primary antibodies, shake 1 min at RT to mix
    a. Typically 1:100, sometimes 1:50
9. Place 24 well dish in humidity chamber at 4°C overnight

Next day

10. Wash 3x 5 min with PBS on med shake
11. Add secondary antibody solution, incubate at RT for 1 hr
    a. 320 μl blocking solution/well
    b. 80μl 1:500-1:1000 hydrazide stock (do 1:500 for a 1mM hydrazide stock)
    c. 1μl secondary/well (for 1:400)
12. Wash 3x 5 min PBS
13. In 500 μl PBS, add 1μl of DAPI (from a 5μg/μl stock) and incubate at RT for 10 min
14. Wash 2x 10min PBS
15. Mount with DAPI media, a square coverslip, and secure to microscope slide using lab tape.

General western blot protocol

Harvest cells (~1 hour)

1) Remove media
2) Wash 2x with 1x PBS in flask
3) Trypsinize cells and add back media
4) Transfer cells to a 15ml conical tube
5) Spin and suction off media
6) Spin 2x in 1x PBS and suction off media
7) Add 200ul lysis buffer
    a. 100ul P2, P3, and PI to 10mL of RIPA (good for ~1 week)
8) Spin 12,000rpm for 10 min in cold room
9) Remove the supernatant to a new labeled tube
10) Remove 100ul of the supernatant for protein analysis (i.e. BCA assay), and freeze

BCA Assay (~1 hour)

Refer to the following link for how to make standards:
https://www.thermofisher.com/order/catalog/product/23225

1) Making working reagent (50A:1B)
    a. Total ul needed = (9 standards + 1 sample) * (1 replicate) * 200 ul + extra
    b. Volume Reagent B = Total ul needed/50
    c. Volume Reagent A = Total ul needed – Volume Reagent B
2) Add 10ul each standard to a well
3) Add 10ul sample in duplicate
4) Add 200ul of working reagent to each well
5) Incubate at 37C for 30 min
6) Plate reader
    a. Omega program → Select “User” → Run
    b. Test setup → Test protocol → Absorbance → “BCA Assay”
    c. Edit → Layout → delete selected wells & select new wells
    d. START
    e. “Results” → “Open last test run”
    f. Excel Report → export report to Excel
    g. Save As → Isakson → “CAR”
7) Ensure all samples are within reported values of the standards. If not, dilute selected samples and rerun the assay.
8) Calculate protein concentrations of samples in ug/ul using an Excel calculator

Sample Preparation (~1 hour)

Sample to loading buffer 2x (2x LB) is 4:1 (example: 21 ul sample to 7 ul 2x LB)

1) Calculate how many ul to run on the gel to get 20-40ug protein
    a. Total well volume ~45ul for the 10 well 4-12% gel
2) Add sample to 1.7ml tube, followed by 2x LB
3) Heat 95C for 5 mins, then place on ice until use
4) Begin loading the gel OR store samples in -20C until the next day

Loading gel (~1.5 hours)

1) Make sure you have enough “running buffer” if not make some up.

   a. **Running buffer:** 50ml 20X MOPS running buffer in 950ml of diH2O
2) Set up your gel rig and figure the orientation for your samples and marker
3) Load samples and 5ul kaleidoscope protein marker to wells
4) Run at 170v for 70 min or until the dye runs off, on ice or 20v overnight in the cold room

Transfer (~1.5 hours)

1) Make sure you have transfer buffer made up
   a. **Transfer buffer:** 150ml 100% methanol in 1350ml 1x Stock buffer
   b. **Stock buffer:** 144g glycine, 30.5g Tris base, diH2O up to 10L
2) Trim nitrocellulose membrane to fit gel
   a. If using PVDF make sure you soak the membrane in methanol until translucent then wash with DI water 2x
3) Set up your transfer "book" Black on the bottom, then 1 sponge, then 2 filter papers, gel, membrane, 2 filter papers (roll out membrane w/ medium pressure),1-2 sponges, and red on top. Slide to lock in place.
4) Place in transfer rig black to black and clear to red
5) Place lid on black to black and red to red
6) Run transfer at 100v for 1 hour
7) Carefully check to make sure marker transferred before completely taking apart "book". If needed, close book and transfer for longer.

Revert Total Protein Stain, Imaging, & Quantification (~0.5 hours)

Refer to LICOR protocol for two channel detection (saved in Dropbox)
The three solutions: REVERT Total Protein Stain, Wash Solution, and Reversal Solution

1) Place transferred membrane into a bin for Revert Total Protein Analysis
2) Rinse membrane in water
3) Incubate in 5ml REVERT Total Protein Stain for 5 min with gentle shaking
4) Pour out REVERT Total Protein Stain into the "recycle" container
5) Rinse membrane twice with Wash solution
   a. **Wash solution**: 6.7% (v/v) Glacial Acetic Acid, 30% (v/v) Methanol, in water
6) Image the membrane in the 700nm channel
   a. Label it REVERT total protein
7) Rinse with 5ml of Reversal Solution for 5 min with gentle shaking
   a. **Reversal solution:** 0.1% (w/v) NaOH pellets, 30% (v/v) Methanol in water
8) Rinse with water

Block (~1.5 hours)

1) Block for 1 hour at RT and medium shake in 3% BSA in TBS (about ~15-20ml per small or large box)
   a. 0.6g BSA in 20ml TBS
2) Wash 3x in TBS/T for 5 min at a medium shake

Primary AB (overnight)

Note: can only do two primary antibodies with westerns because there are only two IR dyes

1) Make 5% BSA in TBST (~0.02% Tween 20)
    a. 2.5g in 50ml TBST
    b. 1.5g in 30ml TBST
    c. 0.75g in 15ml TBST
2) Add antibody in 8ml (small box) or 14ml (large box) of 5% BSA in TBS/T to the slide box
    a. 1:1000 → ex) 8ul or 14ul
    b. 1:2000 → ex) 4ul or 7ul
    c. 1:5000 → ex)1.6 ul or 2.8ul
    d. 1:10,000 → ex) 0.8ul or 1.4ul
        i. If have two small boxes, then try to make the antibody solutions together to pipet a volume greater than or equal to 1ul. If only one small box, then use 10ml to pipet 1ul for a 1:10,000 dilution
3) Place box on a rocker at medium shake in the cold room

Secondary AB (~2 hours)

1) Wash 2x in TBST 2x for 10 min on a medium shake
2) Add secondary IR dyes in 5% BSA in TBS/T
    a. 8ml for small box, 14ml for large box
    b. 1:10,000 → ex) 0.8ul or 1.4ul
3) Incubate on medium shake at RT for at least 1 hour
4) Wash 3x in TBST for 10 min on a medium shake
5) Bring blot to Licor for imaging

Stripping & Storing (~10 min)

NewBlot Nitrocellulose 5x Stripping Buffer (saved in Dropbox)

1) Dilute to 1X in diH2O
2) Incubate blot in 5X stripping buffer for 10 min at high shake
3) Rinse blot 3x in 1X TBS
4) Store blot in 1X TBS until further processing

Master code for determining HIEL spatial distribution

```
%
% This code analyzes spatial distribution of holes in the internal
 elastic
% lamina (HIEL) and myoendothelial junction (MEJ) localized lipids/
proteins
% in the following sections:
%
%
% % %  SECTION ONE
%
% % %  Thresholds and identifies holes in the internal elastic lamina
% % %  (HIEL). These are objects void of fluorescent signal.
%
%
% % %  SECTION TWO
%
% % %  Thresholds and identifies a fluorescent signal that
% % %  represents an protein of interest that will be used to evaluate
 the
% % %  spatial pattern of the HIEL. In this example, claudin 5
 (cldn5), is
% % %  the fluorescent signal and will be referred to throughout.
%
%
% % %  SECTION THREE
%
% % %  This is a quality control section that removes objects
 identified as
% % %  HIEL that do not meet the circularity requirement. In this
 section,
% % %  there is also the option to manually add back in HIEL removed
 by
% % %  circularity, and to remove additional nonspecific HIEL that may
 have
% % %  been detected.
%
%
% % %  SECTION FOUR
%
% % %  This section runs simulations to evaluate the spatial pattern
 of
% % %  HIEL with respect to the fluorescent signal that was
 thresholded in
% % %  section two. This will refer to 3 separate Matlab function
 files.
%
%
% % %  SECTION FIVE
%
% % %  Thresholds and identifies high intensity fluorescent puncta
 that
```

ExampleCode.m

```
  % % %  overlaps in HIEL. This is useful to determine the extent of
 protein
% % %  localization in the HIEL. In this example phosphatidylserine,
 or PS,
% % %  may be referred to throughout.
%
%
% % %  SECTION SIX
%
% % %  This section runs simulations to evaluate the spatial pattern
 of
% % %  fluorescent puncta in HIEL with respect to the fluorescent
 signal
% % %  that was thresholded in section two. This will refer to 3
 separate
% % %  Matlab function files.
%
%
% % %  SECTION SEVEN
%
% % %  Saves all matrices and variables that will be used for
 analysis.
%
%
%
%
%%
%%%%%
% % % % % % % % %  SECTION ONE
%%%%%
%%
%
%
% Number of iterations that the Monte Carlo, Positive, and Negative
 control
% simulations will be run.
sim1=1; % For HIEL (section1) to fluorescent signal (section2)
sim2 =1; % For puncta-HIEL (section 5) to fluorescent signal
 (section2)
% Keep simulations at 1 iteration while troubleshooting code.
% Recommended to increase to 1000 simulations for final data.
% Will need to run on a virtual supercomputing cluster.


% Define range of pixels wish to be included for analysis.
lowlim1_X = 0; %adjust all based on image/ROI
uplim1_X = 1024;
lowlim1_Y = 0;
uplim1_Y = 1024;
Pixel_min = 0;
Pixel_max = 1024;
% In this example, all pixels of a 1024x1024 image are considered.
```

ExampleCode.m

```
  % Define RGB file. Must be an RGB image (can do that in
ImageJ). RGB = imread('M9V7Z1_hydr.png');

% Convert to grayscale.
I=rgb2gray(RGB);

% Blur the image.
P = fspecial('motion',5,40); %adjust to optimize
% Step 2 of blurring.
I2 = imfilter(I,P,'replicate');

% Idenitfy puncta of interest by converting the blurred image to
 binary.
bw
 =imbinarize(I2,'adaptive','ForegroundPolarity',...
      'dark','Sensitivity',0.1); %adjust to optimize
% In this example, the 'puncta' of interest are actually areas void of
 fluorescent signal.
% For this reason, 'dark' option is selected. For identification of
% fluorescent puncta, you do not need the specifications of
% 'ForegroundPolarity' and 'dark'.


% Refine the identification of HIEL.
SE = strel('disk',5); % ajust to optimize
I3 = imerode(bw,SE);


% % FIGURE 1
% % Show boundaries of ROI on top of the originial image.
% % Visual confirmation that HIEL are being correctly identified.

Figure1 =figure;
[B_M9V7Z1A1,L] = bwboundaries(I3); %detected outline of ROIs.
imshow(I3); hold on; %show detected outline
imshow(I); hold on;  %show original image
colors=('c');
m = size(B_M9V7Z1A1,1);
n = size (B_M9V7Z1A1,2);
area = zeros(m,n);
stats = zeros(m,n);
stats = regionprops(L,'Area');

% Plot boundaries of ROIs.
for k = 1:length(B_M9V7Z1A1)
  boundary = B_M9V7Z1A1{k};
    cidx = mod(k,length(colors))+1;
    plot(boundary(:,2), boundary(:,1),...
       colors(cidx),'LineWidth',2);

      area(k) = stats(k).Area;
% % %  actual number of pixels in the area
```

ExampleCode.m

```
  % % add text to show object numbers
  rndRow = ceil(length(boundary)/(mod(rand*k,7)+1));
  col = boundary(rndRow,2); row = boundary(rndRow,1);
  h = text(col+1, row-1, num2str(L(row,col)));
  set(h,'Color',colors(cidx),'FontSize',12,'FontWeight','bold');
% %   randomize text position for better visibility

end

area = transpose(area);


% % Convert cell array of border pixels and plot centers of each
 object
Q = cellfun(@mean,B_M9V7Z1A1, 'UniformOutput', false);
% get the average of the pixels along the border to calculate center
 of ROI
% NOTE that both Q and b are cell arrays


H = cell2mat(Q);
% % % H is a matrix, which is needed to plot the various coordinates

X = H(:,2:2:end);
Y = H(:,1:2:end);

% % % plots the X,Y coordinates of H (centers of the IEL holes)
plot(X,Y,'.','MarkerSize',12, 'Color', 'm');

% Draw vertical and horizontal lines on the image to see the image
 area you
% are analyzing.  This is only relevant if you want to analyze a small
 area
% of the original image.
xline(lowlim1_X);hold on;
xline(uplim1_X);hold on;
yline(lowlim1_Y);hold on;
yline(uplim1_Y);hold on;
saveas(Figure1, '/Users/claireruddiman/Dropbox/_MEJ Paper/_Figures/
Github/M9V7Z1A1_Analysis/Figure1.png');
hold off;

% Round the final coordinates of HIEL center detection and store in
 matrix.
coord_M9V7Z1A1 = horzcat(round(X),round(Y));
%
%
%
%%
%%%%%
% % % % % % % % %  SECTION TWO
%%%%%
```

ExampleCode.m

```
%%
%
 %
%
% Threshold fluorescent signal claudin 5 (cldn5) EC borders
% (interendothelial junctions).


% Define RGB file. Must be an RGB image (can do that in ImageJ).
% This is fluorescent signal that will be used to define HIEL spatial
% pattern.
RGB_ = imread('M9V7Z1_cldn5_1.png');

% Convert to grayscale.
I_=rgb2gray(RGB_);

% Blur the image.
P_ = fspecial('motion',5,30);
% Step 2 of blurring.
I2_ = imfilter(I_,P_,'replicate');

% Identify puncta of interest by converting the blurred image to
 binary.
bw_ =imbinarize(I2_,'adaptive','Sensitivity',0.1);
%adjust to optimize

% Refine the identification of fluorescent signal.
SE_ = strel('rectangle',[4,1]); % % % pixel size of disk that helps to
 define the IEL holes
I4_ = imerode(bw_,SE_);
se_ = strel('rectangle',[10,1]);
I5_ = imclose(I4_,se_);
I3_ = bwareaopen(I5_,100);

% Plot the result of thresholding the fluorescent signal.
figure
imshow(I3_)
[rows,cols] = find(I3_); % Extract XY coordinates from I3_, which is
 the claudin5 final binary image
claudin5_full_M9V7Z1A1 = horzcat(cols,rows);

% Removes any fluoresecent signal from analysis that is outside of the
%  desired range.
claudin5_full_M9V7Z1A1(claudin5_full_M9V7Z1A1(:, 1) < lowlim1_X &
 (claudin5_full_M9V7Z1A1(:, 1) >= Pixel_min), :) = [];
claudin5_full_M9V7Z1A1(claudin5_full_M9V7Z1A1(:, 1) <= Pixel_max &
 (claudin5_full_M9V7Z1A1(:, 1) > uplim1_X), :) = [];
claudin5_full_M9V7Z1A1(claudin5_full_M9V7Z1A1(:, 2) < lowlim1_Y &
 (claudin5_full_M9V7Z1A1(:, 2) >= Pixel_min), :) = [];
claudin5_full_M9V7Z1A1(claudin5_full_M9V7Z1A1(:, 2) <= Pixel_max &
 (claudin5_full_M9V7Z1A1(:, 2) > uplim1_Y), :) = [];
```

ExampleCode.m

```
% Define sizes of HIEL and fluorescent signal matrices.
[mmm nnn] = size(coord_M9V7Z1A1);
nnn = mmm;
[mmmm nnnn] = size(claudin5_full_M9V7Z1A1);
nnnn = mmmm;
  distance_ = zeros(nnn,mmmm);
%
%
%
%%
%%%%%
% % % % % % % % %  SECTION THREE
%%%%%
%%
%
%
% Remove objects which do not correspond to IEL holes through a
% circularity prediction.


% % FIGURE 2
colors2=('m');
Figure2 = figure;

imshow(I3); hold on;
imshow(I); hold on;

% Display vertical lines to indicate analyzed area.
xline(lowlim1_X);hold on;
xline(uplim1_X);hold on;
yline(lowlim1_Y);hold on;
yline(uplim1_Y);hold on;


% Begin loop to check circularity of detected HIEL
for k = 1:length(B_M9V7Z1A1)
    boundary = B_M9V7Z1A1{k};
    cidx = mod(k,length(colors))+1;
    plot(boundary(:,2), boundary(:,1),...
       colors(cidx),'LineWidth',2);

    % circumference of an HIEL, identified by the number of pixels.
 not as accurate as c_f2. see below.
    c(k)=size(B_M9V7Z1A1{k},1);

    % HIEL area
    area(k) = stats(k).Area;

    % calculate circularity
    metric(k) = (4*pi*area(k))/c(k)^2 ;

    % HIEL area
```

ExampleCode.m

```
        AA(k) = stats(k).Area;

        % HIEL radius
        r(k) = sqrt(AA(k)/pi);

        % HIEL diameter
        d(k) = 2*r(k);

        % HIEL circumference, as calculated from area
        c_f2(k) = 2*pi*r(k);
        label(k) = k;
               for j = 1 : mmmm % size of fluorescent signal (cldn5)
      matrix
                    scale_M9V7Z1A1 = 8.6719; % this is the number of
      pixels per micron
                    distance_(k, j) = (sqrt((coord_M9V7Z1A1(k, 1) -
      claudin5_full_M9V7Z1A1(j, 1)) ^ 2 + ...
                (coord_M9V7Z1A1(k, 2) - claudin5_full_M9V7Z1A1(j, 2)) ^
      2))/scale_M9V7Z1A1;
               end

      % if circularity is greater than 0.5 then keep the predicted object
       if metric(k) > 0.50
           G{k} = B_M9V7Z1A1{k};

           % HIEL area
           AA(k) = stats(k).Area;

           % HIEL radius
           r(k) = sqrt(AA(k)/pi);

           % HIEL diameter
           d(k) = 2*r(k);

           % HIEL circumference as calculated from area. this is the most
           % accurate. Use this value for downstream analysis
           c_f2(k) = 2*pi*r(k);


      matrix
label(k) = k;
X(k) = H(k,2:2:end);
Y(k) = H(k,1:2:end);
    for j = 1 : mmmm % size of fluorescent signal (cldn5)

        scale_M9V7Z1A1 = 8.6719;  % this is the number of
        pixels per micron
                    distance_(k, j) = (sqrt((coord_M9V7Z1A1(k, 1) -
      claudin5_full_M9V7Z1A1(j, 1)) ^ 2 + ...
                (coord_M9V7Z1A1(k, 2) - claudin5_full_M9V7Z1A1(j, 2)) ^
      2))/scale_M9V7Z1A1;
```

ExampleCode.m

```
            end

        metric_string = sprintf('%2.2f',metric(k)); % % % store
  circularity values in a string

  text(boundary(1,2)-35,boundary(1,1)+13,metric_string,'Color','b',...
       'FontSize',12,'FontWeight','bold') % % % % print circularity
  values on plot

    % if circularity is less than 0.5 remove the object
     else
           G{k} = [];
        AA (k) = [];
        r(k)=[]; %
        d(k) = [];%
        c_f2(k) = [];%


  matrix
for j = 1 : mmmm % size of fluorescent signal (cldn5)

    scale_M9V7Z1A1 = 8.6719;
    distance_(k, j) = 0;
              end

        label(k) = [];
        X(k) = 0;
        Y(k) = 0;
        boundary = B_M9V7Z1A1{k};
        cidx = mod(k,length(colors2))+1;
        plot(boundary(:,2), boundary(:,1),...
        colors2(cidx),'LineWidth',2);
     end

 end

 saveas(Figure2, '/Users/claireruddiman/Dropbox/_MEJ Paper/_Figures/
 Github/M9V7Z1A1_Analysis/Figure2.png');
 hold off;
 %
 %
 %
 %%
 %%%%%
 % % % % % % % % % MANUALLY ADD BACK OBJECTS REMOVED BY CIRCULARITY
 % (OPTIONAL)
 %%%%%
 %%
 %
 %
 %
 %
```

ExampleCode.m

```
% UNCOMMENT THIS SECTION if you wish to manually add back in any of
 the
% objects removed by circularity.

% % %%Keep some of the values ruled out by circularity
%  for k=[add number of objects in here];
%         G{k} = B_M9V7Z1A1{k};
%         AA(k) = stats(k).Area;
%         r(k) = sqrt(AA(k)/pi)/scale_M9V7Z1A1; %
%         d(k) = 2*r(k); %
%         c_f2(k) = 2*pi*r(k);%
%         label(k) = k;
%         X(k) = H(k,2:2:end);
%         Y(k) = H(k,1:2:end);
%
  %               for j = 1 : mmmm % size of fluorescent signal
 (cldn5) matrix
%                 scale_M9V7Z1A1 = 8.6719;  % this is the number of
 pixels per micron
%                 distance_(k, j) = (sqrt((coord_M9V7Z1A1(k, 1) -
 claudin5_full_M9V7Z1A1(j, 1)) ^ 2 + ...
%             (coord_M9V7Z1A1(k, 2) - claudin5_full_M9V7Z1A1(j, 2)) ^
 2))/scale_M9V7Z1A1;
%             end
%
%         metric_string = sprintf('%2.2f',metric(k)); % % % store
 circularity values in a string
%
 text(boundary(1,2)-35,boundary(1,1)+13,metric_string,'Color','b',...
%        'FontSize',12,'FontWeight','bold') % % % % print circularity
 values on plot
%
%  end
%
%%

%
%%
%%%%%
% % % % % % % % % MANUALLY REMOVE ADDITIONAL NONSPECIFIC OBJECTS
 (OPTIONAL)
%%%%%
%%
%
%
%
%
G{1}=[]; % OBJECT 1 IS NONSPECIFIC.
% G{2}=[]; % ADD A LINE FOR EACH OBJECT THAT YOU WISH TO REMOVE.


F2 = (G(~cellfun('isempty',G))); % F2 is the cell array that excludes
```

ExampleCode.m

```
 circularity values not within range
        F = transpose(F2);

distance_(1,:) = 0; % OBJECT 1 IS NONSPECIFIC.
% distance_(2,:) = 0; % ADD A LINE FOR EACH OBJECT THAT YOU WISH TO
 REMOVE.

          distance_(~any(distance_,2),:) = []; %delete rows where all
 values are zero
          distance_sort_old = transpose(sort(distance_,2)); %sorting
          distance_avgMIN_hist_M9V7Z1A1 =
 transpose((distance_sort_old(1,:))); %%include this to be able
 to plot a histogram of the minimum distances for each IEL hole to
 claudin 5
          distance_avgMIN_M9V7Z1A1= mean(distance_sort_old(:,1));
%
          Total = 100; %flexible, could also do multiple of these?
            distance_sort_M9V7Z1A1 = distance_sort_old(1:Total,
 1:size(distance_sort_old,2)); % take top 1000 values from this array


X(1) = 0; % OBJECT 1 IS NONSPECIFIC.
% X(2) = 0; % ADD A LINE FOR EACH OBJECT THAT YOU WISH TO REMOVE.


        X=transpose(X);
        X(:,~any(X,1)) = []; %rows
        X=transpose(X);



Y(1) = 0; % OBJECT 1 IS NONSPECIFIC.
% Y(2) = 0; % ADD A LINE FOR EACH OBJECT THAT YOU WISH TO REMOVE.


        Y=transpose(Y);
        Y(:,~any(Y,1)) = []; %rows
        Y=transpose(Y);


AA(1) = 0; % OBJECT 1 IS NONSPECIFIC.
% AA(2) = 0; % ADD A LINE FOR EACH OBJECT THAT YOU WISH TO REMOVE.


        AA( :,~any(AA,1) ) = []; %rows
        AREA_final =transpose(AA);


c_f2(1) = 0; % OBJECT 1 IS NONSPECIFIC.
% c_f2 (2) = 0; % ADD A LINE FOR EACH OBJECT THAT YOU WISH TO REMOVE.

        c_f2( :,~any(c_f2,1) ) = []; %rows
```

ExampleCode.m

```
        C_final =transpose(c_f2);


r(1) = 0; % OBJECT 1 IS NONSPECIFIC.
% r (2) = 0; % ADD A LINE FOR EACH OBJECT THAT YOU WISH TO REMOVE.

        r( :,~any(r,1) ) = []; %rows
        r_final =transpose(r);


d(1) = 0; % OBJECT 1 IS NONSPECIFIC.
% d (2) = 0; % ADD A LINE FOR EACH OBJECT THAT YOU WISH TO REMOVE.
        d( :,~any(d,1) ) = []; %rows
        d_final =transpose(d);


label(1) = 0; % OBJECT 1 IS NONSPECIFIC.
% label (2) = 0; % ADD A LINE FOR EACH OBJECT THAT YOU WISH TO REMOVE.

        label( :,~any(label,1) ) = []; %rows
        label_final =transpose(label);


coord_M9V7Z1A1 = horzcat(round(X),round(Y));


%%Export a list of the final hole numbers
Param_M9V7Z1A1 =
 horzcat(label_final,AREA_final,r_final,C_final,X,Y,...
 distance_avgMIN_hist_M9V7Z1A1)

AvgRadius_M9V7Z1A1 = mean(Param_M9V7Z1A1(:,3));
StdDevRadius = AvgRadius_M9V7Z1A1/4.2;

% Keep values only within desired analysis range.
Param_M9V7Z1A1(Param_M9V7Z1A1(:, 5) < lowlim1_X & (Param_M9V7Z1A1(:,
 5) >= Pixel_min), :) = [];
Param_M9V7Z1A1(Param_M9V7Z1A1(:, 5) <= Pixel_max & (Param_M9V7Z1A1(:,
 5) > uplim1_X), :) = [];
Param_M9V7Z1A1(Param_M9V7Z1A1(:, 6) < lowlim1_Y & (Param_M9V7Z1A1(:,
 6) >= Pixel_min), :) = [];
Param_M9V7Z1A1(Param_M9V7Z1A1(:, 6) <= Pixel_max & (Param_M9V7Z1A1(:,
 6) > uplim1_Y), :) = [];

% Calculate image area in microns, used for downstream analysis.
ImageArea_M9V7Z1A1 = ((uplim1_X-lowlim1_X)/scale_M9V7Z1A1) *
 ((uplim1_Y-lowlim1_Y)/scale_M9V7Z1A1) ;

PartialImage_Height_M9V7Z1A1 = (uplim1_Y-lowlim1_Y);
PartialImage_Width_M9V7Z1A1 = (uplim1_X-lowlim1_X);
```

ExampleCode.m

```
% Define number of HIEL detected
IELHoles_M9V7Z1A1 = length(coord_M9V7Z1A1);

% Calculate number of HIEL per image area.
HolesPerArea_M9V7Z1A1 = IELHoles_M9V7Z1A1/ImageArea_M9V7Z1A1;

coord_M9V7Z1A1 = horzcat(Param_M9V7Z1A1(:,5),Param_M9V7Z1A1(:,6));

% Distance
distance_avgMIN_hist_M9V7Z1A1 = Param_M9V7Z1A1(:,7);
distance_avgMIN_M9V7Z1A1 = mean(Param_M9V7Z1A1(:,7));
distance_sort_M9V7Z1A1 = transpose(distance_sort_M9V7Z1A1);
distance_sort_XY_M9V7Z1A1 = horzcat(X,Y,distance_sort_M9V7Z1A1);


distance_sort_XY_M9V7Z1A1(distance_sort_XY_M9V7Z1A1(:, 1) < lowlim1_X
 & (distance_sort_XY_M9V7Z1A1(:, 1) >= Pixel_min), :) = [];
distance_sort_XY_M9V7Z1A1(distance_sort_XY_M9V7Z1A1(:, 1) <= Pixel_max
 & (distance_sort_XY_M9V7Z1A1(:, 1) > uplim1_X), :) = [];
distance_sort_XY_M9V7Z1A1(distance_sort_XY_M9V7Z1A1(:, 2) < lowlim1_Y
 & (distance_sort_XY_M9V7Z1A1(:, 2) >= Pixel_min), :) = [];
  distance_sort_XY_M9V7Z1A1(distance_sort_XY_M9V7Z1A1(:, 2) <=
 Pixel_max & (distance_sort_XY_M9V7Z1A1(:, 2) > uplim1_Y), :) = [];


distance_sort_XY_M9V7Z1A1(:,1) = []; %remove first column (X)
distance_sort_XY_M9V7Z1A1(:,1) = []; %comment out if using full range
 for Y

distance_sort_XY_M9V7Z1A1 = transpose(distance_sort_XY_M9V7Z1A1);

distance_sort_M9V7Z1A1 = distance_sort_XY_M9V7Z1A1;

% Transpose for exporting
distance_avgMIN_hist_M9V7Z1A1 =
 transpose(distance_avgMIN_hist_M9V7Z1A1);


% % FIGURE 3
% Plot the boundary of HIEL and center of HIEL over top of the image.

Figure3 = figure;
imshow(I); hold on;

for k = 1:length(F)
  boundary = F{k};
    cidx = mod(k,length(colors))+1;
    plot(boundary(:,2), boundary(:,1),...
       colors(cidx),'LineWidth',2);

% %   add text to show object numbers
```

ExampleCode.m

```
  rndRow = ceil(length(boundary)/(mod(rand*k,7)+1));
  col = boundary(rndRow,2); row = boundary(rndRow,1);
  h = text(col+1, row-1, num2str(L(row,col)));
  set(h,'Color',colors(cidx),'FontSize',12,'FontWeight','bold');
%   randomize text position for better visibility

end

% % Convert cell array of border pixels and plot centers of each
 object
Q = cellfun(@mean,F, 'UniformOutput', false);
% get the average of the pixels along the border to calculate center
 of ROI
% NOTE that both Q and b are cell arrays

H = cell2mat(Q);
% % % H is a matrix, which is needed to plot the various coordinates

X = H(:,2:2:end);
Y = H(:,1:2:end);

plot(X,Y,'.','MarkerSize',12, 'Color', 'm'); hold on;
xline(lowlim1_X);hold on;
xline(uplim1_X);hold on;
  yline(lowlim1_Y);hold on;
yline(uplim1_Y);hold on;
saveas(Figure3, '/Users/claireruddiman/Dropbox/_MEJ Paper/_Figures/
Github/M9V7Z1A1_Analysis/Figure3.png');
hold off;



% % FIGURE 4
% Plot HIEL centers on XY plot
Y1=Y;
Figure4 =figure;
plot(X,Y1,'.','MarkerSize',10, 'Color', 'm'); hold on;
xlim([0 1024])
ylim([0 1024])
saveas(Figure4, '/Users/claireruddiman/Dropbox/_MEJ Paper/_Figures/
Github/M9V7Z1A1_Analysis/Figure4.png');
hold off;

% % FIGURE 5
% Plot HIEL centers with respect to other fluorescent signal of
 interest
Figure5 =figure;
plot(claudin5_full_M9V7Z1A1(:,1),
 claudin5_full_M9V7Z1A1(:,2),'.','MarkerSize',2, 'Color',  'c');
 hold on
plot(coord_M9V7Z1A1(:,1),
 coord_M9V7Z1A1(:,2),'.','MarkerSize',12, 'Color', 'm'); hold on;
```

ExampleCode.m

```
xlim([0 1024]);
ylim([0 1024]);
saveas(Figure5, '/Users/claireruddiman/Dropbox/_MEJ Paper/_Figures/
Github/M9V7Z1A1_Analysis/Figure5.png');
hold off;



% % FIGURE 6
% Visual check to verify accuracy of thresholding
% Plot centers and secondary fluorescent signal of interest ontop of
 the
% original fluorescent image
RGB_merge = imread('M9V7Z1_DAPI_cldn5_PS_hydr.png');
Figure6_copy =figure;
imshow(RGB_merge);
hold on;
plot(claudin5_full_M9V7Z1A1(:,1),
 claudin5_full_M9V7Z1A1(:,2),'.','MarkerSize',2, 'Color',  'w')
hold on
plot(coord_M9V7Z1A1(:,1),
 coord_M9V7Z1A1(:,2),'.','MarkerSize',12, 'Color', 'm')
hold on;
  colors3=('k');
for k = 1:length(F)
  boundary_J = F{k};
    cidx = mod(k,length(colors))+1;
    plot(boundary_J(:,2), boundary_J(:,1),...
       colors3(cidx),'LineWidth',2);

% %   add text to show object numbers
  rndRow = ceil(length(boundary_J)/(mod(rand*k,7)+1));
  col = boundary_J(rndRow,2); row = boundary_J(rndRow,1);
  h = text(col+1, row-1, num2str(L(row,col)));
  set(h,'Color',colors2(cidx),'FontSize',8,'FontWeight','bold');
%   randomize text position for better visibility

end
saveas(Figure6_copy, '/Users/claireruddiman/Dropbox/_MEJ Paper/
_Figures/Github/M9V7Z1A1_Analysis/Figure16_copy.png');
hold off;
%
%
%
%
%%
%%%%%
% % % % % % % % %  SECTION FOUR
%%%%%
%%
%
%
```

ExampleCode.m

```
%
%%%%%%%%%%%%%%%%%%%%%%%%%%%%%%%%%%%%%%%%%%%%%%%%%%%%%%%%%%%%%%%%%%%
%
%
% % Begin Monte Carlo simulation
ite = 1;
D = cell(100, 1);
Min_d = cell(100,1);
Min_d_hist = cell(100,1);
distance_mc = zeros(mmmm,nnn);

% This loop commnicates with the ExampleMonteCarlo file.m
for jj=1:sim2 % sim2 is defined at the beginning of this code and
 indicates how many times the simulation will be run

 [distance_mc_sort_M9V7Z1A1,distance_mc_avgMIN_M9V7Z1A1,...
 distance_mc_avgMIN_hist_M9
 = ExampleMonteCarlo(claudin5_full_M9V7Z1A1);
    D{jj} = distance_mc_sort_M9V7Z1A1;
    Min_d{jj} = distance_mc_avgMIN_M9V7Z1A1;
    Min_d_hist{jj} = distance_mc_avgMIN_hist_M9V7Z1A1;
end

% Analyze Monte Carlo simulation
Min_d;
  D;
%top 10000 is defined in the monte carlo simulation
Dtr = cellfun(@(x)transpose(x), D(:,1),'uniformOutput',false); %
 transpose

Dd_new_M9V7Z1A1 = cellfun(@(x)sort(x), D,'uniformOutput',false); %sort
 each cell from low to high
    %average each cell element by element to get 1 final matrix. then
 use this
    %for ddlow etc.
Dd_new_avg_M9V7Z1A1 = mean(cat(3,Dd_new_M9V7Z1A1{:}),3); %average
 output for MC simulations, sort high to low for each HIEL

% %sort by column (each random circle) low to high (distance to
 claudin 5)
Ddlow_M9V7Z1A1 = sort(Dd_new_avg_M9V7Z1A1);


% lowest 100 distances to claudin 5 for each of the simulated IEL
 holes
Total = 100;
Dd_new_avg_top1000 = Dd_new_avg_M9V7Z1A1(1:Total);
%
%
%%%%%%%%%%%%%%%%%%%%%%%%%%%%%%%%%%%%%%%%%%%%%%%%%%%%%%%%%%%%%%%%%%%
%
%
```

ExampleCode.m

```
%Begin simulated positive control
%
ite = 1;
D_pc = cell(100, 1);
Min_p_pc = cell(100,1);
Min_d_hist_pc = cell(100,1);
distance_pc = zeros(mmmm,nnn);

% This loop commnicates with the ExamplePositiveControl file.m
for jj=1:sim2 % sim2 is defined at the beginning of this code and
 indicates how many times the simulation will be run.

 [distance_pc_sort_M9V7Z1A1,distance_pc_avgMIN_M9V7Z1A1,...
 distance_pc_avgMIN_hist_M9
 = ExamplePositiveControl(claudin5_full_M9V7Z1A1,coord_M9V7Z1A1);
    D_pc{jj} = distance_pc_sort_M9V7Z1A1;
    Min_p_pc{jj} = distance_pc_avgMIN_M9V7Z1A1;
    Min_d_hist_pc{jj} = distance_pc_avgMIN_hist_M9V7Z1A1;
end

% Analyze positive control2 simulation
Min_p_pc;

D_pc;
%top 100 is defined in the positive control simulation
Dtr_pc = cellfun(@(x)transpose(x), D_pc(:,1),'uniformOutput',false); %
 transpose
  Dd_new_pc_M9V7Z1A1 = cellfun(@(x)sort(x),
 D_pc,'uniformOutput',false); %sort each cell from low to high
    %average each cell element by element to get 1 final matrix. then
 use this
    %for ddlow etc.
Dd_new_avg_pc_M9V7Z1A1 =
 mean(cat(3,Dd_new_pc_M9V7Z1A1{:}),3); %average output for MC
 simulations, sort high to low for each IEL hole

% %sort by column (each circle) low to high (distance to claudin 5)
Ddlow_pc_M9V7Z1A1 = sort(Dd_new_avg_pc_M9V7Z1A1,2);

% lowest 100 distances to claudin 5 for each of the simulated IEL
 holes
Total = 100;
Dd_new_avg_top_pce_M9V7Z1A1 = Ddlow_pc_M9V7Z1A1(1:Total);
%
%
%
%%%%%%%%%%%%%%%%%%%%%%%%%%%%%%%%%%%%%%%%%%%%%%%%%%%%%%%%%%%%%%%%%%%%%%%%%%%%%%%%%
%
%
%
%Begin simulated negative control
%
```

```
ite = 1;
D_nc = cell(100, 1);
Min_d_nc = cell(100,1);
Min_d_hist_nc = cell(100,1);
distance_nc = zeros(mmmm,nnn);

% This loop commnicates with the ExampleNegativeControl file.m
for jj=1:sim2 % sim2 is defined at the beginning of this code and
 indicates how many times the simulation will be run.

 [distance_nc_sort_M9V7Z1A1,distance_nc_avgMIN_M9V7Z1A1,...
 distance_nc_avgMIN_hist_M9
 = ExampleNegativeControl(claudin5_full_M9V7Z1A1,coord_M9V7Z1A1);
    D_nc{jj} = distance_nc_sort_M9V7Z1A1;
    Min_d_nc{jj} = distance_nc_avgMIN_M9V7Z1A1;
    Min_d_hist_nc{jj} = distance_nc_avgMIN_hist_M9V7Z1A1;
end

% Analyze neg control simulation
Min_d_nc;

D_nc;
%top 100 is defined within the neg control file.
Dtr_nc_M9V7Z1A1 = cellfun(@(x)transpose(x),
 D_nc(:,1),'uniformOutput',false); % transpose

Dd_new_nc_M9V7Z1A1 = cellfun(@(x)sort(x),
 D_nc,'uniformOutput',false); %sort each cell from low to high
    %average each cell element by element to get 1 final matrix. then
 use this
      %for ddlow etc.
Dd_new_avg_nc_M9V7Z1A1 =
 mean(cat(3,Dd_new_nc_M9V7Z1A1{:}),3); %average output for MC
 simulations, sort high to low for each IEL hole

%sort by column (each circle) low to high (distance to claudin 5)
Ddlow_nc_M9V7Z1A1 = sort(Dd_new_avg_nc_M9V7Z1A1,2);

% lowest 100 distances to claudin 5 for each of the simulated IEL
 holes
Total = 100;
Dd_new_avg_top_pce_M9V7Z1A1 = Ddlow_nc_M9V7Z1A1(1:Total);
%
%
%
%
%%
%%%%%
% % % % % % % % %  SECTION FIVE
%%%%%
%%
%
```

ExampleCode.m

```
%
%
%
%%%%%%%%%%%%%%%%%%%%%%%%%%%%PUNCTA DETECTION%%%%%%%%%%%%%%%%%%%%%%%%%%%%
%%%%
%%%%%%%%%%%%%%%%%%%%%%%%%%%%PUNCTA DETECTION%%%%%%%%%%%%%%%%%%%%%%%%%%%%
%%%%
%%%%%%%%%%%%%%%%%%%%%%%%%%%%PUNCTA DETECTION%%%%%%%%%%%%%%%%%%%%%%%%%%%%
%%%%
%%%%%%%%%%%%%%%%%%%%%%%%%%%%PUNCTA DETECTION%%%%%%%%%%%%%%%%%%%%%%%%%%%%
%%%%

% Define RGB file. Must be an RGB image (can do that in ImageJ).
% This file is the puncta that are localized to HIEL.
RGB = imread('M9V7Z1_PS.png');

% convert to grayscale
I_p=rgb2gray(RGB);
figure; imshow(I_p); % display grayscale

% Blur the image.
P = fspecial('motion',1);
% Blur step 2.
I2_p = imfilter(I_p,P,'replicate');

figure; imshow(I2_p); %display after blurring

% Idenitfy puncta of interest by converting the blurred image to
 binary.
bw_p =imbinarize(I2_p,'adaptive','Sensitivity',0.1); %adjust to
 optimize
  % Refine the identification of puncta.
SE = strel('disk',3); %adjust to optimize
I3_p = imerode(bw_p,SE);%adjust to optimize
I4_p = bwpropfilt(I3_p,'Area',[2 100]);

Figure2p = figure; hold on; imshow(I4_p); hold off;

% Read in more RGB images to use in figures throughout section
RGB_4 = imread('M9V7Z1_PS_hydr.png');
RGB_merge = imread('M9V7Z1_DAPI_cldn5_PS_hydr.png');


% Threshold puncta fluoresence images into 20 different levels
thresh = multithresh(I_p,20); % adjust levels bassed  on how strong or
 weak your puncta signal are

imshow(I_p);
seg_I = imquantize(I_p, thresh);
RGB_2 = label2rgb(seg_I);
figure;
imshow(RGB_2)
```

ExampleCode.m

```
% Consider only the 20th level of threshold (highest) as the
 definition of
% puncta.
I4_p =  seg_I~=0 & seg_I~=1 & seg_I~=2 & seg_I~=3 &  seg_I~=4 &...
 seg_I~=5 & seg_I~=6 & seg_I~=7 & seg_I~=8 & seg_I~=9 & seg_I~=10 &
 seg_I~=11 &...
 seg_I~=12 & seg_I~=13 & seg_I~=14 & seg_I~=15 & seg_I~=16 & seg_I~=17
 & seg_I~=18 & seg_I~=19;% & seg_I~=8

[B_p,L_p] = bwboundaries(I4_p);


% % FIGURE 3P
% Plot HIEL centers with respect to other fluorescent signal of
 interest

Figure3p_test = figure;
RGB_3 = label2rgb(I4_p);

imshow(RGB_4); hold on;

colors=('k');
for k = 1:length(B_p)
    boundary = B_p{k};
    cidx = mod(k,length(colors))+1;
    plot(boundary(:,2), boundary(:,1),...
       colors(cidx),'LineWidth',2);

% %   add text to show object numbers
  rndRow = ceil(length(boundary)/(mod(rand*k,7)+1));
  col = boundary(rndRow,2); row = boundary(rndRow,1);
  h = text(col+1, row-1, num2str(L_p(row,col)));
    set(h,'Color',colors(cidx),'FontSize',8);
% %   randomize text position for better visibility

end
hold on;

saveas(Figure3p_test, '/Users/claireruddiman/Dropbox/_MEJ Paper/
_Figures/Github/M9V7Z1A1_Analysis/Figure3p_test.png');
hold off;


G_p_check = cell2mat(B_p);
X_p_check = G_p_check(:,2:2:end);
Y_p_check = G_p_check(:,1:2:end);
Figure_verifypuncta =figure; imshow(RGB_4); hold on; plot(X_p_check,
 Y_p_check, '.', 'Color', 'y', 'MarkerSize',5);
saveas(Figure_verifypuncta, '/Users/claireruddiman/Dropbox/_MEJ Paper/
_Figures/Github/M9V7Z1A1_Analysis/Figure_verifypuncta.png');
```

ExampleCode.m

```
hold off;


% Calculate centerpoints of puncta

Figure_p_centers =figure;
hold on;
Q_p = cellfun(@mean,B_p, 'UniformOutput', false);
% get the average of the pixels along the border to calculate center

Q_p(cellfun(@(Q_p) any(isnan(Q_p)),Q_p)) = [];
H_p = cell2mat(Q_p);
% NOTE both Q and b are cell arrays

% plots the X_p,Y_p coordinates of H (centers of puncta)
X_p = H_p(:,2:2:end);
Y_p = H_p(:,1:2:end);
plot(X_p,Y_p,'.','MarkerSize',5, 'Color', 'm');

saveas(Figure_p_centers, '/Users/claireruddiman/Dropbox/_MEJ Paper/
_Figures/Github/M9V7Z1A1_Analysis/Figure_p_centers.png');
hold off;
coord_p_centers_M9V7Z1A1 = horzcat(round(X_p),round(Y_p));


% % UNCOMMENT if want to analyze within certain bounds.
% % Only consider puncta within the specified bounds of analysis
% coord_p_centers_M9V7Z1A1(coord_p_centers_M9V7Z1A1(:, 1) < lowlim1_X
 & (coord_p_centers_M9V7Z1A1(:, 1) >= Pixel_min), :) = [];
% coord_p_centers_M9V7Z1A1(coord_p_centers_M9V7Z1A1(:, 1) <= Pixel_max
 & (coord_p_centers_M9V7Z1A1(:, 1) > uplim1_X), :) = [];
% coord_p_centers_M9V7Z1A1(coord_p_centers_M9V7Z1A1(:, 2) < lowlim1_Y
 & (coord_p_centers_M9V7Z1A1(:, 2) >= Pixel_min), :) = [];
% coord_p_centers_M9V7Z1A1(coord_p_centers_M9V7Z1A1(:, 2) <= Pixel_max
 & (coord_p_centers_M9V7Z1A1(:, 2) > uplim1_Y), :) = [];


% Uncomment this this code if want to consider only a specific area of
 image

% % EXAMPLE: if only want to consider ones that are between
 200<X_p<700
% % where 200 and 700 are pixel bounds
% lowlim1 = 200;
% uplim1 = 700;
% puncta_final(puncta_final(:,1) < lowlim1, :) = [];
% puncta_final(puncta_final(:,1) > uplim1, :) = [];

puncta_final_M9V7Z1A1 = coord_p_centers_M9V7Z1A1;
```

ExampleCode.m

```
% % FIGURE PUNCTA CHECK
% Plot detected puncta centers on top of IEL image.

FigurePunctaCheck = figure;
RGb_merge2 = imread('M9V7Z1_hydr.png');
imshow(RGb_merge2); hold on;


 for i =1:length(coord_p_centers_M9V7Z1A1)

 plot(coord_p_centers_M9V7Z1A1(i,1),coord_p_centers_M9V7Z1A1(i,2),...
  '.','MarkerSize 'b')
   labels2(i) = cellstr(num2str(([0+i])));
   text(coord_p_centers_M9V7Z1A1(i,1), coord_p_centers_M9V7Z1A1(i,2),
 labels2(i), 'VerticalAlignment', 'bottom',...
  'HorizontalAlignment', 'right', 'Color
 end

xline(lowlim1_X, 'Color','w');hold on;
xline(uplim1_X,'Color','w');hold on;
yline(lowlim1_Y,'Color','w');hold on;
yline(uplim1_Y,'Color','w');hold on;
FigurePunctaOverlapCheck_2.InvertHardcopy = 'off';


 saveas(FigurePunctaCheck, '/Users/claireruddiman/Dropbox/_MEJ Paper/
_Figures/Github/M9V7Z1A1_Analysis/FigurePunctaCheck.png');
 hold off;



% % FIGURE PUNCTA CHECK 2
% Plot detected puncta centers on top of IEL+puncta image

FigurePunctaCheck2 = figure;
imshow(RGB_4); hold on;
   for i =1:length(coord_p_centers_M9V7Z1A1)

 plot(coord_p_centers_M9V7Z1A1(i,1),...
 coord_p_centers_M9V7Z1A1(i,2), '.','MarkerSize 'b')
   labels2(i) = cellstr(num2str(([0+i])));
   text(coord_p_centers_M9V7Z1A1(i,1), coord_p_centers_M9V7Z1A1(i,2),
 labels2(i), 'VerticalAlignment', 'bottom',...
  'HorizontalAlignment', 'right', 'Color
 end


xline(lowlim1_X, 'Color','w');hold on;
xline(uplim1_X,'Color','w');hold on;
yline(lowlim1_Y,'Color','w');hold on;
yline(uplim1_Y,'Color','w');hold on;
```

ExampleCode.m

```
FigurePunctaOverlapCheck_2.InvertHardcopy = 'off';


 saveas(FigurePunctaCheck2, '/Users/claireruddiman/Dropbox/_MEJ Paper/
_Figures/Github/M9V7Z1A1_Analysis/FigurePunctaCheck2.png');
 hold off;


% % UNCOMMENT if want to analyze within certain bounds.

% puncta_final_M9V7Z1A1(puncta_final_M9V7Z1A1(:, 1) < lowlim1_X &
 (puncta_final_M9V7Z1A1(:, 1) > Pixel_min), :) = [];
% puncta_final_M9V7Z1A1(puncta_final_M9V7Z1A1(:, 1) < Pixel_max &
 (puncta_final_M9V7Z1A1(:, 1) > uplim1_X), :) = [];
% puncta_final_M9V7Z1A1(puncta_final_M9V7Z1A1(:, 2) < lowlim1_Y &
 (puncta_final_M9V7Z1A1(:, 2) > Pixel_min), :) = [];
% puncta_final_M9V7Z1A1(puncta_final_M9V7Z1A1(:, 2) < Pixel_max &
 (puncta_final_M9V7Z1A1(:, 2) > uplim1_Y), :) = [];

%puncta_final(puncta_final(:, 1) < 400 & (puncta_final(:, 1) > 780) &
 (puncta_final(:, 2) < 200) & (puncta_final(:,2)>210), :) = [];
%Remove when  X_p 358-382 and Y_p 709 - 724
% puncta_final(puncta_final(:, 1) < 395 & (puncta_final(:, 1) > 350) &
 (puncta_final(:, 2) < 745) & (puncta_final(:,2)>700), :) = [];




%%%
%%%
%%%
% % % The next several figures are visual checks to confirm that the
 code
% % % is thresholding and detecting the correct objects.
%%%
%%%
%%%


Figure9p = figure;
  imshow(RGB); hold on;
plot(puncta_final_M9V7Z1A1(:,1),
 puncta_final_M9V7Z1A1(:,2), '.','MarkerSize',2, 'Color',  'c');
 hold on;
saveas(Figure9p, '/Users/claireruddiman/Dropbox/_MEJ Paper/_Figures/
Github/M9V7Z1A1_Analysis/Figure9p.png');
xline(lowlim1_X, 'Color','w');hold on;
xline(uplim1_X,'Color','w');hold on;
yline(lowlim1_Y,'Color','w');hold on;
yline(uplim1_Y,'Color','w');hold on;
hold off;
```

ExampleCode.m

```
RGB_merge = imread('M9V7Z1_PS.png');
Figure9p = figure;
imshow(RGB_merge); hold on;
plot(puncta_final_M9V7Z1A1(:,1),
 puncta_final_M9V7Z1A1(:,2), '.','MarkerSize',2, 'Color',  'c');
 hold on;
saveas(Figure9p, '/Users/claireruddiman/Dropbox/_MEJ Paper/_Figures/
Github/M9V7Z1A1_Analysis/Figure9p.png');
xline(lowlim1_X, 'Color','w');hold on;
xline(uplim1_X,'Color','w');hold on;
yline(lowlim1_Y,'Color','w');hold on;
yline(uplim1_Y,'Color','w');hold on;
hold off;

RGB_merge = imread('M9V7Z1_PS.png');
Figure_puncta_centers = figure;
imshow(RGB_merge); hold on;
plot(coord_p_centers_M9V7Z1A1(:,1),
 coord_p_centers_M9V7Z1A1(:,2), '.','MarkerSize',2, 'Color',  'w');
 hold on;
saveas(Figure_puncta_centers, '/Users/claireruddiman/Dropbox/_MEJ
 Paper/_Figures/Github/M9V7Z1A1_Analysis/Figure_puncta_centers.png');
xline(lowlim1_X, 'Color','w');hold on;
xline(uplim1_X,'Color','w');hold on;
yline(lowlim1_Y,'Color','w');hold on;
yline(uplim1_Y,'Color','w');hold on;
hold off;


%
%%
%%%%%
% % % % % % % % %  PUNCTA CALCULATIONS
%%%%%
%%
%

% Calculate distance of puncta centers to HIEL centers.

for k = 1:length(coord_p_centers_M9V7Z1A1)
   label_p(k) = k;
end

label_p = transpose(label_p);

% Define distance of PS puncta to HIEL center that defines it as
% being in an HIEL.
Threshold_p = 0.75; % in microns

% Calculate the distances of ALL puncta to ALL HIEL
distance_p_M9V7Z1A1 = pdist2(coord_M9V7Z1A1,coord_p_centers_M9V7Z1A1);
```

ExampleCode.m

```
% Sort distances
distance_p_M9V7Z1A1 = sort(distance_p_M9V7Z1A1);
distance_p_ALLPUNCTA_M9V7Z1A1=(transpose(distance_p_M9V7Z1A1(1,:))); %
 distance of all puncta to nearest IEL hole

% Convert distances to microns
distance_p_M9V7Z1A1 = distance_p_M9V7Z1A1/scale_M9V7Z1A1;
distance_p_thresh = distance_p_M9V7Z1A1;

% Remove distances that are above the threshold.
distance_p_thresh(distance_p_thresh > Threshold_p) = NaN;
distance_p_min_M9V7Z1A1 = transpose(distance_p_thresh(1,:));

distance_p_min_final_M9V7Z1A1 =
 distance_p_min_M9V7Z1A1(~isnan(distance_p_min_M9V7Z1A1));

% Add in puncta labels to the remaining distances in order to
% identify the puncta that overlap with HIEL.
distance_p_min_M9V7Z1A1 = horzcat(label_p, distance_p_min_M9V7Z1A1);
distance_p_min_index_M9V7Z1A1 =
 distance_p_min_M9V7Z1A1(~isnan(distance_p_min_M9V7Z1A1(:,2)));

% Report puncta label and its distance to HIEL in a matrix.
distance_p_min_final_M9V7Z1A1 = horzcat(distance_p_min_index_M9V7Z1A1,
 distance_p_min_final_M9V7Z1A1);


% This matrix contains the puncta that were identified as
% overlapping with HIEL, with their distances to HIEL centers
% reported (within the thresholded limit of Threshold_p =0.75
% microns).
distance_p_min_final_M9V7Z1A1_copy_orig =
 distance_p_min_final_M9V7Z1A1;
%
%
%
%%%%
%%%%
% % % % MANUALLY REMOVE PUNCTA (if they were incorrectly identified as
 overlapping with HIEL)
% % % % using row numbers of distance_p_min_final_M9V7Z1A1 matrix
% % % % and the "TF" system below.
%%%%
%%%%
 %
%
%
TF1 =distance_p_min_final_M9V7Z1A1(:,1) ==30;
TF2 =distance_p_min_final_M9V7Z1A1(:,1) ==31;
TF3 =distance_p_min_final_M9V7Z1A1(:,1) ==60;
TF4 =distance_p_min_final_M9V7Z1A1(:,1) ==59;
TF5 =distance_p_min_final_M9V7Z1A1(:,1) ==66;
```

ExampleCode.m

```
%       TF6 =distance_p_min_final_M9V7Z1A1(:,1) ==NEWNUMBER;
%
TFall = TF1 | TF2 | TF3 | TF4 | TF5 ; % | TF6 ;
distance_p_min_final_M9V7Z1A1(TFall, :)=[];
%
%


%%
% % FIGURE
% % Visual confirmation that threshold of 0.75um correctly identifies
 a
% % puncta overlapping with HIEL.
%%


RGb_merge2 = imread('M9V7Z1_hydr.png'); %%this is the figure that has
 the puncta and the IEL holes only
FigurePunctaOverlapCheck = figure;
PunctaIndex_M9V7Z1A1 = horzcat(label_p, coord_p_centers_M9V7Z1A1);
imshow(RGb_merge2); hold on;

% These are the labels that correspond to the puncta identifier. Must
 MANUALLY copy
% and paste these from distance_p_min_final_M9V7Z1A1.
labels =
 cellstr(num2str(([[[[[[3;12;13;22;23;24;32;37;38;39;41;...
 43;55;56;61;63;64;65;67;68


 for i = distance_p_min_final_M9V7Z1A1(:,1)
   plot(PunctaIndex_M9V7Z1A1(i,2),
 PunctaIndex_M9V7Z1A1(i,3), '.','MarkerSize',12, 'Color',  'b')
   text(PunctaIndex_M9V7Z1A1(i,2), PunctaIndex_M9V7Z1A1(i,3),
 labels, 'VerticalAlignment', 'bottom',…
  'HorizontalAlignment', 'right','Color','m'
 end

xline(lowlim1_X, 'Color','w');hold on;
xline(uplim1_X,'Color','w');hold on;
yline(lowlim1_Y,'Color','w');hold on;
yline(uplim1_Y,'Color','w');hold on;
FigurePunctaOverlapCheck_2.InvertHardcopy = 'off';

 saveas(FigurePunctaOverlapCheck, '/Users/claireruddiman/
Dropbox/_MEJ Paper/_Figures/Github/M9V7Z1A1_Analysis/
FigurePunctaOverlapCheck.png');
 hold off;

%%
% % FIGURE
% % Visual confirmation that threshold of 0.75um correctly identifies
```

ExampleCode.m

```
 a
% % puncta overlapping with HIEL.
%%

FigurePunctaOverlapCheck_2 = figure;
PunctaIndex_M9V7Z1A1 = horzcat(label_p, coord_p_centers_M9V7Z1A1);
imshow(RGB_merge); hold on;



 for i = distance_p_min_final_M9V7Z1A1(:,1)
   plot(PunctaIndex_M9V7Z1A1(i,2),
 PunctaIndex_M9V7Z1A1(i,3), '.','MarkerSize',12, 'Color',  'b')
   text(PunctaIndex_M9V7Z1A1(i,2), PunctaIndex_M9V7Z1A1(i,3),
 labels, 'VerticalAlignment', 'bottom',...
  'HorizontalAlignment', 'right', 'Color', '
 end

xline(lowlim1_X, 'Color','w');hold on;
xline(uplim1_X,'Color','w');hold on;
yline(lowlim1_Y,'Color','w');hold on;
yline(uplim1_Y,'Color','w');hold on;
FigurePunctaOverlapCheck_2.InvertHardcopy = 'off';

saveas(FigurePunctaOverlapCheck_2, '/Users/claireruddiman/
Dropbox/_MEJ Paper/_Figures/Github/M9V7Z1A1_Analysis/
FigurePunctaOverlapCheck_2.png');
hold off;


% Calculate the distance of puncta to claudin5
distance_p_cldn5_M9V7Z1A1 =
 pdist2(claudin5_full_M9V7Z1A1,coord_p_centers_M9V7Z1A1);
distance_p_cldn5_M9V7Z1A1 = sort(distance_p_cldn5_M9V7Z1A1);
distance_p_cldn5_M9V7Z1A1 = distance_p_cldn5_M9V7Z1A1/scale_M9V7Z1A1;
distance_p_cldn5_M9V7Z1A1 = transpose(distance_p_cldn5_M9V7Z1A1(1,:));

distance_p_cldn5_M9V7Z1A1_Label = horzcat(label_p,
 distance_p_cldn5_M9V7Z1A1);


% These are the labels that correspond to the puncta identifier. Must
 MANUALLY copy
% and paste these from distance_p_min_final_M9V7Z1A1.
distance_p_cldn5_overlap_M9V7Z1A1 = distance_p_cldn5_M9V7Z1A1([[[[[[[[3
 12 13 22 23 24 32 37 38 39 41 43 55 56 61 63 64 65 67 68]]]]]]]]);
distance_p_min_final_overlap_M9V7Z1A1 =
horzcat(distance_p_min_final_M9V7Z1A1,...
distance_p_cldn5_overlap_M9V7Z1A1);
  #puncta, dist to nearest HIEL, dist to nearest cldn5
  % Final matirx that includes puncta number, distance to closest
 HIEL, and minimum distance to claudin5.
```

ExampleCode.m

```
distance_ALLPUNCTA_final_M9V7Z1A1= horzcat(label_p,
 distance_p_ALLPUNCTA_M9V7Z1A1, distance_p_cldn5_M9V7Z1A1); % #puncta,
 dist to nearest HIEL, dist to nearest cldn5


% Calculate proportion of HIEL that have a puncta
% number of IEL holes
Total_HIEL_M9V7Z1A1 = length(coord_M9V7Z1A1);
PS_pos_M9V7Z1A1 = length(distance_p_min_index_M9V7Z1A1); %length of
PercentPosHIEL_M9V7Z1A1 = PS_pos_M9V7Z1A1/Total_HIEL_M9V7Z1A1;


% Calculate proportion of puncta overlying HIEL.
Total_Puncta_M9V7Z1A1 = length(coord_p_centers_M9V7Z1A1);
PercentPunctaWithHIELOverlap_M9V7Z1A1 = PS_pos_M9V7Z1A1/
Total_Puncta_M9V7Z1A1;
%
%
%
%
%%
%%%%%
% % % % % % % % %  SECTION SIX
%%%%%
%%
%
%
%
%
% % begin Monte Carlo simulation for puncta to claudin5
ite = 1;
D = cell(100, 1);
Min_d_nc = cell(100,1);
Min_d_hist_nc = cell(100,1);
distance_mc_p = zeros(mmmm,nnn);
N_mc_p = length(coord_M9V7Z1A1);


% This loop communicates with ExampleMonteCarloPuncta.m
for jj=1:sim1 % sim1 is defined at the beginning of this code and
 indicates how many times the simulation will be run.

 [distance_mc_p_sort_M9V7Z1A1,distance_mc_p_avgMIN_M9V7Z1A1,...
 distance_mc_p_avgMIN_M
 = ExampleMonteCarloPuncta(claudin5_full_M9V7Z1A1,N_mc_p);
    D{jj} = distance_mc_p_sort_M9V7Z1A1;
    Min_d_nc{jj} = distance_mc_p_avgMIN_M9V7Z1A1;
    Min_d_hist_nc{jj} = distance_mc_p_avgMIN_M9V7Z1A1_hist;
end


% Analyze Monte Carlo simulation
```

ExampleCode.m

```
Min_d_nc;

D;
%top 100 is defined in the monte carlo simulation
Dtr = cellfun(@(x)transpose(x), D(:,1),'uniformOutput',false); %
 transpose


Dd_new = cellfun(@(x)sort(x), D,'uniformOutput',false); %sort each
 cell from low to high
    %average each cell element by element to get 1 final matrix. then
 use this
    %for Ddlow_p_M9V7Z1A1 etc.
Dd_new_p_avg_M9V7Z1A1 = mean(cat(3,Dd_new{:}),3); %average output for
 mc_p simulations, sort high to low for each IEL hole

Ddlow_p_M9V7Z1A1 = sort(Dd_new_p_avg_M9V7Z1A1); %sort by column (each
 random circle) low to high (distance to claudin 5)
Ddlow_p_M9V7Z1A12 = sort(Dd_new_p_avg_M9V7Z1A1);
Ddlow_p_M9V7Z1A13 = sort(Dd_new_p_avg_M9V7Z1A1);
Ddlow_p_M9V7Z1A14 = sort(Dd_new_p_avg_M9V7Z1A1);
Ddlow_p_M9V7Z1A15 = sort(Dd_new_p_avg_M9V7Z1A1);

% % lowest 100 distances to claudin 5 for each of the simulated IEL
 holes
Total = 100;
Dd_new_p_avg_M9V7Z1A1_top1000 = Dd_new_p_avg_M9V7Z1A1(1:Total);
%
%
%%%%%%%%%%%%%%%%%%%%%%%%%%%%%%%%%%%%%%%%%%%%%%%%%%%%%%%%%%%%%%%%%%%%%%%
%
%
%begin simulated positive control

ite = 100;
D_pc = cell(100, 1);
Min_p_pc = cell(100,1);
Min_d_hist_pc = cell(100,1);
distance_pc = zeros(mmmm,nnn);

% This code communicates with ExamplePositiveControlPuncta.m
for jj=1:sim1 % sim1 is defined at the beginning of this code and
 indicates how many times the simulation will be run.

 [distance_pc_p_sort_M9V7Z1A1,distance_pc_p_avgMIN_M9V7Z1A1,...
 distance_pc_p_avgMIN_M
 =
 ExamplePositiveControlPuncta(claudin5_full_M9V7Z1A1,...
 coord_p_centers_M9V7Z1A1,Punc D_pc{jj} = distance_pc_p_sort_M9V7Z1A1;
    Min_p_pc{jj} = distance_pc_p_avgMIN_M9V7Z1A1;
    Min_d_hist_pc{jj} = distance_pc_p_avgMIN_M9V7Z1A1_hist;
end
```

ExampleCode.m

```
% Analyze positive control simulation
Min_p_pc;
  D_pc;
%top 100 is defined in the positive control simulation
Dtr_pc = cellfun(@(x)transpose(x), D_pc(:,1),'uniformOutput',false); %
 transpose

Dd_new_p_pc = cellfun(@(x)sort(x), D_pc,'uniformOutput',false); %sort
 each cell from low to high

Dd_new_p_avg_M9V7Z1A1_pc = mean(cat(3,Dd_new_p_pc{:}),3); %average
 output for mc_p simulations, sort high to low for each IEL hole

Ddlow_p_M9V7Z1A1_pc = sort(Dd_new_p_avg_M9V7Z1A1_pc,2); %sort by
 column (each random circle) low to high (distance to claudin 5)
Ddlow_p_M9V7Z1A12_pc = sort(Dd_new_p_avg_M9V7Z1A1_pc,2);
Ddlow_p_M9V7Z1A13_pc = sort(Dd_new_p_avg_M9V7Z1A1_pc,2);
Ddlow_p_M9V7Z1A14_pc = sort(Dd_new_p_avg_M9V7Z1A1_pc,2);
Ddlow_p_M9V7Z1A15_pc = sort(Dd_new_p_avg_M9V7Z1A1_pc,2);

% % lowest 100 distances to claudin 5 for each of the simulated IEL
 holes
Total = 100;
Dd_new_p_avg_M9V7Z1A1_top_pce = Ddlow_p_M9V7Z1A1_pc(1:Total);
%
%
%
%%%%%%%%%%%%%%%%%%%%%%%%%%%%%%%%%%%%%%%%%%%%%%%%%%%%%%%%%%%%%%%%%%%%%%%
%
%
%
%begin simulated negative control

ite = 1;
D_nc = cell(100, 1);
Min_d_nc = cell(100,1);
Min_d_hist_nc = cell(100,1);
distance_nc = zeros(mmmm,nnn);

% This code communicates with ExampleNegativeControlPuncta.m
for jj=1:sim1 %sim1 is defined at the beginning of this code and
 indicates how many times the simulation will be run.

 [distance_nc_p_sort_M9V7Z1A1,distance_nc_p_avgMIN_M9V7Z1A1,...
 distance_nc_p_avgMIN_M
 =
 ExampleNegativeControlPuncta(claudin5_full_M9V7Z1A1,...
 coord_p_centers_M9V7Z1A1, PunctaIndex_M9V7Z1A1);
    D_nc{jj} = distance_nc_p_sort_M9V7Z1A1;
    Min_d_nc{jj} = distance_nc_p_avgMIN_M9V7Z1A1;
    Min_d_hist_nc{jj} = distance_nc_p_avgMIN_M9V7Z1A1_hist;
```

ExampleCode.m

```
end

% Analyze neg control simulation
Min_d_nc;

D_nc;
  %top 100 is defined within the neg control file.
Dtr_nc = cellfun(@(x)transpose(x), D_nc(:,1),'uniformOutput',false); %
 transpose

Dd_new_p_nc = cellfun(@(x)sort(x), D_nc,'uniformOutput',false); %sort
 each cell from low to high
Dd_new_p_avg_M9V7Z1A1_nc = mean(cat(3,Dd_new_p_nc{:}),3); %average
 output for mc_p simulations, sort high to low for each IEL hole
Ddlow_p_M9V7Z1A1_nc = sort(Dd_new_p_avg_M9V7Z1A1_nc,2); %sort by
 column (each random circle) low to high (distance to claudin 5)
Ddlow_p_M9V7Z1A12_nc = sort(Dd_new_p_avg_M9V7Z1A1_nc,2);
Ddlow_p_M9V7Z1A13_nc = sort(Dd_new_p_avg_M9V7Z1A1_nc,2);
Ddlow_p_M9V7Z1A14_nc = sort(Dd_new_p_avg_M9V7Z1A1_nc,2);
Ddlow_p_M9V7Z1A15_nc = sort(Dd_new_p_avg_M9V7Z1A1_nc,2);


% % lowest 100 distances to claudin 5 for each of the simulated IEL
 holes
Total = 100;
Dd_new_p_avg_M9V7Z1A1_top_pce = Ddlow_p_M9V7Z1A1_nc(1:Total);
%
%
%
%
%%
%%%%%
% % % % % % % % % %  SECTION SEVEN
%%%%%
%%
%
%
%
%
```

```
      % Save all the worthwhile variables into a file.

save('Puncta_Cldn5_Partial_M9V7Z1A1.mat', 'claudin5_full_M9V7Z1A1',...
 'coord_M9V7Z1A1', 'B_M9V7Z1A1','distance_sort_M9V7Z1A1','distance_avgMIN_M9V7Z1A1',
'distance_avgMIN_hist_M9V7Z1A1',...
    'distance_nc_sort_M9V7Z1A1','distance_nc_avgMIN_M9V7Z1A1',
'distance_nc_avgMIN_hist_M9V7Z1A1','Dd_new_avg_M9V7Z1A1',...
'Dd_new_avg_pc_M9V7Z1A1','Dd_new_avg_nc_M9V7Z1A1', 'Ddlow_M9V7Z1A1','Ddlow_nc_M9V7Z1A1',...
    'Ddlow_pc_M9V7Z1A1','distance_mc_avgMIN_M9V7Z1A1',...
'distance_mc_avgMIN_hist_M9V7Z1A1','distance_pc_sort_M9V7Z1A1',...
    'distance_pc_avgMIN_M9V7Z1A1', 'distance_pc_avgMIN_hist_M9V7Z1A1',...
'Param_M9V7Z1A1', 'scale_M9V7Z1A1', 'PartialImage_Height_M9V7Z1A1',...
'PartialImage_Width_M9V7Z1A1','ImageArea_M9V7Z1A1',...
    'IELHoles_M9V7Z1A1', 'HolesPerArea_M9V7Z1A1', 'coord_p_centers_M9V7Z1A1',...
 'puncta_final_M9V7Z1A1', 'distance_p_M9V7Z1A1', 'distance_p_thresh',...
  'distance_p_min_final_M9V7Z1A1', 'distance_p_min_M9V7Z1A1', ...
 'distance_p_min_index_M9V7Z1A1','Total_HIEL_M9V7Z1A1','PS_pos_M9V7Z1A1',...
 'PercentPosHIEL_M9V7Z1A1', 'Total_Puncta_M9V7Z1A1',...
 'PercentPunctaWithHIELOverlap_M9V7Z1A1',  'distance_nc_p_sort_M9V7Z1A1',...
'distance_nc_p_avgMIN_M9V7Z1A1', ...
     'distance_nc_p_avgMIN_M9V7Z1A1_hist','Dd_new_p_avg_M9V7Z1A1',...
'Dd_new_p_avg_M9V7Z1A1_pc','Dd_new_p_avg_M9V7Z1A1_nc', 'Ddlow_p_M9V7Z1A1',...
'Ddlow_p_M9V7Z1A1_nc',...
'Ddlow_p_M9V7Z1A1_pc','distance_mc_p_avgMIN_M9V7Z1A1',...
 'distance_mc_p_avgMIN_M9V7Z1A1_hist',...
'distance_pc_p_sort_M9V7Z1A1','distance_pc_p_avgMIN_M9V7Z1A1',...
'distance_pc_p_avgMIN_M9V7Z1A1_hist',  'distance_ALLPUNCTA_final_M9V7Z1A1',...
'distance_p_min_final_overlap_M9V7Z1A1','distance_p_cldn5_overlap_M9V7Z1A1');
```

Published with MATLAB® R2019b

MonteCarlo simulation for HIEL

```
function [distance_mc_sort_M9V7Z1A1, distance_mc_avgMIN_M9V7Z1A1,
distance_mc_avgMIN_hist_M9V7Z1A1] =
ExampleMonteCarlo(claudin5_full_M9V7Z1A1)

% Manually adjust. This is the number of simulated HIEL centers
 (should match # detected in ExampleCode).
N_mc = 64;

m_mc = size(N_mc,1);
n_mc = size (N_mc,2);
r_mc = zeros(m_mc,n_mc);
xy_mc = zeros(m_mc,n_mc);

% pixel bounds of analyzed area
xlow = 0;
xhigh = 1024;
ylow = 0;
yhigh =1024;

    xhigh = xhigh - xlow;
    yhigh = yhigh - ylow;

    for  i=1:N_mc

            % choose a random radius for the simulated HIEL
            r_mc(i) = round(normrnd(9.66,1.99));
            % First variable is mean of HIEL size detected in
 ExampleCode
            % Second is standard deviation of HIEL size detected in
 ExampleCode

            % generate a new HIEL simulated center that is within the
            % bounds of the analyzed area
            newpt_mc = @()r_mc(i)+ round([((xhigh-2*r_mc(i))*
 rand((1))+xlow) ((yhigh-2*r_mc(i))* rand((1))+ylow)]);

            xy_mc = newpt_mc();  % matrix to store XY coordinates
            fails = 0;     % to avoid looping forever not
 test
 %  generate  new  HIEl  center  while
 size(xy_mc,1) < N_mc pt = newpt_mc();
% test distance to all other points. the goal is to

        % have two overlapping HIEL.
        if all(pdist2(xy_mc, pt) > 2*r_mc(i))
            xy_mc = [xy_mc; pt];  % add it if it passes the

            fails = 0;      % reset failure counter
                  else
                  % increase failure counter,
                      ails = fails + 1;
```

ExampleMonteCarlo.m

```
                    % give up if exceeded some threshold
                    if fails > 5000
                                error('this is taking too long...');

        end hold off


    end

end
   end
    %%Plot the result of one simulation!
    %COMMENT OFF all of this plot when you are ready to run >1 simulation,
     or
    %you will get a plot for every simulation and that takes up a lot of
    %memory.

    %%%%
    Figure_mc_example = figure; hold on;
    plot(claudin5_full_M9V7Z1A1(:,1),
     claudin5_full_M9V7Z1A1(:,2),'.','MarkerSize',8, 'Color',  'c');
     hold on;

    %%preallocate space
    centers_mc = zeros (m_mc,n_mc);
        for j=1:size(xy_mc,1)
              centers_mc = [xy_mc(j,1), xy_mc(j,2)];
              viscircles(centers_mc, r_mc(j), 'color', 'k');
    %         end
        end
        hold on;
        xlim([0 1024]);
        ylim([0 1024]);
        saveas(Figure_mc_example, '/Users/claireruddiman/Dropbox/_MEJ
     Paper/_Figures/Github/M9V7Z1A1_Analysis/Figure_mc_example.png');
        hold off;
    % %end


    % % % % Calculate distances between center points

    % Define sizes of matrices.
    [mmm_mc nnn_mc] = size(xy_mc);
    nnn_mc = mmm_mc;
    [mmmm nnnn] = size(claudin5_full_M9V7Z1A1);

    % distance_mc - nearest cldn5 coordinate to any give HIEL
    distance_mc_M9V7Z1A1 = zeros(nnn_mc,mmm_mc);


    for i = 1 : nnn_mc % shorter, "coord_M9V7Z1A1"
        for j = 1 : mmmm %longer, "claudin5"
```

ExampleMonteCarlo.m

```
        scale = 8.6719; % this is the number of pixels per micron
        distance_mc_M9V7Z1A1(i, j) = (sqrt((xy_mc(i, 1) -
 claudin5_full_M9V7Z1A1(j, 1)) ^ 2 + ...
            (xy_mc(i, 2) - claudin5_full_M9V7Z1A1(j, 2)) ^ 2))/scale;
        %     slope(i,j) = (coord_M9V7Z1A1(i, 2) - coord_M9V7Z1A1(j,
 2))/(coord_M9V7Z1A1(i, 1) - coord_M9V7Z1A1(j, 1));
    end
end

% Calculate the average min distance of HIEL to claudin 5 staining.
    distance_mc_M9V7Z1A1 = transpose(distance_mc_M9V7Z1A1);
    distance_mc_sort_old = sort(distance_mc_M9V7Z1A1, 1); % sort
 distances within each column
    distance_mc_sort_old = sortrows(distance_mc_sort_old.',1).'; %sort
 by first row
    [~,inx]=sort(distance_mc_sort_old(1,:));  %sort by first row
    distance_mc_sort_old = distance_mc_sort_old(:,inx);  %sort by
 first row

    % This is the matrix to be used for downstream analysis!!!
    % This is the minimum distance of simulated HIEL to claudin 5
    distance_mc_avgMIN_hist_M9V7Z1A1 = (distance_mc_sort_old(1,:));

    % This is the average value of the matrix above.
    distance_mc_avgMIN_M9V7Z1A1= mean(distance_mc_sort_old(1,:));

% take top 100 distances measured from this array. the first row
 indicates
% the minimum distance measured for each HIEL to claudin5.
% Save 100 just in case it can be used in downstream analysis.
Total = 100;
distance_mc_sort_M9V7Z1A1 = distance_mc_sort_old(1:Total, 1:N_mc);
clear distance_mc_sort_old; % delete original array
clear distance_mc_M9V7Z1A1;

end
```

Published with MATLAB® R2019

ExampleMonteCarlo.m

Positive control simulation for HIEL

```
function [distance_pc_sort_M9V7Z1A1, distance_pc_avgMIN_M9V7Z1A1,
distance_pc_avgMIN_hist_M9V7Z1A1] =
ExamplePositiveControl(claudin5_full_M9V7Z1A1, coord_M9V7Z1A1)
N_pc = 64; % #HIEL identified in ExampleCode
scale =8.6719; %scale for how many pixels equal 1 micron AvgRadius =
9.66; %average HIEL radius in pixels identfied in
       ExampleCode
totalPoints = size(claudin5_full_M9V7Z1A1,1);

lowlimX = 0;
upperlimX = 1024;
newX_pc_2 = (lowlimX-upperlimX).*rand(10000,1) + upperlimX;

lowlimY = 0;
upperlimY = 1024;
newY_pc_2 = (lowlimY-upperlimY).*rand(10000,1) + upperlimY;

PC_xycoord_2 = [round(newX_pc_2) round(newY_pc_2)];


x_pc = PC_xycoord_2(:,1); y_pc =
PC_xycoord_2(:,2);


minAllowableDistance = 1;
      numberOfPoints = N_pc+1; % make this equal to 1 more than the number
       of IEL holes
nMax = 10000;

% Initialize first point.
keeperX = x_pc(1); keeperY =
y_pc(1);

% Try dropping down more points. counter
= 2;
k =1 ; %

      while counter < numberOfPoints & k < totalPoints
          k=k+1; %%
        % Get a trial point.
        thisX = x_pc(k);
        thisY = y_pc(k);
        thisXY = horzcat(thisX,thisY);

        % See how far is is away from existing keeper points.
        distances = sqrt((thisX-keeperX).^2 + (thisY - keeperY).^2);
        distances2 = pdist2(thisXY, claudin5_full_M9V7Z1A1);
        minDistance2 = min(distances2);
        minDistance = min(distances);

      %   Create the new point if it is within 1.5*scale of fluorescent
       signal
```

ExamplePositiveControl.m

```
%         (claudin5 in this example), and if it is within the
%         specified analyzed area.
          if  length(thisX)< numberOfPoints && minDistance2 >=0 &&
       minDistance2 <scale*1.5 && minDistance > AvgRadius &&...
                  thisX <upperlimX && thisX > lowlimX && thisY <upperlimY &&
       thisY >lowlimY
              % must alter the above line if only analyzing a partial image
          keeperX(counter) = thisX;
          keeperY(counter) = thisY;
          counter = counter + 1;

          else length(keeperX) < numberOfPoints
              k= k+1;

          end
end

keeperX = transpose(keeperX); keeperY =
transpose(keeperY);
xycoord_PC = horzcat(keeperX,keeperY); Missing_values =

numberOfPoints - length(xycoord_PC);


[mmm_pc nnn_pc] = size(xycoord_PC);
nnn_pc = mmm_pc;

[mmmm nnnn] = size(claudin5_full_M9V7Z1A1); distance_pc_M9V7Z1A1 =
zeros(nnn_pc,mmm_pc);

      for i = 1 : nnn_pc % shorter, "coord_M9V7Z1A1"
          for j = 1 : mmmm %longer, "claudin5"
              scale = 8.6719;
              distance_pc_M9V7Z1A1(i, j) = (sqrt((xycoord_PC(i, 1) -
       claudin5_full_M9V7Z1A1(j,1)) ^ 2 + ...
                  (xycoord_PC(i, 2) - claudin5_full_M9V7Z1A1(j,2)) ^ 2))/
scale;
          end
end

      % Calculate the average min distance of simulated HIEL to claudin 5
       staining.
distance_pc_M9V7Z1A1 = transpose(distance_pc_M9V7Z1A1); distance_pc_sort_old
= sort(distance_pc_M9V7Z1A1, 1); % sort distances
       within each column
      distance_pc_sort_old = sortrows(distance_pc_sort_old.',1).'; %sort by
       first row
[~,inx]=sort(distance_pc_sort_old(1,:));  %sort by first row
distance_pc_sort_old = distance_pc_sort_old(:,inx);  %sort by first
       row

% This is the matrix to be used for downstream analysis!!!
```

ExamplePositiveControl.m

```
% This is the minimum distance of simulated HIEL to claudin 5
distance_pc_avgMIN_hist_M9V7Z1A1 = (distance_pc_sort_old(1,:));

 % This is the average value of the matrix above.
distance_pc_avgMIN_M9V7Z1A1= mean(distance_pc_sort_old(1,:));


      % Keep top 100 closest distances of HIEL to claudin5 in case needed
       for
% future analyses. Total =
100;
      distance_pc_sort_M9V7Z1A1 = distance_pc_sort_old(1:Total, 1:N_pc); %
       take top 100 values from this array

howmanyzeros = nnz(~distance_pc_sort_M9V7Z1A1);

% % COMMENT OUT THIS SECTION WHEN INCREASING NUMBER OF SIMULATIONS >1
% % % %FIGURE 5
      % % confirm that the positive control is working with this visual
       check
Figure_pos_ctrl_partial_cldn5 =figure;
plot(claudin5_full_M9V7Z1A1(:,1),
       claudin5_full_M9V7Z1A1(:,2),'.','MarkerSize',2, 'Color',  'c');
       hold on
      plot(coord_M9V7Z1A1(:,1),
       coord_M9V7Z1A1(:,2),'.','MarkerSize',12, 'Color', 'm'); hold on;
plot(xycoord_PC(:,1),
 xycoord_PC(:,2),'.','MarkerSize',12, 'Color', 'b'); hold on;
xlim([0 1024]);
ylim([0 1024]);
      legend('Claudin5','1st order artery', 'Positive
       Control','FontSize',12);
saveas(Figure_pos_ctrl_partial_cldn5, '/Users/claireruddiman/ Dropbox/_MEJ
Paper/_Figures/Github/M9V7Z1A1_Analysis/ Figure_pos_ctrl_partial_cldn5.png');
hold off;
      %

end
```

Published with MATLAB® R2019b

ExamplePositiveControl.m

Negative control simulation for HIEL

```
function [distance_nc_sort_M9V7Z1A1, distance_nc_avgMIN_M9V7Z1A1,
distance_nc_avgMIN_hist_M9V7Z1A1] =
ExampleNegativeControl(claudin5_full_M9V7Z1A1,coord_M9V7Z1A1)
    N_nc = 64;    % #HIEL identified in ExampleCode
    scale =8.6719; %scale for how many pixels equal 1 micron
    AvgRadius = 9.66; %average HIEL radius in pixels identfied in
 ExampleCode
    totalPoints = size(claudin5_full_M9V7Z1A1,1);


    lowlimX = 0;
    upperlimX = 1024;
    newX_nc_2 = (lowlimX-upperlimX).*rand(10000,1) + upperlimX;

    lowlimY = 0;
    upperlimY = 1024;
    newY_nc_2 = (lowlimY-upperlimY).*rand(10000,1) + upperlimY;

    NC_xycoord_2 = [round(newX_nc_2) round(newY_nc_2)];
    x_nc = NC_xycoord_2(:,1);
    y_nc = NC_xycoord_2(:,2);


    minAllowableDistance = 1;
    numberOfPoints = N_nc+1; %make this equal to 1 more than the
 number of IEL holes
    nMax = 10000;

% Initialize first point.
    keeperX = x_nc(1);
    keeperY = y_nc(1);

% Try dropping down more points.
    counter = 2;
    k =1 ; %

while counter < numberOfPoints & k < totalPoints
    k=k+1; %%
  % Get a trial point.
  thisX = x_nc(k);
  thisY = y_nc(k);
  thisXY = horzcat(thisX,thisY);

  % See how far is is away from existing keeper points.

  distances = sqrt((thisX-keeperX).^2 + (thisY - keeperY).^2);
  distances2 = pdist2(thisXY, claudin5_full_M9V7Z1A1);
  minDistance2 = min(distances2);
  minDistance = min(distances);

%   Create the new point if it is between 1.5*scale and 4.5*scale
 distance
```

ExampleNegativeControl.m

```
%   of fluorescent signal (claudin 5 in this case) and if it is within
 the
%   specified analyzed area
    if  length(thisX)< numberOfPoints && minDistance2 >scale*1.5 &&
 minDistance2 <scale*4.5 && minDistance > AvgRadius &&...
            thisX <upperlimX && thisX > lowlimX && thisY <upperlimY &&
 thisY >lowlimY
        % must alter the above line if only analyzing a partial image
    keeperX(counter) = thisX;
    keeperY(counter) = thisY;
    counter = counter + 1;

    else length(keeperX) < numberOfPoints
        k= k+1;
%     counter = counter + 0;
%
    end
end

    keeperX = transpose(keeperX);
    keeperY = transpose(keeperY);
    xycoord_NC = horzcat(keeperX,keeperY);


    Missing_values = numberOfPoints - length(xycoord_NC);



[mmm_nc nnn_nc] = size(xycoord_NC);
nnn_nc = mmm_nc;

[mmmm nnnn] = size(claudin5_full_M9V7Z1A1);
distance_mc = zeros(nnn_nc,mmm_nc);

for i = 1 : nnn_nc % shorter, "coord_M9V7Z1A1"
    for j = 1 : mmmm %longer, "claudin5"
        scale = 8.6719;
        distance_nc_M9V7Z1A1(i, j) = (sqrt((xycoord_NC(i, 1) -
 claudin5_full_M9V7Z1A1(j,1)) ^ 2 + ...
            (xycoord_NC(i, 2) - claudin5_full_M9V7Z1A1(j,2)) ^ 2))/
scale;
    end
end

    distance_nc_M9V7Z1A1 = transpose(distance_nc_M9V7Z1A1);
    distance_nc_sort_old = sort(distance_nc_M9V7Z1A1, 1); % sort
 distances within each column
    distance_nc_sort_old = sortrows(distance_nc_sort_old.',1).'; %sort
 by first row
    [~,inx]=sort(distance_nc_sort_old(1,:));  %sort by first row
    distance_nc_sort_old = distance_nc_sort_old(:,inx);  %sort by
 first row
```

ExampleNegativeControl.m

```
    % This is the matrix to be used for downstream analysis!!!
    % This is the minimum distance of simulated HIEL to claudin 5
    distance_nc_avgMIN_hist_M9V7Z1A1 = (distance_nc_sort_old(1,:));

    % This is the average value of the matrix above.
    distance_nc_avgMIN_M9V7Z1A1= mean(distance_nc_sort_old(1,:));

    % Keep top 100 closest distances of HIEL to claudin5 in case
 needed for
    % future analyses.
    Total = 100;
    distance_nc_sort_M9V7Z1A1 = distance_nc_sort_old(1:Total,
 1:N_nc); % take top 1000 values from this array

    howmanyzeros_M9V7Z1A1 = nnz(~distance_nc_sort_M9V7Z1A1);

% % COMMENT OUT THIS SECTION WHEN INCREASING NUMBER OF SIMULATIONS >1
% % % %FIGURE 5
% % confirm that the positive control is working with this visual
 check
Figure_neg_ctrl_partial_cldn5 =figure;
plot(claudin5_full_M9V7Z1A1(:,1),
 claudin5_full_M9V7Z1A1(:,2),'.','MarkerSize',2, 'Color',  'c');
 hold on
plot(coord_M9V7Z1A1(:,1),
 coord_M9V7Z1A1(:,2),'.','MarkerSize',12, 'Color', 'm'); hold on;
plot(xycoord_NC(:,1),
 xycoord_NC(:,2),'.','MarkerSize',12, 'Color', 'k'); hold on;
xlim([0 1024]);
ylim([0 1024]);
legend('Claudin5','1st order artery', 'Negative
 Control','FontSize',12);
saveas(Figure_neg_ctrl_partial_cldn5, '/Users/claireruddiman/
Dropbox/_MEJ Paper/_Figures/Github/M9V7Z1A1_Analysis/
Figure_neg_ctrl_partial_cldn5.png');
hold off;

end
```

Published with MATLAB® R2019b

ExampleNegativeControl.m

MonteCarlo simulation for puncta

```
function [distance_mc_p_sort_M9V7Z1A1,
       distance_mc_p_avgMIN_M9V7Z1A1, distance_mc_p_avgMIN_hist_M9V7Z1A1] =
       ExampleMonteCarloPuncta(claudin5_full_M9V7Z1A1, N_mc_p)

      % pixel bounds of analyzed area
      m_mc_p  =  size(N_mc_p,1);
      n_mc_p = size (N_mc_p,2);
      r_mc_p = zeros(m_mc_p,n_mc_p);
      xy_mc_p = zeros(m_mc_p,n_mc_p);

      xlow_p = 0;
      xhigh_p = 1024;
      ylow_p = 0;
      yhigh_p =1024;

      xhigh_p = xhigh_p - xlow_p;
      yhigh_p = yhigh_p - ylow_p;
      % % preallocate storage for r for speed
      % for k = 1:length(hi_mc)
          for  i=1:N_mc_p

                    % choose a random radius for the simulated HIEL
                    r_mc_p(i) = round(normrnd(9.32,1.99));
                    % First variable is mean of HIEL size detected in
       ExampleCode
                    % Second is standard deviation of HIEL size detected in
       ExampleCod

                    % generate a new HIEL simulated center that is within the
                    % bounds of the analyzed area
                    newpt_mc_p = @()r_mc_p(i)+ round([((xhigh_p-2*r_mc_p(i))*
       rand((1))+xlow_p)  ((yhigh_p-2*r_mc_p(i))* rand((1))+ylow_p)]);

                    xy_mc_p = newpt_mc_p();  % matrix to store XY coordinates
                    fails = 0;      % to avoid looping forever

                    while size(xy_mc_p,1) < N_mc_p

                   % generate new point and test distance
                    pt = newpt_mc_p();
                    % test distance to all other points. the goal is to not
                        % have two overlapping puncta
                        if all(pdist2(xy_mc_p, pt) > 2*r_mc_p(i)) %
                            xy_mc_p = [xy_mc_p; pt];   % add it
                            fails = 0;      % reset failure counter
                        else
                % increase failure counter,
                            fails = fails + 1;
                % give up if exceeded some threshold
                                if fails > 5000
```

ExampleMonteCarloPuncta.m

```
error('this is taking too long...');
end
 end
    end

        end

      hold off

      %%Plot the result of one simulation!
      %COMMENT OFF all of this plot when you are ready to run >1 simulation,
       or
      %you will get a plot for every simulation and that takes up a lot of
      %memory.

      N_mc_p_puncta = 20; %MANUALLY ADJUST THIS. Number of HIEL that are
       filled with punctate in the image
      Simulated_Puncta = datasample(xy_mc_p, N_mc_p_puncta);

      %%
      Figure_mc_p_example = figure; hold on;
      plot(claudin5_full_M9V7Z1A1(:,1),
       claudin5_full_M9V7Z1A1(:,2),'.','MarkerSize',8, 'Color',  'c');
       hold on;
      centers_mc_p = zeros (m_mc_p,n_mc_p);
          for j=1:size(Simulated_Puncta,1)

                centers_mc_p = [xy_mc_p(j,1), xy_mc_p(j,2)];
                viscircles(centers_mc_p, r_mc_p(j), 'color', 'k');
          end
          hold on;
          xlim([0 1024]);
          ylim([0 1024]);
          saveas(Figure_mc_p_example, '/Users/claireruddiman/Dropbox/_MEJ
       Paper/_Figures/Github/M9V7Z1A1_Analysis/Figure_mc_example.png');
          hold off;


      % % % % Calculate distances between center points

      % Define sizes of matrices.
      [mmm_mc_p nnn_mc_p] = size(Simulated_Puncta);

      % distance_mc - nearest cldn5 coordinate to any give puncta
      distance_mc_p_M9V7Z1A1 = zeros(nnn_mc_p,mmm_mc_p);


      for i = 1 : N_mc_p_puncta % shorter, "coord_M9V7Z1A1"
          for j = 1 : length(claudin5_full_M9V7Z1A1) %longer, "claudin5"
              scale = 8.6719;
```

ExampleMonteCarloPuncta.m

```
        distance_mc_p_M9V7Z1A1(i, j) = (sqrt((Simulated_Puncta(i, 1) -
 claudin5_full_M9V7Z1A1(j, 1)) ^ 2 + ...
            (Simulated_Puncta(i, 2) - claudin5_full_M9V7Z1A1(j, 2)) ^
 2))/scale;
        %     slope(i,j) = (coord_M9V7Z1A1(i, 2) - coord_M9V7Z1A1(j,
 2))/(coord_M9V7Z1A1(i, 1) - coord_M9V7Z1A1(j, 1));
    end
end

% Calculate the average min distance of HIEL to claudin 5 staining.
distance_mc_p_M9V7Z1A1 = transpose(distance_mc_p_M9V7Z1A1);
distance_mc_p_sort_old = sort(distance_mc_p_M9V7Z1A1, 1); % sort
 distances within each column
distance_mc_p_sort_old = sortrows(distance_mc_p_sort_old.',1).'; %sort
 by first row
[~,inx]=sort(distance_mc_p_sort_old(1,:));  %sort by first row
distance_mc_p_sort_old = distance_mc_p_sort_old(:,inx);  %sort by
 first row

% This is the matrix to be used for downstream analysis!!!
% This is the minimum distance of simulated HIEL to claudin 5
distance_mc_p_avgMIN_hist_M9V7Z1A1 = (distance_mc_p_sort_old(1,:));

% This is the average value of the matrix above.
distance_mc_p_avgMIN_M9V7Z1A1= mean(distance_mc_p_sort_old(1,:));


% take top 100 distances measured from this array. the first row
 indicates
% the minimum distance measured for each HIEL to claudin5.
% Save 100 just in case it can be used in downstream analysis.
Total = 100;
distance_mc_p_sort_M9V7Z1A1 = distance_mc_p_sort_old(1:Total,
 1:N_mc_p_puncta);

clear distance_mc_p_sort_old; % delete original array
clear distance_mc_p_M9V7Z1A1;


end
```

Published with MATLAB® R2019b

ExampleMonteCarloPuncta.m

Positive control simulation for puncta

```
function [distance_pc_sort_M9V7Z1A1, distance_pc_avgMIN_M9V7Z1A1,
                distance_pc_avgMIN_hist_M9V7Z1A1] =
            ExamplePositiveControlPuncta(claudin5_full_M9V7Z1A1,
              coord_p_centers_M9V7Z1A1, PunctaIndex_M9V7Z1A1)
N_pc = 64; % #HIEL identified in ExampleCode
scale =8.6719;  %scale for how many pixels equal 1 micron AvgRadius
= 9.66; %average HIEL radius in pixels identfied in
       ExampleCode
totalPoints = size(claudin5_full_M9V7Z1A1,1);

lowlimX = 0;
upperlimX = 1024;
newX_pc_2 = (lowlimX-upperlimX).*rand(10000,1) + upperlimX;

lowlimY = 0;
upperlimY = 1024;
newY_pc_2 = (lowlimY-upperlimY).*rand(10000,1) + upperlimY;

PC_xycoord_2 = [round(newX_pc_2) round(newY_pc_2)];

x_pc = PC_xycoord_2(:,1); y_pc =
PC_xycoord_2(:,2);

minAllowableDistance = 1;
      numberOfPoints = N_pc+1; %make this equal to 1 more than the number of
       IEL holes
nMax = 10000;

% Initialize first point.
keeperX = x_pc(1); keeperY =
y_pc(1);

% Try dropping down more points. counter
= 2;
k =1 ; %

      while counter < numberOfPoints & k < totalPoints
          k=k+1; %%
        % Get a trial point.
        thisX = x_pc(k);
        thisY = y_pc(k);
        thisXY = horzcat(thisX,thisY);

        % See how far is is away from existing keeper points.
        distances = sqrt((thisX-keeperX).^2 + (thisY - keeperY).^2);
        distances2 = pdist2(thisXY, claudin5_full_M9V7Z1A1);
        minDistance2 = min(distances2);
        minDistance = min(distances);

      %   Create the new point if it is within 1.5*scale of fluorescent
       signal
```

ExamplePositiveControlPuncta.m

```
%         (claudin5 in this example), and if it is within the
%         specified analyzed area.
          if  length(thisX)< numberOfPoints && minDistance2 >=0 &&
       minDistance2 <scale*1.5 && minDistance > AvgRadius &&...
                  thisX <upperlimX && thisX > lowlimX && thisY <upperlimY &&
       thisY >lowlimY
                % must alter the above line if only analyzing a partial image
          keeperX(counter) = thisX;
          keeperY(counter) = thisY;
          counter = counter + 1;

          else length(keeperX) < numberOfPoints
              k= k+1;

          end
end

keeperX = transpose(keeperX); keeperY =
transpose(keeperY);
xycoord_PC_M9V7Z1A1 = horzcat(keeperX,keeperY);


      N_puncta=20; %MANUALLY ADJUST THIS. Number of HIEL that are filled
       with punctate in the image
xycoord_PC_M9V7Z1A1 = datasample(xycoord_PC_M9V7Z1A1, N_puncta);

Missing_values = numberOfPoints - length(xycoord_PC_M9V7Z1A1);

[mmm_pc nnn_pc] = size(xycoord_PC_M9V7Z1A1); nnn_pc =
mmm_pc;

[mmmm nnnn] = size(claudin5_full_M9V7Z1A1); distance_pc_M9V7Z1A1 =
zeros(nnn_pc,mmm_pc);

      for i = 1 : nnn_pc % shorter, "coord_p_centers_M9V7Z1A1"
          for j = 1 : mmmm %longer, "claudin5"
              scale = 8.6719;
              distance_pc_M9V7Z1A1(i, j) = (sqrt(( xycoord_PC_M9V7Z1A1(i, 1)
       - claudin5_full_M9V7Z1A1(j,1)) ^ 2 + ...
                    (xycoord_PC_M9V7Z1A1(i, 2) - claudin5_full_M9V7Z1A1(j,2))
       ^ 2))/scale;
          end
end

      % Calculate the average min distance of simulated puncta to claudin 5
       staining.
distance_pc_M9V7Z1A1 = transpose(distance_pc_M9V7Z1A1); distance_pc_sort_old
= sort(distance_pc_M9V7Z1A1, 1); % sort distances
       within each column
      distance_pc_sort_old = sortrows(distance_pc_sort_old.',1).'; %sort by
       first row
```

ExamplePositiveControlPuncta.m

```
[~,inx]=sort(distance_pc_sort_old(1,:));  %sort by first row
      distance_pc_sort_old = distance_pc_sort_old(:,inx);  %sort by first
       row

% This is the matrix to be used for downstream analysis!!!
% This is the minimum distance of simulated puncta to claudin 5
distance_pc_avgMIN_hist_M9V7Z1A1 = (distance_pc_sort_old(1,:));

% This is the average value of the matrix above.
distance_pc_avgMIN_M9V7Z1A1= mean(distance_pc_sort_old(1,:));

      % Keep top 100 closest distances of HIEL to claudin5 in case needed
       for
% future analyses. Total =
100;
      distance_pc_sort_M9V7Z1A1 = distance_pc_sort_old(1:Total,
       1:N_puncta); % take top 1000 values from this array

howmanyzeros = nnz(~distance_pc_sort_M9V7Z1A1);

%%Plot the result of one simulation!
      %COMMENT OFF all of this plot when you are ready to run >1 simulation,
       or
%you will get a plot for every simulation and that takes up a lot of
%memory.

% %FIGURE 5
Figure_pos_ctrl_partial_cldn5 =figure;
plot(claudin5_full_M9V7Z1A1(:,1),
       claudin5_full_M9V7Z1A1(:,2),'.','MarkerSize',2, 'Color',  'c');
       hold on
hold on;
       for i = N_puncta
         plot(PunctaIndex_M9V7Z1A1(i,2),
       PunctaIndex_M9V7Z1A1(i,3), '.','MarkerSize',12, 'Color',  'b')
       end
 hold on; plot(xycoord_PC_M9V7Z1A1(:,1),
 xycoord_PC_M9V7Z1A1(:,2),'.','MarkerSize',12, 'Color', 'b'); hold on;
xlim([0 1024]);
ylim([0 1024]);
      legend('Claudin5','1st order artery', 'Positive
       Control','FontSize',12);
saveas(Figure_pos_ctrl_partial_cldn5, '/Users/claireruddiman/ Dropbox/_MEJ
Paper/_Figures/Github/M9V7Z1A1_Analysis/ Figure_pos_ctrl_partial_cldn5.png');
      hold off;

      end
```

Published with MATLAB® R2019b

ExamplePositiveControlPuncta.m

Negative control simulation for puncta

```
      function [distance_nc_sort_M9V7Z1A1, distance_nc_avgMIN_M9V7Z1A1,
      distance_nc_avgMIN_hist_M9V7Z1A1] =
      ExampleNegativeControlPuncta(claudin5_full_M9V7Z1A1...
      coord_M9V7Z1A1,PunctaIndex_M9
N_nc = 64;  % #HIEL identified in ExampleCode
scale =8.6719; %scale for how many pixels equal 1 micron AvgRadius =
9.66;%average HIEL radius in pixels identfied in
       ExampleCode
totalPoints = size(claudin5_full_M9V7Z1A1,1);

lowlimX = 0;
upperlimX = 1024;
newX_nc_2 = (lowlimX-upperlimX).*rand(10000,1) + upperlimX;

lowlimY = 0;
upperlimY = 1024;
newY_nc_2 = (lowlimY-upperlimY).*rand(10000,1) + upperlimY;

NC_xycoord_2 = [round(newX_nc_2) round(newY_nc_2)]; x_nc =
NC_xycoord_2(:,1);
y_nc = NC_xycoord_2(:,2);

minAllowableDistance = 1;
      numberOfPoints = N_nc+1; %make this equal to 1 more than the number of
       IEL holes
nMax = 10000;

% Initialize first point.
keeperX = x_nc(1); keeperY =
y_nc(1);

% Try dropping down more points. counter =
2;
k =1 ; %

      while counter < numberOfPoints & k < totalPoints
          k=k+1; %%
        % Get a trial point.
        thisX = x_nc(k);
        thisY = y_nc(k);
        thisXY = horzcat(thisX,thisY);

        % See how far is is away from existing keeper points.
        distances = sqrt((thisX-keeperX).^2 + (thisY - keeperY).^2);
        distances2 = pdist2(thisXY, claudin5_full_M9V7Z1A1);
        minDistance2 = min(distances2);
        minDistance = min(distances);

          if  length(thisX)< numberOfPoints && minDistance2 >scale*1.5 &&
       minDistance2 <scale*4.5 && minDistance > AvgRadius &&...
```

ExampleNegativeControlPuncta.m

```
                thisX <upperlimX && thisX > lowlimX && thisY <upperlimY &&
       thisY >lowlimY  %% CHANGE FOR PARTIAL

           keeperX(counter) = thisX;
           keeperY(counter) = thisY;
           counter = counter + 1;

           else length(keeperX) < numberOfPoints
               k= k+1;
           end
end


           keeperX = transpose(keeperX);
           keeperY = transpose(keeperY);
           xycoord_NC = horzcat(keeperX,keeperY);


           N_puncta=20; %MANUALLY ADJUST THIS. Number of HIEL that are filled
       with punctate in the image
           xycoord_NC = datasample(xycoord_NC, N_puncta);


           Missing_values = numberOfPoints - length(xycoord_NC);


[mmm_nc nnn_nc] = size(xycoord_NC); nnn_nc =
mmm_nc;

[mmmm nnnn] = size(claudin5_full_M9V7Z1A1); distance_mc =
zeros(nnn_nc,mmm_nc);

      for i = 1 : nnn_nc % shorter, "coord_M9V7Z1A1"
          for j = 1 : mmmm %longer, "claudin5"
              scale = 8.6719;
              distance_nc_M9V7Z1A1(i, j) = (sqrt((xycoord_NC(i, 1) -
       claudin5_full_M9V7Z1A1(j,1)) ^ 2 + ...
                  (xycoord_NC(i, 2) - claudin5_full_M9V7Z1A1(j,2)) ^ 2))/
scale;
              %     slope(i,j) = (coord_M9V7Z1A1(i, 2) - coord_M9V7Z1A1(j,
       2))/(coord_M9V7Z1A1(i, 1) - coord_M9V7Z1A1(j, 1));
          end
end

      % Calculate the average min distance of simulated puncta to claudin 5
       staining.
distance_nc_M9V7Z1A1 = transpose(distance_nc_M9V7Z1A1); distance_nc_sort_old
= sort(distance_nc_M9V7Z1A1, 1); % sort distances
       within each column
      distance_nc_sort_old = sortrows(distance_nc_sort_old.',1).'; %sort by
       first row
```

ExampleNegativeControlPuncta.m

```
[~,inx]=sort(distance_nc_sort_old(1,:));  %sort by first row
distance_nc_sort_old = distance_nc_sort_old(:,inx);  %sort by first
       row

% This is the matrix to be used for downstream analysis!!!
% This is the minimum distance of simulated puncta to claudin 5
distance_nc_avgMIN_hist_M9V7Z1A1 = (distance_nc_sort_old(1,:));

% This is the average value of the matrix above.
distance_nc_avgMIN_M9V7Z1A1= mean(distance_nc_sort_old(1,:));
      % Keep top 100 closest distances of HIEL to claudin5 in case needed
       for
% future analyses.
Total = 100;
      distance_nc_sort_M9V7Z1A1 = distance_nc_sort_old(1:Total,
       1:N_puncta); % take top 1000 values from this array

          howmanyzeros_M9V7Z1A1 = nnz(~distance_nc_sort_M9V7Z1A1);

%%Plot the result of one simulation!
      %COMMENT OFF all of this plot when you are ready to run >1 simulation,
       or
%you will get a plot for every simulation and that takes up a lot of
%memory.

%FIGURE 5
Figure_neg_ctrl_partial_cldn5 =figure;
plot(claudin5_full_M9V7Z1A1(:,1),
       claudin5_full_M9V7Z1A1(:,2),'.','MarkerSize',2, 'Color',  'c');
       hold on
hold on;
       for i = N_puncta
         plot(PunctaIndex_M9V7Z1A1(i,2),
       PunctaIndex_M9V7Z1A1(i,3), '.','MarkerSize',12, 'Color',  'b')
       end
       hold on;

plot(xycoord_NC(:,1),
 xycoord_NC(:,2),'.','MarkerSize',12, 'Color', 'k'); hold on; xlim([0
1024]);
ylim([0 1024]);
      legend('Claudin5','1st order artery', 'Negative
       Control','FontSize',12);
saveas(Figure_neg_ctrl_partial_cldn5, '/Users/claireruddiman/
Dropbox/_MEJ Paper/_Figures/Github/M9V7Z1A1_Analysis/
Figure_neg_ctrl_partial_cldn5.png');
      hold off;

      end
```

Published with MATLAB® R2019b

ExampleNegativeControlPuncta.m

Matlab file to combine data across multiple images

```
      %%The purpose of this script is to combine final data sets
analyzed
      %%obtained across several images that were analyzed
       with the "ExampleCode"
      %%analysis template.


      %Names of images included:
          %M2V1Z1A1
          %M2V2Z1A1
          %M2V2Z1A1
          %M2V2Z2A1
          %M2V2Z2A1
          %M2V2Z3A1
          %M2V2Z3A2
          %M3V3Z2
          %M3V3Z3A1
          %M3V3Z3A2
          %M3V3Z3A3
          %M3V3Z1A1
          %M3V3Z1A2
          %M3V3Z1A3
          %M3V1Z2A1
          %M4V1Z1A1
          %M4V1Z1A2
          %M4V2Z1A1


      %SECTION 1 - BASIC INFORMATION
      %How many images
          scale1  =  6.7448;  %number  of
          pixels  per  micron  scale2  =
          8.679;  %number of pixels per
          micron ImageNumber_3 = 22;

      %Number of HIEL (use length of Param)
      IELHoles_3 = length(Param_M2V1Z1A1) + length(Param_M2V1Z1A2)
       +length(Param_M2V2Z1A1)+length(Param_M2V2Z1A2)+...
          length(Param_M2V2Z2A1)+ length(Param_M2V2Z3A1)+
       length(Param_M2V2Z3A2)+ length(Param_M3V3Z2)+
       length(Param_M3V3Z3A1)+...

       length(Param_M3V3Z3A2)+length(Param_M3V3Z3A3)+length(Param_M3V3Z1A
          1)+length(Param length(Param_M3V1Z2A1)+
       length(Param_M4V1Z1A1)+length(Param_M4V1Z1A2)+length(Param_M4V2Z1A
          1)+length(Param
          length(Param_M12V2Z1A1)+length(Param_M16V1Z3A1);
      IELHolesAvg_3 = IELHoles_3/ImageNumber_3;

      %Average Radius per image
      AvgRadius_3 = mean((mean(Param_M2V1Z1A1(:,3))/scale1) +
       (mean(Param_M2V1Z1A2(:,3))/scale1)+ (mean(Param_M2V2Z1A1(:,3))/
      scale1)+...
```

```
                    (mean(Param_M2V2Z1A2(:,3))/scale1)
 +(mean(Param_M2V2Z2A1(:,3))/scale1)+(mean(Param_M2V2Z
3A1(:,3))/ scale1)+...
                    (mean(Param_M2V2Z3A2(:,3))/scale1)+
 (mean(Param_M3V3Z2(:,3))/scale2)+ (mean(Param_M3V3Z3A1(:,3))/
scale2)+...
                    (mean(Param_M3V3Z3A2(:,3))/
scale2)+(mean(Param_M3V3Z3A3(:,3))/scale2)+(mean(Param
_M3V3Z1A1(:,3))/ scale2)+...
                    (mean(Param_M3V3Z1A2(:,3))/
scale2)+(mean(Param_M3V3Z1A3(:,3))/scale2)+(mean(Param
_M3V1Z2A1(:,3))/ scale2)+...
                    (mean(Param_M4V1Z1A1(:,3))/
scale2)+(mean(Param_M4V1Z1A2(:,3))/scale2)+(mean(Param
_M4V2Z1A1(:,3))/ scale2)+...
                    (mean(Param_M9V6Z1A1(:,3))/
scale2)+(mean(Param_M9V3Z1A1(:,3))/
scale2)+(mean(Param_M12V2Z1A1(:,3))/
scale2)+(mean(Param_M16V1Z3A1(:,3))/scale2));

%All radii for every HIEL detected
RadiiDist_3 = transpose (horzcat(transpose((Param_M2V1Z1A1(:,3)/
scale1)),transpose((Param_M2V1Z1A2(:,3)/
scale1)),transpose((Param_M2V2Z1A1(:,3)/scale1)),...
                    transpose((Param_M
2V2Z1A2(:,3)/ scale1)) ,
transpose((Param_M2V2Z2A1(:,3)/
scale1)),transpose((Param_M2V2Z3A1(:,3
)/scale1)),...
                    transpose((Param_M
2V2Z3A2(:,3)/ scale1)),
transpose((Param_M3V3Z2(:,3)/scale2))
,
 transpose((Param_M3V3Z3A1(:,3)/scale2)),...
                    transpose((Param_M3V3Z3A2(:,3)/
scale2)),transpose((Param_M3V3Z3A3(:,3)/
scale2)),transpose((Param_M3V3Z1A1(:,3)/scale2)),...
                    transpose((Param_M3V3Z1A2(:,3)/
scale2)),transpose((Param_M3V3Z1A3(:,3)/
scale2)),transpose((Param_M3V1Z2A1(:,3)/scale2)),...
                    transpose((Param_M4V1Z1A1(:,3)/
scale2)),transpose((Param_M4V1Z1A2(:,3)/
scale2)),transpose((Param_M4V2Z1A1(:,3)/scale2)),...
                    transpose((Param_M9V3Z1A1(:,3)/
scale2)),transpose((Param_M9V6Z1A1(:,3)/
scale2)),transpose((Param_M12V2Z1A1(:,3)/scale2)),...
                    transpose((Param_M16V1Z3A1(:,3)/scale2))));


%Total Area Analyzed in microns
TotalArea_3 = ImageArea_M2V1Z1A1 + ImageArea_M2V1Z1A2
 + ImageArea_M2V2Z1A1 + ImageArea_M2V2Z1A2+...
ImageArea_M2V2Z2A1+ImageArea_M2V2Z3A1+ImageArea_M2V2Z3A2+FullImage_
Area_M3V3Z2+Ima
```

```
ImageArea_M3V3Z3A3+ImageArea_M3V3Z1A1+ImageArea_M3V3Z1A2+ImageArea_
M3V3Z1A3+ImageA
+ImageArea_M9V6Z1A1+ImageArea_M9V3Z1A1+ImageArea_M12V2Z1A1+ImageAre
a_M16V1Z3A1;

%Total Area by mouse
TotalArea_3_M2 = ImageArea_M2V1Z1A1 + ImageArea_M2V1Z1A2 +...
    ImageArea_M2V2Z1A1 + ImageArea_M2V2Z1A2
 +ImageArea_M2V2Z2A1+ImageArea_M2V2Z3A1+ImageArea_M2V2
Z3A2; TotalVessels_M2 = 2;

TotalArea_3_M3 =
 FullImage_Area_M3V3Z2+ImageArea_M3V3Z3A1+ImageArea_M3
 V3Z3A2+...

 ImageArea_M3V3Z3A3+ImageArea_M3V3Z1A1+ImageArea_M3V3Z1A2+ImageArea
 _M3V3Z1A3
 +ImageArea_M3V1Z2A1
; TotalVessels_M3 =
2;

TotalArea_3_M4 = ImageArea_M4V1Z1A1+ ImageArea_M4V1Z1A2
 +ImageArea_M4V2Z1A1
; TotalVessels_M4 =
2;


TotalArea_3_M9 = ImageArea_M9V3Z1A1+
ImageArea_M9V6Z1A1; TotalVessels_M9 = 2;

TotalArea_3_M12 = ImageArea_M12V2Z1A1;
TotalVessels_M12 = 1;


TotalArea_3_M16 = ImageArea_M16V1Z3A1;
TotalVessels_M16 = 1;


%Density of HIEL


Correct_HolesPerArea_M2V1Z1A1 =
length(coord_M2V1Z1A1)/ ImageArea_M2V1Z1A1;
Correct_HolesPerArea_M2V1Z1A2 =
length(coord_M2V1Z1A2)/ ImageArea_M2V1Z1A2;
Correct_HolesPerArea_M2V2Z1A1 =
length(coord_M2V2Z1A1)/ ImageArea_M2V2Z1A1;
Correct_HolesPerArea_M2V2Z1A2 =
length(coord_M2V2Z1A2)/ ImageArea_M2V2Z1A2;
Correct_HolesPerArea_M2V2Z2A1 =
length(coord_M2V2Z2A1)/ ImageArea_M2V2Z2A1;
Correct_HolesPerArea_M2V2Z3A1 =
length(coord_M2V2Z3A1)/ ImageArea_M2V2Z3A1;
```

```
Correct_HolesPerArea_M2V2Z3A2 =
length(coord_M2V2Z3A2)/ ImageArea_M2V2Z3A2;
Correct_HolesPerArea_M3V3Z2 = length(coord_M3V3Z2)/
FullImage_Area_M3V3Z2;
Correct_HolesPerArea_M3V3Z3A1 =
length(coord_M3V3Z3A1)/ ImageArea_M3V3Z3A1;
Correct_HolesPerArea_M3V3Z3A2 =
length(coord_M3V3Z3A2)/ ImageArea_M3V3Z3A2;
Correct_HolesPerArea_M3V3Z3A3 =
length(coord_M3V3Z3A3)/ ImageArea_M3V3Z3A3;
Correct_HolesPerArea_M3V3Z1A1 =
length(coord_M3V3Z1A1)/ ImageArea_M3V3Z1A1;
Correct_HolesPerArea_M3V3Z1A2 =
length(coord_M3V3Z1A2)/ ImageArea_M3V3Z1A2;
Correct_HolesPerArea_M3V3Z1A3 =
length(coord_M3V3Z1A3)/ ImageArea_M3V3Z1A3;
Correct_HolesPerArea_M3V1Z2A1 =
length(coord_M3V1Z2A1)/ ImageArea_M3V1Z2A1;
Correct_HolesPerArea_M4V1Z1A1 =
length(coord_M4V1Z1A1)/ ImageArea_M4V1Z1A1;
Correct_HolesPerArea_M4V1Z1A2 =
length(coord_M4V1Z1A2)/ ImageArea_M4V1Z1A2;
Correct_HolesPerArea_M4V2Z1A1 =
length(coord_M4V2Z1A1)/ ImageArea_M4V2Z1A1;
Correct_HolesPerArea_M9V3Z1A1 =
length(coord_M9V3Z1A1)/ ImageArea_M9V3Z1A1;
Correct_HolesPerArea_M9V6Z1A1 =
length(coord_M9V6Z1A1)/ ImageArea_M9V6Z1A1;
Correct_HolesPerArea_M12V2Z1A1 =
length(coord_M12V2Z1A1)/ ImageArea_M12V2Z1A1;
Correct_HolesPerArea_M16V1Z3A1 =
length(coord_M16V1Z3A1)/ ImageArea_M16V1Z3A1;



Correct_HolesPerArea_3_dist                                          =
 transpose(horzcat(Correct_HolesPerArea_M2V1Z1A1,Correct_HolesPerAr
 ea_M2V1Z1A2,Cor
Correct_HolesPerArea_M2V2Z1A2,Correct_HolesPerArea_M2V2Z2A1,Correct
_HolesPerArea_M
Correct_HolesPerArea_M3V3Z2,Correct_HolesPerArea_M3V3Z3A1,Correct_H
olesPerArea_M3V
Correct_HolesPerArea_M3V3Z1A1,Correct_HolesPerArea_M3V3Z1A2,Correct
_HolesPerArea_M
Correct_HolesPerArea_M4V1Z1A2,Correct_HolesPerArea_M4V2Z1A1,Correct
_HolesPerArea_M



HIEL_radi =
(horzcat(transpose(Param_M2V1Z1A1(:,3)/scale1),...
transpose(Param_M2V1Z1A2(:,3)/scale1),...
transpose(Param_M2V2Z1A1(:,3)/scale1),...
```

```
transpose(Param_M2V2Z1A2(:,3)/scale1),...
transpose(Param_M2V2Z2A1(:,3)/scale1),...
transpose(Param_M2V2Z3A1(:,3)/scale1),...
transpose(Param_M2V2Z3A2(:,3)/scale1),...
transpose(Param_M3V3Z2(:,3)/scale2),...
transpose(Param_M3V3Z3A1(:,3)/scale2),...
transpose(Param_M3V3Z3A2(:,3)/scale2),...
transpose(Param_M3V3Z3A3(:,3)/scale2),...
transpose(Param_M3V3Z1A1(:,3)/scale2),...
transpose(Param_M3V3Z1A2(:,3)/scale2),...
transpose(Param_M3V3Z1A3(:,3)/scale2),...
transpose(Param_M3V1Z2A1(:,3)/scale2),...
transpose(Param_M4V1Z1A1(:,3)/scale2),...
transpose(Param_M4V1Z1A2(:,3)/scale2),...
transpose(Param_M4V2Z1A1(:,3)/scale2),...
transpose(Param_M9V3Z1A1(:,3)/scale2),...
transpose(Param_M9V6Z1A1(:,3)/scale2),...
transpose(Param_M12V2Z1A1(:,3)/scale2),...
transpose(Param_M16V1Z3A1(:,3)/scale2)));



HIEL_radi =
transpose(HIEL_radi
); HIEL_radi_mean =
mean(HIEL_radi);



%SECTION 2 - AVERAGE MINIMUM DISTANCE

%Average Minimum Distance of HIEL to
Claudin5 AvgMinIEL_3 =
mean((distance_avgMIN_M2V1Z1A1 +
 distance_avgMIN_M2V1Z1A2 +
    distance_avgMIN_M2V2Z1A1+...
    distance_avgMIN_M2V2Z1A2+
    distance_avgMIN_M2V2Z2A1+
 distance_avgMIN_M2V2Z3A1+ distance_avgMIN_M2V2Z3A2 +
 distance_avgMIN_M3V3Z2+...
    distance_avgMIN_M3V3Z3A1 +
 distance_avgMIN_M3V3Z3A2+ distance_avgMIN_M3V3Z3A3+
 distance_avgMIN_M3V3Z1A1+
 distance_avgMIN_M3V3Z1A2+...
    distance_avgMIN_M3V3Z1A3+
 distance_avgMIN_M3V1Z2A1+distance_avgMIN_M4V1Z1A1+distance_avgMIN_
 M4V1Z1A2+distan

 +distance_avgMIN_M9V3Z1A1+distance_avgMIN_M9V6Z1A1+distance_avgMIN
 _M12V2Z1A1+dist

%Average Minimum Distance Monte Carlo
Simulations AvgMinMC_3 =
```

```
mean((distance_mc_avgMIN_M2V1Z1A1 +
 distance_mc_avgMIN_M2V1Z1A2 + distance_mc_avgMIN_M2V2Z1A1 +...
    distance_mc_avgMIN_M2V2Z1A2
 +distance_mc_avgMIN_M2V2Z2A1+distance_mc_avgMIN_M2V2Z3A1+distance_
 mc_avgMIN_M2V2Z

 distance_mc_avgMIN_M3V3Z3A1+distance_mc_avgMIN_M3V3Z3A2+distance_m
 c_avgMIN_M3V3Z3

 distance_mc_avgMIN_M3V3Z1A3+distance_mc_avgMIN_M3V1Z2A1+distance_m
 c_avgMIN_M4V1Z1

 distance_mc_avgMIN_M9V6Z1A1+distance_mc_avgMIN_M9V3Z1A1+distance_m
 c_avgMIN_M12V2Z


%Average Minimum Distance Positive Control
Simulations AvgMinPC_3 =
mean((distance_pc_1um_avgMIN_M2V1Z1A1 +
 distance_pc_1um_avgMIN_M2V1Z1A2+
 distance_pc_1um_avgMIN_M2V2Z1A1+...

 distance_pc_1um_avgMIN_M2V2Z1A2+distance_pc_1um_avgMIN_M2V2Z2A1+di
 stance_pc_1um_a

 distance_pc_1um_avgMIN_M3V3Z3A1+distance_pc_1um_avgMIN_M3V3Z3A2+di
 stance_pc_1um_a

 distance_pc_1um_avgMIN_M3V3Z1A3+distance_pc_1um_avgMIN_M3V1Z2A1+di
 stance_pc_1um_a

 distance_pc_1um_avgMIN_M9V6Z1A1+distance_pc_1um_avgMIN_M9V3Z1A1+di
 stance_pc_1um_a


%Average Minimum Distance Negative Control
Simulations AvgMinNC_3 =
mean((distance_nc_avgMIN_M2V1Z1A1 +
 distance_nc_avgMIN_M2V1Z1A2 + distance_nc_avgMIN_M2V2Z1A1+...

 distance_nc_avgMIN_M2V2Z1A2+distance_nc_avgMIN_M2V2Z2A1+distance_n
 c_avgMIN_M2V2Z3

 distance_nc_avgMIN_M3V3Z3A1+distance_nc_avgMIN_M3V3Z3A2+distance_n
 c_avgMIN_M3V3Z3

 distance_nc_avgMIN_M3V3Z1A3+distance_nc_avgMIN_M3V1Z2A1+distance_n
 c_avgMIN_M4V1Z1

 distance_nc_avgMIN_M9V3Z1A1+distance_nc_avgMIN_M9V6Z1A1+distance_n
 c_avgMIN_M12V2Z
```

```
%SECTION 3 - SHORTEST DIST TO CLDN5 FOR EACH IEL HOLE (DISTRIBUTION)

%Minimum Distance HIEL to Cldn5
DISTRIBUTION MinIELhist_3 =
 horzcat(distance_avgMIN_hist_M2V1Z1A1,distance_avgMIN_hist_M2V1Z1A
 2,distance_avgM

 distance_avgMIN_hist_M2V2Z1A2,distance_avgMIN_hist_M2V2Z2A1,distan
 ce_avgMIN_hist_

 distance_avgMIN_M3V3Z2_hist,distance_avgMIN_hist_M3V3Z3A1,distance
 _avgMIN_hist_M3

 distance_avgMIN_hist_M3V3Z1A1,distance_avgMIN_hist_M3V3Z1A2,distan
 ce_avgMIN_hist_

 distance_avgMIN_hist_M4V1Z1A2,distance_avgMIN_hist_M4V2Z1A1,distan
    ce_avgMIN_hist_ distance_avgMIN_hist_M16V1Z3A1);
MinIELhist_3_length = length(MinIELhist_3);

%Minimum Distance HIEL to Cldn5 Monte Carlo
DISTRIBUTION MinMChist_3 =
 horzcat(distance_mc_avgMIN_hist_M2V1Z1A1,distance_mc_avgMIN_hist_M
 2V1Z1A2,distanc

 distance_mc_avgMIN_hist_M2V2Z1A2,distance_mc_avgMIN_hist_M2V2Z2A1,
 distance_mc_avg

 distance_mc_avgMIN_M3V3Z2_hist,distance_mc_avgMIN_hist_M3V3Z3A1,di
 stance_mc_avgMI

 distance_mc_avgMIN_hist_M3V3Z1A1,distance_mc_avgMIN_hist_M3V3Z1A2,
 distance_mc_avg

 distance_mc_avgMIN_hist_M4V1Z1A2,distance_mc_avgMIN_hist_M4V2Z1A1,
 distance_mc_avg

 distance_mc_avgMIN_hist_M12V2Z1A1,distance_mc_avgMIN_hist_M16V1Z3
A1) ; MinMChist_3_length = length(MinMChist_3);


%Minimum Distance HIEL to Cldn5 Positive Control
DISTRIBUTION MinPChist_3 =
 horzcat(distance_pc_1um_avgMIN_hist_M2V1Z1A1,distance_pc_1um_avgMI
 N_hist_M2V1Z1A2

 distance_pc_1um_avgMIN_hist_M2V2Z1A2,distance_pc_1um_avgMIN_hist_M
 2V2Z2A1,distanc

 distance_pc_1um_avgMIN_M3V3Z2_hist,distance_pc_1um_avgMIN_hist_M3V
 3Z3A1,distance_

 distance_pc_1um_avgMIN_hist_M3V3Z1A1,distance_pc_1um_avgMIN_hist_M
 3V3Z1A2,distanc
```

```
 distance_pc_1um_avgMIN_hist_M4V1Z1A2,distance_pc_1um_avgMIN_hist_M
 4V2Z1A1,distanc

 distance_pc_1um_avgMIN_hist_M12V2Z1A1,distance_pc_1um_avgMIN_hist
_M16V1Z3A1) ; MinPChist_3_length = length(MinPChist_3);



%Minimum HIEL to Cldn5 Distance Negative Control
DISTRIBUTION MinNChist_3 =
horzcat(distance_nc_avgMIN_hist_M2V1Z1A1,
 distance_nc_avgMIN_hist_M2V1Z1A2,distance_nc_avgMIN_hist_M2V1Z1A2,
 ...

 distance_nc_avgMIN_hist_M2V2Z1A2,distance_nc_avgMIN_hist_M2V2Z2A1,
 distance_nc_avg

 distance_nc_avgMIN_M3V3Z2_hist,distance_nc_avgMIN_hist_M3V3Z3A1,di
 stance_nc_avgMI

 distance_nc_avgMIN_hist_M3V3Z1A1,distance_nc_avgMIN_hist_M3V3Z1A2,
 distance_nc_avg

 distance_nc_avgMIN_hist_M4V1Z1A2,distance_nc_avgMIN_hist_M4V2Z1A1,
 distance_nc_avg

 distance_nc_avgMIN_hist_M12V2Z1A1,distance_nc_avgMIN_hist_M16V1Z3
A1) ; MinNChist_3_length = length(MinNChist_3);


%double check that all of the datasets are the same length.
%     if MinIELhist_3_length ~=
 MinMChist_3_length ~= MinPChist_3_length
 ~=MinPCEhist_3_length ~=MinNChist_3_length
%
%         error('does not match')
%     else
%         print('good to go')
%
%     end
%
%
%MinDist_3 =
 horzcat(transpose(MinPChist_3),transpose(MinMChist_3),transpose(Mi
 nNChist_3),tran transpose(MinPCEhist_3));

MinDist_3 =
 horzcat(transpose(MinMChist_3),transpose(MinNChist_3),transpose(Mi
 nIELhist_3), transpose(MinPCEhist_3));


%%FIGURE Average
minimum distance.
AvgMinDistance =
```

```
figure;
edges = linspace(0,5,21);%beginning of range, end of range, # of
bins
+1
histogram(MinPChist_3, 'BinEdges',
 edges, 'FaceColor','b', 'Normalization',
'probability'); hold on;
histogram(MinNChist_3, 'BinEdges',
 edges, 'FaceColor','w','EdgeColor', 'k', 'Normalization',
'probability'); hold on;
histogram(MinMChist_3, 'BinEdges',
 edges, 'FaceColor','k', 'Normalization',
'probability'); hold on;
histogram(MinIELhist_3, 'BinEdges',
 edges, 'FaceColor','m', 'Normalization',
'probability'); hold on;
xlabel('Distance to Claudin 5 stain (um)',
'FontSize', 10); ylabel('% Centers',
'FontSize', 10);
legend('Positive Control','Negative Control','Monte
 Carlo Simulations','3rd order
 artery','FontSize',12);
title('Minimum distance to interendothelial junction');
AvgMinDistance.InvertHardcopy = 'off'; %removes the
 default option of a white background so that the
 white claudin5_ coordinates show up correctly on the
 saved image
saveas(AvgMinDistance, '/Users/claireruddiman/AnalysisFiles/
CombinedAnalysis3rd/AvgMinDistance.png');
hold off;
```

%SECTION 4 - DISTRIBUTION OF SHORTEST 100 DISTANCES (IEL TO CLDN5)

```
% Avg Top 100, averaged across all
analyses IEL Top100IEL_3 =
horzcat(distance_sort_M2V1Z1A1,
 distance_sort_M2V1Z1A2,distance_sort_
 M2V2Z1A1, distance_sort_M2V2Z1A2,
 distance_sort_M2V2Z2A1,...

 distance_sort_M2V2Z3A1,distance_sort_M2V2Z3A2,distance_sort_M3V3Z2
 ,distance_sort_

 distance_sort_M3V3Z1A1,distance_sort_M3V3Z1A2,distance_sort_M3V3Z1
 A3,distance_sor

 distance_sort_M9V6Z1A1,distance_sort_M9V3Z1A1,distance_sort_M12V2Z
 1A1,distance_so

% Avg Top 100, averaged across all analyses
Monte Carlo Top100MC_3 =
horzcat(Dd_new_avg_M2V1Z1A1,
```

```
Dd_new_avg_M2V1Z1A2,
 Dd_new_avg_M2V2Z1A1, Dd_new_avg_M2V2Z1A2, Dd_new_avg_M2V2Z2A1,...

 Dd_new_avg_M2V2Z3A1,Dd_new_avg_M2V2Z3A2,Dd_new_avg_M3V3Z2,Dd_new_a
 vg_M3V3Z3A1,Dd_

 Dd_new_avg_M3V3Z1A1,Dd_new_avg_M3V3Z1A2,Dd_new_avg_M3V3Z1A3,Dd_new
 _avg_M3V1Z2A1,D

 Dd_new_avg_M9V6Z1A1,Dd_new_avg_M9V3Z1A1,Dd_new_avg_M12V2Z1A1,Dd_ne
 w_avg_M16V1Z3A1

% Avg Top 100, averaged across all analyses Positive
Control Top100PC_3 =
 horzcat(Dd_new_avg_pc_M2V1Z1A1,Dd_new_avg_pc_M2V1Z1A2,Dd_new_avg_p
 c_M2V2Z1A1, Dd_new_avg_pc_M2V2Z1A2,Dd_new_avg_pc_M2V2Z2A1,...

 Dd_new_avg_pc_M2V2Z3A1,Dd_new_avg_pc_M2V2Z3A2,Dd_new_avg_M3V3Z2_pc
 ,Dd_new_avg_pc_

 Dd_new_avg_pc_M3V3Z1A1,Dd_new_avg_pc_M3V3Z1A2,Dd_new_avg_pc_M3V3Z1
 A3,Dd_new_avg_p

 Dd_new_avg_pc_M9V6Z1A1,Dd_new_avg_pc_M9V3Z1A1,Dd_new_avg_pc_M12V2Z
 1A1,Dd_new_avg_

% Avg Top 100, averaged across all analyses negative
control Top100NC_3 =
 horzcat(Dd_new_avg_nc_M2V1Z1A1,Dd_new_avg_nc_M2V1Z1A2,Dd_new_avg_n
 c_M2V2Z1A1, Dd_new_avg_nc_M2V2Z1A2,Dd_new_avg_nc_M2V2Z2A1,...

 Dd_new_avg_nc_M2V2Z3A1,Dd_new_avg_nc_M2V2Z3A2,Dd_new_avg_M3V3Z2_nc
 ,Dd_new_avg_nc_

 Dd_new_avg_nc_M3V3Z1A1,Dd_new_avg_nc_M3V3Z1A2,Dd_new_avg_nc_M3V3Z1
 A3,Dd_new_avg_n

 Dd_new_avg_nc_M9V6Z1A1,Dd_new_avg_nc_M9V3Z1A1,Dd_new_avg_nc_M12V2Z
 1A1,Dd_new_avg_


Top100Distances = figure;
edges = linspace(0,6,31);%beginning of range, end of range, # of
bins
+1
histogram(Top100PC_3, 'BinEdges',
 edges, 'FaceColor','b', 'Normalization',
'probability'); hold on;
histogram(Top100NC_3, 'BinEdges',
 edges, 'FaceColor','w','EdgeColor', 'k', 'Normalization',
'probability'); hold on;
histogram(Top100MC_3, 'BinEdges',
 edges, 'FaceColor','k', 'Normalization',
'probability'); hold on;
```

```
histogram(Top100IEL_3, 'BinEdges',
 edges, 'FaceColor','m', 'Normalization',
'probability'); hold on;
xlabel('Distance to Claudin 5 stain (um)',
'FontSize', 10); ylabel('% Centers',
'FontSize', 10);
legend('Positive Control','Negative Control','Monte
 Carlo Simulations','3rd order
 artery','FontSize',12);
title('Shortest 100 distances per IEL hole to claudin 5');
Top100Distances.InvertHardcopy = 'off'; %removes the
 default option of a white background so that the
 white claudin5_ coordinates show up correctly on the
 saved image
saveas(Top100Distances, '/Users/claireruddiman/AnalysisFiles/
CombinedAnalysis3rd/Top100Distances.png');
hold off;

save('3rdorderRivanna.mat', 'IELHoles_3',
'IELHolesAvg_3','AvgRadius_3', 'AvgMinIE
'AvgMinNC_3','MinIELhist_3','MinMChist_3','MinPChist_3','MinPCEhist
_3','MinNChist_');
```

Published with MATLAB® R201

References

1. Michel RP, Hu F, Meyrick BO. Myoendothelial junctional complexes in postobstructive pulmonary vasculopathy: a quantitative electron microscopic study. Exp Lung Res. 1995;21(3):437-52.
2. Chadha PS, Liu L, Rikard-Bell M, Senadheera S, Howitt L, Bertrand RL, et al. Endothelium-dependent vasodilation in human mesenteric artery is primarily mediated by myoendothelial gap junctions intermediate conductance calcium-activated K+ channel and nitric oxide. J Pharmacol Exp Ther. 2011;336(3):701-8.
3. Rhodin JA. The ultrastructure of mammalian arterioles and precapillary sphincters. J Ultrastruct Res. 1967;18(1):181-223.
4. Moore DH, Ruska H. The fine structure of capillaries and small arteries. J Biophys Biochem Cytol. 1957;3(3):457-62.
5. Sandow SL, Hill CE. Incidence of myoendothelial gap junctions in the proximal and distal mesenteric arteries of the rat is suggestive of a role in endothelium-derived hyperpolarizing factor-mediated responses. Circ Res. 2000;86(3):341-6.
6. Edwards G, Dora KA, Gardener MJ, Garland CJ, Weston AH. K+ is an endothelium-derived hyperpolarizing factor in rat arteries. Nature. 1998;396(6708):269-72.
7. Kemp BK, Cocks TM. Evidence that mechanisms dependent and independent of nitric oxide mediate endothelium-dependent relaxation to bradykinin in human small resistance-like coronary arteries. Br J Pharmacol. 1997;120(5):757-62.
8. Garland CJ, Dora KA. EDH: endothelium-dependent hyperpolarization and microvascular signalling. Acta Physiol (Oxf). 2017;219(1):152-61.
9. Dora KA, Sandow SL, Gallagher NT, Takano H, Rummery NM, Hill CE, et al. Myoendothelial gap junctions may provide the pathway for EDHF in mouse mesenteric artery. J Vasc Res. 2003;40(5):480-90.
10. Shu X, Ruddiman CA, Keller TCSt, Keller AS, Yang Y, Good ME, et al. Heterocellular Contact Can Dictate Arterial Function. Circ Res. 2019;124(10):1473-81.
11. Shimokawa H, Yasutake H, Fujii K, Owada MK, Nakaike R, Fukumoto Y, et al. The importance of the hyperpolarizing mechanism increases as the vessel size decreases in endothelium-dependent relaxations in rat mesenteric circulation. J Cardiovasc Pharmacol. 1996;28(5):703-11.
12. Hong K, Cope EL, DeLalio LJ, Marziano C, Isakson BE, Sonkusare SK. TRPV4 (Transient Receptor Potential Vanilloid 4) Channel-Dependent Negative Feedback Mechanism Regulates Gq Protein-Coupled Receptor-Induced Vasoconstriction. Arterioscler Thromb Vasc Biol. 2018;38(3):542-54.
13. Sonkusare SK, Dalsgaard T, Bonev AD, Hill-Eubanks DC, Kotlikoff MI, Scott JD, et al. AKAP150-dependent cooperative TRPV4 channel gating is central to endothelium-dependent vasodilation and is disrupted in hypertension. Sci Signal. 2014;7(333):ra66.
14. Adapala RK, Talasila PK, Bratz IN, Zhang DX, Suzuki M, Meszaros JG, et al. PKCalpha mediates acetylcholine-induced activation of TRPV4-dependent

calcium influx in endothelial cells. Am J Physiol Heart Circ Physiol. 2011;301(3):H757-65.
15. Sandow SL, Neylon CB, Chen MX, Garland CJ. Spatial separation of endothelial small- and intermediate-conductance calcium-activated potassium channels (K(Ca)) and connexins: possible relationship to vasodilator function? J Anat. 2006;209(5):689-98.
16. Goto K, Ohtsubo T, Kitazono T. Endothelium-Dependent Hyperpolarization (EDH) in Hypertension: The Role of Endothelial Ion Channels. Int J Mol Sci. 2018;19(1).
17. Welsh DG, Segal SS. Role of EDHF in conduction of vasodilation along hamster cheek pouch arterioles in vivo. AmJPhysiol Heart CircPhysiol. 2000;278(6):H1832-H9.
18. Crane GJ, Gallagher N, Dora KA, Garland CJ. Small- and intermediate-conductance calcium-activated K+ channels provide different facets of endothelium-dependent hyperpolarization in rat mesenteric artery. J Physiol. 2003;553(Pt 1):183-9.
19. Eichler I, Wibawa J, Grgic I, Knorr A, Brakemeier S, Pries AR, et al. Selective blockade of endothelial Ca2+-activated small- and intermediate-conductance K+-channels suppresses EDHF-mediated vasodilation. Br J Pharmacol. 2003;138(4):594-601.
20. Gaete PS, Lillo MA, Ardiles NM, Perez FR, Figueroa XF. Ca2+-activated K+ channels of small and intermediate conductance control eNOS activation through NAD(P)H oxidase. Free Radic Biol Med. 2012;52(5):860-70.
21. Sonkusare SK, Dalsgaard T, Bonev AD, Nelson MT. Inward rectifier potassium (Kir2.1) channels as end-stage boosters of endothelium-dependent vasodilators. J Physiol. 2016;594(12):3271-85.
22. Ledoux J, Taylor MS, Bonev AD, Hannah RM, Solodushko V, Shui B, et al. Functional architecture of inositol 1,4,5-trisphosphate signaling in restricted spaces of myoendothelial projections. Proc Natl Acad Sci U S A. 2008;105(28):9627-32.
23. Biwer LA, Good ME, Hong K, Patel RK, Agrawal N, Looft-Wilson R, et al. Non-Endoplasmic Reticulum-Based Calr (Calreticulin) Can Coordinate Heterocellular Calcium Signaling and Vascular Function. Arterioscler Thromb Vasc Biol. 2018;38(1):120-30.
24. Biwer LA, Taddeo EP, Kenwood BM, Hoehn KL, Straub AC, Isakson BE. Two functionally distinct pools of eNOS in endothelium are facilitated by myoendothelial junction lipid composition. Biochim Biophys Acta. 2016;1861(7):671-9.
25. Yu J, Bergaya S, Murata T, Alp IF, Bauer MP, Lin MI, et al. Direct evidence for the role of caveolin-1 and caveolae in mechanotransduction and remodeling of blood vessels. J Clin Invest. 2006;116(5):1284-91.
26. Saliez J, Bouzin C, Rath G, Ghisdal P, Desjardins F, Rezzani R, et al. Role of caveolar compartmentation in endothelium-derived hyperpolarizing factor-mediated relaxation: Ca2+ signals and gap junction function are regulated by caveolin in endothelial cells. Circulation. 2008;117(8):1065-74.

27. Goedicke-Fritz S, Kaistha A, Kacik M, Markert S, Hofmeister A, Busch C, et al. Evidence for functional and dynamic microcompartmentation of Cav-1/TRPV4/K(Ca) in caveolae of endothelial cells. Eur J Cell Biol. 2015;94(7-9):391-400.
28. Lu T, Wang XL, Chai Q, Sun X, Sieck GC, Katusic ZS, et al. Role of the endothelial caveolae microdomain in shear stress-mediated coronary vasorelaxation. J Biol Chem. 2017;292(46):19013-23.
29. Isakson BE, Best AK, Duling BR. Incidence of protein on actin bridges between endothelium and smooth muscle in arterioles demonstrates heterogeneous connexin expression and phosphorylation. Am J Physiol Heart Circ Physiol. 2008;294(6):H2898-904.
30. Hakim CH, Jackson WF, Segal SS. Connexin isoform expression in smooth muscle cells and endothelial cells of hamster cheek pouch arterioles and retractor feed arteries. Microcirculation. 2008;15(6):503-14.
31. Sandow SL, Looft-Wilson R, Doran B, Grayson TH, Segal SS, Hill CE. Expression of homocellular and heterocellular gap junctions in hamster arterioles and feed arteries. Cardiovasc Res. 2003;60(3):643-53.
32. Mather S, Dora KA, Sandow SL, Winter P, Garland CJ. Rapid Endothelial Cell–Selective Loading of Connexin 40 Antibody Blocks Endothelium-Derived Hyperpolarizing Factor Dilation in Rat Small Mesenteric Arteries. Circulation Research. 2005;97(4):399-407.
33. Cheng C, van Haperen R, de Waard M, van Damme LC, Tempel D, Hanemaaijer L, et al. Shear stress affects the intracellular distribution of eNOS: direct demonstration by a novel in vivo technique. Blood. 2005;106(12):3691-8.
34. Straub AC, Billaud M, Johnstone SR, Best AK, Yemen S, Dwyer ST, et al. Compartmentalized connexin 43 s-nitrosylation/denitrosylation regulates heterocellular communication in the vessel wall. Arterioscler Thromb Vasc Biol. 2011;31(2):399-407.
35. Bardin N, Anfosso F, Masse JM, Cramer E, Sabatier F, Le Bivic A, et al. Identification of CD146 as a component of the endothelial junction involved in the control of cell-cell cohesion. Blood. 2001;98(13):3677-84.
36. Heberlein KR, Straub AC, Best AK, Greyson MA, Looft-Wilson RC, Sharma PR, et al. Plasminogen activator inhibitor-1 regulates myoendothelial junction formation. Circ Res. 2010;106(6):1092-102.
37. Heberlein KR, Han J, Straub AC, Best AK, Kaun C, Wojta J, et al. A novel mRNA binding protein complex promotes localized plasminogen activator inhibitor-1 accumulation at the myoendothelial junction. Arterioscler Thromb Vasc Biol. 2012;32(5):1271-9.
38. Straub AC, Butcher JT, Billaud M, Mutchler SM, Artamonov MV, Nguyen AT, et al. Hemoglobin alpha/eNOS coupling at myoendothelial junctions is required for nitric oxide scavenging during vasoconstriction. Arterioscler Thromb Vasc Biol. 2014;34(12):2594-600.
39. Straub AC, Lohman AW, Billaud M, Johnstone SR, Dwyer ST, Lee MY, et al. Endothelial cell expression of haemoglobin alpha regulates nitric oxide signalling. Nature. 2012;491(7424):473-7.

40. Isakson BE. Localized expression of an Ins(1,4,5)P3 receptor at the myoendothelial junction selectively regulates heterocellular Ca2+ communication. J Cell Sci. 2008;121(Pt 21):3664-73.
41. Isakson BE, Ramos SI, Duling BR. Ca2+ and inositol 1,4,5-trisphosphate-mediated signaling across the myoendothelial junction. Circ Res. 2007;100(2):246-54.
42. Bagher P, Beleznai T, Kansui Y, Mitchell R, Garland CJ, Dora KA. Low intravascular pressure activates endothelial cell TRPV4 channels, local Ca2+ events, and IKCa channels, reducing arteriolar tone. Proc Natl Acad Sci U S A. 2012;109(44):18174-9.
43. McCallinhart PE, Biwer LA, Clark OE, Isakson BE, Lilly B, Trask AJ. Myoendothelial Junctions of Mature Coronary Vessels Express Notch Signaling Proteins. Front Physiol. 2020;11:29.
44. Biwer LA, Isakson BE. Endoplasmic reticulum-mediated signalling in cellular microdomains. Acta Physiol (Oxf). 2017;219(1):162-75.
45. Yap FC, Weber DS, Taylor MS, Townsley MI, Comer BS, Maylie J, et al. Endothelial SK3 channel-associated Ca2+ microdomains modulate blood pressure. Am J Physiol Heart Circ Physiol. 2016;310(9):H1151-63.
46. Cannon RE, Peart JC, Hawkins BT, Campos CR, Miller DS. Targeting blood-brain barrier sphingolipid signaling reduces basal P-glycoprotein activity and improves drug delivery to the brain. Proc Natl Acad Sci U S A. 2012;109(39):15930-5.
47. Hartmannsgruber V, Heyken WT, Kacik M, Kaistha A, Grgic I, Harteneck C, et al. Arterial response to shear stress critically depends on endothelial TRPV4 expression. PLoS One. 2007;2(9):e827.
48. Balsinde J, Winstead MV, Dennis EA. Phospholipase A(2) regulation of arachidonic acid mobilization. FEBS Lett. 2002;531(1):2-6.
49. Luo W, Liu B, Zhou Y. The endothelial cyclooxygenase pathway: Insights from mouse arteries. Eur J Pharmacol. 2016;780:148-58.
50. Brandes RP, Schmitz-Winnenthal FH, Feletou M, Godecke A, Huang PL, Vanhoutte PM, et al. An endothelium-derived hyperpolarizing factor distinct from NO and prostacyclin is a major endothelium-dependent vasodilator in resistance vessels of wild-type and endothelial NO synthase knockout mice. Proc Natl Acad Sci U S A. 2000;97(17):9747-52.
51. Earley S, Heppner TJ, Nelson MT, Brayden JE. TRPV4 forms a novel Ca2+ signaling complex with ryanodine receptors and BKCa channels. Circ Res. 2005;97(12):1270-9.
52. Schmidt K, de Wit C. Endothelium-Derived Hyperpolarizing Factor and Myoendothelial Coupling: The in vivo Perspective. Front Physiol. 2020;11:602930.
53. Beyer S, Kelly RG, Miquerol L. Inducible Cx40-Cre expression in the cardiac conduction system and arterial endothelial cells. Genesis. 2011;49(2):83-91.
54. Johnstone S, Isakson B, Locke D. Biological and biophysical properties of vascular connexin channels. Int Rev Cell Mol Biol. 2009;278:69-118.

55. Isakson BE, Damon DN, Day KH, Liao Y, Duling BR. Connexin40 and connexin43 in mouse aortic endothelium: evidence for coordinated regulation. Am J Physiol Heart Circ Physiol. 2006;290(3):H1199-205.
56. Isakson BE, Duling BR. Heterocellular contact at the myoendothelial junction influences gap junction organization. Circ Res. 2005;97(1):44-51.
57. Boettcher M, de Wit C. Distinct endothelium-derived hyperpolarizing factors emerge in vitro and in vivo and are mediated in part via connexin 40-dependent myoendothelial coupling. Hypertension. 2011;57(4):802-8.
58. Chaytor AT, Evans WH, Griffith TM. Central role of heterocellular gap junctional communication in endothelium-dependent relaxations of rabbit arteries. J Physiol. 1998;508 (Pt 2):561-73.
59. Segal SS, Duling BR. Conduction of vasomotor responses in arterioles: a role for cell-to-cell coupling? Am J Physiol. 1989;256(3 Pt 2):H838-45.
60. Yashiro Y, Duling BR. Integrated Ca(2+) signaling between smooth muscle and endothelium of resistance vessels. Circ Res. 2000;87(11):1048-54.
61. Dora KA, Doyle MP, Duling BR. Elevation of intracellular calcium in smooth muscle causes endothelial cell generation of NO in arterioles. Proc Natl Acad Sci U S A. 1997;94(12):6529-34.
62. Tran CH, Taylor MS, Plane F, Nagaraja S, Tsoukias NM, Solodushko V, et al. Endothelial Ca2+ wavelets and the induction of myoendothelial feedback. Am J Physiol Cell Physiol. 2012;302(8):C1226-42.
63. Kerr PM, Tam R, Ondrusova K, Mittal R, Narang D, Tran CH, et al. Endothelial feedback and the myoendothelial projection. Microcirculation. 2012;19(5):416-22.
64. Furchgott RF, Zawadzki JV. The obligatory role of endothelial cells in the relaxation of arterial smooth muscle by acetylcholine. Nature. 1980;288(5789):373-6.
65. Huang PL, Huang Z, Mashimo H, Bloch KD, Moskowitz MA, Bevan JA, et al. Hypertension in mice lacking the gene for endothelial nitric oxide synthase. Nature. 1995;377(6546):239-42.
66. Rees DD, Palmer RM, Hodson HF, Moncada S. A specific inhibitor of nitric oxide formation from L-arginine attenuates endothelium-dependent relaxation. Br J Pharmacol. 1989;96(2):418-24.
67. Zhao Y, Vanhoutte PM, Leung SW. Vascular nitric oxide: Beyond eNOS. J Pharmacol Sci. 2015;129(2):83-94.
68. Feil R, Lohmann SM, de Jonge H, Walter U, Hofmann F. Cyclic GMP-dependent protein kinases and the cardiovascular system: insights from genetically modified mice. Circ Res. 2003;93(10):907-16.
69. Morgan JP, Morgan KG. Stimulus-specific patterns of intracellular calcium levels in smooth muscle of ferret portal vein. J Physiol. 1984;351:155-67.
70. Somlyo AP, Somlyo AV. Ca2+ sensitivity of smooth muscle and nonmuscle myosin II: modulated by G proteins, kinases, and myosin phosphatase. Physiol Rev. 2003;83(4):1325-58.
71. Taylor DA, Stull JT. Calcium dependence of myosin light chain phosphorylation in smooth muscle cells. J Biol Chem. 1988;263(28):14456-62.

72. Sleek GE, Duling BR. Coordination of mural elements and myofilaments during arteriolar constriction. Circ Res. 1986;59(6):620-7.
73. Clifford PS, Ella SR, Stupica AJ, Nourian Z, Li M, Martinez-Lemus LA, et al. Spatial distribution and mechanical function of elastin in resistance arteries: a role in bearing longitudinal stress. Arterioscler Thromb Vasc Biol. 2011;31(12):2889-96.
74. Yashiro Y, Duling BR. Participation of intracellular Ca2+ stores in arteriolar conducted responses. Am J Physiol Heart Circ Physiol. 2003;285(1):H65-73.
75. Chaytor AT, Martin PE, Edwards DH, Griffith TM. Gap junctional communication underpins EDHF-type relaxations evoked by ACh in the rat hepatic artery. Am J Physiol Heart Circ Physiol. 2001;280(6):H2441-50.
76. Sandow SL, Gzik DJ, Lee RM. Arterial internal elastic lamina holes: relationship to function? J Anat. 2009;214(2):258-66.
77. Dzau VJ, Safar ME. Large conduit arteries in hypertension: role of the vascular renin-angiotensin system. Circulation. 1988;77(5):947-54.
78. Heberlein KR, Straub AC, Isakson BE. The myoendothelial junction: breaking through the matrix? Microcirculation. 2009;16(4):307-22.
79. Taugner R, Kirchheim H, Forssmann WG. Myoendothelial contacts in glomerular arterioles and in renal interlobular arteries of rat, mouse and Tupaia belangeri. Cell Tissue Res. 1984;235(2):319-25.
80. Keller TCt, Butcher JT, Broseghini-Filho GB, Marziano C, DeLalio LJ, Rogers S, et al. Modulating Vascular Hemodynamics With an Alpha Globin Mimetic Peptide (HbalphaX). Hypertension. 2016;68(6):1494-503.
81. Lechauve C, Butcher JT, Freiwan A, Biwer LA, Keith JM, Good ME, et al. Endothelial cell alpha-globin and its molecular chaperone alpha-hemoglobin-stabilizing protein regulate arteriolar contractility. J Clin Invest. 2018;128(11):5073-82.
82. Billaud M, Lohman AW, Straub AC, Parpaite T, Johnstone SR, Isakson BE. Characterization of the thoracodorsal artery: morphology and reactivity. Microcirculation. 2012;19(4):360-72.
83. Johnstone SR, Ross J, Rizzo MJ, Straub AC, Lampe PD, Leitinger N, et al. Oxidized phospholipid species promote in vivo differential cx43 phosphorylation and vascular smooth muscle cell proliferation. Am J Pathol. 2009;175(2):916-24.
84. Straub AC, Zeigler AC, Isakson BE. The myoendothelial junction: connections that deliver the message. Physiology (Bethesda). 2014;29(4):242-9.
85. Billaud M, Lohman AW, Johnstone SR, Biwer LA, Mutchler S, Isakson BE. Regulation of cellular communication by signaling microdomains in the blood vessel wall. Pharmacol Rev. 2014;66(2):513-69.
86. Behringer EJ, Socha MJ, Polo-Parada L, Segal SS. Electrical conduction along endothelial cell tubes from mouse feed arteries: confounding actions of glycyrrhetinic acid derivatives. Br J Pharmacol. 2012;166(2):774-87.
87. Strobaek D, Teuber L, Jorgensen TD, Ahring PK, Kjaer K, Hansen RS, et al. Activation of human IK and SK Ca2+ -activated K+ channels by NS309 (6,7-dichloro-1H-indole-2,3-dione 3-oxime). Biochim Biophys Acta. 2004;1665(1-2):1-5.

88. Craig J, Martin W. Dominance of flow-mediated constriction over flow-mediated dilatation in the rat carotid artery. Br J Pharmacol. 2012;167(3):527-36.
89. Emerson GG, Segal SS. Electrical coupling between endothelial cells and smooth muscle cells in hamster feed arteries: role in vasomotor control. CircRes. 2000;87(6):474-9.
90. Heberlein KR, Han J, Straub AC, Best AK, Kaun C, Wojta J, et al. A novel mRNA binding protein complex promotes localized plasminogen activator inhibitor-1 accumulation at the myoendothelial junction. Arteriosclerosis, Thrombosis, and Vascular Biology. 2012;32(5):1271-9.
91. Gerhardt H, Betsholtz C. Endothelial-pericyte interactions in angiogenesis. Cell Tissue Res. 2003;314(1):15-23.
92. Rondina MT, Weyrich AS, Zimmerman GA. Platelets as cellular effectors of inflammation in vascular diseases. Circ Res. 2013;112(11):1506-19.
93. Petri B, Phillipson M, Kubes P. The physiology of leukocyte recruitment: an in vivo perspective. J Immunol. 2008;180(10):6439-46.
94. Sangwung P, Zhou G, Lu Y, Liao X, Wang B, Mutchler SM, et al. Regulation of endothelial hemoglobin alpha expression by Kruppel-like factors. Vasc Med. 2017;22(5):363-9.
95. Ahn SJ, Fancher IS, Bian JT, Zhang CX, Schwab S, Gaffin R, et al. Inwardly rectifying K(+) channels are major contributors to flow-induced vasodilatation in resistance arteries. J Physiol. 2017;595(7):2339-64.
96. Ahn SJ, Fancher IS, Granados ST, Do Couto NF, Hwang CL, Phillips SA, et al. Cholesterol-Induced Suppression of Endothelial Kir Channels Is a Driver of Impairment of Arteriolar Flow-Induced Vasodilation in Humans. Hypertension. 2022;79(1):126-38.
97. Ottolini M, Hong K, Sonkusare SK. Calcium signals that determine vascular resistance. Wiley Interdiscip Rev Syst Biol Med. 2019:e1448.
98. Han H, Rosenhouse-Dantsker A, Gnanasambandam R, Epshtein Y, Chen Z, Sachs F, et al. Silencing of Kir2 channels by caveolin-1: cross-talk with cholesterol. J Physiol. 2014;592(18):4025-38.
99. Barbera N, Granados ST, Vanoye CG, Abramova TV, Kulbak D, Ahn SJ, et al. Cholesterol-induced suppression of Kir2 channels is mediated by decoupling at the inter-subunit interfaces. iScience. 2022;25(5):104329.
100. Dabertrand F, Harraz OF, Koide M, Longden TA, Rosehart AC, Hill-Eubanks DC, et al. PIP2 corrects cerebral blood flow deficits in small vessel disease by rescuing capillary Kir2.1 activity. Proc Natl Acad Sci U S A. 2021;118(17).
101. Voelker DR. Biochemistry of Lipids, Lipoproteins, and Membranes. Amsterdam: Elsevier; 1996.
102. Duncan AL, Corey RA, Sansom MSP. Defining how multiple lipid species interact with inward rectifier potassium (Kir2) channels. Proc Natl Acad Sci U S A. 2020;117(14):7803-13.
103. Yeung T, Gilbert GE, Shi J, Silvius J, Kapus A, Grinstein S. Membrane phosphatidylserine regulates surface charge and protein localization. Science. 2008;319(5860):210-3.

104. Cheng WWL, D'Avanzo N, Doyle DA, Nichols CG. Dual-mode phospholipid regulation of human inward rectifying potassium channels. Biophys J. 2011;100(3):620-8.
105. Fan Z, Makielski JC. Anionic phospholipids activate ATP-sensitive potassium channels. J Biol Chem. 1997;272(9):5388-95.
106. Beeler GW, Jr., Reuter H. Voltage clamp experiments on ventricular myocarial fibres. J Physiol. 1970;207(1):165-90.
107. Kurachi Y. Voltage-dependent activation of the inward-rectifier potassium channel in the ventricular cell membrane of guinea-pig heart. J Physiol. 1985;366:365-85.
108. Brown DA, Gahwiler BH, Griffith WH, Halliwell JV. Membrane currents in hippocampal neurons. Prog Brain Res. 1990;83:141-60.
109. Gahwiler BH, Brown DA. GABAB-receptor-activated K+ current in voltage-clamped CA3 pyramidal cells in hippocampal cultures. Proc Natl Acad Sci U S A. 1985;82(5):1558-62.
110. Sims SM, Dixon SJ. Inwardly rectifying K+ current in osteoclasts. Am J Physiol. 1989;256(6 Pt 1):C1277-82.
111. Kettenmann H, Banati R, Walz W. Electrophysiological behavior of microglia. Glia. 1993;7(1):93-101.
112. Greger R, Bleich M, Schlatter E. Ion channels in the thick ascending limb of Henle's loop. Ren Physiol Biochem. 1990;13(1-2):37-50.
113. Hagiwara S, Miyazaki S, Moody W, Patlak J. Blocking effects of barium and hydrogen ions on the potassium current during anomalous rectification in the starfish egg. J Physiol. 1978;279:167-85.
114. Lewis DL, Ikeda SR, Aryee D, Joho RH. Expression of an inwardly rectifying K+ channel from rat basophilic leukemia cell mRNA in Xenopus oocytes. FEBS Lett. 1991;290(1-2):17-21.
115. Johnson TD, Marrelli SP, Steenberg ML, Childres WF, Bryan RM, Jr. Inward rectifier potassium channels in the rat middle cerebral artery. Am J Physiol. 1998;274(2):R541-7.
116. Silver MR, DeCoursey TE. Intrinsic gating of inward rectifier in bovine pulmonary artery endothelial cells in the presence or absence of internal Mg2+. J Gen Physiol. 1990;96(1):109-33.
117. Aziz Q, Thomas AM, Gomes J, Ang R, Sones WR, Li Y, et al. The ATP-sensitive potassium channel subunit, Kir6.1, in vascular smooth muscle plays a major role in blood pressure control. Hypertension. 2014;64(3):523-9.
118. Levitan I. Cholesterol and Kir channels. IUBMB Life. 2009;61(8):781-90.
119. Lopes CM, Zhang H, Rohacs T, Jin T, Yang J, Logothetis DE. Alterations in conserved Kir channel-PIP2 interactions underlie channelopathies. Neuron. 2002;34(6):933-44.
120. Plaster NM, Tawil R, Tristani-Firouzi M, Canun S, Bendahhou S, Tsunoda A, et al. Mutations in Kir2.1 cause the developmental and episodic electrical phenotypes of Andersen's syndrome. Cell. 2001;105(4):511-9.
121. Beuckelmann DJ, Nabauer M, Erdmann E. Alterations of K+ currents in isolated human ventricular myocytes from patients with terminal heart failure. Circ Res. 1993;73(2):379-85.

122. Zaritsky JJ, Eckman DM, Wellman GC, Nelson MT, Schwarz TL. Targeted disruption of Kir2.1 and Kir2.2 genes reveals the essential role of the inwardly rectifying K(+) current in K(+)-mediated vasodilation. Circ Res. 2000;87(2):160-6.
123. Anumonwo JM, Lopatin AN. Cardiac strong inward rectifier potassium channels. J Mol Cell Cardiol. 2010;48(1):45-54.
124. Hibino H, Inanobe A, Furutani K, Murakami S, Findlay I, Kurachi Y. Inwardly rectifying potassium channels: their structure, function, and physiological roles. Physiol Rev. 2010;90(1):291-366.
125. Katz B. The efferent regulation of the muscle spindle in the frog. J Exp Biol. 1949;26(2):201-17.
126. Hutter OF, Noble D. Rectifying properties of heart muscle. Nature. 1960;188:495.
127. Hodgkin AL, Huxley AF, Katz B. Measurement of current-voltage relations in the membrane of the giant axon of Loligo. J Physiol. 1952;116(4):424-48.
128. Ficker E, Taglialatela M, Wible BA, Henley CM, Brown AM. Spermine and spermidine as gating molecules for inward rectifier K+ channels. Science. 1994;266(5187):1068-72.
129. Lopatin AN, Makhina EN, Nichols CG. Potassium channel block by cytoplasmic polyamines as the mechanism of intrinsic rectification. Nature. 1994;372(6504):366-9.
130. Tao X, Avalos JL, Chen J, MacKinnon R. Crystal structure of the eukaryotic strong inward-rectifier K+ channel Kir2.2 at 3.1 A resolution. Science. 2009;326(5960):1668-74.
131. Whorton MR, MacKinnon R. Crystal structure of the mammalian GIRK2 K+ channel and gating regulation by G proteins, PIP2, and sodium. Cell. 2011;147(1):199-208.
132. Heginbotham L, Lu Z, Abramson T, MacKinnon R. Mutations in the K+ channel signature sequence. Biophys J. 1994;66(4):1061-7.
133. Yang J, Yu M, Jan YN, Jan LY. Stabilization of ion selectivity filter by pore loop ion pairs in an inwardly rectifying potassium channel. Proc Natl Acad Sci U S A. 1997;94(4):1568-72.
134. Leyland ML, Dart C, Spencer PJ, Sutcliffe MJ, Stanfield PR. The possible role of a disulphide bond in forming functional Kir2.1 potassium channels. Pflugers Arch. 1999;438(6):778-81.
135. Hansen SB, Tao X, MacKinnon R. Structural basis of PIP2 activation of the classical inward rectifier K+ channel Kir2.2. Nature. 2011;477(7365):495-8.
136. Whorton MR, MacKinnon R. X-ray structure of the mammalian GIRK2-betagamma G-protein complex. Nature. 2013;498(7453):190-7.
137. Pegan S, Arrabit C, Slesinger PA, Choe S. Andersen's syndrome mutation effects on the structure and assembly of the cytoplasmic domains of Kir2.1. Biochemistry. 2006;45(28):8599-606.
138. Nichols CG, Lopatin AN. Inward rectifier potassium channels. Annu Rev Physiol. 1997;59:171-91.
139. Baronas VA, Kurata HT. Inward rectifiers and their regulation by endogenous polyamines. Front Physiol. 2014;5:325.

140. Vanhaesebroeck B, Leevers SJ, Ahmadi K, Timms J, Katso R, Driscoll PC, et al. Synthesis and function of 3-phosphorylated inositol lipids. Annu Rev Biochem. 2001;70:535-602.
141. McLaughlin S, Wang J, Gambhir A, Murray D. PIP(2) and proteins: interactions, organization, and information flow. Annu Rev Biophys Biomol Struct. 2002;31:151-75.
142. Huang CL, Feng S, Hilgemann DW. Direct activation of inward rectifier potassium channels by PIP2 and its stabilization by Gbetagamma. Nature. 1998;391(6669):803-6.
143. Lee SJ, Wang S, Borschel W, Heyman S, Gyore J, Nichols CG. Secondary anionic phospholipid binding site and gating mechanism in Kir2.1 inward rectifier channels. Nat Commun. 2013;4:2786.
144. Arikketh D, Nelson R, Vance JE. Defining the importance of phosphatidylserine synthase-1 (PSS1): unexpected viability of PSS1-deficient mice. J Biol Chem. 2008;283(19):12888-97.
145. Yeagle PL. Cholesterol and the cell membrane. Biochim Biophys Acta. 1985;822(3-4):267-87.
146. Romanenko VG, Rothblat GH, Levitan I. Modulation of endothelial inward-rectifier K+ current by optical isomers of cholesterol. Biophys J. 2002;83(6):3211-22.
147. Tikku S, Epshtein Y, Collins H, Travis AJ, Rothblat GH, Levitan I. Relationship between Kir2.1/Kir2.3 activity and their distributions between cholesterol-rich and cholesterol-poor membrane domains. Am J Physiol Cell Physiol. 2007;293(1):C440-50.
148. Ambrosini E, Sicca F, Brignone MS, D'Adamo MC, Napolitano C, Servettini I, et al. Genetically induced dysfunctions of Kir2.1 channels: implications for short QT3 syndrome and autism-epilepsy phenotype. Hum Mol Genet. 2014;23(18):4875-86.
149. Epshtein Y, Chopra AP, Rosenhouse-Dantsker A, Kowalsky GB, Logothetis DE, Levitan I. Identification of a C-terminus domain critical for the sensitivity of Kir2.1 to cholesterol. Proc Natl Acad Sci U S A. 2009;106(19):8055-60.
150. Rosenhouse-Dantsker A, Epshtein Y, Levitan I. Interplay Between Lipid Modulators of Kir2 Channels: Cholesterol and PIP2. Comput Struct Biotechnol J. 2014;11(19):131-7.
151. Singer SJ, Nicolson GL. The fluid mosaic model of the structure of cell membranes. Science. 1972;175(4023):720-31.
152. Alberts B jA, Lewis J et al. Molecular Biology of the Cell. 4th edition. . New York: Garland Science; 2002.
153. Balasubramanian K, Schroit AJ. Aminophospholipid asymmetry: A matter of life and death. Annu Rev Physiol. 2003;65:701-34.
154. Yu K, Whitlock JM, Lee K, Ortlund EA, Cui YY, Hartzell HC. Identification of a lipid scrambling domain in ANO6/TMEM16F. Elife. 2015;4:e06901.
155. Nagata S, Suzuki J, Segawa K, Fujii T. Exposure of phosphatidylserine on the cell surface. Cell Death Differ. 2016;23(6):952-61.

156. Gibellini F, Smith TK. The Kennedy pathway--De novo synthesis of phosphatidylethanolamine and phosphatidylcholine. IUBMB Life. 2010;62(6):414-28.
157. Kuge O, Nishijima M. Phosphatidylserine synthase I and II of mammalian cells. Biochim Biophys Acta. 1997;1348(1-2):151-6.
158. Bergo MO, Gavino BJ, Steenbergen R, Sturbois B, Parlow AF, Sanan DA, et al. Defining the importance of phosphatidylserine synthase 2 in mice. J Biol Chem. 2002;277(49):47701-8.
159. Calzada E, Onguka O, Claypool SM. Phosphatidylethanolamine Metabolism in Health and Disease. Int Rev Cell Mol Biol. 2016;321:29-88.
160. Bevers EM, Comfurius P, van Rijn JL, Hemker HC, Zwaal RF. Generation of prothrombin-converting activity and the exposure of phosphatidylserine at the outer surface of platelets. Eur J Biochem. 1982;122(2):429-36.
161. Lhermusier T, Chap H, Payrastre B. Platelet membrane phospholipid asymmetry: from the characterization of a scramblase activity to the identification of an essential protein mutated in Scott syndrome. J Thromb Haemost. 2011;9(10):1883-91.
162. Suzuki J, Umeda M, Sims PJ, Nagata S. Calcium-dependent phospholipid scrambling by TMEM16F. Nature. 2010;468(7325):834-8.
163. van den Eijnde SM, Boshart L, Baehrecke EH, De Zeeuw CI, Reutelingsperger CP, Vermeij-Keers C. Cell surface exposure of phosphatidylserine during apoptosis is phylogenetically conserved. Apoptosis. 1998;3(1):9-16.
164. Williamson P, Schlegel RA. Transbilayer phospholipid movement and the clearance of apoptotic cells. Biochim Biophys Acta. 2002;1585(2-3):53-63.
165. Grinstein JGKaS. Lipid-mediated Protein Signaling2013.
166. Bevers EM, Wiedmer T, Comfurius P, Shattil SJ, Weiss HJ, Zwaal RF, et al. Defective Ca(2+)-induced microvesiculation and deficient expression of procoagulant activity in erythrocytes from a patient with a bleeding disorder: a study of the red blood cells of Scott syndrome. Blood. 1992;79(2):380-8.
167. Hanayama R, Tanaka M, Miwa K, Shinohara A, Iwamatsu A, Nagata S. Identification of a factor that links apoptotic cells to phagocytes. Nature. 2002;417(6885):182-7.
168. Hannun YA, Loomis CR, Bell RM. Activation of protein kinase C by Triton X-100 mixed micelles containing diacylglycerol and phosphatidylserine. J Biol Chem. 1985;260(18):10039-43.
169. Nishizuka Y. The role of protein kinase C in cell surface signal transduction and tumour promotion. Nature. 1984;308(5961):693-8.
170. Dimmeler S, Fleming I, Fisslthaler B, Hermann C, Busse R, Zeiher AM. Activation of nitric oxide synthase in endothelial cells by Akt-dependent phosphorylation. Nature. 1999;399(6736):601-5.
171. Fairn GD, Hermansson M, Somerharju P, Grinstein S. Phosphatidylserine is polarized and required for proper Cdc42 localization and for development of cell polarity. Nat Cell Biol. 2011;13(12):1424-30.

172. Yeung T, Heit B, Dubuisson JF, Fairn GD, Chiu B, Inman R, et al. Contribution of phosphatidylserine to membrane surface charge and protein targeting during phagosome maturation. J Cell Biol. 2009;185(5):917-28.
173. Vance JE, Tasseva G. Formation and function of phosphatidylserine and phosphatidylethanolamine in mammalian cells. Biochim Biophys Acta. 2013;1831(3):543-54.
174. Uchida Y, Hasegawa J, Chinnapen D, Inoue T, Okazaki S, Kato R, et al. Intracellular phosphatidylserine is essential for retrograde membrane traffic through endosomes. Proc Natl Acad Sci U S A. 2011;108(38):15846-51.
175. Chung J, Torta F, Masai K, Lucast L, Czapla H, Tanner LB, et al. INTRACELLULAR TRANSPORT. PI4P/phosphatidylserine countertransport at ORP5- and ORP8-mediated ER-plasma membrane contacts. Science. 2015;349(6246):428-32.
176. Mochizuki S, Miki H, Zhou R, Noda Y. The involvement of oxysterol-binding protein related protein (ORP) 6 in the counter-transport of phosphatidylinositol-4-phosphate (PI4P) and phosphatidylserine (PS) in neurons. Biochem Biophys Rep. 2022;30:101257.
177. Trinh MN, Brown MS, Goldstein JL, Han J, Vale G, McDonald JG, et al. Last step in the path of LDL cholesterol from lysosome to plasma membrane to ER is governed by phosphatidylserine. Proc Natl Acad Sci U S A. 2020;117(31):18521-9.
178. Daumke O, Lundmark R, Vallis Y, Martens S, Butler PJ, McMahon HT. Architectural and mechanistic insights into an EHD ATPase involved in membrane remodelling. Nature. 2007;449(7164):923-7.
179. Pike LJ, Han X, Gross RW. Epidermal growth factor receptors are localized to lipid rafts that contain a balance of inner and outer leaflet lipids: a shotgun lipidomics study. J Biol Chem. 2005;280(29):26796-804.
180. Fairn GD, Schieber NL, Ariotti N, Murphy S, Kuerschner L, Webb RI, et al. High-resolution mapping reveals topologically distinct cellular pools of phosphatidylserine. J Cell Biol. 2011;194(2):257-75.
181. Hirama T, Das R, Yang Y, Ferguson C, Won A, Yip CM, et al. Phosphatidylserine dictates the assembly and dynamics of caveolae in the plasma membrane. J Biol Chem. 2017;292(34):14292-307.
182. Fuller N, Benatti CR, Rand RP. Curvature and bending constants for phosphatidylserine-containing membranes. Biophys J. 2003;85(3):1667-74.
183. Kooijman EE, Chupin V, Fuller NL, Kozlov MM, de Kruijff B, Burger KN, et al. Spontaneous curvature of phosphatidic acid and lysophosphatidic acid. Biochemistry. 2005;44(6):2097-102.
184. Hirama T, Lu SM, Kay JG, Maekawa M, Kozlov MM, Grinstein S, et al. Membrane curvature induced by proximity of anionic phospholipids can initiate endocytosis. Nat Commun. 2017;8(1):1393.
185. Maekawa M, Fairn GD. Complementary probes reveal that phosphatidylserine is required for the proper transbilayer distribution of cholesterol. J Cell Sci. 2015;128(7):1422-33.

186. Flores-Nascimento MC, Orsi FL, Yokoyama AP, Pereira FG, Lorand-Metze I, De Paula EV, et al. Diagnosis of Scott syndrome in patient with bleeding disorder of unknown cause. Blood Coagul Fibrinolysis. 2012;23(1):75-7.
187. Sohn M, Ivanova P, Brown HA, Toth DJ, Varnai P, Kim YJ, et al. Lenz-Majewski mutations in PTDSS1 affect phosphatidylinositol 4-phosphate metabolism at ER-PM and ER-Golgi junctions. Proc Natl Acad Sci U S A. 2016;113(16):4314-9.
188. Sousa SB, Jenkins D, Chanudet E, Tasseva G, Ishida M, Anderson G, et al. Gain-of-function mutations in the phosphatidylserine synthase 1 (PTDSS1) gene cause Lenz-Majewski syndrome. Nat Genet. 2014;46(1):70-6.
189. Pike LJ. Lipid rafts: bringing order to chaos. J Lipid Res. 2003;44(4):655-67.
190. Palade GE, Bruns RR. Structural modulations of plasmalemmal vesicles. J Cell Biol. 1968;37(3):633-49.
191. Stan RV. Structure of caveolae. Biochim Biophys Acta. 2005;1746(3):334-48.
192. Yamada E. The fine structure of the gall bladder epithelium of the mouse. J Biophys Biochem Cytol. 1955;1(5):445-58.
193. Rothberg KG, Heuser JE, Donzell WC, Ying YS, Glenney JR, Anderson RG. Caveolin, a protein component of caveolae membrane coats. Cell. 1992;68(4):673-82.
194. Fujita A, Cheng J, Tauchi-Sato K, Takenawa T, Fujimoto T. A distinct pool of phosphatidylinositol 4,5-bisphosphate in caveolae revealed by a nanoscale labeling technique. Proc Natl Acad Sci U S A. 2009;106(23):9256-61.
195. Chidlow JH, Jr., Sessa WC. Caveolae, caveolins, and cavins: complex control of cellular signalling and inflammation. Cardiovasc Res. 2010;86(2):219-25.
196. Yguerabide J, Schmidt JA, Yguerabide EE. Lateral mobility in membranes as detected by fluorescence recovery after photobleaching. Biophys J. 1982;40(1):69-75.
197. Yamamoto K, Ando J. Vascular endothelial cell membranes differentiate between stretch and shear stress through transitions in their lipid phases. Am J Physiol Heart Circ Physiol. 2015;309(7):H1178-85.
198. Yamamoto K, Ando J. Emerging Role of Plasma Membranes in Vascular Endothelial Mechanosensing. Circ J. 2018;82(11):2691-8.
199. Jander K, Greulich J, Gonnissen S, Ale-Agha N, Goy C, Jakobs P, et al. Extra-Nuclear Functions of the Transcription Factor Grainyhead-Like 3 in the Endothelium-Interaction with Endothelial Nitric Oxide Synthase. Antioxidants (Basel). 2021;10(3).
200. Ottolini M, Daneva Z, Chen YL, Cope EL, Kasetti RB, Zode GS, et al. Mechanisms underlying selective coupling of endothelial Ca(2+) signals with eNOS vs. IK/SK channels in systemic and pulmonary arteries. J Physiol. 2020;598(17):3577-96.
201. Ottolini M, Hong K, Cope EL, Daneva Z, DeLalio LJ, Sokolowski JD, et al. Local Peroxynitrite Impairs Endothelial Transient Receptor Potential Vanilloid 4

Channels and Elevates Blood Pressure in Obesity. Circulation. 2020;141(16):1318-33.
202. Rohacs T, Chen J, Prestwich GD, Logothetis DE. Distinct specificities of inwardly rectifying K(+) channels for phosphoinositides. J Biol Chem. 1999;274(51):36065-72.
203. Del Vecchio K, Stahelin RV. Investigation of the phosphatidylserine binding properties of the lipid biosensor, Lactadherin C2 (LactC2), in different membrane environments. J Bioenerg Biomembr. 2018;50(1):1-10.
204. Andersen MH, Graversen H, Fedosov SN, Petersen TE, Rasmussen JT. Functional analyses of two cellular binding domains of bovine lactadherin. Biochemistry. 2000;39(20):6200-6.
205. Shi J, Heegaard CW, Rasmussen JT, Gilbert GE. Lactadherin binds selectively to membranes containing phosphatidyl-L-serine and increased curvature. Biochim Biophys Acta. 2004;1667(1):82-90.
206. Dasgupta SK, Guchhait P, Thiagarajan P. Lactadherin binding and phosphatidylserine expression on cell surface-comparison with annexin A5. Transl Res. 2006;148(1):19-25.
207. Mather S, Dora KA, Sandow SL, Winter P, Garland CJ. Rapid endothelial cell-selective loading of connexin 40 antibody blocks endothelium-derived hyperpolarizing factor dilation in rat small mesenteric arteries. CircRes. 2005;97(4):399-407.
208. Shen N, Zheng J, Liu H, Xu K, Chen Q, Chen Y, et al. Barium chloride impaired Kir2.1 inward rectification in its stably transfected HEK 293 cell lines. Eur J Pharmacol. 2014;730:164-70.
209. Lin CJ, Staiculescu MC, Hawes JZ, Cocciolone AJ, Hunkins BM, Roth RA, et al. Heterogeneous Cellular Contributions to Elastic Laminae Formation in Arterial Wall Development. Circ Res. 2019;125(11):1006-18.
210. Wilson C, Zhang X, Lee MD, MacDonald M, Heathcote HR, Alorfi NMN, et al. Disrupted endothelial cell heterogeneity and network organization impair vascular function in prediabetic obesity. Metabolism. 2020;111:154340.
211. Lee MD, Wilson C, Saunter CD, Kennedy C, Girkin JM, McCarron JG. Spatially structured cell populations process multiple sensory signals in parallel in intact vascular endothelium. Sci Signal. 2018;11(561).
212. Nakatsu F, Kawasaki A. Functions of Oxysterol-Binding Proteins at Membrane Contact Sites and Their Control by Phosphoinositide Metabolism. Front Cell Dev Biol. 2021;9:664788.
213. Ma D, Zerangue N, Lin YF, Collins A, Yu M, Jan YN, et al. Role of ER export signals in controlling surface potassium channel numbers. Science. 2001;291(5502):316-9.
214. Stockklausner C, Ludwig J, Ruppersberg JP, Klocker N. A sequence motif responsible for ER export and surface expression of Kir2.0 inward rectifier K(+) channels. FEBS Lett. 2001;493(2-3):129-33.
215. Razani B, Engelman JA, Wang XB, Schubert W, Zhang XL, Marks CB, et al. Caveolin-1 null mice are viable but show evidence of hyperproliferative and vascular abnormalities. J Biol Chem. 2001;276(41):38121-38.

216. Arcangeli A, Becchetti A. Complex functional interaction between integrin receptors and ion channels. Trends Cell Biol. 2006;16(12):631-9.
217. Sengupta S, Rothenberg KE, Li H, Hoffman BD, Bursac N. Altering integrin engagement regulates membrane localization of Kir2.1 channels. J Cell Sci. 2019;132(17).
218. Sohn M, Korzeniowski M, Zewe JP, Wills RC, Hammond GRV, Humpolickova J, et al. PI(4,5)P2 controls plasma membrane PI4P and PS levels via ORP5/8 recruitment to ER-PM contact sites. J Cell Biol. 2018;217(5):1797-813.
219. Wong LC, Langille BL. Developmental remodeling of the internal elastic lamina of rabbit arteries: effect of blood flow. Circ Res. 1996;78(5):799-805.
220. Di Russo J, Luik AL, Yousif L, Budny S, Oberleithner H, Hofschroer V, et al. Endothelial basement membrane laminin 511 is essential for shear stress response. EMBO J. 2017;36(2):183-201.
221. Humphries JD, Byron A, Humphries MJ. Integrin ligands at a glance. J Cell Sci. 2006;119(Pt 19):3901-3.
222. Zhou X, Rowe RG, Hiraoka N, George JP, Wirtz D, Mosher DF, et al. Fibronectin fibrillogenesis regulates three-dimensional neovessel formation. Genes Dev. 2008;22(9):1231-43.
223. Stratman AN, Davis GE. Endothelial cell-pericyte interactions stimulate basement membrane matrix assembly: influence on vascular tube remodeling, maturation, and stabilization. Microsc Microanal. 2012;18(1):68-80.
224. Bloksgaard M, Leurgans TM, Nissen I, Jensen PS, Hansen ML, Brewer JR, et al. Elastin organization in pig and cardiovascular disease patients' pericardial resistance arteries. J Vasc Res. 2015;52(1):1-11.
225. Fischer GM, Llaurado JG. Collagen and elastin content in canine arteries selected from functionally different vascular beds. Circ Res. 1966;19(2):394-9.
226. Schwartz E, Adamany AM, Blumenfeld OO. Isolation and characterization of the internal elastic lamina from calf thoracic aorta. Exp Mol Pathol. 1981;34(3):299-306.
227. Lee RM. Morphology of cerebral arteries. Pharmacol Ther. 1995;66(1):149-73.
228. Harkness ML, Harkness RD, McDonald DA. The collagen and elastin content of the arterial wall in the dog. Proc R Soc Lond B Biol Sci. 1957;146(925):541-51.
229. Dobrin PB. Mechanical properties of arteries. Physiol Rev. 1978;58(2):397-460.
230. Unemori EN, Bouhana KS, Werb Z. Vectorial secretion of extracellular matrix proteins, matrix-degrading proteinases, and tissue inhibitor of metalloproteinases by endothelial cells. J Biol Chem. 1990;265(1):445-51.
231. Carnes WH, Abraham PA, Buonassisi V. Biosynthesis of elastin by an endothelial cell culture. Biochem Biophys Res Commun. 1979;90(4):1393-9.
232. Cantor JO, Keller S, Parshley MS, Darnule TV, Darnule AT, Cerreta JM, et al. Synthesis of crosslinked elastin by an endothelial cell culture. Biochem Biophys Res Commun. 1980;95(4):1381-6.

233. Damiano V, Tsang A, Weinbaum G, Christner P, Rosenbloom J. Secretion of elastin in the embryonic chick aorta as visualized by immunoelectron microscopy. Coll Relat Res. 1984;4(2):153-64.
234. Myers PR, Tanner MA. Vascular endothelial cell regulation of extracellular matrix collagen: role of nitric oxide. Arterioscler Thromb Vasc Biol. 1998;18(5):717-22.
235. Sechler JL, Corbett SA, Wenk MB, Schwarzbauer JE. Modulation of cell-extracellular matrix interactions. Ann N Y Acad Sci. 1998;857:143-54.
236. Rohwedder I, Montanez E, Beckmann K, Bengtsson E, Duner P, Nilsson J, et al. Plasma fibronectin deficiency impedes atherosclerosis progression and fibrous cap formation. EMBO Mol Med. 2012;4(7):564-76.
237. Shapiro SD, Endicott SK, Province MA, Pierce JA, Campbell EJ. Marked longevity of human lung parenchymal elastic fibers deduced from prevalence of D-aspartate and nuclear weapons-related radiocarbon. J Clin Invest. 1991;87(5):1828-34.
238. Ozsvar J, Yang C, Cain SA, Baldock C, Tarakanova A, Weiss AS. Tropoelastin and Elastin Assembly. Front Bioeng Biotechnol. 2021;9:643110.
239. Kagan HM, Sullivan KA. Lysyl oxidase: preparation and role in elastin biosynthesis. Methods Enzymol. 1982;82 Pt A:637-50.
240. Sandberg LB, Weissman N, Gray WR. Structural features of tropoelastin related to the sites of cross-links in aortic elastin. Biochemistry. 1971;10(1):52-6.
241. Reichheld SE, Muiznieks LD, Lu R, Sharpe S, Keeley FW. Sequence variants of human tropoelastin affecting assembly, structural characteristics and functional properties of polymeric elastin in health and disease. Matrix Biol. 2019;84:68-80.
242. Debelle L, Tamburro AM. Elastin: molecular description and function. Int J Biochem Cell Biol. 1999;31(2):261-72.
243. Rauscher S, Pomes R. The liquid structure of elastin. Elife. 2017;6.
244. Schmelzer CEH, Heinz A, Troilo H, Lockhart-Cairns MP, Jowitt TA, Marchand MF, et al. Lysyl oxidase-like 2 (LOXL2)-mediated cross-linking of tropoelastin. FASEB J. 2019;33(4):5468-81.
245. Wagenseil JE, Mecham RP. New insights into elastic fiber assembly. Birth Defects Res C Embryo Today. 2007;81(4):229-40.
246. Ritz-Timme S, Laumeier I, Collins M. Age estimation based on aspartic acid racemization in elastin from the yellow ligaments. Int J Legal Med. 2003;117(2):96-101.
247. Kielty CM, Sherratt MJ, Shuttleworth CA. Elastic fibres. J Cell Sci. 2002;115(Pt 14):2817-28.
248. Sakai LY, Keene DR, Glanville RW, Bachinger HP. Purification and partial characterization of fibrillin, a cysteine-rich structural component of connective tissue microfibrils. J Biol Chem. 1991;266(22):14763-70.
249. Carta L, Pereira L, Arteaga-Solis E, Lee-Arteaga SY, Lenart B, Starcher B, et al. Fibrillins 1 and 2 perform partially overlapping functions during aortic development. J Biol Chem. 2006;281(12):8016-23.
250. Brown-Augsburger P, Broekelmann T, Mecham L, Mercer R, Gibson MA, Cleary EG, et al. Microfibril-associated glycoprotein binds to the carboxyl-

terminal domain of tropoelastin and is a substrate for transglutaminase. J Biol Chem. 1994;269(45):28443-9.
251. Jensen SA, Reinhardt DP, Gibson MA, Weiss AS. Protein interaction studies of MAGP-1 with tropoelastin and fibrillin-1. J Biol Chem. 2001;276(43):39661-6.
252. Henderson M, Polewski R, Fanning JC, Gibson MA. Microfibril-associated glycoprotein-1 (MAGP-1) is specifically located on the beads of the beaded-filament structure for fibrillin-containing microfibrils as visualized by the rotary shadowing technique. J Histochem Cytochem. 1996;44(12):1389-97.
253. Timpl R, Sasaki T, Kostka G, Chu ML. Fibulins: a versatile family of extracellular matrix proteins. Nat Rev Mol Cell Biol. 2003;4(6):479-89.
254. Yanagisawa H, Davis EC, Starcher BC, Ouchi T, Yanagisawa M, Richardson JA, et al. Fibulin-5 is an elastin-binding protein essential for elastic fibre development in vivo. Nature. 2002;415(6868):168-71.
255. Zanetti M, Braghetta P, Sabatelli P, Mura I, Doliana R, Colombatti A, et al. EMILIN-1 deficiency induces elastogenesis and vascular cell defects. Mol Cell Biol. 2004;24(2):638-50.
256. Faury G, Pezet M, Knutsen RH, Boyle WA, Heximer SP, McLean SE, et al. Developmental adaptation of the mouse cardiovascular system to elastin haploinsufficiency. J Clin Invest. 2003;112(9):1419-28.
257. Zacchigna L, Vecchione C, Notte A, Cordenonsi M, Dupont S, Maretto S, et al. Emilin1 links TGF-beta maturation to blood pressure homeostasis. Cell. 2006;124(5):929-42.
258. Ning Cui MH, Raouf A. Khalil. Chapter One - Biochemical and Biological Attributes of Matrix Metalloproteinases. Progress in Molecular Biology and Translational Science2017.
259. Miekus N, Luise C, Sippl W, Baczek T, Schmelzer CEH, Heinz A. MMP-14 degrades tropoelastin and elastin. Biochimie. 2019;165:32-9.
260. Patterson ML, Atkinson SJ, Knauper V, Murphy G. Specific collagenolysis by gelatinase A, MMP-2, is determined by the hemopexin domain and not the fibronectin-like domain. FEBS Lett. 2001;503(2-3):158-62.
261. Galis ZS, Khatri JJ. Matrix metalloproteinases in vascular remodeling and atherogenesis: the good, the bad, and the ugly. Circ Res. 2002;90(3):251-62.
262. Zaltsman AB, Newby AC. Increased secretion of gelatinases A and B from the aortas of cholesterol fed rabbits: relationship to lesion severity. Atherosclerosis. 1997;130(1-2):61-70.
263. Li DY, Brooke B, Davis EC, Mecham RP, Sorensen LK, Boak BB, et al. Elastin is an essential determinant of arterial morphogenesis. Nature. 1998;393(6682):276-80.
264. Wagenseil JE, Nerurkar NL, Knutsen RH, Okamoto RJ, Li DY, Mecham RP. Effects of elastin haploinsufficiency on the mechanical behavior of mouse arteries. Am J Physiol Heart Circ Physiol. 2005;289(3):H1209-17.
265. Heil J, Olsavszky V, Busch K, Klapproth K, de la Torre C, Sticht C, et al. Bone marrow sinusoidal endothelium controls terminal erythroid differentiation and reticulocyte maturation. Nat Commun. 2021;12(1):6963.

266. Zhong J, Yang HC, Kon V, Fogo AB, Lawrence DA, Ma J. Vitronectin-binding PAI-1 protects against the development of cardiac fibrosis through interaction with fibroblasts. Lab Invest. 2014;94(6):633-44.
267. Severs NJ, Rothery S, Dupont E, Coppen SR, Yeh HI, Ko YS, et al. Immunocytochemical analysis of connexin expression in the healthy and diseased cardiovascular system. Microsc Res Tech. 2001;52(3):301-22.
268. Wong LH, Copic A, Levine TP. Advances on the Transfer of Lipids by Lipid Transfer Proteins. Trends Biochem Sci. 2017;42(7):516-30.
269. Lehto M, Laitinen S, Chinetti G, Johansson M, Ehnholm C, Staels B, et al. The OSBP-related protein family in humans. J Lipid Res. 2001;42(8):1203-13.
270. Anniss AM, Apostolopoulos J, Dworkin S, Purton LE, Sparrow RL. An oxysterol-binding protein family identified in the mouse. DNA Cell Biol. 2002;21(8):571-80.
271. Jaworski CJ, Moreira E, Li A, Lee R, Rodriguez IR. A family of 12 human genes containing oxysterol-binding domains. Genomics. 2001;78(3):185-96.
272. Zhou Y, Wohlfahrt G, Paavola J, Olkkonen VM. A vertebrate model for the study of lipid binding/transfer protein function: conservation of OSBP-related proteins between zebrafish and human. Biochem Biophys Res Commun. 2014;446(3):675-80.
273. Levine TP, Munro S. Targeting of Golgi-specific pleckstrin homology domains involves both PtdIns 4-kinase-dependent and -independent components. Curr Biol. 2002;12(9):695-704.
274. Im YJ, Raychaudhuri S, Prinz WA, Hurley JH. Structural mechanism for sterol sensing and transport by OSBP-related proteins. Nature. 2005;437(7055):154-8.
275. Olkkonen VM. OSBP-Related Protein Family in Lipid Transport Over Membrane Contact Sites. Lipid Insights. 2015;8(Suppl 1):1-9.
276. Mesmin B, Bigay J, Moser von Filseck J, Lacas-Gervais S, Drin G, Antonny B. A four-step cycle driven by PI(4)P hydrolysis directs sterol/PI(4)P exchange by the ER-Golgi tether OSBP. Cell. 2013;155(4):830-43.
277. Di Paolo G, De Camilli P. Phosphoinositides in cell regulation and membrane dynamics. Nature. 2006;443(7112):651-7.
278. Del Bel LM, Brill JA. Sac1, a lipid phosphatase at the interface of vesicular and nonvesicular transport. Traffic. 2018;19(5):301-18.
279. Koponen A, Pan G, Kivela AM, Ralko A, Taskinen JH, Arora A, et al. ORP2, a cholesterol transporter, regulates angiogenic signaling in endothelial cells. FASEB J. 2020;34(11):14671-94.
280. Lee SJ, Ren F, Zangerl-Plessl EM, Heyman S, Stary-Weinzinger A, Yuan P, et al. Structural basis of control of inward rectifier Kir2 channel gating by bulk anionic phospholipids. J Gen Physiol. 2016;148(3):227-37.
281. Knutsen RH, Beeman SC, Broekelmann TJ, Liu D, Tsang KM, Kovacs A, et al. Minoxidil improves vascular compliance, restores cerebral blood flow, and alters extracellular matrix gene expression in a model of chronic vascular stiffness. Am J Physiol Heart Circ Physiol. 2018;315(1):H18-H32.
282. Kassai B, Bouye P, Gilbert-Dussardier B, Godart F, Thambo JB, Rossi M, et al. Minoxidil versus placebo in the treatment of arterial wall hypertrophy in

children with Williams Beuren Syndrome: a randomized controlled trial. BMC Pediatr. 2019;19(1):170.
283. Zargham R, Touyz RM, Thibault G. alpha 8 Integrin overexpression in de-differentiated vascular smooth muscle cells attenuates migratory activity and restores the characteristics of the differentiated phenotype. Atherosclerosis. 2007;195(2):303-12.